The Dissertation Committee for Cesar Mattos de Salles Soares Certifies that this is the approved version of the following Dissertation:

Continuous Learning of Analytical and Machine Learning Rate of Penetration (ROP) Models for Real-Time Drilling Optimization

Committee:

Kenneth Gray, Supervisor

Hugh Daigle

Michael Pyrcz

Harry Millwater

Neilkunal Panchal

Continuous Learning of Analytical and Machine Learning Rate of Penetration (ROP) Models for Real-Time Drilling Optimization

by

Cesar Mattos de Salles Soares

Dissertation

Presented to the Faculty of the Graduate School of

The University of Texas at Austin

in Partial Fulfillment

of the Requirements

for the Degree of

Doctor of Philosophy

The University of Texas at Austin

August 2018

Dedication

To my parents, Deborah and Jair, to my brother, Dante, and to my wife, Elifnaz.

Acknowledgements

Abstract

Continuous Learning of Analytical and Machine Learning Rate of Penetration (ROP) Models for Real-Time Drilling Optimization

Cesar Mattos de Salles Soares, Ph.D.

The University of Texas at Austin, 2018

Supervisor: Kenneth Gray

Oil and gas operators strive to reach hydrocarbon reserves by drilling wells in the safest and fastest possible manner, providing indispensable energy to society at reduced costs while maintaining environmental sustainability. Real-time drilling optimization consists of selecting operational drilling parameters that maximize a desirable measure of drilling performance. Drilling optimization efforts often aspire to improve drilling speed, commonly referred to as rate of penetration (ROP). ROP is a function of the forces and moments applied to the bit, in addition to mud, formation, bit and hydraulic properties. Three operational drilling parameters may be constantly adjusted at surface to influence ROP towards a drilling objective: weight on bit (WOB), drillstring rotational speed (RPM), and drilling fluid (mud) flow rate.

In the traditional, analytical approach to ROP modeling, inflexible equations relate WOB, RPM, flow rate and/or other measurable drilling parameters to ROP and empirical model coefficients are computed for each rock formation to best fit field data. Over the last decade, enhanced data acquisition technology and widespread cheap computational power have driven a surge in applications of machine learning (ML) techniques to ROP

prediction. Machine learning algorithms leverage statistics to uncover relations between any prescribed inputs (features/predictors) and the quantity of interest (response). The biggest advantage of ML algorithms over analytical models is their flexibility in model form. With no set equation, ML models permit segmentation of the drilling operational parameter space. However, increased model complexity diminishes interpretability of how an adjustment to the inputs will affect the output. There is no single ROP model applicable in every situation.

This study investigates all stages of the drilling optimization workflow, with emphasis on real-time continuous model learning. Sensors constantly record data as wells are drilled, and it is postulated that ROP models can be retrained in real-time to adapt to changing drilling conditions. Cross-validation is assessed as a methodology to select the best performing ROP model for each drilling optimization interval in real-time. Constrained to rig equipment and operational limitations, drilling parameters are optimized in intervals with the most accurate ROP model determined by cross-validation. Dynamic range and full range training data segmentation techniques contest the classical lithology-dependent approach to ROP modeling. Spatial proximity and parameter similarity sample weighting expand data partitioning capabilities during model training. The prescribed ROP modeling and drilling parameter optimization scenarios are evaluated according to model performance, ROP improvements and computational expense.

Table of Contents

List of Tables

List of Figures

Chapter 1: Introduction and Background

In a quest to access abundant energy resources, oil and gas companies drill wells through the Earth's crust to strike hydrocarbon reservoirs in older geological rock formations. Well construction requires translational, rotational and hydraulic energy systems. Drilling rigs supply the power and equipment necessary to handle large quantities of heavy pipe and create boreholes. Threaded joints of steel pipe compose the drillstring, which serves as the conduit for both axial and rotational forces imparted by the drill bit on rock formations. Axial force is provided by the weight of drillstring components, supported by a hook at the end of the rig's travelling block. Drilling line is strung through the traveling block and the crown block to gain mechanical advantage. The drawworks motor reels drilling line in and out, manipulating the tension in the drilling line (hookload) and controlling the amount of axial force that reaches the bit. Modern rigs contain a top drive motor. Connected to the drillstring at the surface, the top drive produces torque needed to break rock downhole. Hydraulic energy is generated by robust pumps and transmitted to the bottom of the well by the drilling fluid. Drilling fluid, also known as drilling mud, is pumped inside the drillpipe, through the bit nozzles and back up to the surface via the annular space between the drillstring and the wellbore. Drilling mud serves a variety of purposes, such as providing the primary pressure barrier preventing formation fluids from reaching the wellbore, cooling the bit from heat created by friction and circulating drilled rock cuttings to the surface.

Before the well construction process begins, engineers devote a considerable amount of time to trajectory planning, drill bit, mud, and drillstring design and baseline operational parameters selection according to historical field knowledge and equipment constraints. Operational parameters related to the three energy systems described are

controlled at the surface to optimize drilling: axial force at the bit, drillstring rotational speed and drilling fluid flow rate. Real-time adjustment of these variables allows for drilling faster, reducing vibrations and/or preventing drilling dysfunctions.

Data collected by sensors at the surface and downhole are key drivers for fine-tuning drilling operational parameters. With drilling rigs instrumented to measure ever-increasing volumes of data, machine learning and data analytics have emerged as a dominant trend in drilling optimization. Contemporary articles in oil and gas news websites have emphasized the importance of the digitization revolution in the industry. Veazey (2018) states that 400 oil and gas employees in key leadership roles agree that insights derived from data can contribute to 16% reduction in operating costs. Hart (2018) reports that artificial intelligence can cut costs by 20% in drilling and completions operations. Zborowski (2018) describes the efforts of an operator to facilitate data processing and analysis with centralized databases, citing a reduction in average well drilling time from a month to 12 days in the Eagle Ford shale play due to data analytics. Papers presented in recent conferences corroborate these viewpoints, indicating a prevalent tendency in the oil and gas industry towards advanced analytics solutions (Cao *et al.*, 2018). Liu *et al.* (2018) unveil one such example related to drilling optimization, introducing a real-time data analytics application built with an agile development strategy. Oil and gas companies have just begun to realize the vast rewards attained from data analytics, which can add enormous value to drilling speed modeling and optimization of operational drilling parameters.

1.1. PROBLEM STATEMENT

Drilling optimization refers to the process of designing equipment and selecting operational parameters to minimize the cost of drilling a well. In this context, drilling speed, commonly referred to as rate of penetration (ROP), emerges as a key performance

metric (Judzis *et al*., 2007, Auwal *et al*., 2012, Armenta *et al*., 2015). Sikes (1936) identified six factors that influence the ROP attained on the field: rock formation, hole diameter, hole cleaning and hydraulics, weight on bit (WOB), rotational speed (RPM), and bit type. Formation properties, such as confined compressive strength (CCS), abrasiveness, heterogeneity, pore pressure and permeability, profoundly impact ROP. Although rock strength may be estimated from sonic travel times and other electric log properties (Onyia, 1988) with logging-while-drilling (LWD) tools, low-frequency mud pulse telemetry downhole data is not appropriate for real-time applications and wired pipe technology does not prove itself economical in most plays. Drilling programs certainly plan for varying lithology, but current technology does not allow for active control over rock properties.

During the planning phase of a well, drilling engineers determine bit, drillstring and mud configurations best suited for drilling through a particular stratigraphic section. In addition to bit diameter, polycrystalline diamond compact (PDC) bit design parameters encompass the number of PDC cutters, PDC cutter siderake angle, and PDC cutter backrake angle. Sinor *et al*. (1998) experimentally evaluated the influence of cutter density, backrake angle, size and rotational speed on ROP, concluding that cutter backrake angle controls ROP and more aggressive (small backrake) cutters drill faster. On the other hand, more aggressive bits tend to wear faster and may produce long rock cuttings that are detrimental to hole cleaning (Hemphill *et al*., 2001). Drill bit manufacturers optimize bit and cutter design parameters for specific applications (Norris *et al*., 1998, Centala *et al*., 2011, Bruton *et al*., 2014, Yan *et al*., 2014, Azar *et al*., 2015) based on the operating company's preference or market needs. However, drillstring composition and bit properties cannot be altered in real-time to mitigate drilling dysfunctions or adjust to formation changes. Similarly, mud density and viscosity affect ROP (Eckel, 1954, Eckel, 1967) but

3

are generally determined in the pre-drill phase to satisfy lithology and hole cleaning constraints and can only be manipulated within an often narrow drilling window.

Drilling is a complex process, and a function of several variables which are difficult or impossible to measure in real-time. As an example, Young (1966) and Young and Gray (1967) have demonstrated that the pressure gradient ahead of the bit, which cannot be measured in the field, governs ROP. The inability to properly measure and/or control these variables while drilling hinders their applicability to real-time optimization. Hence, real-time drilling optimization is delineated by adjustment of three controllable operational drilling parameters: pipe weight force exerted at the bit (WOB), drillstring rotational speed (RPM) and drilling fluid flow rate (q). These variables can be constantly adjusted by the driller (autodriller) at the surface to enhance drilling speed or protect downhole tools from excessive vibrations and dysfunctions. Mathematically, the drilling optimization problem can be formulated as:

$$\text{maximize } v_{ROP} = \frac{dl}{dt} = f(F_b, \omega, q, \Delta p_{dh}, \mu, \sigma_c, d_b, \eta_b, {}^{\Delta h}/_h)$$

and/or

$$\text{minimize } MSE = f(F_b, \omega, \tau_b, v_{ROP}, d_b) \qquad \text{(Teale, 1965)}$$
$$\text{minimize } TSE = f(\Delta \tau_s, \omega, l) \qquad \text{(Ertas } et\ al.\text{, 2013)}$$
$$\text{minimize } DS = f(F_b, \omega, v_{ROP}) \qquad \text{(Menand and Mills, 2017)}$$

$$\text{subject to } F_b < F_{b,max}$$
$$\omega < \omega_{max}$$
$$q > q_{min}$$
$$\tau_s < \tau_{s,max}$$
$$p_b > p_{b,min}$$
$$p_b < p_{b,max}$$
$$\left.\begin{array}{l}\end{array}\right\} \text{Operational Constraints}$$
$$p_s < p_{s,max}$$
$$\frac{\omega \tau_s}{5252} < P_{td,max}$$
$$\frac{q p_s}{1714} < P_{pump,max}$$
$$\left.\begin{array}{l}\end{array}\right\} \text{Rig Equipment Constraints}$$

v_{ROP} (R, ROP): drilling speed (rate of penetration) [ft/hr]
MSE: mechanical specific energy [psi]
TSE: torsional severity estimate
DS: drilling strength [psi]
l (D, MD): well length (measured depth) [ft]
t: time [hr]
F_b (W, WOB): force exerted at the bit (weight on bit) [klb]
ω (N, RPM): rotational (rotary) speed [rev/min]
q (Q): drilling fluid (mud) flow rate [gpm]
Δp_{dh}: downhole pressure differential (overbalance) [psi]
μ: drilling fluid (mud) dynamic viscosity [cP]
σ_c (S, CCS): rock confined compressive strength [psi]
d_b (d, D_b): bit diameter [in]
η_b (EFF_M): bit (mechanical) efficiency
${}^{\Delta h}/_h$ (h, W_f): fractional bit wear
τ_b (T_b, TOB, $DHTRQ$): torque on bit (downhole) [lb-ft]
τ_s (T_s, T, TQ, TRQ, $STRQ$): surface torque [lb-ft]
$\Delta \tau_s$: peak-to-peak surface torque [lb-ft]
p_b (BHP): pressure at the bit (bottomhole pressure) [psi]
p_s: surface pressure [psi]
P_{td}: top drive power [HP]
P_{pump}: pump power [HP]

Figure 1.1: Drilling optimization mathematical representation.

In Figure 1.1, ROP is a function of the three surface drilling variables controllable in real-time. Additionally, penetration rate is influenced by the downhole pressure overbalance at the bit, given by the difference between bottomhole pressure (BHP) and formation pore pressure (Eckel, 1958, Cunningham and Eenink, 1959). As overbalance increases, more force is applied to drilling cuttings near the bit. This chip hold-down phenomena (Garnier and van Lingen, 1959, van Lingen, 1962, Darley, 1965) prevents recently drilled rock fragments from circulating out of the hole, reducing ROP. Warren and Smith (1985) concluded that drilling speed slows down with depth more drastically for impermeable rocks, as the local pore pressure decreases due to an increase in pore volume caused by strain relaxation. Dynamic BHP is determined by the hydrostatic column of drilling fluid, rock cuttings loading ratio in the mud, annular friction losses experienced as mud is circulated back to the surface (dependent on flow rate), and choke backpressure applied at the surface. While BHP can be adjusted by manipulating mud density (increasing/decreasing barite concentration), flow rate (regulating mud pumps) and choke pressure (opening/closing choke valve), this value is constrained between pore pressure and formation fracturing pressure. If BHP falls below pore pressure, an influx of formation fluid ("kick") enters the well, possibly initiating a well control event. On the other hand, excessive BHP can cause the formation to fracture and eventually lead to lost circulation of drilling fluid. Therefore, the BHP and mud density optimization windows are slim due to lithology constraints. In fact, BHP is kept at a fixed value in tight margin wells by controlling the choke valve annular backpressure with managed pressured drilling (MPD) applications (Rehm *et al.*, 2008, Mammadov *et al.*, 2015).

Other factors impacting ROP include bit efficiency and wear. As the bit drills through incremental footage, cutters wear out and bit drilling efficiency is reduced. Bit wear is dependent on cutter geometry, lithology, temperature, WOB and RPM (Sinor and

Warren, 1989). Several studies have attempted to model bit wear (Gouda *et al.*, 2011, Lakhanpal and Samuel, 2017, Liu *et al.*, 2018), but the only current standard measure of wear comes from the International Association of Drilling Contractors (IADC) dull grade evaluation after pulling the bit out of the hole. Mechanical Specific Energy (MSE) measures the energy input needed to drill a unit volume of rock. Bit drilling efficiency (η_b) is defined by the ratio between energy spent in drilling (MSE) and the rock's actual strength in in-situ conditions (CCS). Simon (1963) formulated the rotational energy input per rock volume required for the drilling of oil and gas wells and evaluated the distinct energy requirements for breaking rock, concluding that a large portion of elastic strain energy is consumed by unloading stress waves resulting from crack propagation in a semi-infinite medium below the bit. During drilling, energy is also dissipated along the length of the well in the form of drillstring vibrations and friction with the borehole wall. MSE embodies this wasted energy if calculated with surface data. Dykstra *et al.* (1994) demonstrate that surface measurements may not be indicative of downhole vibrations and vice-versa. The popular specific energy concept was introduced by Teale (1965), combining the work done per drilled rock volume by rotational and axial (thrust) forces at the bit:

$$MSE = \frac{WOB}{A_b} + \frac{120\pi \times RPM \times T}{A_b \times ROP} \tag{1.1}$$

where *MSE* is the mechanical specific energy [psi], *WOB* is the weight on bit [lbf], A_b is the cross-sectional area of the bit [in^2], *RPM* is the rotational speed [rev/min], *T* is the torque [lbf-ft] and *ROP* is the penetration rate [ft/hr]. Several similar formulations defining drilling mechanical energy requirements were derived in the literature, including the ones by Rabia (1985), Pessier and Fear (1992), Dupriest and Koederitz (2005) and Deng *et al.* (2015). Armenta (2008) introduced the influence of bit hydraulics in MSE, renaming the

6

term to Drilling Specific Energy (DSE). Mohan *et al*. (2009) and Rashidi *et al*. (2010b) also developed drilling energy formulations accounting for hydraulic energy contribution. Drilling optimization studies minimizing MSE encompass Farrelly and Rabia (1987), Dupriest (2006), Chen *et al*. (2014) and Zhang *et al.* (2015).

Popularized by Dupriest and Koederitz (2005), MSE is a widespread drilling efficiency metric monitored during drilling. TSE, or torsional severity estimate, was proposed by Ertas *et al*. (2013) to quantify downhole torsional vibrations in real-time and alleviate drilling dysfunctions. This quantity is discussed at length in the next section. In most contemporary drilling operations, rotational energy dominates over thrust when computing MSE values and the first term in Eq. 1.1 can be ignored. Menand and Mills (2017) derived drilling strength to account for this missing axial energy term, restoring the importance of WOB data in drilling field surveillance:

$$DS = \frac{10 \times WOB \times RPM}{d_b \times ROP} \tag{1.2}$$

where *DS* is the drilling strength [psi] and d_b is the bit diameter [in].

Referring back to Fig. 1.1, drilling optimization schemes are limited by operational and rig equipment constraints. WOB has an upper limit according to bit operating range and may also be constrained by pipe buckling. RPM must not exceed downhole tools' ratings. Hole cleaning governs the flow rate lower limit. Surface torque cannot surpass drillpipe make-up torque rating. Bit pressure should be kept within the formation pore pressure and fracturing pressure window. Pressure at surface is constrained by the maximum standpipe pressure (SPP). Top drive power restricts RPM and surface torque, while pump power limits flow rate and surface pressure. These constraints must be satisfied by the drilling optimization objective function, which is highly dependent on the ROP

model utilized. This dissertation investigates fundamental questions in solving the constrained optimization problem of real-time adjustment of drilling parameters (WOB, RPM and flow rate) to drill faster and produce hydrocarbons safely and economically.

1.2. INDUSTRY DRILLING OPTIMIZATION APPROACHES

ExxonMobil's Drilling Advisory System (DAS) is the state of the art in real-time drilling optimization, combining ROP maximization with minimization of MSE and torsional vibrations (stick-slip) from drilling parameters obtained at surface. DAS is the successor of the drilling optimization strategy described by Dupriest and Koederitz (2005) – constantly monitor MSE at the rig and relate MSE trends to the ROP-WOB drilloff curve, identifying drilling inefficiencies and the founder point where optimal drilling parameters maximize ROP:
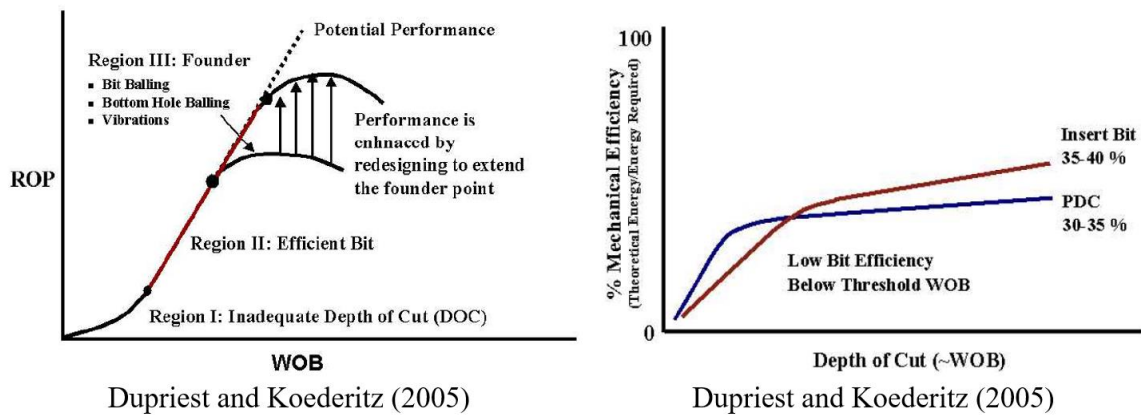
Figure 1.2: ROP vs. WOB and bit efficiency vs. depth of cut (DOC) relationships extracted from Dupriest and Koederitz (2005).

Dupriest and Koederitz (2005) singled out vibrations as the major performance limiter in ExxonMobil's drilling operations globally, emphasizing the need to incorporate vibration mitigation techniques in the drilling optimization workflow. Dupriest *et al.* (2005) demonstrated that by monitoring LWD downhole vibrations data in real-time alongside

MSE, drillers were able to better diagnose ROP limiters and adjust drilling parameters to the optimal founder point in the development of Qatar's North Field. In the following year, Dupriest (2006) reported that the process of identifying ROP limiters and extending the founder point was embedded in all of ExxonMobil's operations, with four and a half million drilled footage per year. Remmert *et al.* (2007) expressed the success of the ROP enhancement program in Qatar once again, noting that it saved the company $54 million in less than two years. The basis of this drilling optimization process was to train field personnel in monitoring MSE and downhole vibrations (when data were available) while drilling and sharing learnings across the rig fleet.

Vibrations modeling provides a more systematic approach to handle drillstring vibrations than pure surveillance of field data. Bailey *et al.* (2008) illustrated ExxonMobil's method to deal with lateral vibrations (bit whirl) by modeling bottomhole assembly (BHA) response in the frequency domain over a range of operating parameters and determining optimal stabilizer placement. Further efforts to mitigate whirl through BHA or bit redesign were reported by Dupriest and Sowers (2009), Bailey *et al.* (2010) and Bailey and Remmert (2010). It is important to note that since these techniques to reduce vibrations rely on altering a BHA component or its placement, the drillstring must be tripped out of the hole and no real-time modifications are possible. Axial vibrations (bit bounce) are not a significant issue when drilling with PDC bits, and torsional vibrations were finally accounted for in real-time by DAS.

The DAS optimization process begins in the planning phase of a well with a soft-string model (Ertas, 2012, Ertas *et al.*, 2013, Ertas *et al.*, 2014) which solves Newton's nonlinear equations of motion for the drillstring subject to external forces (gravity, mud, borehole) and torques based on mechanical properties (E and G), density and size (OD) of drillstring components, well trajectory and mud properties for a vibration-free baseline

case. Boundary conditions are defined at the bit and at surface and can be adjusted to represent different drilling methodologies (e.g. depth of cut control, constant RPM or hookload). The baseline first-order ordinary differential equation system yields pipe stretch, twist, tension and torque with respect to distance from the bit. Linearized torsional responses to harmonic perturbations at the bit around this baseline solution are propagated along the drillstring with transfer matrices to identify the primary stick-slip period (96-97% accuracy) and relate the surface torque envelope to bit RPM amplitude as a function of depth for this primary torsional resonant frequency (85-90% accuracy). While operational parameters (WOB, RPM) influence the magnitude of the modeled forces and torques, the primary torsional resonant frequency and drillstring compliance (twist divided by torque) at such frequency are defined by drillstring composition and wellbore trajectory. Real-time surface measurements of torque, RPM and depth are compared to the primary torsional mode response to estimate the downhole bit RPM envelope and consequently torsional vibrations severity:

$$TSE = \frac{DHRPM_{max} - DHRPM_{avg}}{DHRPM_{avg}} = \frac{\Delta T_s}{\Delta T/_{RPM} \times SRPM} \tag{1.3}$$

where *TSE* is the torsional severity estimate, *DHRPM* is the downhole rotational speed [rev/min], *SRPM* is the surface rotational speed [rev/min], ΔT_s is the peak-to-peak surface torque variation [lbf-ft] and *ΔT/RPM* is the dTorque-per-RPM for the primary stick-slip period as a function of depth determined from the previously described model. A TSE value of 1 represents fully developed stick-slip, where the bit comes to a full stop momentarily. Hence, the TSE value compares current surface drilling measurements to the modeled primary stick-slip mode response to assess the severity of ongoing torsional vibrations.

Chang *et al.* (2014) detail field applications of DAS, showing ROP improvements as high as 35% when the driller follows suggestions provided by the system. DAS starts off in learning mode, guiding the driller in selecting different combinations of WOB and RPM in an effort to explore the operational parameter space. Once the algorithm has captured enough data to characterize the drilling environment, DAS switches into application mode and provides recommendations of operational parameters that maximize a defined objective function:
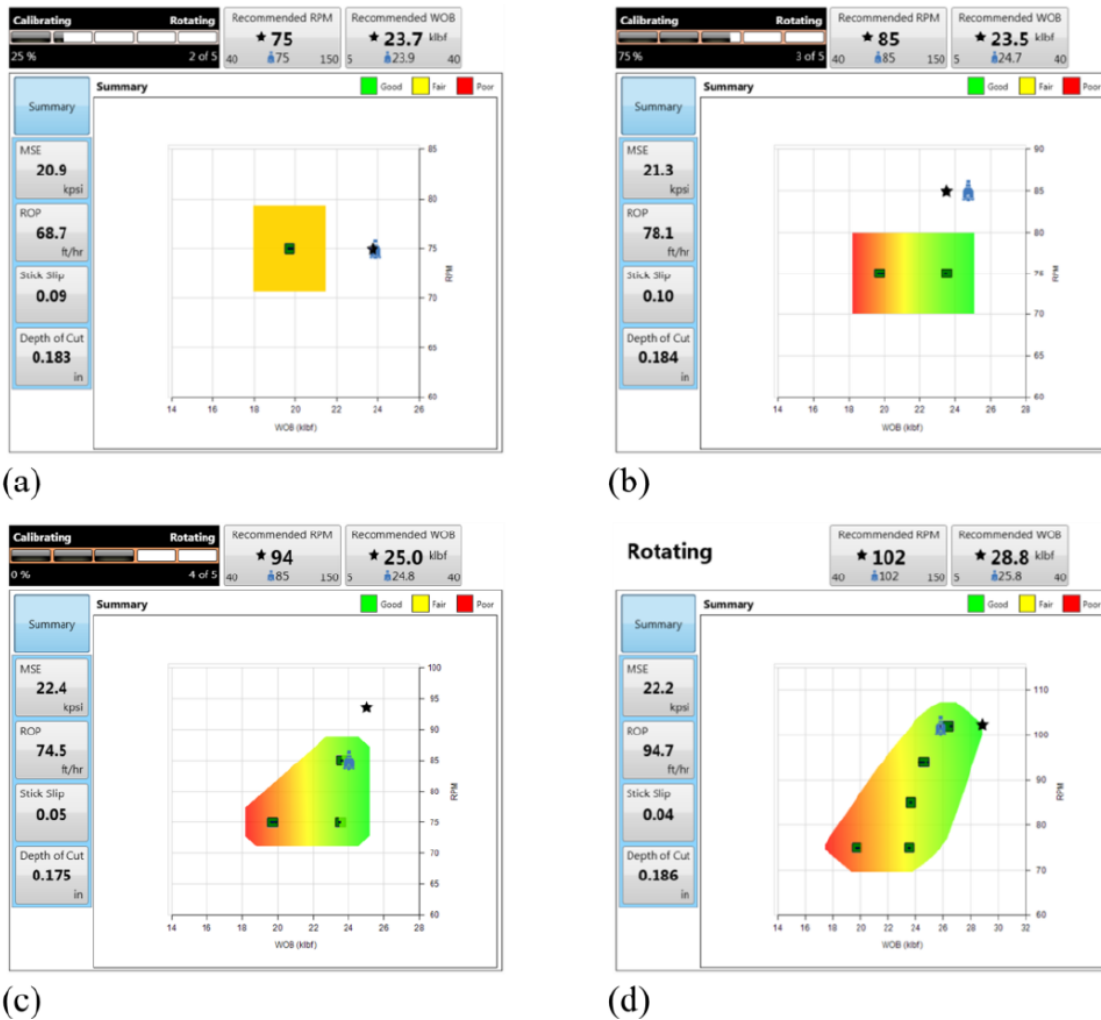
Figure 1.3: DAS user interface extracted from Sanderson *et al.* (2017).

In Fig. 1.3, the black star represents the system's suggested WOB and RPM values during calibration (plots a, b and c) and in optimization (plot d). The heat map illustrates objective function performance in the parameter space. Calibration data must remain stable for a short interval (e.g. 2ft) before being converted to response points, which are then used to fit the response surface. This technique combines data filtering and ROP model fitting into one step. Driver *et al.* (2016) describe a similar strategy by conducting multilinear regression with 5ft data averages. Moraveji and Naderi (2016) also employed response surfaces in fitting ROP models, but not in a real-time setting. Ambrus *et al.* (2017) developed a Bayesian network drilling efficiency model within an optimization workflow that generates WOB-RPM heat maps and operational cones and has been deployed to 20 rigs in North America.

Payette *et al.* (2015) provide one example of an objective function maximized by DAS:

$$OBJ = \frac{ROP}{MSE}\max[0, (1 - \alpha TSE^n)] \tag{1.4}$$

where α and n are real and positive. Incorporation of MSE and TSE in the drilling optimization objective function ensures that ROP is maximized up to the point where it does not cause drilling dysfunctions which would lead to premature bit wear or failure of downhole tools. This compromise in a multi-objective optimization problem is characterized by trade-off surfaces and pareto optimal points, discussed extensively by Boyd and Vandenberghe (2004). The same authors provide the basis for combining any number of objectives in a scalarized multicriterion problem:

12

$$OBJ = \sum_{i=1}^{q} \lambda_i F_i \qquad (1.5)$$

where λ_i is the weight of each F_i objective. Multi-objective drilling optimization methodologies considering bit life are described by Awotunde and Mutasiem (2014) and Guria *et al.* (2014). Both studies employ a bit wear function to account for the time required to trip out, change the bit, and trip back into the hole in addition to the drilling time determined by ROP.

Payette *et al.* (2017) state that DAS monitors depth of cut and bit aggressiveness during drilling to detect changing conditions and revert the system back to learning mode when necessary. Depth of cut is formulated as:

$$DOC = \frac{ROP}{5 \times RPM} \qquad (1.6)$$

where *DOC* is the depth of cut [in/rev]. Studies analyzing DOC in PDC bit drilling have been around for a long time (Gray *et al.*, 1962, Warren and Sinor, 1986). Also referred to as penetration per revolution, DOC is directly proportional to bit torque (Pastusek *et al.*, 2016). Note that the second term in Teale's MSE formulation (Eq. 1.1) is directly proportional to torque and inversely proportional to DOC, indicating that the slope of a torque vs. DOC plot can yield insights about drilling efficiency. Jain *et al.* (2016) describe PDC bits designed with DOC control to mitigate stick-slip. In addition to DOC, bit aggressiveness is also incorporated in DAS' workflow to assess drilling conditions:

$$\mu_b = \frac{36 \times T}{WOB \times d_b} \qquad (1.7)$$

where μ_b is the bit aggressiveness. Defining the WOB required to generate an amount of torque, aggressiveness represents a measurement of how the bit engages a rock formation. The concept of aggressiveness was first introduced as a bit-specific coefficient of sliding friction by Pessier and Fear (1992) and has since been studied by many authors. Rajabov *et al*. (2012) investigated the impact of PDC cutter side rake and back rake angles to bit aggressiveness.

Further successful field applications of ExxonMobil's Drilling Advisory System are presented by Bailey *et al.* (2016), Sanderson *et al.* (2017) and Spivey *et al.* (2017). More recently, Bailey *et al*. (2018) developed a model to estimate TSE distributions for a new well with redesigned drillstring stiffness, torque and RPM based on the TSE histogram of an offset well that experienced drilling dysfunctions. DAS exhibits a proven track record of successful deployments throughout the years, yet no closed-loop drilling control functionality has been reported. Several drilling automation initiatives are progressing across the oil and gas industry, with many companies contending to develop a viable solution. Cayeux *et al*. (2009) discuss the industrialization of drilling automation and early field trials in the North Sea. Florence *et al*. (2015) report on the automation progress achieved by the Society of Petroleum Engineers (SPE) Drilling Systems Automation Technical Section (DSATS). Bilgesu *et al*. (2017) describe application of artificial intelligence (AI) simulated annealing techniques in a DSATS automation competition. Computerized drilling control was suggested as early as Young (1969), and the oil and gas industry is finally edging closer to closed-loop control of drilling parameters.

Operators have invested plenty of capital and time in drilling optimization. In the 1980s, Amoco began developing the first drilling simulators (Millheim and Huggins, 1983a and 1983b, Millheim, 1986). Amoco's simulation efforts continued with Onyia (1987), who used inverted ROP models to create geologic drilling logs (GDLs). Further

simulation initiatives were developed in conjunction with academia (Hareland and Hoberock, 1993, Rampersad *et al*., 1994) and then expanded by Saga Petroleum in the North Sea (Bratli *et al*., 1997, Gjelstad *et al*., 1998). In fact, the North Sea play emerged as an early adopter of drilling optimization simulators. Nygaard *et al*. (2002) proclaim 10-25% savings in drilling costs as a result of an eight-year history of applying inverted ROP models to derive apparent rock strength in a Conoco-Statoil partnership. Joint industry efforts in drilling simulation are still seen today (Sugiura *et al*., 2015).

The first real-time operating center (RTOC) for drilling surveillance was envisioned by Superior Oil and Dresser Mag (Isaacs and Bobo, 1984). One of the RTOC's functions was to clean up field data and store it in a database. Shell started analyzing drilling data for overpressure detection early on (Jorden and Shirley, 1966), and later developed three separate RTOCs in the 21st century (van Oort *et al*., 2005, Gongora *et al*., 2013, Laurens and Kales, 2014). In the mid-1990s, BP already possessed a unified database of drilling data for ROP modeling and optimization (Xu *et al*., 1995). By 2008, the company had invested in real-time WOB and RPM adjustment, predicting the resulting ROP and minimizing cost per foot (Iqbal, 2008). Recently, BP created a well advisor solution in partnership with Kongsburg (Israel *et al*., 2015) and then performed field trials of a closed-loop control drilling system in partnership with Schlumberger (Israel *et al*., 2017). Chevron has taken a slightly different approach to drilling optimization by relying on their knowledge of rock strength and estimating drilling efficiency for ROP prediction (Caicedo *et al*., 2005, Guerrero and Kull, 2007). Petrobras teamed up with Baker Hughes in 2008 and built a team focused on real-time operational parameter optimization (Hougaz *et al*., 2012). Hess employed NOV's wired pipe technology to support closed-loop automation efforts in the Bakken shale play (Trichel *et al*., 2016). CNPC derived a torsional vibrations model in the frequency domain, similar to the one described in ExxonMobil's

DAS papers, to select optimal drilling parameters (Cui *et al.*, 2016). Apache is exploring offset well performance comparison in real-time, integrating visualization of historical drilling parameters in the driller's workflow (Behounek *et al.*, 2017a). Anadarko recently invested in in-house development of a real-time drilling analytics system that can optimize ROP with flexible functionality. With a rapid development strategy, a small team was able to build the proof of concept in three months and bring four data analytics modules into production in eleven months (Cao *et al.*, 2018).

Besides shared achievements with operators, service companies have also pursued their own drilling optimization and automation ambitions. Baker Hughes started using downhole data in drilling optimization in the early 2000s (Robnett *et al.*, 2002). At that time, data analysis was performed manually, and the credibility of downhole measurements was questionable. The authors envisioned closed-loop neural network drilling control. Today, Baker Hughes provides optimization of operational parameters through multivariate linear regression (Driver *et al.*, 2016) and real-time dashboards for performance comparison and visualization (Atwal and Knight, 2016). Schlumberger created Operation Support Centers to assist with manual selection of drilling parameters (Monden and Chia, 2007) and later developed a closed-loop real-time ROP optimization algorithm (Dunlop *et al.*, 2011, Chapman *et al.*, 2012, Dow *et al.*, 2012). Halliburton has established an entire data workflow for digital oilfield solutions (Sankaran *et al.*, 2009). Their software handles all stages of drilling predictive analytics, including data acquisition, validation, processing, storage, visualization and execution of optimization workflows. In 2011, NOV described advisory, semi-autonomous and autonomous real-time drilling optimization for future automation efforts (Koederitz and Johnson, 2011). The company then leveraged its wired pipe technology towards closed-loop downhole WOB control for sliding segments in unconventional plays (Pink *et al.*, 2012, Pink *et al.*, 2013). Weatherford

prioritized integration of geology knowledge in drilling optimization (Webb *et al.*, 2016). Joint service company projects in drilling optimization and automation have been published by Rommetveit *et al.* (2004) and Macpherson *et al.* (2013). SAS institute, an analytics software company, has joined the drilling optimization landscape and provided insights into the real-time vs right-time discussion (Holdaway, 2012). Rig data management companies such as Pason are also entering the drilling optimization market (Kristjansson *et al.*, 2016). The authors describe utilization of historical data to select the best WOB and RPM for drilling each rock formation.

Staying current with industry drilling optimization approaches is paramount in scrutinizing and implementing novel techniques. However, most companies do not disclose specific modeling aspects pertaining to their drilling optimization methodologies. Due to intellectual property and trade secret concerns, their publications in the literature focus on field results rather than detailed description of optimization procedures.

1.3. RESEARCH OBJECTIVE

The objective of this project is to establish a comprehensive real-time drilling optimization workflow that can be utilized by any rig in all types of drilling operations. Every step of the process is investigated, beginning with processing and filtering drilling data, then training analytical and machine learning ROP models with meaningful predictors, and finally selecting optimal operational parameters to drill sections of a well. Emphasis is placed on determining the best way to partition data and retrain ROP models in real-time, ensuring that drilling parameters are optimized to achieve the highest ROP in each drilling interval with the best available model. The optimization workflow in this dissertation encompasses seven ROP models:

- Analytical ROP models: Bingham (1964), Bourgoyne and Young (1974), Hareland and Rampersad (1994), Motahhari *et al.* (2010)
- Machine learning algorithms: random forests (Breiman, 2001), support vector machines (Drucker *et al.*, 1996), neural networks (McCullogh and Pitts, 1943)

ROP predictions derived from the models listed above guide optimization of drilling operational parameters. Eight optimization strategies are evaluated in terms of ROP improvements and computational expense:

- Gradient-based optimization: L-BFGS-B (Byrd *et al.*, 1995), trust region reflective (Branch *et al.*, 1999), SLSQP (Kraft, 1988)
- Direct search optimization: Nelder-Mead (Nelder and Mead, 1965), COBYLA (Powell, 1994), basin-hopping (Wales and Doye, 1997), particle swarm optimization (Kennedy and Eberhart, 1995), brute force search

Drilling optimization is performed in three stages, starting with the classical lithology-dependent approach based on offset well data:

- Lithology-dependent post-drilling optimization: assists in establishing appropriate choices of modeling and optimization methods
- Lithology-dependent real-time drilling interval optimization with continuous model learning: this novel concept proposes ROP model retraining as more data are collected in real-time, taking full advantage of all drilling data available. Cross-validation selects the most accurate ROP model for each drilling interval optimization

- Real-time optimization of drilling parameters with new data segmentation techniques: ROP models are fitted to dynamic or full training data ranges, ignoring formation boundaries. Spatial proximity and parameter similarity sample weighting are introduced to amplify partitioning of the training dataset during model training

No single ROP model is suitable for every drilling scenario encountered on the field. The approach explored in this dissertation involves retaining a collection of analytical and machine learning models which can be trained and evaluated in real-time for best possible performance. Many studies have analyzed the applicability of ROP models in a post-drilling data analysis framework, fitting a model with data from a previously drilled well and selecting optimal WOB, RPM and flow rate for an upcoming well on the same pad. The methodology presented here leverages constant data acquisition during drilling to retrain ROP models in real-time. Training data is segmented in intervals of specified depth length or number of data points. Respecting the traditional lithology dependence of ROP models, the initial batch of training data is collected in the first few feet of a formation. ROP models are fitted to this initial data and the best performing model according to cross-validation is employed in optimizing operational parameters for the next drilling interval. Data are measured as drilling progresses, and ROP models are retrained at the end of each interval with all data accumulated within the formation. The newly fitted model exhibiting the lowest error is used to optimize drilling in the next interval and the process repeats itself until the end of the formation is reached. This continuous learning approach relies on the models' ability to obtain additional knowledge about drilling mechanisms as more data become available. Investigation of ROP model behavior when fed training data incrementally and model performance variation with respect to retraining interval length are topics explored in this study. Fitting ROP models and optimizing drilling parameters

repeatedly may seem computationally prohibitive in real-time, but it is unreasonable to expect adjustment of operational parameters at each foot drilled. Sensible retraining interval lengths account for drilling optimization computational requirements and field applicability.

Historically, model coefficients for analytical ROP models are computed to best fit field data in a specific lithology. If the same approach is applied to real-time training of machine learning models, which typically require considerable amounts of data, formation transition zones can be problematic due to lack of substantial data as drilling begins in a new rock formation. The importance of the classical ROP modeling lithology dependence is questioned by comparing model performance with novel data segmentation methods. This dissertation explores fitting ROP models with a dynamic training data range of defined length, disregarding formation boundaries. Models are still retrained in intervals, but the training dataset spans a stipulated depth range independent of lithology. ROP model training with the full range of collected data is also investigated. Further expanding on the concepts of dynamic and full training dataset ranges, sample weighting techniques assign importance values to individual data points during model fitting. In the first approach, points are weighted according to proximity to the upcoming optimization interval. Just-captured data likely represents the ongoing drilling process more accurately. Therefore, spatially proximal samples carry higher weights and receive more emphasis in model fitting than data obtained in earlier sections. As an alternative weighting procedure, data points with drilling operational parameters similar to the mean near the next optimization interval are prioritized. This second weighting approach assumes that points with comparable drilling parameters are representative of equivalent drilling behavior. ROP model training methodologies directly influence optimization of drilling variables. The author is unaware of any academic work to date specifically focused on examining how to

segment data and retrain ROP models in real-time and the subsequent impact to drilling optimization.

In addition to comparing analytical and machine learning model performance, computational time required for model training and optimizing drilling parameters with each modeling strategy is analyzed to answer imperative questions about the best methodology to optimize drilling operations in real-time:

- How often should ROP models be retrained as new data are recorded? What is the appropriate compromise between model performance, operational viability of adjusting drilling parameters, and computational time?
- Is the lithology dependence of ROP models relevant? Can model performance improve with a dynamic or full training data range which ignores formation boundaries? What is the optimal dynamic range length?
- Does sample weighting reduce model error? Is it best to weight data by spatial relevance or by emphasizing similar operational parameter values?

Bingham (1964), Bourgoyne and Young (1974), Hareland and Rampersad (1994), Motahhari *et al*. (2010) constitute the analytical ROP model equations investigated. Python's *scikit-learn* (Pedregosa *et al*., 2011) implementation of random forests, support vector machines and neural networks compose machine learning algorithms tested for ROP prediction. Hypothesis testing establishes a foundation for assessing the statistical relevance of drilling variables to be included in machine learning ROP models. Grid search and cross-validation define optimal hyperparameters that control machine learning model architecture. Model performance is analyzed by computing a measure of distance between

data collected on the field and modeled ROP. Both absolute value and squared distance error metrics are considered.

Two optimization problems are scrutinized in this dissertation. Gradient-based and direct search optimization techniques are evaluated in fitting analytical ROP model coefficients and selecting optimal operational drilling parameters. Fundamental questions related to assessment of optimization algorithms include:

- What is the most computationally efficient approach to fit analytical ROP model coefficients?

- Which optimization methods achieve optimal drilling parameters without being computationally prohibitive for use in real-time operations? Does the strategy change from analytical to machine leaning ROP models?

- Are more accurate ROP models also harder to optimize? Does improved model performance justify higher computational expense?

- Does the lithology dependence of ROP models make sense from an optimization perspective? Can more satisfactory optimization results (higher ROP and lower computational time) be obtained by training ROP models in a dynamic or full training data range setting? What is the impact of incorporating sample weighting to drilling optimization?

ROP improvement and computational time are the criteria for comparison between optimization methods in determining optimal drilling operational parameters. L-BFGS-B (Byrd *et al.*, 1995), trust region reflective (Branch *et al.*, 1999) and SLSQP (Kraft, 1988) represent the gradient-based techniques analyzed. Direct search methodologies encompass Nelder-Mead (Nelder and Mead, 1965), COBYLA (Powell, 1994), basin-hopping (Wales

and Doye, 1997), particle swarm optimization (Kennedy and Eberhart, 1995), and brute force search. Applications of these optimization methods are conducted with implementations in Python's *scipy.optimize* (Oliphant, 2007) library, except for the particle swarm optimization algorithm programmed in the *pyswarm* (Lee and Castillo-Hair, 2013) Python package.

1.4. DISSERTATION OUTLINE

There are eight chapters in this dissertation. Following this introductory chapter, Chapter 2 reviews the history of ROP modeling in the literature and compares analytical and machine learning modeling methodologies. Chapter 3 presents gradient-based and direct search optimization methods and formulates the two optimization problems related to real-time drilling optimization: model fitting and selection of optimal drilling parameters. Drilling data processing and the dataset utilized in this study are discussed in Chapter 4. Traditional lithology-dependent post-drilling optimization, examined in Chapter 5, guides important decisions on modeling and optimization strategies employed in subsequent chapters. Chapter 6 introduces the concept of real-time continuous ROP model learning and defines the appropriate retraining interval length. Chapter 7 investigates optimization of drilling parameters according to different data segmentation and sample weighting techniques. Chapter 8 summarizes the conclusions, major contributions and future considerations resulting from this work. This dissertation includes material from papers previously published (Soares *et al*., 2016) or to be published (Soares and Gray, 2018, and Soares *et al*., 2018) by the author.

Chapter 2: Rate of Penetration (ROP) Modeling

Successful optimization of drilling parameters is contingent on a model's ability to predict ROP accurately. Hence, reliable models that can estimate the relationships between operational variables and ROP are essential for drilling optimization. This chapter describes ROP relationships with the three controllable surface drilling variables in real-time drilling optimization and reviews the historical progression of ROP modeling in the literature. In the traditional approach to ROP modeling, analytical (closed-form) equations describe the drilling process. Formulations for the four analytical models considered in this study are presented. More recently, machine learning applications to ROP modeling have emerged. Section 2.4 relates statistical concepts in the random forests, support vector machines and neural networks algorithms to common drilling scenarios, making a complex subject tractable to the general drilling audience. Cross-validation and overfitting concepts are introduced, and analytical and machine learning models are compared in terms of bias and variance.

2.1. ROP RELATIONSHIPS WITH WOB, RPM AND FLOW RATE

As discussed in Section 1.1, real-time drilling optimization consists of adjustment of three controllable operational drilling parameters: axial force at the bit (WOB), drillstring rotational speed (RPM) and mud flow rate. Laboratory experiments and field observations of the relationship between WOB and ROP can be found in the literature:
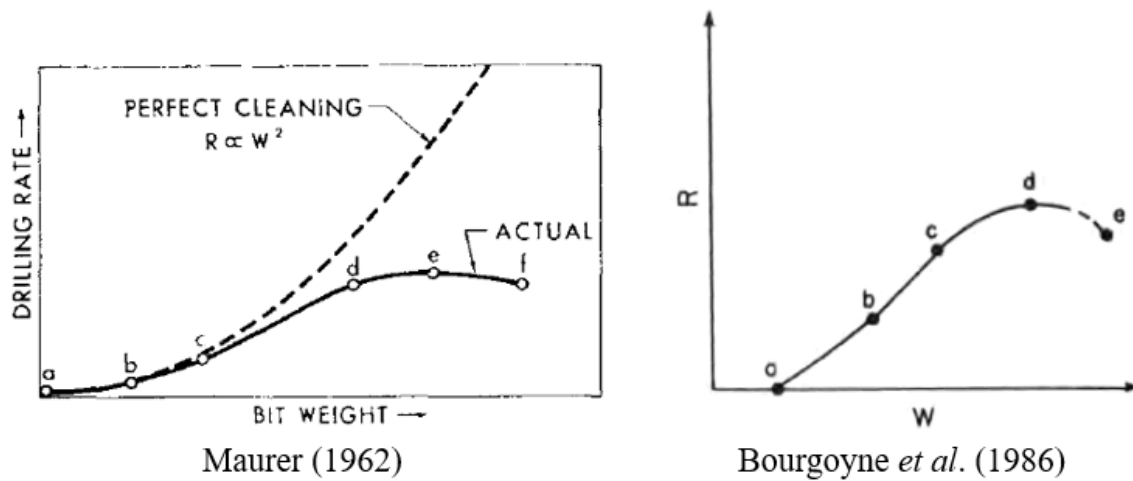
Figure 2.1: ROP vs. WOB relationships extracted from Maurer (1962) and Bourgoyne *et al*. (1986).

Maurer (1962) established that when drilling under perfect hole cleaning conditions, ROP is directly proportional to WOB squared. However, imperfect hole cleaning scenarios experienced on the field cause an increase in ROP due to hookload adjustment (increasing WOB) to generate more rock cuttings and worsen the cleaning problem. The author recognized that field drilling conditions are typically characterized by a linear relationship between WOB and ROP, and that after point "e", the cleaning problem outweighs the benefits of increased weight. Bourgoyne *et al*. (1986) portrayed a ROP-WOB relationship similar to Maurer's but noted that there is a minimum threshold WOB required to begin drilling, represented by point "a". Dupriest and Koederitz (2005) illustrated a response curve for drilloff tests (see Fig. 1.2) divided in three regions, indicating that the relationship between ROP and WOB is linear when the bit is drilling efficiently. The ROP-WOB relation remains linear up until the founder point, or optimum WOB, after which the bit transmits less energy to the rock than the typical 30-40% at peak efficiency and ROP gains with further WOB increase are limited. Gandelman (2012) cited improper hole cleaning,

pipe buckling and drillstring vibrations as the main reasons behind the sub-linear portion of the ROP-WOB response curve.

The ROP-RPM relationship typically observed on the field is less segmented than the previously described ROP-WOB relation:
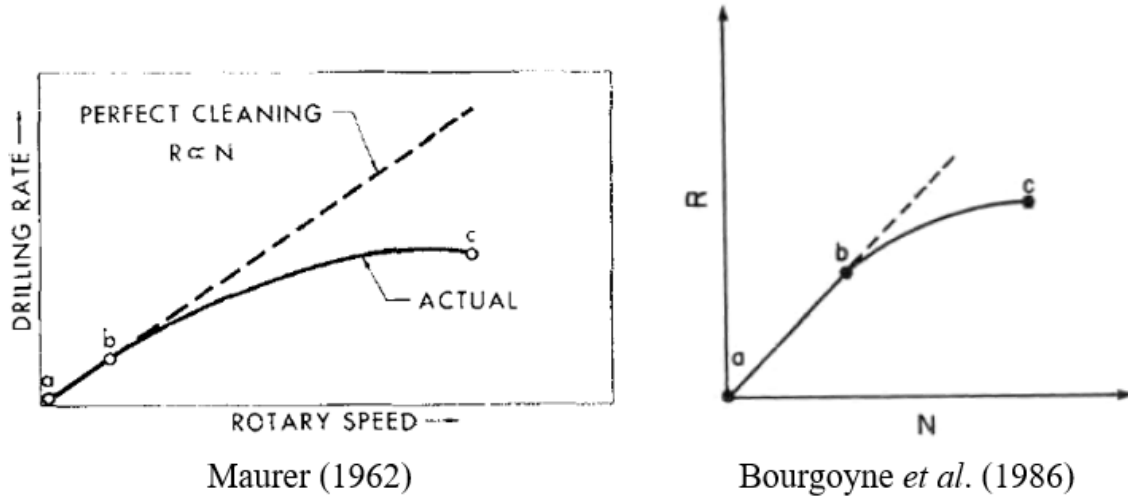
Figure 2.2: ROP vs. RPM relationships extracted from Maurer (1962) and Bourgoyne *et al.* (1986).

Maurer (1962) noted that ROP has a linear relationship with RPM under perfect hole cleaning conditions. As the drillstring rotational speed increases, the bit impacts the rock more often and generates more cuttings that must be cleaned out of the hole. Bourgoyne *et al.* (1986) depicted a very similar RPM-ROP relationship. Gandelman (2012) established that excessive RPM leads to vibrations. The energy dissipated through vibrations is wasted, decreasing ROP and inducing bit wear.

While drilling fluid flow rate provides hydraulic impact energy at the bit nozzles, the overall relationship between ROP and flow rate is not as straightforward as the previous two. Flow rate influences bottomhole pressure (BHP) in competing ways. Annular friction losses increase with increasing flow rate, leading to higher BHP. At the same time, an

increase in flow rate improves hole cleaning and removes high-density rock cuttings near the bit, lowering BHP. With higher BHP, the pressure differential between the wellbore and the formation (overbalance) increases, and the resulting chip hold-down effect reduces ROP (Garnier and van Lingen, 1959, van Lingen, 1962, Darley, 1965). Therefore, the global effect of an adjustment in flow rate to ROP will depend on several factors and in which portion of the hydraulics response curve the driller is currently operating. It is important to remember that flow rate is constrained between the minimum necessary for adequate hole cleaning and a maximum that does not cause excessive BHP to fracture the formation.

2.2. ROP Modeling Chronology

Studies began investigating which variables influence ROP as early as the 1930s. Sikes (1936) determined that six different factors impact ROP: rock formation, hole diameter, hydraulics, WOB, RPM, and bit type. The author also suggested that hole cleaning is the most influential parameter limiting ROP. These early evaluations were of qualitative rather than quantitative nature, offering no predictive power. In the 1950s and early 1960s, many empirical formulations relating ROP to WOB and RPM were developed and grouped together as R-W-N (ROP-WOB-RPM) relationships. Maurer (1962) lists nine R-W-N relations derived by different experimenters, all with distinct exponent and coefficient values. According to Maurer (1962), these field formulations are governed by hole cleaning conditions and cannot be applied universally since they fall on different portions of the ROP-WOB and ROP-RPM response curves. Rowley *et al*. (1961) developed R-W-N relations further by including a combination of linear and quadratic WOB and RPM terms, with a total of six terms (a constant, two linear terms, two quadratic terms, and one interaction term) and six model constants multiplying them. The authors

noted that drilling efficiency increases at a decreasing rate with additional WOB and decreases at a decreasing rate with higher RPM. Galle and Woods (1963) reproduced several optimization curves based on formation abrasiveness and drillability coefficients and a drilling fluid constant for selection of the best WOB and RPM in the field. Bingham's (1964) simple relation between ROP, WOB, RPM and bit diameter represented an important step towards broader applicability of previous R-W-N relations by adding an empirical exponent to the WOB term. This approach of including a formation-dependent WOB exponent in the ROP model formulation was actually originally presented by Murray and Cunningham (1955), who attributed the concept to H. B. Woods.

Hydraulics influence on ROP was first discussed by Eckel and Nolley (1949). The authors concluded that ROP is directly proportional to a term multiplying flow rate and nozzle velocity. In a subsequent study, Eckel (1967) suggested that a Reynolds number function combining hydraulics and mud properties can represent hole cleaning conditions downhole:

$$ROP = K \times WOB^a \times RPM^b \times \left(\frac{kq\rho}{d_n\mu}\right)^c \quad , \qquad 2 < \frac{kq\rho}{d_n\mu} < 100 \qquad (2.1)$$

where K and k are constants and a, b and c are exponents computed for a specific formation, q is the flow rate [gpm], ρ is the mud density [SG], d_n is the bit nozzle diameter [in] and μ is the fluid viscosity [cP]. Eckel (1968) proved that this relation between ROP and the hydraulics Reynolds number term indeed holds with an exponent c value of approximately 0.5.

Bourgoyne and Young (1974) developed the most comprehensive analytical ROP model to date, expressing eight different parameters that affect ROP: formation strength, rock compaction with depth, undercompaction in abnormally pressured formations,

28

pressure differential at the bit, WOB, RPM, bit wear, and hydraulics. Pore pressure prediction (Bourgoyne and Young, 1973) represented one of the early applications of the model. However, the Bourgoyne and Young (BY or B&Y) model became universally renowned due to numerous implementations in workflows optimizing drilling parameters (e.g. Al-Betairi *et al*., 1988, Eren, 2010, Guria *et al*., 2014). This very popular ROP model was originally developed for roller cone bits, but it has also been widely utilized when drilling with PDC bits (Rashidi *et al.*, 2008, Nascimento *et al*., 2015, Mammadov *et al.*, 2015, Wiktorski *et al*., 2017). Since the B&Y model does not include analysis of rock failure mechanisms unique to roller cone bits, such PDC bit applications are acceptable. Recently, experimenters have adapted the B&Y model to specific drilling situations by incorporating small modifications. Eren and Ozbayoglu (2010) applied the B&Y model with a WOB correction for deviated wells. Alum and Egbon (2011) extended B&Y's model by evaluating the influence of annular friction losses (and ECD) and drilling fluid plastic viscosity on ROP under different flow regimes. Wiktorski *et al*. (2017) included dog leg severity and an added ECD term in the B&Y formulation.

All analytical ROP models presented thus far are based on field intuition and/or laboratory testing. They do not evaluate the bit-rock interaction process directly, and their application is independent of bit type. Many of the models developed after B&Y incorporate an analysis of the rock cutting mechanisms downhole, differentiating between roller cone and fixed cutter drag-type (PDC being the most popular) bits. Roller cone bits were widely favored early on, particularly the tricone bit composed of 3 rolling cones that rotate around their own axis and are laden with milled teeth or tungsten carbide inserts (introduced in 1951), drilling the rock in compression with a crushing action (Scott, 1996). PDC bits, the workhorse of the industry today, display fixed cutters composed of a synthetic diamond layer on top of cemented tungsten-carbide substrate, destroying the rock

in shear. Feenstra (1988) reported that the self-sharpening ability of PDC cutters (tungsten carbide wearing at a higher rate than the diamond layer) differentiated PDC bits from other drag bits by allowing faster drilling at lower WOB. The author also stated that PDC bits experienced less chip hold-down but lacked in impact resistance and temperature stability. Warren and Sinor (1994) provided a comprehensive history of PDC bits, noting that the first commercial PDC bit became available to the oil and gas market in 1976. In the beginning of the 1980s, many successful applications in soft to medium rocks were already underway. However, the tendency of PDC bits to whirl and eventually fail due to lateral vibrations prevented their expansion into hard rock territory. At the time of Warren and Sinor's (1994) publishing, bit manufacturers were placing a lot of emphasis on developing whirl-resistant PDC bits, but performance in harder rocks was still unsatisfactory. By 2011, Pessier and Damschan (2011) asserted that PDC bits had overtaken roller cone bits almost entirely, with exception of very specific scenarios. For those unique applications, the authors proposed two hybrid bit designs that combine the continuous shearing mechanism of PDC cutters with the intermittent crushing action provided by roller cone inserts. This hybrid bit concept had been around since the 1980s but displayed lackluster performance (Pessier and Damschan, 2011). Hybrid designs have gained popularity recently, causing many drill bit providers to experiment with innovative configurations (Liu *et al.*, 2016, Crane *et al.*, 2017).

Bit-specific analytical ROP models generally include formation geomechanical properties, as they analyze the rock cutting mechanisms of each bit type. Cunningham (1978) developed a roller cone bit model dependent on rock drilling strength, determined by drilling tests performed in the formation of interest. Warren (1981) derived a ROP model for soft-formation roller cone bits based on dimensional analysis, including two separate terms and a measure of rock strength relative to a specific type of rock. This model

was later improved by accounting for imperfect hole cleaning conditions, resulting in the famous three-term roller-cone bit ROP model with hydraulics and mud properties published by Warren (1987). Winters *et al.* (1987) added a fourth term to Warren's model to incorporate the effects of rock ductility on ROP. Hareland and Hoberock (1993) commented on the difficulty of obtaining rock ductility and cone offset parameters introduced by Winters *et al.* (1987) and modified the Warren (1987) model to include a function of bottomhole differential pressure accounting for chip hold-down effects. Hareland *et al.* (2010) investigated the rock fracturing mechanism of roller-cone bits by measuring the volume of craters created by individual inserts in indentation tests. Model parameters encompass the number of insert penetrations per revolution, number of inserts in contact with the rock and chip formation angle. Kowakwi *et al.* (2012) altered the soft-rock model by Warren (1981) with their own hydraulics function based on HSI (horsepower per square inch), a chip hold-down function, and a bit wear function. ROP models specific to PDC bits tend to be based on force balance at cutter contact points with the rock. Complex input requirements limit the applicability of such models. PDC bit models derived by Hareland and Rampersad (1994) and Motahhari *et al.* (2010) relate operational variables and a simplified interface between cutters and the formation to drilling speed. These two models are utilized throughout this study and formulated in the next section.

Analysis of forces and moments at the bit provide a more complete description of the bit-rock interaction process. However, a full geometric description of the contact points and angles between borehole and bit downhole is required in order to compute stresses on the rock and failure criteria. Dykstra *et al.* (2001) provide an interesting discussion on engineering vs. research models for drillstring dynamics. Force balance ROP models for roller cones have been developed by Umez-Eronini (1983) and Walker *et al.* (1986). Early

fixed-cutter bit-rock interaction models predicting ROP for diamond bits include Appl and Rowley (1968) and Peterson (1976). In the 1980s, Sandia National Laboratories exhibited acute interest in finite element modeling for PDC bits in geothermal drilling: Glowka and Stone (1985) modeled the thermal response of PDC cutters and Glowka (1989) studied PDC bit forces. Other models describing PDC bit forces include Warren and Sinor (1986), Detournay and Defourny (1992) (later extended in Detournay *et al*., 2008, with directional drilling applications in Perneder *et al*., 2012 and validated by Zhou *et al*., 2012), and Gerbaud *et al*. (2016). While force balance models provide valuable insights into how bits operate, they rely on geometric inputs not available in real-time and are better suited for bit design optimization, in a simulation environment. For real-time drilling optimization, practical models relate measurable drilling parameters to ROP. Machine learning (ML) algorithms prove particularly useful in achieving this task.

In the past couple of decades, machine learning has emerged as a prominent modeling approach across several industries. Linear regression represents the simplest of machine learning algorithms. All ML models possess the capability of incorporating any measurable data as inputs (predictors/features) to predict a response through statistics. Analytical ROP models provide a good starting point to define which parameters should be included in ML ROP models and hypothesis testing can ensure the statistical relevance of drilling variables deemed important by analytical model authors (see Section 5.1). It is important to note that in ML communities, the word "parameters" is used in reference to model coefficients learned during the training process, such as the weights in linear regression and neural networks. In drilling, variables that can be adjusted in operations (WOB, RPM, flow rate, etc.) are commonly known as drilling parameters. Throughout this dissertation, the drilling parameters terminology is utilized often and conventional ML model parameters are referred to as model coefficients.

By far, the most popular machine learning algorithm for ROP prediction is neural networks (NN), encountered in the works of Bilgesu *et al*. (1997), Dashevskiy *et al*. (1999), Moran *et al*. (2010), Rahimzadeh *et al*. (2010), Bataee and Mohseni (2011), Arabjamaloei and Shadizadeh (2011), Esmaeili *et al*. (2012), Gandelman (2012), Gidh *et al*. (2012), Jahanbakhshi *et al*. (2012), Evangelatos and Payne (2016), Shi *et al*. (2016), Elkatatny *et al*. (2017) and Amer *et al*. (2017). Adoption of additional ML algorithms to ROP modeling are also found in the literature; Hegde *et al*. (2015, 2017), Hegde (2016), Ansari *et al*. (2016), Mantha and Samuel (2016) and Hegde and Gray (2017) published on implementations of different types of regression, k-nearest neighbors, boosting, random forests (RF) and support vector machines (SVM). Random forests, support vector machines and neural networks are the ML algorithms chosen for this study based on performance and applicability to a wide range of problems. These algorithms are described in Section 2.4.

2.3. ANALYTICAL ROP MODEL EQUATIONS

Four analytical ROP models are implemented throughout this dissertation: the two classic and widely popular Bingham (1964) and Bourgoyne and Young (1974) models, and the two PDC bit models with viable real-time applications in Hareland and Rampersad (1994) and Motahhari *et al*. (2010). Formulations for these four analytical models are presented in this section.

2.3.1. Bingham (1964)

Bingham (1964) developed a simplistic relation to predict ROP based on WOB, RPM and bit diameter. The model assumes that ROP is directly proportional to RPM and describes a power-law relationship between ROP and WOB. This approach appears similar

to R-W-N relations described by Maurer (1962). However, by including a drillability constant (*a*) and an empirical WOB exponent (*b*), computed for each rock formation, Bingham's ROP model alleviated the localized model application issue:

$$ROP = a \left(\frac{WOB}{d_b}\right)^b RPM \qquad (2.2)$$

where *ROP* is the rate of penetration [ft/hr], *a* and *b* are dimensionless constants for each formation, *WOB* is the bit weight [klbf], d_b is the bit diameter [in], and *RPM* is the rotational speed [rev/min]. Nevertheless, both model coefficients (*a* and *b*) are determined for an entire rock formation and cannot account for changing drilling physical behavior in different operational parameter regions:
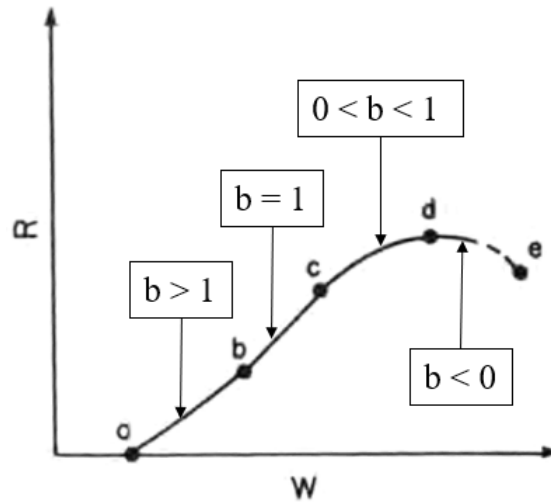
Figure 2.3: ROP vs. WOB relationship adapted from Bourgoyne *et al.* (1986) by adding Bingham WOB exponents (*b*) in a segmented operational parameter space.

Figure 2.3 represents a common flaw of all analytical (closed-form) models, which assume a single equation can predict ROP behavior throughout a formation. Since a set of empirical model coefficients is calculated to best fit all the field data collected in a formation, it must

34

average varying operational conditions encountered while drilling different well segments. The main limitation of analytical ROP models is their inability to represent this segmented operational parameter space, illustrated in Figures 2.1-2.3. Model performance highly depends on coefficient bounds, as reported by Soares (2015) and Soares *et al*. (2016). Bingham coefficient bounds are determined based on similar coefficients in the Bourgoyne and Young (1974) model, with bound values as suggested in Bourgoyne *et al*. (1986) – Bingham's *a* adheres to the same bounds as the drillability constant a_1 in the modified Bourgoyne and Young model and Bingham's *b* follows the WOB exponent a_5 (Table 2.1).

2.3.2. Bourgoyne and Young (1974)

Bourgoyne and Young's (1974) exponential ROP relation and the subsequent Bourgoyne *et al*. (1986) model equation are built upon the concept of formation drillability. This quantity measures the drilling speed obtained while drilling a formation at specified "normal" drilling conditions. Both model formulations, including eight modeled terms which affect ROP, are examined in this section and equivalent terms are shown in chronological order. Starting with the overall ROP model equations:

$$\frac{dD}{dt} = \text{Exp}\left(a_1 + \sum_{j=2}^{8} a_j x_j \right) \qquad \text{Bourgoyne and Young (1974)}$$

$$ROP = (f_1)(f_2)(f_3)(f_4)(f_5)(f_6)(f_7)(f_8) \qquad \text{Bourgoyne } et\ al.\ (1986) \qquad (2.3)$$

where D is the well depth [ft], t is the time [hr], *ROP* is the rate of penetration [ft/hr], a_1 is the formation strength parameter, a_2 is the normal compaction trend exponent, a_3 is the undercompaction exponent, a_4 is the pressure differential exponent, a_5 is the bit weight

exponent, a_6 is the rotational speed exponent, a_7 is the tooth wear exponent, and a_8 is the hydraulic exponent. Functions f_1 through f_8 in Bourgoyne *et al.* (1986) encompass empirical model coefficients a_1 through a_8 from Bourgoyne and Young (1974) and the modeled relationship for each drilling factor (x_1-x_8). Formation drillability is expressed by the coefficient a_1 in Bourgoyne and Young (1974) and by the function f_1 in Bourgoyne *et al.* (1986):

$$x_1 = 1$$

$$f_1 = e^{2.303\,a_1} = K \tag{2.4}$$

Parameter x_2 (and function f_2) represents the normal compaction model for rock strengthening:

$$x_2 = 10,000.0 - D$$

$$f_2 = e^{2.303a_2(10,000-D)} \tag{2.5}$$

Equations 2.5 are normalized to a depth of 10,000ft, indicating that formation drillability is defined at this "normal" drilling depth. This can be seen by plugging in a depth value of 10,000ft in Eqs. 2.5. Regardless of a_2, the values of zero obtained for x_2 and one for f_2 eliminate the influence of the normal compaction drilling factor on ROP when substituted back in Eqs. 2.3. The following model describes undercompaction in abnormally pressured formations:

$$x_3 = D^{0.69}(g_p - 9.0)$$

$$f_3 = e^{2.303\,a_3 D^{0.69}(g_p - 9.0)} \tag{2.6}$$

where g_p is the pore pressure gradient of the rock formation [lbm/gal (ppg)]. Equations 2.6 are normalized to a pore pressure gradient of 9ppg. Bottomhole pressure differential influence on drilling is given by:

$$x_4 = D(g_p - \rho_c)$$

$$f_4 = e^{2.303\,a_4 D(g_p - \rho_c)} \tag{2.7}$$

where ρ_c is the equivalent circulating mud density [lbm/gal]. From the equations above, formation drillability is established at zero overbalance. The bit weight factor is modeled as:

$$x_5 = \ln\left(\frac{\frac{WOB}{d_b} - \left(\frac{WOB}{d_b}\right)_t}{4.0 - \left(\frac{WOB}{d_b}\right)_t} \right)$$

$$f_5 = \left(\frac{\frac{WOB}{d_b} - \left(\frac{WOB}{d_b}\right)_t}{4.0 - \left(\frac{WOB}{d_b}\right)_t} \right)^{a_5} \tag{2.8}$$

where WOB is the weight on bit [klbf] and d_b is the bit diameter [in]. The term containing the subscript t represents the threshold WOB (per inch of bit diameter) required to begin drilling. Although x_5 is expressed as a logarithmic relationship, it becomes a power-law

model equivalent to f_5 after undergoing the exponential operator in the first Eq. 2.3. Normal drilling conditions are characterized by 4klbf/in, or 4,000lbf of weight per inch of bit diameter. Next, the drillstring rotational speed parameter is introduced:

$$x_6 = \ln\left(\frac{RPM}{100}\right)$$

$$f_6 = \left(\frac{RPM}{60}\right)^{a_6} \tag{2.9}$$

where *RPM* is the drillstring rotational speed [rev/min]. As seen in Eqs. 2.9, there is a distinction in RPM normalization from 100rev/min in the original Bourgoyne and Young (1974) model to 60rev/min in the newer Bourgoyne *et al.* (1986) formulation. Bit wear is expressed as:

$$x_7 = -h$$

$$f_7 = e^{-a_7 h} \tag{2.10}$$

where h is the fractional tooth height worn away. The main difference between the two versions of the model shows up in the last function. Previously an exponential relationship with Eckel's hydraulics Reynolds number (introduced in Eq. 2.1), the updated hydraulics model is a power-law function of the hydraulic jet impact force:

$$x_8 = \frac{\rho q}{350 \mu d_n}$$

$$f_8 = \left(\frac{F_j}{1,000}\right)^{a_8} \tag{2.11}$$

38

where ρ is the mud density [lbm/gal], q is the flow rate [gal/min], μ is the apparent viscosity at 10,000 sec^{-1} [cp], d_n is the bit nozzle diameter [in] and F_j is the hydraulic impact force [lbf] exerted on the rock below the bit:

$$F_j = \rho q v_n \left(\frac{\text{lbf}}{32.174 \frac{\text{ft lbm}}{\text{s}^2}} \right) \left(\frac{\text{min}}{60\text{s}} \right) = 0.000518 \rho q v_n \tag{2.12}$$

where v_n is the nozzle velocity [ft/s]. The first Eq. 2.11 normalizes the Reynold's number function developed by Eckel (1967, 1968) by 350, while the second equation is normalized to a hydraulic impact force of 1,000lbf. Fluid velocity through the bit nozzles is given by:

$$v_n = \frac{q}{TFA} \left(\frac{\text{min}}{60\text{s}} \right) \left(\frac{\text{ft}^3}{7.4805\text{gal}} \right) \left(\frac{12\text{in}}{\text{ft}} \right)^2 = 0.3208 \frac{q}{TFA} \tag{2.13}$$

where TFA is the total nozzle flow area [in^2]. Combining Eqs. 2.12 and 2.13, hydraulic impact force reflects a quadratic relationship with flow rate. Bourgoyne *et al.* (1986) demonstrated that hydraulic horsepower at the bit could also be used as the hydraulic parameter of choice for optimization, leading to similar results as the two previous suggested terms. Generally normalized by the bit area (Tibbitts *et al.*, 1981), hydraulic horsepower per square inch (HSI) [HP/in^2] is given by:

$$HSI = \frac{\Delta p_b q}{\pi/4\, d_b{}^2} \left(\frac{\text{HP}}{550 \frac{\text{ft lbf}}{\text{s}}} \right) \left(\frac{\text{ft}^3}{7.4805\text{gal}} \right) \left(\frac{12\text{in}}{\text{ft}} \right)^2 \left(\frac{\text{min}}{60\text{s}} \right)$$

$$HSI = \frac{1}{\pi/4\, d_b{}^2} \frac{\Delta p_b q}{1714.3} \tag{2.14}$$

where Δp_b is the pressure drop across the bit [psi]:

$$\Delta p_b = \frac{\rho q^2}{2 C_d{}^2 TFA^2} \left(\frac{\text{lbf}}{32.174 \frac{\text{ft lbm}}{s^2}} \right) \left(\frac{\text{min}}{60s} \right)^2 \left(\frac{\text{ft}^3}{7.4805 \text{gal}} \right) \left(\frac{12 \text{in}}{\text{ft}} \right)^2$$

$$\Delta p_b = \frac{\rho q^2}{10861 \, TFA^2} \tag{2.15}$$

where C_d is a dimensionless discharge coefficient accounting for friction, typically assigned a value of 0.95. The factor of ½ arises from the kinetic energy term in the conservation of energy derivation (Bourgoyne *et al.*, 1986). Substituting bit pressure drop (Eq. 2.15) into Eq. 2.14, HSI is directly related to flow rate cubed. With hydraulic horsepower at the bit per square inch of bit area representing the hydraulics parameter, the last B&Y model term becomes:

$$f_8 = (HSI)^{a_8} \tag{2.16}$$

The three proposed hydraulic terms are, respectively, linear (hydraulics Reynolds number), quadratic (jet impact force) and cubic (HSI) with respect to flow rate.

Although the Bourgoyne and Young ROP model describes the drilling process thoroughly, many parameters utilized in the model are hard or impossible to measure in real-time with existing technology and must be approximated (e.g. pore pressure gradient, drilling fluid apparent viscosity and bit wear). In addition, the model relies on normalization constants for depth, WOB, RPM and flow rate terms first derived for drill bits from the 1970s. Nascimento *et al.* (2015) and Kutas *et al.* (2015) expose this issue by reporting B&Y model applications from various authors with different normalizing factors and proposing new values themselves. For the dataset analyzed in this dissertation, applying the 4klbf/in WOB normalization to an 8-³/₄in diameter bit defines normal drilling conditions of 35klbf bit weight, outside the bit manufacturer's specified operating range of

3.5-30klbf (*SHARC*, 2015). Another point to consider is that constant parameters in an interval, such as bit diameter, nozzle diameter, mud weight and apparent viscosity, are useful when comparing drilling performance for different bits and drilling fluids. However, B&Y model coefficients a_1-a_8 are empirically determined in very specific operational conditions particular to the given bit and mud. For example, increasing bit diameter results in a larger hole size, altering annular hydraulics and thus the a_8 coefficient. Consequently, validity of coefficients is only guaranteed when the model predicts ROP for the exact same bit, drilling fluid, formation and in similar operating conditions. Therefore, the author contends that the same B&Y coefficient values are not applicable across a range of bits or muds and that one model coefficient can absorb all constant parameter effects. The newly proposed modified Bourgoyne and Young formulation eliminates normalizing factors and constant parameters, simplifying the model to rely on measurements of the core variables in real-time drilling optimization:

$$ROP = a_1 D^{a_2} WOB^{a_5} RPM^{a_6} q^{a_8} \qquad (2.17)$$

Bourgoyne *et al*. (1986) suggested a range of values for coefficients a_5-a_8. Several studies in the literature (Bahari and Seyed, 2007, Bahari *et al*., 2008, Rahimzadeh *et al*., 2011, Anemangely *et al*., 2017) agree on the same bounds for coefficients a_1-a_4:

Table 2.1: Model coefficient bounds for Bourgoyne *et al.* (1986) and modified
Bourgoyne and Young ROP models.

Typical Bourgoyne and Young Model Bounds		
Coefficient	Lower Bound	Upper Bound
a_1	0.5	1.9
a_2	0.000001	0.0005
a_3	0.000001	0.0009
a_4	0.000001	0.0001
a_5	0.5	2
a_6	0.4	1
a_7	0.3	1.5
a_8	0.3	0.6

Coefficient Bounds for Modified Model		
Coefficient	Lower Bound	Upper Bound
a_1	0.0001	10000
a_2	-2	0
a_5	0.5	2
a_6	0.4	1
a_8	0.3	2

For the novel proposed formulation, coefficient bounds for WOB and RPM terms' exponents (a_5 and a_6) are maintained at the recommended values, reinforced by the response curves illustrated in Figures 2.1 and 2.2. Bounds for the all-encompassing a_1 coefficient are expanded to incorporate the influence of removed constant parameters and normalizing factors. Maurer's (1962) perfect cleaning ROP theory states that drilling speed is inversely proportional to the square of rock strength. Coefficient a_2 accounts for this rock compaction factor with depth as a proxy for rock strength, and bounds proposed for the modified model formulation in Table 2.1 reflect Maurer's relationship. Lastly, the three hydraulic terms suggested by Bourgoyne *et al.* (1986) are linear, quadratic and cubed with respect to flow rate. The original upper bound for the hydraulics term exponent a_8 (0.6) is adapted in the modified formulation to reflect the appropriate flow rate correlation range ($3^{0.6} = 1.933$). Equation 2.15 for pressure drop across the bit also supports a squared relation with flow rate at maximum.

2.3.3. Hareland and Rampersad (1994)

Hareland and Rampersad (1994) applied conservation of mass to describe the penetration of a single bit cutter into the formation. The model assumes that each cutter

compresses and removes a volume of rock proportional to the contact area and the WOB applied. The general Hareland and Rampersad (1994) ROP model equation for drag bits is:

$$ROP = \frac{a}{(RPM^b \; WOB^c)} \frac{14.14 \; N_c \; RPM \; A_v}{d_b} \tag{2.18}$$

where ROP is the rate of penetration [ft/hr], a, b, and c are cutter geometry correction factors, WOB is the weight on bit [klbf], RPM is the drillstring rotational speed [rev/min], N_c is the number of cutters, A_v is the area of rock compressed in front of a single cutter [in^2] and d_b is the bit diameter [in]. The contact area between a cutter and the rock formation is defined in terms of cutter penetration P [in]:

$$P = \frac{2W_{mech}}{\pi \; d_c \; \sigma_c} \tag{2.19}$$

where W_{mech} is the mechanical loading (WOB) per cutter [lbf], d_c is the cutter diameter [in] and σ_c is the uniaxial (unconfined) compressive rock strength [psi]. For PDC bits, Hareland and Rampersad (1994) characterizes A_v as:

$$A_v = \cos\alpha \sin\theta \left[\left(\frac{d_c}{2}\right)^2 cos^{-1}\left(1 - \frac{2P}{\cos\theta \; d_c}\right) \right.$$
$$\left. - \left(\frac{d_c P}{\cos\theta} - \frac{P^2}{(\cos\theta)^2}\right)^{0.5} \left(\frac{d_c P}{2\cos\theta}\right) \right] \tag{2.20}$$

where α is the cutter side rake angle and θ is the cutter back rake angle. Conducting dimensional analysis on Eq. 2.20 reveals an inconsistency in units. The overall quantity A_v has units of area [in^2], while P has units of length [in]. Analyzing the two expressions inside

the square brackets separately, the parameter inside the inverse cosine is dimensionless and the trigonometric function is then multiplied by the initial $[\text{in}^2]$ portion, producing consistent units for the first term. Next, the expression inside the radical has units of $[\text{in}^2]$, resulting in units of $[\text{in}]$. Its multiplying term has units $[\text{in}^2]$, culminating in conflicting $[\text{in}^3]$ units for the second term inside the square brackets. Examining A_v behavior with varying WOB in Eq. 2.20:
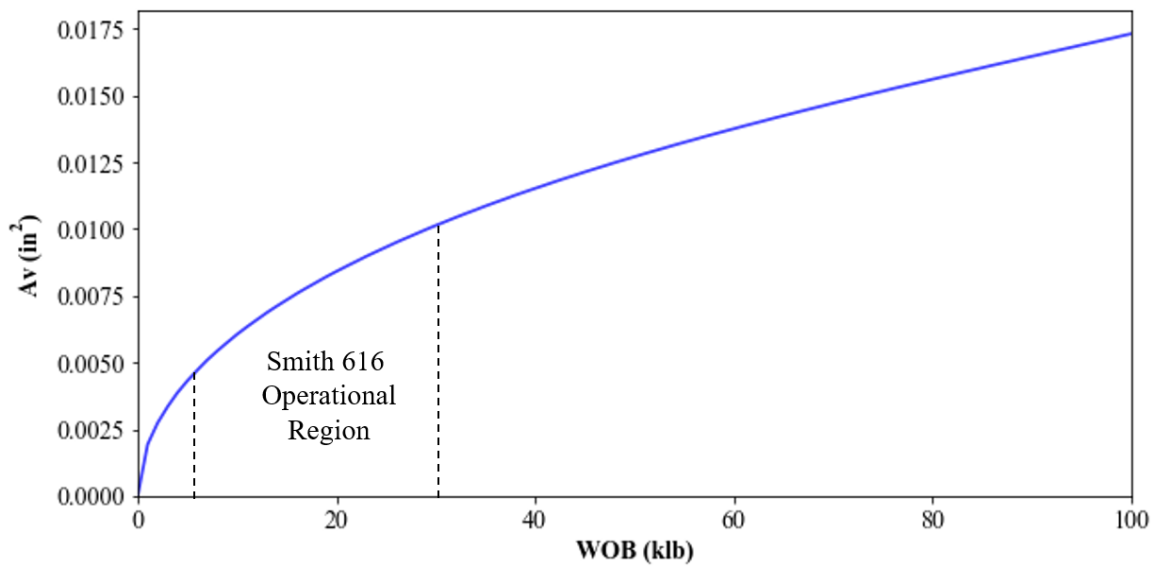
Figure 2.4: A_v vs. WOB relationship for Hareland and Rampersad (1994) PDC bit ROP model formulation.

Figure 2.4 was reproduced with typical bit design and rock strength values of $\alpha = 30°$, $\theta = 10°$, $N_c = 38$, $d_c = 0.63\text{in}$, and $\sigma_c = 10,000\text{psi}$. From Eq. 2.18, the overall relationship between ROP and WOB depends on both A_v and the empirical model coefficient c:

$$ROP \propto \frac{A_v}{WOB^c} \tag{2.21}$$

44

Coefficient c appears in the denominator of Eqs. 2.18 and 2.21, detracting from the ROP-WOB relation encountered in A_v. Zooming in on the manufacturer's WOB operating range for the Smith 616 PDC bit (*SHARC*, 2015) utilized to drill the Williston Basin well analyzed in this study and varying the c coefficient from 0.1 to 0.6:
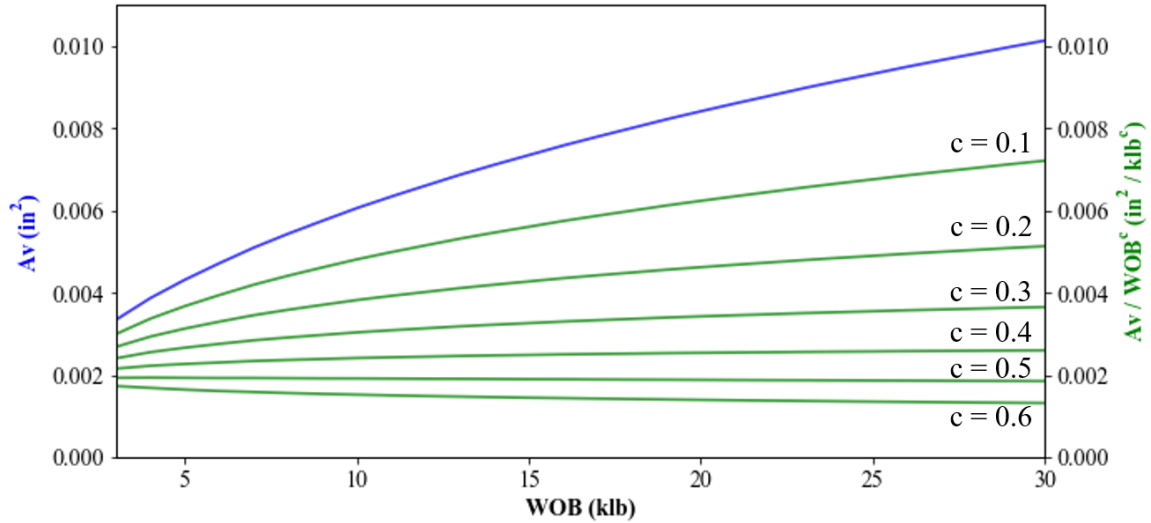
Figure 2.5: Total WOB contribution for Hareland and Rampersad (1994) PDC bit ROP model in the Smith 616 PDC bit operating range.

Figure 2.5 indicates that A_v is approximately proportional to the square root of WOB in the conventional bit weight operational range with the original Hareland and Rampersad (1994) PDC bit ROP model formulation. The model will produce a negative WOB effect on ROP for any value of c greater than 0.5.

The initial Hareland and Rampersad (1994) drag bit model was derived for natural diamond bits, with A_v expressed as:

$$A_v = \left(\frac{d_c}{2}\right)^2 cos^{-1}\left(1 - \frac{2P}{d_c}\right) - (d_c P - P^2)^{0.5}\left(\frac{d_c}{2} - P\right) \qquad (2.22)$$

45

Recreating Fig. 2.4 for this definition of rock area compressed in front of a cutter:
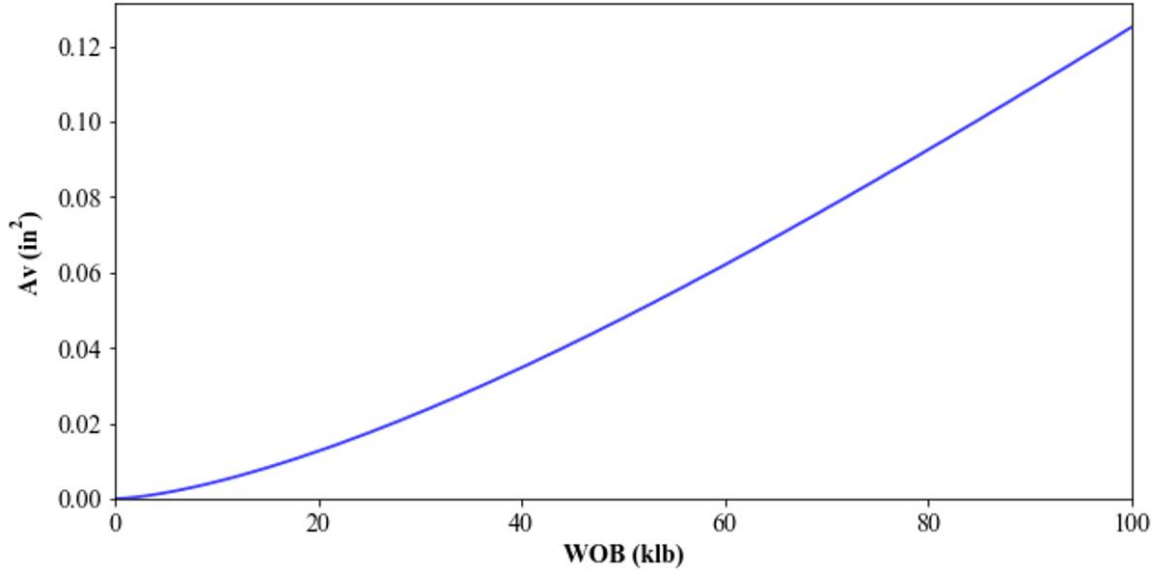
Figure 2.6: A_v vs. WOB relationship for Hareland and Rampersad (1994) natural diamond bit ROP model formulation.

Figure 2.6 illustrates a profoundly distinct A_v-*WOB* relation when compared to Figure 2.4. Contrasting Eqs. 2.20 and 2.22, the A_v formulation for PDC bits includes a multiplication by the cosine of cutter siderake and sine of backrake angles, and all terms containing P are divided by the cosine of the backrake angle. The only exception to this pattern arises in the last term, which was demonstrated to possess incompatible units. Hence, the author proposes a new version of A_v for PDC bits, following the template from the natural diamond bit derivation:

$$A_v = \cos\alpha\sin\theta\left[\left(\frac{d_c}{2}\right)^2 cos^{-1}\left(1 - \frac{2P}{\cos\theta\ d_c}\right) - \left(\frac{d_c P}{\cos\theta} - \frac{P^2}{\cos^2\theta}\right)^{0.5}\left(\frac{d_c}{2} - \frac{P}{\cos\theta}\right)\right] \tag{2.23}$$

With this suggested formulation, A_v behavior with WOB mirrors the desired relationship displayed in Fig 2.6:
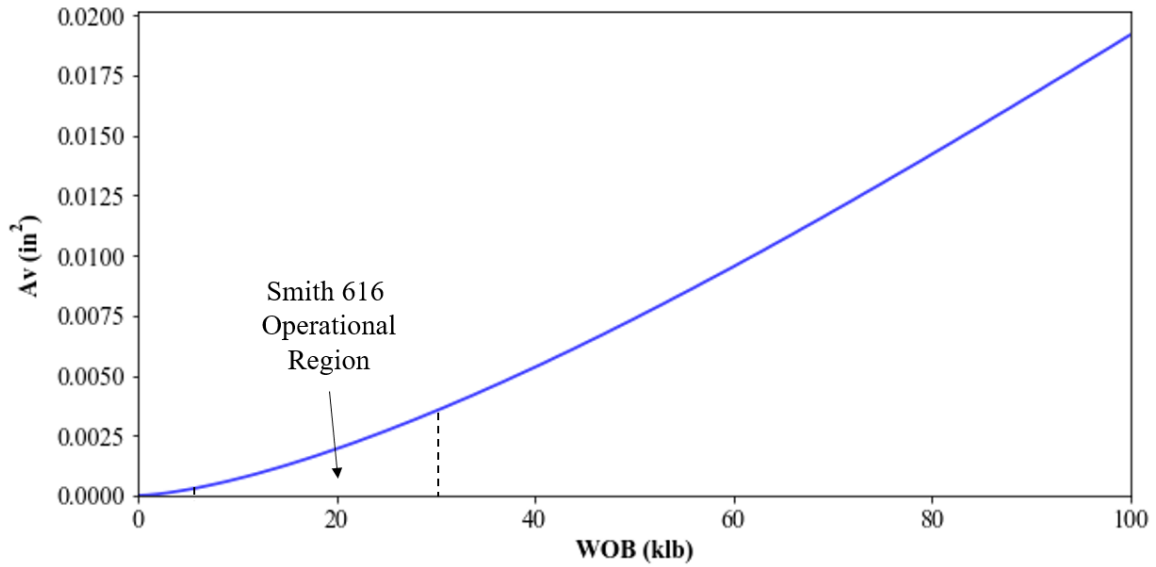
Figure 2.7: Corrected A_v vs. WOB relationship for Hareland and Rampersad (1994) PDC bit ROP model.

Now, the total WOB contribution to the model is investigated varying c between 1 and 1.5:
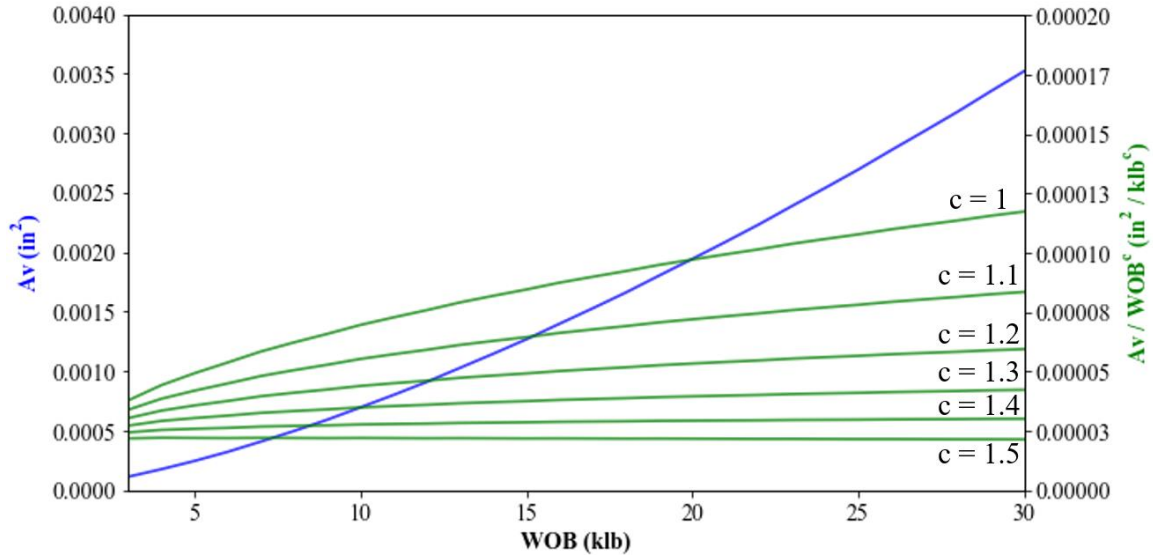
Figure 2.8: Total WOB contribution for corrected Hareland and Rampersad (1994) PDC bit ROP model in the Smith 616 PDC bit operating range.

In the figure above, A_v exhibits a power-law relation with WOB with an exponent of approximately 1.5 within the Smith 616 PDC bit operational weight range. Therefore, coefficient c values are restricted from a minimum of -0.5 to a maximum of 1 to conform with the WOB exponent bounds of 0.5 to 2 proposed by Bourgoyne *et al.* (1986) and presented in Table 2.1. The final form of the corrected Hareland and Rampersad (1994) PDC bit model is given by:

$$ROP = W_f \frac{a}{(RPM^b \ WOB^c)} \frac{14.14 \ N_c \ RPM}{d_b} \cos \alpha \sin \theta$$

$$\left[\left(\frac{d_c}{2} \right)^2 cos^{-1} \left(1 - \frac{4 \ W_{mech}}{\pi \cos \theta \ d_c^2 \ \sigma_c} \right) \right.$$

$$\left. - \left(\frac{2 \ W_{mech}}{\pi \cos \theta \ \sigma_c} - \frac{4 \ W_{mech}^2}{(\pi \cos \theta \ d_c \ \sigma_c)^2} \right)^{0.5} \left(\frac{d_c}{2} - \frac{W_{mech}}{\pi \cos \theta \ d_c \ \sigma_c} \right) \right] \quad (2.24)$$

where W_f is a bit wear function. The slight modification from its original version included in the model formulation above ensures units consistency and appropriate ROP behavior

with varying WOB. Other coefficient bounds are established with basis on the corresponding modified Bourgoyne and Young model coefficients (Table 2.1):

Table 2.2: Model coefficient bounds for corrected Hareland and Rampersad (1994) PDC bit ROP model.

Coefficient	Lower Bound	Upper Bound
a	0.0001	10000
b	0	0.6
c	-0.5	1

2.3.4. Motahhari *et al.* (2010)

Motahhari *et al.* (2010) utilized the same mass conservation principle as Hareland and Rampersad (1994) to derive a PDC bit model for positive displacement mud motor applications:

$$ROP = W_f \left(\frac{G \; RPM_t^{\gamma} \; WOB^{\propto}}{d_b \; S} \right) \tag{2.25}$$

where ROP is the rate of penetration [ft/hr], G is a model coefficient related to bit-rock interactions and bit geometry, α and γ are ROP model exponents, W_f is a bit wear function, WOB is the weight on bit [klbf], RPM_t is the total bit rotational speed resulting from mud motor and drillstring rotational speeds [rev/min], d_b is the bit diameter [in] and S is the confined compressive rock strength (CCS) [psi]. Geometrical relations describing the area of rock compressed in front of a single cutter, similar to Hareland and Rampersad's (1994) A_v (Eq. 2.22), are included in the bit wear function W_f in the Motahhari *et al.* (2010) model formulation.

The bit wear function in Eqs. 2.24 and 2.25 accounts for a reduction in cutter-rock contact area and cutter penetration with incremental wear. Many publications have sought to model W_f (Hareland and Rampersad, 1994, Rahimzadeh *et al.*, 2010, Motahhari *et al.*, 2010, Rashidi *et al.*, 2010a, Liu *et al.*, 2014), introducing additional model coefficients and rock properties (such as abrasion) not measurable in real-time. Therefore, in this study, the wear function W_f is assumed to have a simplistic linear relationship with depth, reaching the reported IADC dull grading evaluation at the end of the bit run:

$$W_f = 1 - \frac{\overline{\Delta h}}{8}\left(\frac{D - D_s}{D_e - D_s}\right) \tag{2.26}$$

where $\overline{\Delta h}$ is the average IADC dull grading measure of wear in inner and outer cutter rows (on a scale from 0 to 8), D is the current drilling depth, D_s is the depth at the start of the bit run and D_e is the depth at the end of the bit run. Eq. 2.26 represents a measure of bit efficiency, yielding a value of one for a new bit at the start of a bit run ($D = D_s$). At full efficiency ($W_f = 1$), the wear function does not impact the predicted ROPs in Eqs. 2.24 and 2.25. As the bit wears out during drilling, Eq. 2.26 expresses a linear loss in efficiency with depth until the bit reaches an efficiency of $1 - \frac{\overline{\Delta h}}{8}$ at the end of the bit run ($D = D_e$), resulting in a gradual predicted ROP reduction.

Coefficient bounds for the Motahhari *et al.* (2010) ROP model are determined from bounds for analogous Bourgoyne and Young (1974) model coefficients, with values suggested in Bourgoyne *et al.* (1986) – Motahhari *et al.*'s G coefficient is bounded according to the drillability constant a_1 in the modified Bourgoyne and Young model, α follows the WOB exponent a_5 and γ complies with the same bounds as the RPM exponent a_6 (Table 2.1).

2.4. MACHINE LEARNING ALGORITHMS

Flexibility in model form allows ML algorithms to overcome analytical ROP models' inability to segment the drilling operational parameter space (as shown in Fig. 2.3). With no predefined equation, hyperparameters specific to each algorithm control model architecture. ML hyperparameters are prescribed by the human user before model training, while parameters, such as the weights of a neural network, are learned during the training phase. In this section, a simplified explanation of the random forests, support vector machines and neural networks algorithms is provided in the context of segmenting drilling features into distinct operational regions. Section 5.4 describes the hyperparameter optimization process, in addition to a more detailed description of each algorithm's hyperparameters. Machine learning techniques have been applied extensively in several industries and the reader is referred to a few publications for further in-depth technical description of the algorithms: Bishop (2006): *Pattern Recognition and Machine Learning*; Hastie *et al.* (2009): *The Elements of Statistical Learning: Data Mining, Inference, and Prediction*; Murphy (2012): *Machine Learning: A Probabilistic Perspective*; Abu-Mostafa *et al.* (2012): *Learning from Data*; and James *et al.* (2013): *An Introduction to Statistical Learning with Applications in R*.

2.4.1. Random Forests

Consider a hypothetical drilling scenario in which the leading factor affecting ROP behavior is whether drillstring rotational speed is over 60rev/min. A decision tree ROP model splits the dataset into two groups according to this criterion. Data points with RPM lower than 60rev/min are grouped together and their average ROP represents the modeled response for the entire cluster. The same procedure is applied to points with rotational speed exceeding 60rev/min. Now, suppose that high WOB values combined with high

RPM lead to severe hole cleaning issues and ROP actually slows down. By inserting an interior node testing for excessive WOB in the branch with RPM greater than 60rev/min, the decision tree model accounts for the inadequate hole cleaning situation:
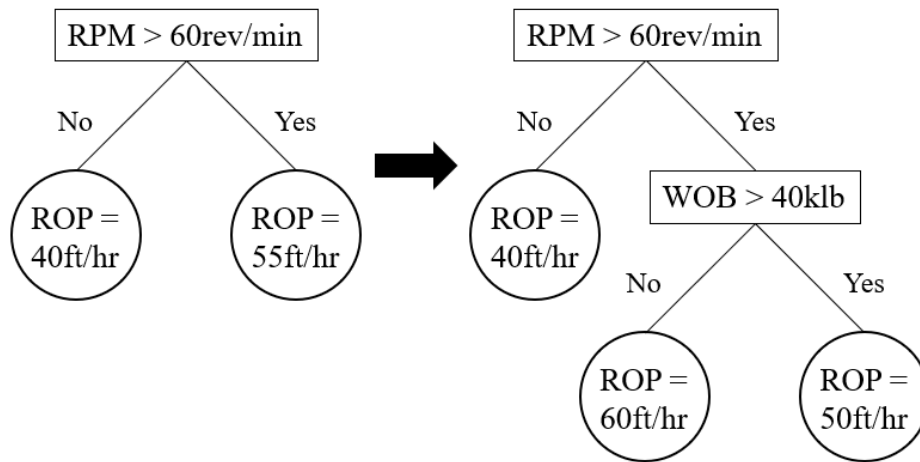
Figure 2.9: Decision trees for ROP prediction in hypothetical scenario.

Figure 2.9 illustrates that even though ROP may be higher with an increase in RPM or WOB individually, the combined effect of raising those variables may lead to ROP reduction. The terminal nodes (leaves) represent different regions of the operational space. While analytical ROP models cannot segment the response of a single variable (WOB, shown in Fig. 2.3), decision trees are able to identify drilling conditions encountered in operational regions defined by two or more drilling features (RPM and WOB, for the rightmost tree in Fig. 2.9).

Segmentation in the WOB-RPM parameter space can be visualized while examining a different hypothetical drilling scenario modeled with a decision tree:
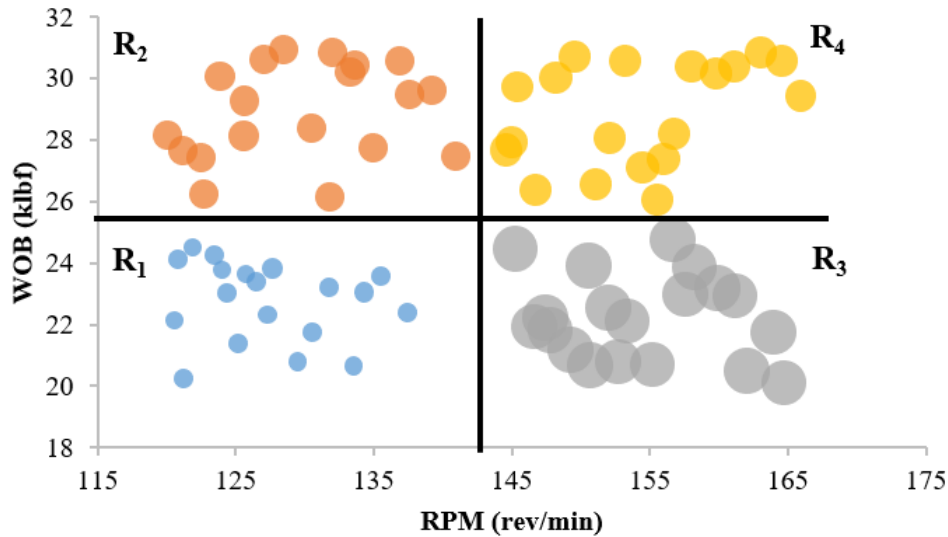
Figure 2.10: Segmentation of WOB-RPM space by a decision tree model. Larger bubble diameters represent increasing ROP.

The figure above is divided into four regions (R_1-R_4). In R_1, low WOB and RPM values lead to a baseline low ROP. Maintaining low RPM and increasing WOB leads to higher ROP values (R_2). Within region R_3, ROP increases considerably by keeping WOB low and increasing RPM in relation to R_1. However, as WOB is increased in relation to R_3, ROP actually decreases (R_4). This behavior is similar to the situation encountered in the hypothetical scenario presented in Fig 2.9. Independent increases in WOB and RPM result in higher ROP, but high WOB and RPM values combined lead to hole cleaning issues and ROP reduction.

In a realistic field drilling scenario, the simple trees presented in Fig. 2.9 will likely perform poorly in predicting ROP. They could be grown further, with more internal nodes that divide the dataset into additional regions. However, deeper trees suffer from high variance, meaning that a small change in the training data will modify the tree structure considerably and yield vastly different predictions. In order to overcome high variance, researchers have designed algorithms that grow multiple distinct deep trees and then

53

average out the predictions of all trees for each data point. Random forests (RF) implements this concept by only considering a random subgroup of variables for each internal node split to decorrelate the trees (Ho, 1995). Breiman (2001) improved the original random forests algorithm by introducing bootstrap aggregating (bagging). In this newer RF version, considered the standard contemporarily, trees are trained on a random subset of the training data sampled uniformly and with replacement (bootstrap sampling). The number of features to be considered at each split, number of trees, and how deep trees grow are all hyperparameters of the random forests algorithm and further discussed in Section 5.4.

2.4.2. Support Vector Machines

The maximal margin hyperplane provides another method of splitting up the drilling operational parameter space. A hyperplane divides a space of any dimensions in two. In a two-dimensional space, a hyperplane is simply a line, whereas in a three-dimensional space, it is represented by a plane. Suppose that, in a separate hypothetical scenario, drilling is progressing efficiently and ROP approaches a linear relationship with RPM. However, when the drillstring rotational speed exceeds 150rev/min, severe drilling vibrations occur and ROP behavior becomes erratic. These two operational regions (efficient drilling and high vibrations) are linearly separable with respect to RPM, and the maximal margin hyperplane will be defined by the line located at the greatest distance from data points in both groups:
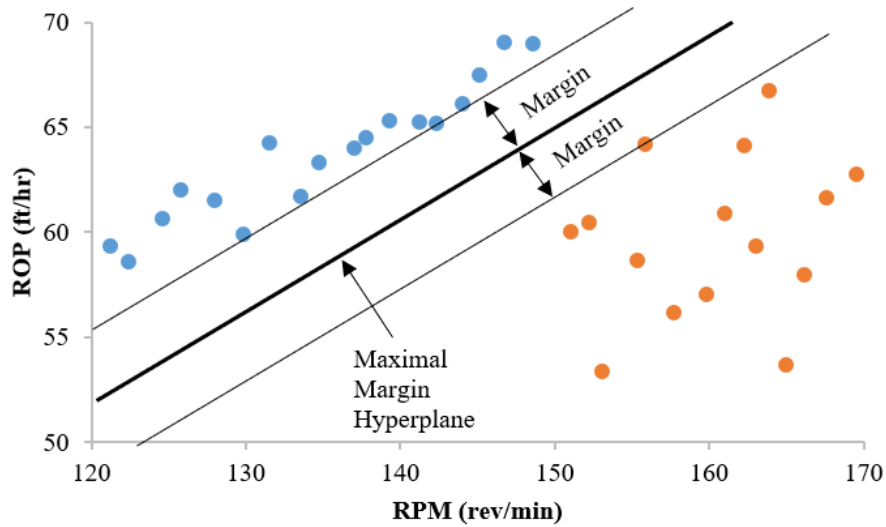
Figure 2.11: Maximal margin hyperplane separating efficient drilling (blue) and high vibrations (orange) data.

Note that the maximal margin hyperplane is entirely based on the data points situated right at the margins. These two points in the figure above, equidistant from the hyperplane, are referred to as support vectors. Figure 2.11 displays an idealized case for detection of a drilling dysfunction. Considering additional drilling parameters and in actual field conditions, it is unreasonable to expect acquisition of linearly separable data distinguishing efficient drilling from high vibrations, inadequate hole cleaning or bit balling operational regions. Support vector machines (SVM) overcome this issue by allowing some data points to violate the margin, a soft-margin (Cortes and Vapnik, 1995), and by mapping input data to a higher-dimensional space with non-linear kernel functions (Boser *et al.*, 1992). A cost hyperparameter controls the amount of margin violations tolerated. Popular choices for the kernel model, which is also a hyperparameter, include polynomial and radial basis functions. SVM's extension to regression problems (support vector regression machines) incorporates an ε-insensitive loss function (Drucker *et al.*,

1996). The ε hyperparameter defines a threshold distance from model predictions, and training data points inside this region (ε-tube) are ignored and assigned zero loss.

2.4.3. Neural Networks

Neural networks bear such designation due to analogies to the human brain. Computational units are termed neurons (McCullogh and Pitts, 1943), which communicate with one another in analogous manner to biological neurons' synapses. A neural network is composed of an input layer, one or more hidden layers, and an output layer. Neurons in the first hidden layer aggregate a weighted linear combination of any relevant measurements prescribed in the input layer and add non-linearity through activation functions. Their outputs are recombined in subsequent hidden layers until the modeled response is obtained in the output layer. Much of the hype surrounding neural networks comes from the fact that it has been proven that given enough neurons, a single hidden layer neural network serves as a universal approximator for any continuous function (Hornik *et al.*, 1989). Arehart (1990) published one of the first applications of neural networks to a drilling problem, predicting bit wear with ROP, WOB, torque, RPM and HSI as inputs. In a drilling speed modeling framework, features such as depth, WOB, RPM and flow rate are fed into the input layer and then combined in hidden layers to produce ROP as the output:
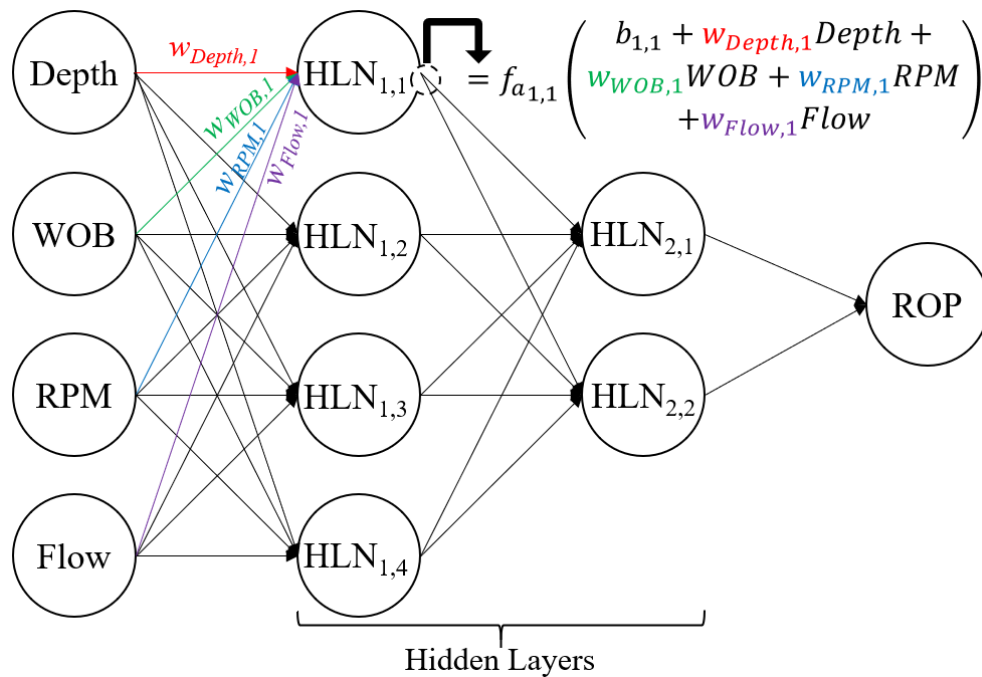
Figure 2.12: Neural network architecture with depth, WOB, RPM, and flow rate as inputs, 4 neurons in the first hidden layer (HLN – hidden layer neuron with activation function f_a), 2 neurons in the second hidden layer and ROP as output. Term $b_{1,1}$ comes from a bias term (not shown).

The highlighted output for the first neuron in the first hidden layer produces a transformation of the original data, discovering new features that represent relations between these inputs. Neurons in the second hidden layer link the outputs of the four previous neurons and generate their own features, finally yielding the predicted ROP in the output layer. Weights for each neuron connection are computed through the back-propagation algorithm (Rumelhart *et al.*, 1986). The number of hidden layers, number of neurons in each hidden layer and activation function of each neuron are hyperparameters that define the neural network architecture.

2.5. ANALYTICAL AND MACHINE LEARNING ROP MODELING COMPARISON

Increased flexibility provided by ML algorithms allows for modeling of more complex functions, a desirable trait for the highly non-linear problem of estimating ROP. However, increased model complexity also creates a couple of significant downsides in reduced interpretability and risk of overfitting. The simple decision trees in Fig. 2.9 are straightforward to interpret, but such interpretability is greatly diminished as the random forests algorithm averages out multiple deep trees to improve predictive accuracy. On the other hand, analytical ROP model equations easily reveal the effect of a step-wise change in a drilling parameter (e.g. WOB) to ROP but their oversimplification is not conducive to modeling complicated problems. Complexity in model form invokes the bias-variance trade-off, an important topic in ML applications discussed in this section.

2.5.1. Bias-Variance Trade-Off

Model complexity induces a compromise between bias and variance. Variance, as mentioned earlier, measures the impact of modifying the training dataset on model predictions. The simplest possible model is given by a constant, represented by a horizontal line in a 2D plot. Such model will have zero variance, since no matter what training data are provided, the model will always produce the same output. On the other hand, bias relates to the simplification error caused by representing complex relationships with rudimentary models. If the previous constant model (horizonal line) is applied to an intricate problem, it will be extremely biased and likely highly inaccurate. Conversely, fitting a curve traversing every training data point will result in a very complicated model with low bias. However, small changes to a few data points will impact the model and its predictions profoundly, exemplifying high variance. This bias-variance trade-off indicates

that an appropriate level of model complexity is necessary to achieve both low bias and low variance.

In the context of ROP modeling, analytical models tend to be highly biased. Analytical ROP models presented in Section 2.3 generally assume that drilling speed is a power-law function of a few measurable variables, even though the drilling process is much more complicated. The amount of bias varies between models, as the more intricate Bourgoyne and Young (1974) formulation is not as biased as Bingham's (1964) simplistic equation. Variance, on the other hand, typically remains low for analytical models with bounded coefficients. Even if the response of a few data points is slightly modified, overall model predictions will not vary significantly. Machine learning algorithms can handle any number of variables as inputs. Ideally, a perfectly unbiased ML ROP model would incorporate measurements from all phenomena affecting drilling in an architecture flexible enough to fully represent their true interactions. In reality, current technology is not sufficient to provide direct measurements of all drilling variables and the issue is aggravated when considering real-time data availability. As machine learning models get more complex in model form, their bias decreases but additional variance is introduced. Complex models are also at risk of overfitting the training data.

Measurement noise may be fitted in addition to signal if the chosen model form is more complex than the true response function. Consider an experiment in which five data points have been collected:

(a) *Learning from Data* (2012)   (b) Adapted from *Learning from Data* (2012)
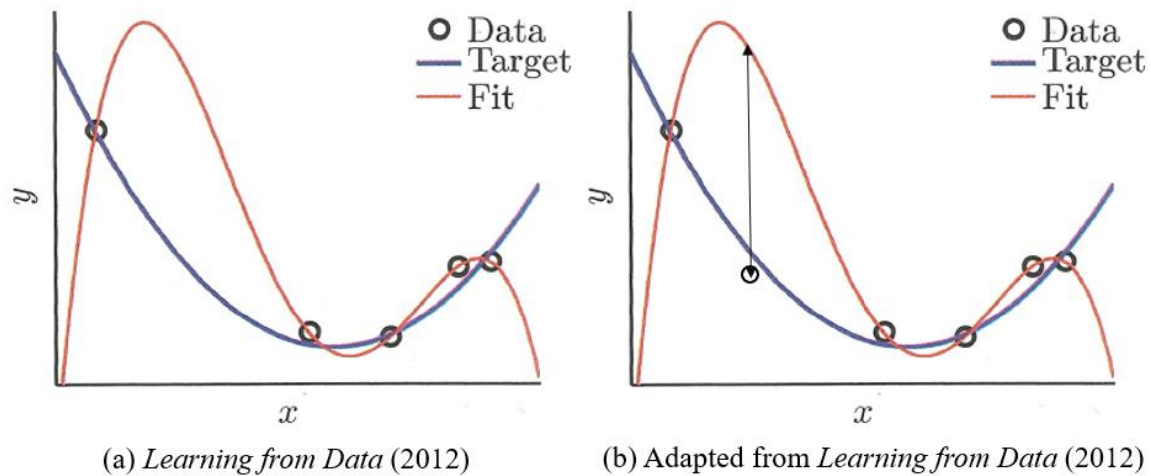
Figure 2.13: Overfitting example from Abu-Mostafa *et al.* (2012): *Learning from Data* page 120.

In the left plot of the figure above (Fig 2.13a), a 4th order polynomial (red) can perfectly fit the five data points in the training dataset. The model will exhibit zero error with the data measured thus far. However, the target function (blue) is quadratic, and if a new data point is collected (Fig 2.13b), it may fall far away from the fitted red curve. Model error at the new point, represented by the black arrow, is very high. This discrepancy between model performance on training data and new data, caused by overfitting, reveals that the model will not generalize well. Overfitting presents a substantial concern with complex machine learning models. Hence, ML model error must be evaluated on data unseen by ML algorithms during the training phase. Such data, denominated test data, yield an error metric typically referred to as the test error. Models benefit by learning from as much data as possible, implying that it is undesirable to leave out a portion of available data when fitting the model in order to evaluate test error.

2.5.2. Cross-Validation

Cross-validation (CV) is a valuable technique to estimate test error without holding out data points from the training dataset for ensuing model testing. The process starts by randomly splitting the dataset into k folds (groups). Then, models are trained iteratively with data from all but one fold and test error is computed with the left-out fold. The CV error is given by the average of test errors from all iterations. The following figure illustrates the 10-fold ($k = 10$) cross-validation procedure with drilling data:

Data Row	TVD (ft)	ROP (ft/hr)	WOB (klb)	RPM (rev/min)	FLOW (gpm)
1	7091.25	89.59	22.06	40.00	334.36
2	7092.00	94.38	20.95	40.00	336.00
3	7092.75	93.40	20.16	40.00	336.05

98	7163.00	88.28	19.59	40.00	336.00
99	7163.75	58.71	22.85	39.95	335.16
100	7164.50	71.73	18.34	40.03	334.93

k	Data Rows
1	17, 33, 36, 65, 69, 80, 81, 82, 84, 93
2	10, 31, 32, 39, 44, 51, 52, 56, 78, 92
3	2, 19, 27, 35, 38, 46, 62, 73, 94, 97
4	23, 34, 40, 48, 54, 59, 67, 88, 95, 99
5	15, 26, 41, 45, 53, 77, 83, 86, 91, 98
6	3, 4, 21, 24, 43, 49, 55, 58, 74, 87
7	8, 30, 42, 47, 60, 66, 70, 89, 90, 100
8	7, 13, 14, 22, 57, 61, 63, 68, 85, 96
9	6, 11, 18, 20, 25, 28, 29, 50, 71, 76
10	1, 5, 9, 12, 16, 37, 64, 72, 75, 79

Iteration	Training Folds	Test Fold	Test Error
1	2-10	1	5.57%
2	1, 3-10	2	16.94%
3	1, 2, 4-10	3	9.01%
4	1-3, 5-10	4	10.72%
5	1-4, 6-10	5	12.93%
6	1-5, 7-10	6	9.67%
7	1-6, 8-10	7	7.75%
8	1-7, 9, 10	8	4.90%
9	1-8, 10	9	8.79%
10	1-9	10	3.48%
		CV Error	8.98%

Figure 2.14: 10-fold cross-validation for ROP modeling.

Cross-validation assesses a model's ability to generalize using the training dataset. Analytical ROP models are restricted in model form by bounded coefficients and tend to

display similar performance with respect to training and test data. However, for consistency purposes, cross-validation will also be applied to analytical ROP models in this study.

Chapter 3: Drilling Optimization Problem Formulations

Real-time drilling optimization encompasses two distinct optimization problems. First, an ROP model which accurately represents the drilling process must be trained. This optimization problem involves finding model coefficients that best fit field data, bounded by sensible values as discussed in Chapter 2. Then, optimal drilling parameters (WOB, RPM, flow rate), bounded by operational and rig equipment limitations, are selected according to the trained model to maximize ROP. This chapter presents an overview of gradient-based and direct search optimization methods and formulations of the two optimization problems of interest. Implementations of ML algorithms, such as the ones in Python's *scikit-learn* (Pedregosa *et al*., 2011) utilized in this study, contain their own particular training scheme. In Section 3.2, three possible loss functions for fitting analytical model coefficients are described and model performance metrics are introduced.

3.1. OPTIMIZATION METHODS

Mankind has solved optimization problems since ancient history. From the allocation of materials and manpower to construct cities and roads in the most efficient manner to calculating the shortest travel path, optimization has been ubiquitous in human life. Optimization problems are generally framed in terms of minimizing an objective function, which indicates a measurement of performance, of one or more variables:

$$\text{minimize} \quad f(x_1, \dots, x_n) = f(\vec{x}) \tag{3.1}$$

where $f : \mathbf{R}^n \to \mathbf{R}$ is the objective function and x_1 through x_n are the decision variables. This objective function notation illustrates that the function *f* maps *n* real-valued inputs into

63

one real-valued output. The solution to the problem posed in Eq. 3.1 is to find the vector of variables corresponding to the lowest value of the objective function:

$$f(\vec{x}^*) \leq f(\vec{x}) \tag{3.2}$$

where $\vec{x}^*$ is the globally optimal solution if Eq. 3.2 is satisfied for the entire domain of the objective function f. In problems with complex objective functions, solvers generally seek the less ambitious goal of satisfying Eq. 3.2 within a neighborhood, arriving at a local optimum.

Mathematical advancements in solving optimization problems became possible with the invention of Calculus in the 17th century, independently by Isaac Newton and Gottfried Leibniz. In 1755, Leonhard Euler's *Institutiones Calculi Differentialis* (Foundations of Differential Calculations) book defined the first-order (first derivative) necessary optimality condition for unconstrained optimization problems with a continuously differentiable objective function of several variables (Forst and Hoffmann, 2010):

$$\nabla f(\vec{x}^*) = 0 \tag{3.3}$$

where $\vec{x}^*$ represents a vector of variables that minimizes the objective function locally. This condition states that the gradient of the objective function must equal zero (stationary point) at a local extremum. Eq. 3.3 is a necessary condition for optimality, but it does not generally guarantee that $\vec{x}^*$ is indeed a local minimum. Second-order (second derivative) requirements are needed to guarantee (sufficient condition) local optimality. A function's Hessian matrix, composed of second-order partial derivatives, provides information about

the curvature of its graph. The second-order sufficient optimality condition for twice differentiable functions states that the Hessian matrix must be positive definite at a local minimum:

$$\vec{s}^T \, \nabla^2 f(\vec{x}^*) \, \vec{s} > 0, \quad \forall \vec{s} \neq 0 \tag{3.4}$$

All eigenvalues of a positive definite matrix are positive. Since the second derivative represents the rate of change of the first derivative, Eq. 3.4 implies that first derivatives are increasing and the function has upward curvature at a local minimum. A less-strict second-order necessary optimality condition requires the Hessian matrix to be positive semi-definite $(\vec{s}^T \, \nabla^2 f(\vec{x}^*) \, \vec{s} \geq 0, \quad \forall \vec{s})$.

Most real-life problems are bounded by constraints, meaning that decision variables must fall within a feasible region. Adding equality and inequality constraints to the unconstrained optimization problem described in Eq. 3.1:

$$
\begin{aligned}
\text{minimize} \quad & f(\vec{x}) \\
\text{subject to} \quad & g_i(\vec{x}) \leq 0, \quad i = 1, \dots, m \\
& h_i(\vec{x}) = 0, \quad i = 1, \dots, p
\end{aligned}
\tag{3.5}
$$

Eq. 3.5 represents the standard form of a constrained optimization problem. Joseph-Louis Lagrange's 1797 publication *Théorie des Fonctions Analytiques* (Theory of Analytical Functions) was a pioneering study of optimization problems with equality constraints (Forst and Hoffmann, 2010). The method of Lagrange multipliers introduces dual variables to incorporate a weighted sum of the constraints into the objective function, yielding the Lagrangian function:

65

$$L\left(\vec{x},\vec{\lambda},\vec{v}\right) = f(\vec{x}) + \sum_{i=1}^{m} \lambda_i g_i(\vec{x}) + \sum_{i=1}^{p} v_i h_i(\vec{x}) \qquad (3.6)$$

where λ_i is the Lagrange multiplier (dual variable) for the ith inequality constraint and v_i is the Lagrange multiplier (dual variable) for the ith equality constraint. In Eq. 3.6, the Lagrangian function formulation introduces a penalty, or displeasure, for any violation of the constraints g_i and h_i. The Lagrange dual problem seeks to find optimal $\vec{\lambda}^*$ and $\vec{v}^*$ values that provide the best lower bound for the associated primal problem in Eq. 3.5 (Boyd and Vandenberghe, 2004). More than a hundred and fifty years after Lagrange's publication, Kuhn and Tucker (1951) generalized the method of Lagrange multipliers for inequality constraints (Eq. 3.6 includes this generalization). Afterwards, it was discovered that Karush (1939) had already arrived at equivalent results. Hence, the first-order necessary optimality conditions for constrained problems, implemented in many contemporary solvers, are known as the Karush-Kuhn-Tucker (KKT) conditions. Accounting for constraints, the stationarity condition presented in Eq. 3.3 becomes:

$$\nabla_{\vec{x}} L\left(\vec{x}^*, \vec{\lambda}^*, \vec{v}^*\right) = 0$$

$$\nabla f(\vec{x}^*) + \sum_{i=1}^{m} \lambda_i^* \nabla g_i(\vec{x}^*) + \sum_{i=1}^{p} v_i^* \nabla h_i(\vec{x}^*) = 0 \qquad (3.7)$$

Eq. 3.7 describes one of the KKT conditions. Additional feasibility conditions are given by:

$$g_i(\vec{x}^*) \leq 0, \quad i = 1, \dots, m$$

$$h_i(\vec{x}^*) = 0, \quad i = 1, \dots, p$$

$$\lambda_i^* \geq 0, \qquad i = 1, \dots, m \tag{3.8}$$

Finally, the last KKT first-order constrained optimality condition represents complementary slackness:

$$\lambda_i^* g_i(\vec{x}^*) = 0, \quad i = 1, \dots, m \tag{3.9}$$

Since all g_i are nonpositive, Eq. 3.9 indicates that all λ_i^* Lagrange multipliers are equal to zero except when the ith inequality constraint is active ($g_i(\vec{x}^*) = 0$). This is an important property for drilling parameter optimization and is further discussed in Section 3.3.

For a limited amount of easy constrained optimization problems, it is possible to solve the KKT system of equations analytically. However, interesting, complex problems must be solved iteratively by numerical methods. Starting from an initial guess $\vec{x}_0$, optimization algorithms seek improved objective function values with passing iterations until they converge to an optimal value $\vec{x}^*$. In line search, an example of a common optimization strategy, a search direction is specified to move from the current iteration point towards a better solution:

$$\vec{x}_{k+1} = \vec{x}_k + \alpha_k \vec{p}_k \tag{3.10}$$

where $\vec{p}_k$ is the search direction at iteration k and α_k is the step length. As indicated by the optimality conditions in Eqs. 3.3, 3.4 and 3.7, information about the gradient and Hessian of the objective function is useful in defining a search direction. Intuitively, the gradient of

a function at a point establishes the direction of fastest change, providing a natural search direction selection. Therefore, a large class of optimization methodologies are gradient-based, relying on the gradient, and oftentimes Hessian, of the objective function to select the next iteration step.

One obstacle to successful implementation of gradient-based techniques arises from the requirement that the objective function must be continuously differentiable (and twice differentiable if Hessian information is utilized). Gradients and Hessians can be approximated with finite difference techniques, although loss of accuracy often occurs due to operations with small numbers (Powell, 1998). In addition, the objective function must be sufficiently smooth for these approximations to effectively represent the true derivatives. Hence, a second class of optimization methods are derivative-free, conducting direct search for optimal values. Direct search optimization algorithms sample the optimization space broadly with spaced out guesses driven by heuristics, using no information about the gradient of the objective function.

Both gradient-based and direct search methods are explored throughout this dissertation to solve the two relevant optimization problems: fitting ROP models and selecting the best operational drilling parameters to drill a well segment. The eight optimization algorithms investigated are summarized in the table below and further discussed in Sections 3.1.1 and 3.1.2:

Table 3.1: Optimization methods considered for the two problems in real-time drilling optimization.

Optimization Method	Gradient-Based	Direct Search	Bounds	Constraints
L-BFGS-B	✓		✓	
Trust Region Reflective	✓		✓	
SLSQP	✓		✓	✓
Nelder-Mead		✓		
COBYLA		✓		✓
Basin-Hopping	✓	✓	✓	✓
Particle Swarm Optimization		✓	✓	✓
Brute Force		✓	✓	

Basin-hopping can fall into either gradient-based or direct search categories, as it employs any local optimization methodology (such as the five preceding ones in Table 3.1) and introduces a randomized global stepping procedure in search of the global optimum. In addition to the gradient-based vs. direct search distinction, algorithms are classified as to whether they can handle bounds and/or constraints. Design variable bounds are a type of constraint and can be formulated as such even if an algorithm does not explicitly accept bounds as inputs (e.g. COBYLA). All eight optimization techniques in Table 3.1 are applied as implemented in Python's *scipy.optimize* (Oliphant, 2007) library with the exception of particle swarm optimization, which is carried out with Python's *pyswarm* (Lee and Castillo-Hair, 2013) package.

For simplicity, vector notations are omitted ($\vec{x}_k = x_k$) and gradient and Hessian functions at each iteration point are defined in the following sections as:

$$f_k = f(x_k)$$
$$g_k = \nabla f(x_k)$$
$$H_k = \nabla^2 f(x_k) \tag{3.11}$$

69

3.1.1. Gradient-Based Optimization

Newton's classical optimization algorithm iteratively computes an optimal solution by approximating the objective function in the vicinity of each point with a second-order Taylor series expansion (quadratic model):

$$f(x_k + s_k) \approx f_k + g_k{}^T s_k + \frac{1}{2} s_k{}^T H_k s_k = m_k(s_k) \tag{3.12}$$

where s_k is the step to be taken at iteration k and m_k is the objective function model at iteration k. The model m_k is minimized by setting its gradient with respect to s_k equal to zero:

$$\nabla_{s_k} m_k = 0 \tag{3.13}$$

The solution to Eq. 3.13 yields the Newton step, which minimizes the value of the approximated objective function (Eq. 3.12) at each iteration:

$$s_k^N = -H_k{}^{-1} g_k \tag{3.14}$$

Equation 3.14 demonstrates that Newton's method relies on computation of the gradient and Hessian of the objective function locally. It is important to note that the Hessian matrix must be invertible for the Newton step to be defined. Newton's optimization algorithm performs well when the quadratic model in Eq. 3.12 provides a good approximation to the objective function. For certain iterations, the Newton step formulated in Eq. 3.14 can move the next guess far away from the current point and the model approximation may not hold.

In this case, it is possible that the objective function value is not reduced, and the algorithm will not converge to an optimal solution.

Two common approaches in optimization may be implemented with Newton's method to mitigate this convergence issue. Line search, introduced in Eq. 3.10, incorporates a variable step length. Comparing the iterative role of the Newton step to Eq. 3.10:

$$s_k^N = \alpha_k p_k \qquad (3.15)$$

Now, the Newton direction is defined as:

$$p_k^N = -H_k^{-1} g_k \qquad (3.16)$$

From Eq. 3.15, the classic Newton algorithm performs a Newton step in the Newton direction with constant step length (α_k) equal to one. In the line search modified Newton method, the step length can be reduced to ensure that the quadratic model approximation of the objective function is reliable. The line search problem is defined as finding the step length that minimizes Eq. 3.12:

$$\text{minimize} \quad f(x_k + \alpha_k p_k) \qquad (3.17)$$

where $p_k = p_k^N$ for the line search modified Newton method. The problem above is frequently solved approximately with a restricted amount of trials to reduce computational expense (Nocedal and Wright, 2006).

Trust region is the second strategy that can improve convergence of the classical Newton algorithm. This technique ensures that iteration step sizes remain within a sub-region (the trust region) where the quadratic approximation of the objective function is satisfactory. Typically specified by a radius, since the trust region is often spherical in shape, the size of the trust region is influenced by the ratio between the true objective function value reduction and the reduction predicted by the quadratic model (in the previous iteration):

$$r_k = \frac{f(x_k) - f(x_k + s_k)}{m_k(0) - m_k(s_k)} \tag{3.18}$$

The trust region size in iteration $k+1$ is adjusted according to the value of r_k, representing the latest agreement between the objective function and its quadratic model. If the value of r_k is small or negative, there is little trust in the model and the trust region shrinks. On the other hand, the closest r_k is to one, the more reliable the model is, and the trust region expands. Both trust region and line search methodologies approximate the objective function locally with a Taylor series quadratic model (Eq. 3.12). In line search, the search direction is established from the model and, subsequently, the appropriate step length is calculated. Contrary to line search, trust region approaches first define a maximum step size and then simultaneously compute the distance and direction that result in the biggest objective function decrease (Nocedal and Wright, 2006).

As previously mentioned, a critical obstacle to the application of Newton's method and its line search and trust region modifications emerges as the Hessian matrix must be invertible. If the Hessian is not positive definite at an iteration point, there is no invertibility guarantee. In addition, it may be impossible to formulate the Hessian explicitly and

72

numerical calculations are frequently computationally expensive. Quasi-Newton methods overcome this problem by replacing the true Hessian with an approximation which is typically forced to be symmetric and positive definite. The approximate Hessian is updated at every iteration based on gradient changes from previous steps. Rewriting the quadratic objective function model (Eq. 3.12) in terms of possible moves to coordinate x and substituting the true Hessian H_k by the approximate Hessian B_k:

$$m_k(x) = f_k + g_k{}^T(x - x_k) + \frac{1}{2}(x - x_k)^T B_k(x - x_k) \qquad (3.19)$$

Note that since B_k is approximated from the gradient of the objective function, only first-order derivative information is necessary for implementation of quasi-Newton methods. The search direction for quasi-Newton line search algorithms becomes:

$$p_k = -B_k{}^{-1}g_k \qquad (3.20)$$

There are several distinct approaches to updating $B_k{}^{-1}$. A very popular quasi-Newton update is known as the BFGS (Broyden–Fletcher–Goldfarb–Shanno) formula, proposed in works published by the four authors in 1970 (Fletcher, 1987).

The BFGS approximate Hessian update is employed in many contemporary optimization algorithms. In Table 3.1, L-BFGS-B (Byrd *et al*., 1995) is the first optimization strategy considered for solving the two main optimization problems in this dissertation. L-BFGS-B is a quasi-Newton optimization method abiding by the BFGS Hessian approximation. The preceding "L" refers to storing a limited memory, smaller dimension (low-rank) BFGS matrix at each update to alleviate computational

requirements. The succeeding "B" indicates that the algorithm can handle bound constraints, imposing lower and upper limits on each design variable. As described by Byrd *et al.* (1995), L-BFGS-B establishes search directions complying with the specified bounds by minimizing the quadratic model with respect to variables that are not actively constrained (held at the bounds) and then performs a line search to determine the appropriate step length.

Next in Table 3.1, the trust region reflective (TRF) algorithm was designed for bound-constrained nonlinear optimization problems by solving the first-order optimality conditions formulated in Branch *et al.* (1999). Instead of computing the exact, yet computationally expensive, trust region step that minimizes the quadratic model, TRF approximates the optimal step by only considering two possible directions of movement (low-dimensional subspace) as suggested by Byrd *et al.* (1988). The directions considered vary depending on whether the Hessian approximation is positive definite. If that is indeed the case, the steepest descent $(-g_k)$ and quasi-Newton $(-B_k{}^{-1}g_k)$ directions compose the explored subspace. Otherwise, corrections to the quasi-Newton direction are applied. TRF's *scipy.optimize* (Oliphant, 2007) implementation is restricted to least-squares problems, so this method is only applied to analytical ROP model fitting (Section 3.2).

Unlike the two previous gradient-based algorithms, sequential least-squares programming (SLSQP) can handle bound, equality and inequality constraints (Kraft, 1988). SLSQP also employs a quadratic model approximation to define search directions, but it does so with the Lagrangian as the objective function in order to tackle additional constraints. Updates to the approximate second-order derivative of the Lagrangian are analogous to BFGS updates, and line search is performed to determine the optimal step length. SLSQP's ability to manage inequality and equality constraints is a major advantage in optimizing drilling operational parameters.

74

3.1.2. Direct Search Optimization

Complex objective functions can be non-smooth, possessing non-differentiable and sometimes even discontinuous segments. In such intricate optimization problems, the gradient is not defined in the entire objective function's domain and gradient estimation techniques such as finite difference will fail miserably around discontinuous sections. Therefore, even though derivatives provide knowledge about the rate of change and curvature of a function, a second class of optimization methods do not utilize any gradient information and rely solely on function evaluations. Some authors refer to them as derivative-free methods. Others, such as Powell (1994, 1998) and Kolda *et al*. (2003), label them direct search methods. The latter denomination is utilized in this study; it is preferred since it is more descriptive of the nature of these algorithms, which operate by broadly sampling the objective function and implementing heuristics to locate improved function values.

According to Powell (1998, 2007), the Nelder-Mead (Nelder and Mead, 1965) or downhill simplex algorithm is one of the most popular direct search methods for unconstrained optimization problems. A *n*-dimensional simplex is a *n*-polytope given by the smallest convex set that encloses its *n*+1 vertices. In simpler terms, simplices extend the concept of a triangle to any dimensions. Hence, simplices are triangles in two-dimensional spaces and tetrahedrons in three-dimensional spaces. Unconstrained determination of optimal WOB, RPM and flow rate values to drill a well section as fast as possible is a three-dimensional problem. When solving it with the Nelder-Mead method, the algorithm starts with an initial simplex (in this case, a tetrahedron) and evaluates the objective function (ROP model) at its vertices. At each iteration, update rules adjust the vertex with the least desirable function value (lowest ROP) and produce a new simplex.

Simplices can elongate or contract according to local objective function behavior, aiming to converge towards the optimal value.

COBYLA (Powell, 1994), or constrained optimization by linear approximation, is also based on the concept of simplices. However, instead of only considering the worst objective function value at one of the simplex's vertices in each iteration, COBYLA uses all vertices' function evaluations to construct a linear polynomial that best approximates the objective function locally. Then, the linear polynomial is minimized based on information about its derivative and a trust region radius to find a new vertex with improved objective function value. Note that the derivative of the linear model is utilized, but not the derivative of the true objective function. Constraints are introduced by a merit function which adds penalties to constraint violations to the original objective function, in a similar manner to Lagrange's method. Newly obtained vertex coordinates must reveal a lower merit function piecewise linear approximation value than the previous optimal, ensuring that constraints are satisfied.

Basin-hopping (Wales and Doye, 1997) combines local optimization operations, performed by an optimization algorithm of choice (such as the ones described above and in the previous section), with a Monte Carlo global stepping algorithm. By introducing randomness and possibly accepting a move that worsens the objective function value, basin-hopping strives to locate the global optimum rather than remaining stuck at local optima. Each local search is preceded by a stochastic (random) perturbation and local minima coordinates are accepted according to the Metropolis criterion if less optimal than the current global optimum. Local optimization can be achieved by either gradient-based or direct search methods, depending on user specification. For the drilling optimization problems in this dissertation, the COBYLA algorithm was chosen as the local minimization procedure for basin-hopping based on performance and ability to handle constraints.

Particle swarm optimization (Kennedy and Eberhart, 1995), or PSO, is a member of swarm intelligence procedures inspired by biological systems in nature. The method carries a number of possible solutions (particles) that communicate with each other, iteratively updating their position and velocity towards an improved solution. PSO enforces constraints by only storing feasible solutions in the particles' memories. Particles are initialized in the feasible space with random position and velocity and eventually converge to the optimal solution, as exemplified in the figure below for the ROP maximization problem:
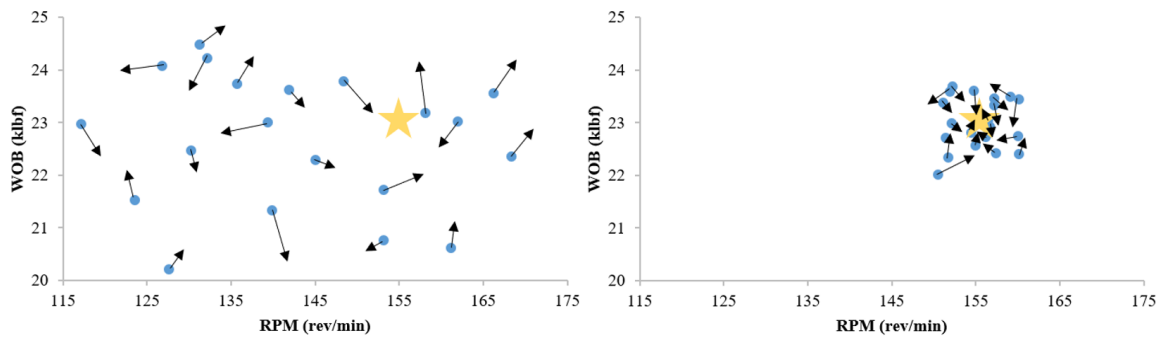
Figure 3.1: ROP maximization by WOB and RPM adjustment with the particle swarm optimization algorithm. Blue dots are particles, black arrows represent particles' velocities and the yellow star indicates the optimal ROP solution.

The left plot in Fig. 3.1 represents the randomly initialized PSO particles at the beginning of the optimization process and the plot on the right displays convergence towards the optimal ROP value. PSO has been applied with relative success to B&Y ROP model fitting by Anemangely *et al*. (2017) and to optimization of drilling parameters in the works of Gandelman (2012), Self *et al*. (2016) and Hegde and Gray (2018). This population-based approach shares similarities with other evolutionary optimization methods applied in

drilling optimization, such as the genetic algorithm (Bahari *et al.*, 2008) and the shuffled frog leaping algorithm (Yi *et al.*, 2014).

Finally, brute force search evaluates the objective function with every possible combination of parameters within a pre-defined grid. This methodology is the only one that always guarantees a global optimal solution given a fine enough grid. However, without any clever heuristics on objective function sampling, computational requirements for searching through every single feasible alternative can be extremely demanding. Thus, real-time application of this optimization strategy may prove computationally prohibitive.

3.2. ANALYTICAL ROP MODEL FITTING

ROP model fitting is, in itself, an optimization problem. In this process, model coefficients are computed to minimize the difference between data observed on the field and values calculated by the model. These differences are commonly referred to as residuals:

$$r_i = ROP_{Field,i} - ROP_{Model,i} \tag{3.21}$$

where r_i represents the residual for ith data point. Residuals are the main components of a loss (or cost) function, the objective to be minimized in a model fitting optimization problem. Different loss functions can be enforced, affecting how the ROP model is trained.

3.2.1. Loss Functions

Traditionally, the most common cost function in model fitting is represented by the sum of the squares of residuals. The optimization's objective is to minimize such loss:

$$\min\left(\sum_{i=1}^{N_1} r_i{}^2\right) = \min\left(\sum_{i=1}^{N_1}\left(ROP_{Field,i} - ROP_{Model,i}\right)^2\right) \tag{3.22}$$

where N_1 is the number of points in the training dataset. The sum of squared differences in the equation above is also known as l_2 loss. Euclidian distance, or l_2-norm, arises from the square root of the squared difference between model prediction and measured value at a point.

Suppose ROP can be modeled as a simplistic power-law relationship with WOB:

$$ROP_{Model,i} = 3\left(WOB_{Field,i}\right)^b \tag{3.23}$$

where b is the WOB exponent that best represents this relation (conforming with Bingham's ROP model nomenclature). As suggested by Bourgoyne *et al*. (1986), WOB exponent values should be bounded between 0.5 and 2. The optimization problem of fitting the ROP model in Eq. 3.23 with l_2 loss becomes:

$$\min\left(\sum_{i=1}^{N_1}\left(ROP_{Field,i} - 3\left(WOB_{Field,i}\right)^b\right)^2\right)$$

$$\tag{3.24}$$

subject to $\quad 0.5 \leq b \leq 2$

In the equation above, the sum of residuals squared is a function of the model coefficient b. A conceivable representation of the relationship between l_2 loss and WOB exponent b values for a number N_1 of data points is illustrated as:
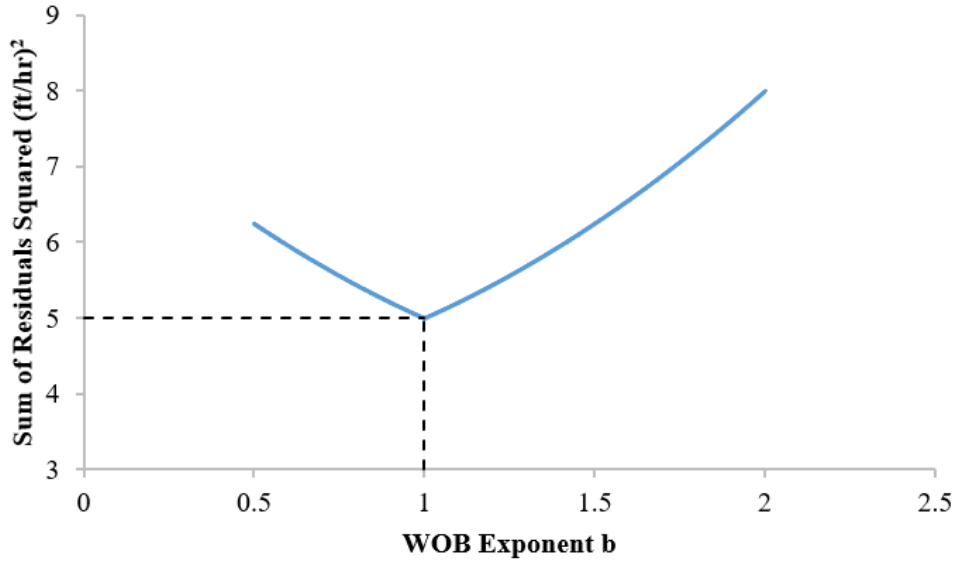
Figure 3.2: Sum of residuals squared vs. WOB exponent for a simplistic ROP power-law model.

In this hypothetical scenario, ROP has a true linear relationship with WOB ($b^* = 1$), laying in the efficient portion of the drilling response curve described by Dupriest and Koederitz (2005). From Fig. 3.2, the derivative of the loss function with respect to WOB exponent b has a value of zero at the optimal b^* for the problem formulated in Eq. 3.24:

$$\frac{d \sum_{i=1}^{N_1} r_i^2}{db}\Big|_{b=b^*} = 0 \tag{3.25}$$

Equation 3.25 represents the unconstrained first-order local optimality condition introduced in Section 3.1 (Eq. 3.3). For the ROP model described in Eq. 3.23, Eq. 3.25 can be solved analytically for the optimal coefficient b^*. However, this simplistic power-law relationship between ROP and WOB is likely not representative of all field drilling conditions. A more realistic ROP model includes the effect of additional drilling

parameters. Rewriting the modified B&Y model (Section 2.3.2) in terms of θ parameters (ML model coefficients' customary notation):

$$ROP = \theta_1 D^{\theta_2} WOB^{\theta_3} RPM^{\theta_4} q^{\theta_5} \tag{3.26}$$

The unconstrained stationarity condition for the above model is given by the gradient of the squared sum of residuals with respect to the five θ model coefficients:

$$\nabla_\theta \sum_{i=1}^{N_1} r_i^2 = \frac{\partial \sum_{i=1}^{N_1} r_i^2}{\partial \theta_j \big|_{j=1}^{5}} = \begin{bmatrix} \dfrac{\partial \sum_{i=1}^{N_1} r_i^2}{\partial \theta_1} \\[2mm] \dfrac{\partial \sum_{i=1}^{N_1} r_i^2}{\partial \theta_2} \\[2mm] \dfrac{\partial \sum_{i=1}^{N_1} r_i^2}{\partial \theta_3} \\[2mm] \dfrac{\partial \sum_{i=1}^{N_1} r_i^2}{\partial \theta_4} \\[2mm] \dfrac{\partial \sum_{i=1}^{N_1} r_i^2}{\partial \theta_5} \end{bmatrix} \Big|_{\theta=\theta^*} = 0 \tag{3.27}$$

where subscript j represents each of the θ_1 through θ_5 parameters. This system of equations can be difficult to solve, and most solvers compute a numerical solution iteratively as described in Section 3.1.

As another popular alternative, the model fitting loss function can invoke the absolute difference between field data and modeled values:

$$\min\left(\sum_{i=1}^{N_1} |r_i|\right) = \min\left(\sum_{i=1}^{N_1} |ROP_{Field,i} - ROP_{Model,i}|\right) \tag{3.28}$$

Fitting a model with the absolute difference (l_1-norm) cost function improves robustness to data outliers. With l_2 loss, substantial differences between modeled values and measured data are amplified by the squared relationship, causing the model to excessively adjust to outliers. On the other hand, l_1 loss solutions are frequently less stable, oscillating considerably. Furthermore, the absolute value function is not continuously smooth, as its derivative is not defined at zero. An additional loss function option is given by the Huber norm (Huber, 1964), which implements squared difference cost for small residual values and absolute difference cost after residuals grow past a pre-defined distance:

$$L_{H,i}(r_i, \delta) = \begin{cases} r_i^2/2 & \text{if } |r_i| \leq \delta \\ \delta|r_i| - \delta^2/2 & \text{if } |r_i| > \delta \end{cases} \tag{3.29}$$

where $L_{H,i}$ is the Huber loss for ith data point and δ is a distance parameter governing the transition from quadratic to absolute difference penalties. This loss function approach combines advantages from both l_1 and l_2 losses: the derivative is defined in the entire function's domain and data outliers are not overly dominant. Again, the model fitting optimization problem is related to minimizing residuals:

$$\min\left(\sum_{i=1}^{N_1} L_{H,i}\right)$$

$$= \min\left(\sum_{i=1}^{N_1} \begin{cases} \left(ROP_{Field,i} - ROP_{Model,i}\right)^2/2 & \text{if } |r_i| \leq \delta \\ \delta|ROP_{Field,i} - ROP_{Model,i}| - \delta^2/2 & \text{if } |r_i| > \delta \end{cases}\right) \tag{3.30}$$

Comparing the three possible loss functions with residuals for a generic ROP model fitting problem:
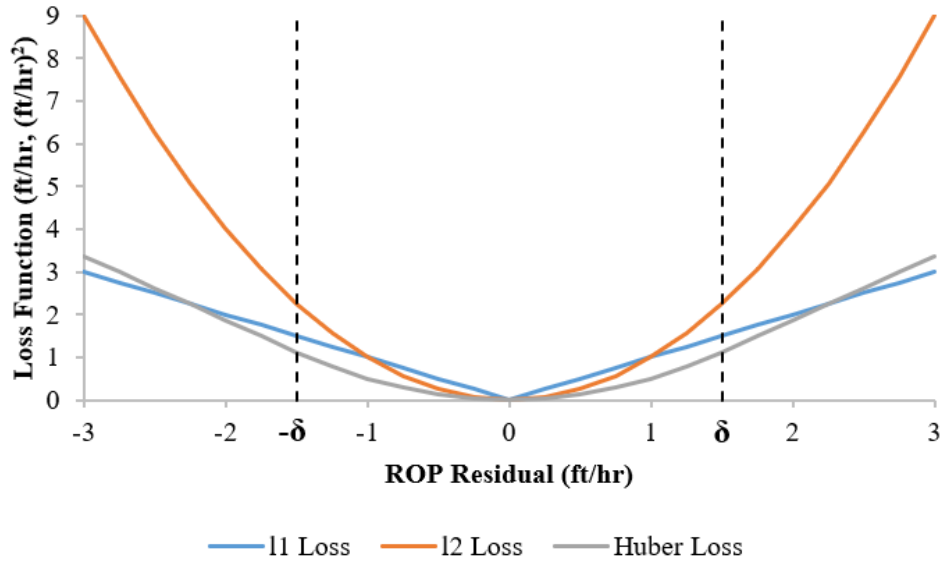
Figure 3.3: ROP residuals and resulting l_1, l_2, and Huber loss function values.

In Fig. 3.3, l_2 loss (orange) is quadratic throughout and grows much faster than the other two cost functions as residual values increase. Huber loss (gray) behavior is controlled by the δ parameter. Note that the l_1 loss (blue) derivative is not defined at zero. Section 5.2 explores the choice of cost function between l_1, l_2 and Huber losses in analytical ROP model fitting for the dataset investigated in this study.

3.2.2. Performance Metrics

Error metrics related to both l_1 and l_2 loss functions will be reported for analytical and ML ROP models. First, absolute error is defined by normalizing the absolute difference between modeled and measured values at each data point by the ROP value observed on the field and then averaging these values for the entire test set:

$$Absolute\ Error = \frac{1}{N_2} \sum_{j=1}^{N_2} \frac{\left|ROP_{Field,j} - ROP_{Model,j}\right|}{ROP_{Field,j}} \tag{3.31}$$

83

where N_2 is the number of points in the test dataset. Note that model error is evaluated on a test dataset (N_2), different from the training dataset (N_1) utilized in model fitting.

The square root of the mean of squared residuals yields RMSE (root-mean-squared-error), a useful metric with the same units as the quantity being modeled:

$$RMSE = \sqrt{\frac{1}{N_2}\sum_{j=1}^{N_2}\left(ROP_{Field,j} - ROP_{Model,j}\right)^2} \tag{3.32}$$

One substantial disadvantage of RMSE as an error standard is that RMSE is a relative measurement, incapable of quantifying error significance without knowledge of the quantity mean. Suppose the RMSE of a ROP model in a certain formation is 10ft/hr. If the average ROP in that formation is 200ft/hr, then the model predicts ROP with only 5% error on average. However, if the same RMSE value is observed in a formation with an average ROP of 20ft/hr, it will represent 50% mean error. Therefore, in order to compare RMSE across different formations in a meaningful scale, the author proposes normalizing it by the mean ROP in the test dataset:

$$Normalized\ RMSE = \frac{\sqrt{\frac{1}{N_2}\sum_{j=1}^{N_2}\left(ROP_{Field,j} - ROP_{Model,j}\right)^2}}{\frac{1}{N_2}\sum_{j=1}^{N_2}ROP_{Field,j}} \tag{3.33}$$

In this dissertation, analytical and ML ROP model performance is computed by Eqs. 3.31 and 3.33 (in percentages).

3.3. Selection of Optimal Drilling Parameters

Pastusek *et al.* (2016) stated that modern autodrillers control the rotation speed of the drawworks drum to maintain ROP, WOB or mud motor differential pressure setpoints. The controller accounts for drum diameter, number of drilling line wraps on the drum, number of lines strung through the crown and traveling block sheaves, and drum speed in order to limit ROP. Alternatively, it rotates the drum as fast as possible (for highest ROP) while satisfying other constraints. Separately, the top drive adjusts drillstring rotational speed for the desired RPM. In a subsequent paper, Pastusek *et al.* (2018) noted an ongoing goal of developing a new penetration per revolution control mode for autodrillers that corrects ROP according to drillstring and mud motor RPM changes. Drilling fluid circulation rate is controlled by the stroke rate and liner size of the rig pumps. The controllers described yield three real-time drilling optimization design variables: WOB, RPM and mud flow rate.

As illustrated in the opening chapter, optimization of drilling parameters is performed by solving an objective function subject to some constraints (see Fig. 1.1). One example of a drilling objective function implemented in ExxonMobil's Drilling Advisory System (Eq. 1.4, extracted from Payette *et al.*, 2015) includes both MSE and an estimation of torsional vibrations severity in its formulation. The approach presented here assumes that the range of operational drilling parameters established by the constraints prevents excessive vibrations or other drilling dysfunctions, simplifying the problem's objective to ROP maximization with respect to the three controllable surface variables:

$$\max_{WOB,RPM,q} ROP = -\min_{WOB,RPM,q} (-ROP) = -\min_{WOB,RPM,q} \left(-f(D,WOB,RPM,q)\right)$$

$$\text{subject to} \quad WOB_{min} \leq WOB \leq WOB_{max}$$

$$0 \leq RPM \leq RPM_{max}$$

$$q_{min} \leq q \leq q_{max}$$

$$0 \leq T \leq T_{max}$$

$$0 \leq \frac{RPM \times T}{5252} \leq P_{TD}$$

$$0 \leq \frac{q \times SPP}{1714} \leq P_{pump} \tag{3.34}$$

Optimization problems are generally formulated in terms of minimizing an objective function, as discussed in Section 3.1. ROP maximization is achieved by minimizing *-ROP* and applying a sign change to the result.

Downhole tools' ratings, hydraulics, and rig equipment power limitations constrain the drilling process. Constraints for selection of optimal drilling parameters in Eq. 3.34 are:

- WOB must remain within the bit manufacturer's specified operating range
- RPM is limited by rotational speeds that do not damage BHA components
- Flow rate is bounded between the minimum required for adequate hole cleaning and a maximum which does not cause BHP to exceed formation fracturing pressure
- Surface torque must not exceed drillpipe make-up torque rating
- Top drive power is split between surface torque and drillstring rotational speed
- Total horsepower provided by all rig pumps produces a trade-off between drilling mud flow rate and standpipe pressure (SPP) at surface

Torque is not controlled directly, but rather monitored as function of WOB via bit aggressiveness. Rewriting Eq. 1.7 for torque:

$$T = \frac{\mu_b WOB d_b}{3}\left(\frac{\text{ft}}{12\text{in}}\right) = \frac{\mu_b WOB d_b}{36} \tag{3.35}$$

where the bit aggressiveness μ_b, dependent on lithology, relates weight on bit and arm of torque to the amount of torque obtained.

The optimal parameter selection problem in Eq. 3.34 does not encompass all field drilling constraints. It provides a starting point with basic constraints and supplementary functionality may be added as needed. Pressure control, not explicitly formulated in the constraints, is paramount in drilling. However, accurate information about the pore pressure and fracture gradient drilling window and a realistic hydraulics model to forecast downhole pressures are fundamental requirements to effectively control surface and well pressures. Thus, mud flow rate serves as a proxy for pressure oversight and SPP is kept at average field values.

Performance of a drilling optimization simulation is measured by its ability to achieve high ROP as predicted by an accurate model. The type of ROP model employed in the objective function significantly influences the appropriate selection of optimization algorithm. With the simplistic power-law ROP model in Eq. 3.23, bit weight is easily optimized by computing the model's derivative with respect to WOB:

$$\frac{dROP}{dWOB} = 3b\left(WOB_{Field,i}\right)^{b-1} \tag{3.36}$$

Setting Eq. 3.36 equal to zero defines the first-order unconstrained optimality condition. With more complex ROP models, optimization becomes harder. There is no ideal

optimization methodology for every situation, since optimization algorithm efficiency depends on the ROP model designated in the objective function. Gradient-based and direct search techniques introduced in Section 3.1 are explored in optimizing drilling parameters with both analytical and ML ROP models. It is important to remember that some optimization methods presented earlier only handle design variable bound constraints. SLSQP, COBYLA, basin-hopping and PSO are the algorithms in Table 3.1 that can account for rig equipment power limitations.

Analytical ROP models described in Section 2.3 are formulated as closed-form equations. Even if their gradients with respect to WOB, RPM and flow rate cannot be written out explicitly, finite difference gradient estimation techniques can approximate them accurately. Hence, analytical ROP models are expected to be conducive to optimization with gradient-based techniques. When performed with the method of Lagrange multipliers (such as in SLSQP), gradient-based ROP maximization has the major benefit of revealing active drilling constraints. This is a direct result of the complementary slackness KKT condition (Eq. 3.9), which suggests that Lagrange multipliers are only nonzero for active constraints at a local optimum. Information about active constraints is crucial in redesigning drilling tools and processes or upgrading rig equipment to extend ROP performance limits. If analytical ROP models represent convex functions, global optimal drilling parameters can be determined with cheap computational power. The geometric interpretation of a convex function is that the chord between any two points lies above its graph (Boyd and Vandenberghe, 2004). Bingham (1964), modified Bourgoyne and Young, and Motahhari *et al*. (2010) ROP models can be shown to be convex. Inequality constraints in Eq. 3.34 are also in convex form, yielding a convex program with convex ROP model objective. In a convex program, a local optimum is the global optimum, and the KKT conditions are sufficient for local (and global) optimality. Out of the four

analytical models in Section 2.3, only B&Y (and its modified version proposed for real-time drilling optimization) accounts for and is capable of optimizing mud flow rate.

Machine learning ROP models (Section 2.4) are not characterized by a closed-form equation. Due to segmentation of the parameter space (Fig. 2.10), ML models' gradients are difficult to approximate, and efficient optimization of drilling parameters likely demands direct search methods. Direct search optimization requires many objective function evaluations and is possibly computationally intractable in real-time. Gradient-based and direct search optimization algorithms will be assessed in terms of computational efficiency and finding operational drilling parameters that lead to the highest ROP improvements with both analytical and ML ROP models. Python's *scipy.optimize* (Oliphant, 2007) and *pyswarm* (Lee and Castillo-Hair, 2013) packages will be employed, facilitating coding of objective functions and constraints.

Chapter 4: Drilling Data: Measurements, Processing and Williston Basin Dataset

ROP models presented in Chapter 2 are trained to reproduce drilling behavior from field data measured during drilling operations. Knowledge of biases and sources of error in data recording, processing and transmission establishes a vital foundation for ROP modeling. Data quality profoundly impacts a model's ability to predict accurate responses. The biggest assumption in building effective models is that the data correctly capture measured quantities and can be trusted. Unfortunately, this is often not the case with drilling data. WOB data are the biggest source of error in ROP modeling. Studies in the literature indicate as much as 100% WOB measurement error in certain wells (Kolnes *et al.*, 2007). In this chapter, rig drilling data workflows and data filtering techniques are discussed. Section 4.3 describes the dataset analyzed in this dissertation, a vertical portion of a Bakken shale horizontal well in North Dakota's Williston Basin.

4.1. DRILLING DATA WORKFLOWS

Accelerometers, gyroscopes, magnetometers, strain gauges, pressure transducers and temperature sensors measure drilling data both at surface and downhole (Baumgartner and van Oort, 2015). Each sensor carries its own particular sources of error. ROP is typically measured at the surface from the traveling block height derivative. ROP measurements can be severely influenced by pipe stretch due to tension and compression of the drillstring (Xu *et al.*, 1995). Surface WOB is not measured directly, but rather computed relatively from hookload measurements. The reference hookload is obtained at the beginning of drilling each pipe stand when the drillstring is rotating freely off-bottom (stable torque signal) and the pumps are at full speed. This WOB zeroing, or taring, procedure subtracts the buoyed drillstring weight and both mechanical and hydraulic

friction forces at current drilling conditions from the hookload indicator. It must be repeated after connecting every stand of pipe to the drillstring, since weight and friction datum change as the well is drilled deeper. WOB at surface is given by the reduction in reference hookload as the bit exerts pipe weight axial force onto the rock formation.

Florence and Iversen (2010) describe four separate techniques of measuring hookload: the earliest and still most common diaphragm-type hydraulic weight indicator clamped onto the deadline, a similar electrical clamp-on sensor, compression load cells (hydraulic or electrical) in the deadline anchor, and strain gauge load pins underneath the traveling block. All four methodologies are influenced by external factors such as temperature, friction and wear. Weight readings must be calibrated and corrected accordingly. As noted by Cayeux *et al*. (2015), the only manner to measure hookload directly is through an instrumented internal blow-out preventer in the top drive. However, not many contemporary top drives are equipped to measure hookload.

Surface RPM is usually measured by a magnetic proximity switch. Voltage across the sensor is related to top drive current via calibration. The variable frequency drive control of the top drive yields a surface torque value, also subject to calibration. Mud flow rate is given by the product of pump rate (stroke counter), stroke volume and pump efficiency, which is dependent on liner size. It can alternatively be computed by a Coriolis flowmeter (Cayeux *et al.*, 2013). Pressure at the surface is measured by a sensor in the standpipe, which connects the rig's mud pumps to the rotary hose. The rotary hose attaches to the top drive through the gooseneck, delivering mud circulation to the drillpipe and the wellbore. In mud motor drilling applications, the differential pressure across the motor is proportional to the downhole RPM and torque generated by the motor. Neufeldt *et al*. (2018) state that mud motor differential pressure obtained at surface is a relative measurement based on SPP. Similar to hookload (for WOB measurements), SPP taring

must occur frequently, with the bit off-bottom and pumps at full speed, to ensure accurate motor differential pressure data.

There are substantial differences between surface WOB values and the weight that actually reaches the bit downhole. Friction forces created by drillstring contact points with the wellbore detract from the reference hookload as drilling progresses, especially in deviated wells. Kerkar et *al*. (2014) describe downhole WOB estimation from surface hookload, but several corrections must be applied for friction in the travelling and crown block sheaves, wellbore friction, inclination angle, buoyancy factor and differential pressure. Measurement-while-drilling (MWD) tools provide direct readings of downhole WOB data by placing strain gauges in a sub near the bit. Downhole torque can be measured in the same manner. Strain gauge measurements are highly affected by temperature and can be hard to calibrate (Baumgartner, 2017). Gyroscopes and magnetometers measure downhole RPM and vibrations. Baumgartner (2017) reports that a large amount of useful downhole data is readily discarded due to filtering and averaging techniques designed to cope with sensor memory and transmission bandwidth limitations, hampering investigation of high-frequency downhole drilling dynamics.

Mud pulse telemetry has been the industry's preferred method of downhole data transmission to surface for several years. Even with modern technology, pressure pulses in the drilling fluid are affected by mud properties, flow rate and drillstring vibrations. Signal processing algorithms are required to convert data to pressure pulses downhole and back to digital data at surface, adding a second filtering layer to downhole data. Bandwidth of mud pulse telemetry systems is limited to slightly over 6 bits/sec (Emmerich *et al*., 2015), a data rate too slow for real-time drilling optimization. Pink *et al.* (2011) reported successful implementation of several vibration and downhole RPM sensors along the drillstring to diagnose drillstring dynamics issues. These applications were still limited to

post-drilling analysis, as the data were recorded in tool memory. The project eventually evolved into NOV/IntelliServ wired pipe deployments that measure downhole data at multiple points in the drillstring and can reach bandwidths of 57,000 bits/sec (Coley and Edwards, 2013). Craig and Adsit (2014) described wired pipe field experience in over 100 wells and Shishavan *et al*. (2016) demonstrated that it is possible to design a pressure and ROP controller for well control and drilling optimization with high-speed wired pipe downhole data. This technology shows promise for utilization of downhole data in real-time drilling optimization, but it is still cost-prohibitive in most plays. After data reaches the surface, current WITSML (Wellsite Information Transfer Standard Markup Language) data transfer at the rig is limited to 1Hz frequency (Behounek *et al*., 2017a). WITSML rig data can be moved to more powerful computers via the internet for further analysis. Nonetheless, the drilling optimization scheme derived in this dissertation works with basic rig-site computers and data measured at the surface, resulting in as little delay as possible to implementation of optimal operational drilling parameters.

Dividing drilling parameters from the four analytical ROP models described in Section 2.3 into three different data workflow categories:

Table 4.1: Drilling variables for four analytical ROP models divided into data types.

Analytical ROP Model	Bingham (1964)	Bourgoyne & Young (1974)	Hareland and Rampersad (1994)	Motahhari et al. (2010)
Operational Variables				
Weight-on-Bit, WOB	✓	✓	✓	✓
Rotary Speed, RPM	✓	✓	✓	✓
Flow Rate, q		✓		
Well Depth, D		✓		
Equivalent Circulating Density, ρ_c		✓		
Bit Wear, h or W_f		✓	✓	✓
Rock Properties				
Pore Pressure Gradient, g_p		✓		
Unconfined Compressive Strength, σ_c			✓	
Confined Compressive Strength, S				✓
Bit Properties				
Bit Diameter, d_b	✓	✓	✓	✓
Bit Nozzle Diameter, d_n		✓		
PDC Cutters Design Properties				
Number of Cutters, N_c			✓	✓
Cutter Diameter, d_c			✓	
Cutter Siderake Angle, α			✓	
Cutter Backrake Angle, θ			✓	
Drilling Fluid Properties				
Mud Density, ρ		✓		
Apparent Viscosity at 10,000 sec^{-1}, μ		✓		

★ surface measurements available in real-time   ★ uncertain data availability in real-time   ◆ constant during a bit run

Bit design properties are set in the planning phase of a well and remain constant throughout a bit run. Drilling fluid properties are placed in a category of their own – mud additives can be introduced at surface to affect density and viscosity but will require some time to alter properties in the entire circulating system. Depth, WOB, RPM, and flow rate are variables measured at surface and always accessible for ROP prediction in modern rigs. Downhole parameters such as equivalent circulating mud density (ECD) and an estimation of rock strength (via sonic transit times) may be available depending on bottomhole assembly configuration. However, low-frequency mud pulse telemetry downhole data is not appropriate for real-time applications and wired pipe technology does not prove itself

economical in most plays. Bit wear and pore pressure gradient cannot be directly measured in real-time with current technology.

Table 4.1 serves as a starting point for deciding which variables should be included in machine learning (ML) ROP models. By intuition, ML algorithms should consider the same drilling features as analytical models. For real-time systems, surface parameters are emphasized since they are readily available in all contemporary drilling data workflows. As previously described, drilling optimization applications with downhole parameters have questionable practicability in real-time due to limited data transmission rates and several inherent filtering processes. Thus, depth, WOB, RPM and flow rate surface measurements will constitute the basis for analytical and machine learning ROP model inputs in this dissertation. Hypothesis testing (Section 5.1) can confirm the statistical importance of these variables in relation to ROP.

4.2. DATA QUALITY AND SIGNAL PROCESSING

Raw drilling field data are typically plagued by sensor calibration and malfunction issues along some drilled intervals. Additional measurement inaccuracies may result from tracking, represented by correlated errors at adjacent data points in a time series (James *et al.*, 2013). Ensuring good drilling data quality is a crucial first step in obtaining a relevant and effective ROP model. As mentioned in the beginning of this chapter, WOB data (derived from hookload measurements) propagate substantial errors to ROP modeling. Cayeux *et al*. (2013) propose equations to correct for the biggest sources of hookload error: mud hose and umbilicals weights, hoisting system horizontal movement, and sheave friction. Kyllingstad and Thoresen (2018) suggest improvements to reference hookload readings by accounting for buoyancy, nozzle jet lift, cuttings loading downhole and choke back pressure, among other factors. In addition to all these error sources, wellbore

inclination significantly affects WOB measurements due to friction in pipe-wellbore contact points.

Behounek *et al.* (2017b) state that the Operators Group for Data Quality (OGDQ) is pursuing industry standards for sensor calibration and minimum data quality requirements. In the latest IADC/SPE Drilling Conference, held in March 2018, several presented papers focused on improving drilling data quality. Behounek *et al.* (2018) discussed further objectives for OGQD and divided issues with drilling data quality into five categories: systematic, measurement, conversion, calculation and propagation. Kyllingstad and Thoresen (2018) and Neufeldt *et al.* (2018) concentrated on WOB data quality enhancement. The latter study, published by employees from rig data management company Pason, is extremely alarming in regard to field practices related to drilling data. Previously discussed in Section 4.1, WOB taring (zeroing) provides a reference hookload for every pipe stand drilled and is a crucial part of the WOB measuring process. In a study performed with data from 40 wells, Neufeldt *et al.* (2018) discovered that WOB was zeroed correctly in only 8% of all drilled stands:
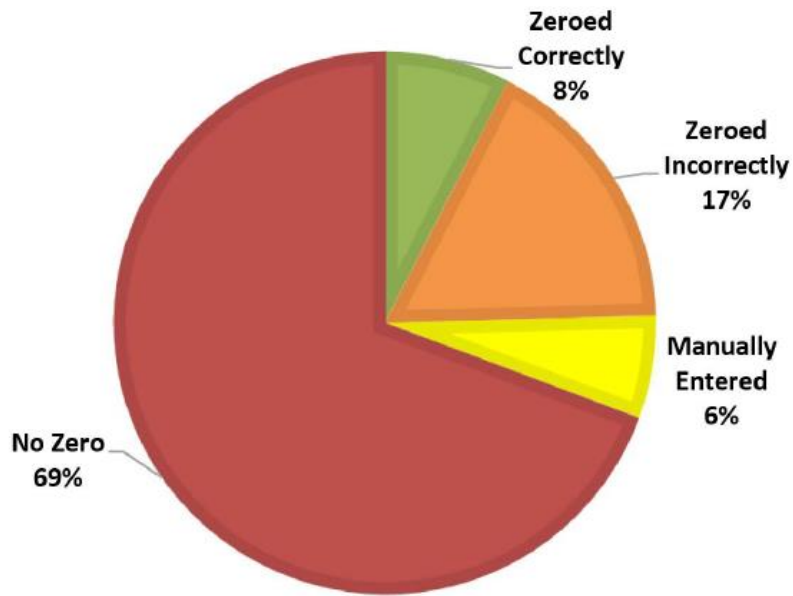
Figure 4.1: WOB zeroing distribution for stands in 40 wells, extracted from Neufeldt *et al*. (2018).

Drillers are occupied with many tasks during operations, such as ensuring the safety of crew members and pursuing drilling performance benchmarks. Fig 4.1 suggests that drillers may be overloaded, forgetting to tare WOB almost 70% of the time.

Neufeldt *et al*. (2018) establish ideal conditions for WOB zeroing: traveling block moving downward at the start of each stand's drilling, a freely rotating drillstring and total pump output. Average WOB measurement errors resulting from improper taring are reported for the 40 wells in the same study:
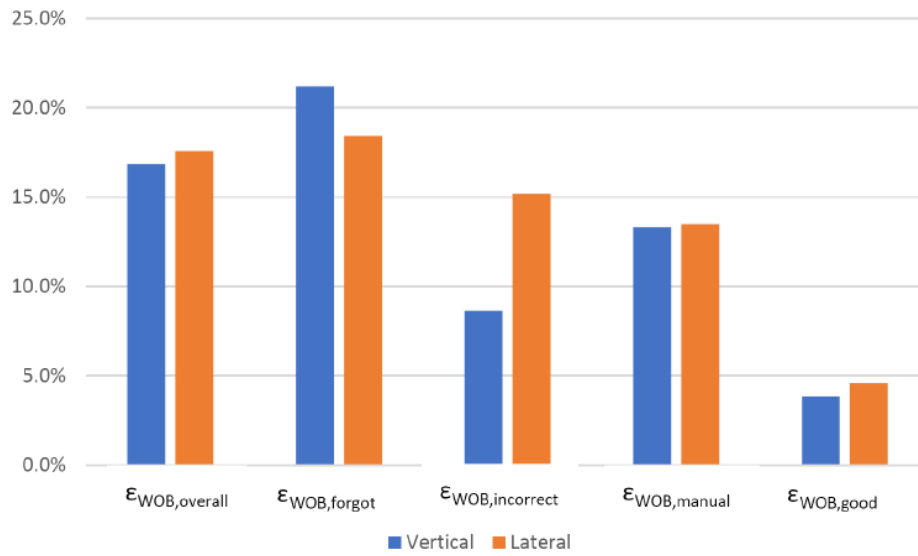
Figure 4.2: Mean WOB errors caused by improper taring procedures in 40 wells, extracted from Neufeldt *et al*. (2018).

Fig 4.2 displays substantial data inaccuracy due to inadequate WOB zeroing. Forgetting to tare WOB for multiple consecutive stands leads to the worst possible scenario. In fact, the experimenters note that 8% of all vertical stands examined displayed WOB errors greater than 30%, mostly due to continuous taring oversight. Since pipe weight is progressively added to the drillstring without proper correction to the hookload reference, recorded WOB values are much higher than actually experienced by the bit. Pipe-wellbore friction in lateral sections (orange) slightly compensates for zeroing omissions, so the issue is less aggravated than in vertical sections (blue). Manual taring entries by the driller also culminate in considerable WOB error. Although small (below 5%), errors are recorded even when WOB is zeroed properly. The researchers responsible for this eye-opening study developed an algorithm to automatically zero WOB, which will hopefully enhance the quality of drilling data in the near future.

More often than not, drilling data have already undergone some form of filtering by the time they are fed as inputs to a model. Several studies have investigated

implementation of data filtering techniques to improve the quality of drilling data. Xu *et al*. (1995) utilized boxplots for detection of data outliers. Kolnes *et al*. (2007) developed a data quality module that combines multiple readings and physics-based models to validate measurements. Lohne *et al*. (2008) described automated calibration of real-time drilling models with an unscented Kalman filter. Ambrus *et al*. (2013) applied Bayesian network methods for data validation, noting that all downhole measurements are susceptible to torsional vibrations. Ashok *et al*. (2016) expanded on this work and presented an entire workflow for data quality assurance, emphasizing on relational redundancy where models can validate data.

An essential distinction must be made between time-based and depth-based data for real-time drilling optimization. With raw time-based data, a low-pass filter may be applied to remove high-frequency noise. Alternatively, Kalman filters are a popular choice to smooth out unstable data spikes. The drilling dataset utilized in this dissertation is depth-based. Therefore, drilling parameter measurements have already been averaged out in depth intervals determined by the service company that collected the data. Frequency-based filtering is not appropriate since the sampling frequency is discontinuous and unknown. Hence, the data filtering strategy adopted with the Williston Basin depth-based dataset, described in the next section, is to remove data outliers in an equivalent manner to boxplot filtering discussed by Xu *et al*. (1995).

4.3. WILLISTON BASIN DATASET

The dataset analyzed in this study consists of depth-based surface data collected in the vertical portion of a horizontal Bakken shale well in the Williston Basin, North Dakota. This vertical well segment was drilled with an 8-^{3}/$_4$in Smith 616 PDC bit (six blades, 16mm cutters) and a five-stage mud motor. The bit was pulled out of the well with IADC dull

grading indicating $^1/_8$ wear in the inner cutter rows, $^2/_8$ wear in the outer rows, and chipped and worn cutters in the shoulder area. These values reveal a fractional cutter wear average of 0.1875 ($^{1.5}/_8$). Drilled through 4,873ft of rock, the interval spans nineteen formations with varying thickness and average ROP:

Table 4.2: Nineteen rock formations included in the Williston Basin dataset.

Rock Formations	Thickness (ft)	ROP (ft/hr)	Data Points	Filtered Data	Filtered Data / ft	Filtered Data / hr
Greenhorn Limestone	151	276	51	46	0.31	84.3
Newcastle Sandstone	286	276	70	67	0.23	64.5
Dakota Sandstone	371	238	158	152	0.41	97.7
Swift Shale	340	228	157	149	0.44	100.0
Rierdon Limestone	566	192	287	269	0.48	91.2
Piper Limestone	236	103	261	238	1.01	104.4
Spearfish Sandstone	244	132	226	210	0.86	113.8
Pine Salt Sandstone	447	62	819	801	1.79	110.5
Broom Creek Sandstone	194	57	406	391	2.02	116.0
Tyler Sandstone	423	57	875	855	2.02	114.2
Kibbey Lime Limestone	36	37	112	109	3.03	112.1
Kibbey Lime Shale	117	38	360	326	2.79	107.0
Charles Sandstone	123	42	278	256	2.08	87.7
Charles Limestone	216	48	475	436	2.02	96.6
Ratcliffe Sandstone	68	60	135	132	1.94	116.4
Base Last Salt Limestone	48	54	103	100	2.09	112.2
Base Last Salt Sandstone	120	39	348	321	2.68	105.7
Mission Canyon Limestone	632	47	1573	1516	2.40	112.3
Lodgepole Limestone	257	42	721	705	2.74	115.5
Total	**4873**		**7415**	**7079**		

In Chapter 5, a different set of empirical analytical model coefficients is calculated for each formation in the table above, maintaining the traditional ROP modeling lithology dependence assumption. Similarly, ML ROP models are trained individually for each formation. The wide range of formations' vertical lengths and amount of data collected adds value to experiments through evaluation of ROP model performance in varying stratigraphic conditions. Shallower formations encompass less measured data points due to high drilling speeds, and ROP modeling may be affected by lower sampling rates. Error metrics presented in Section 3.2.2 are weighted by both vertical length and number of data points in a formation.

This depth-based dataset had already been processed by the operator and/or service company, although no clear depth or time intervals can be detected (as evidenced by the last two columns of Table 4.2). Sampling irregularities were probably caused by the removal of data points containing negative parameter values. Nevertheless, data quality was still hampered by sensor malfunction in some segments, yielding unrealistic WOB and ROP measurements. ROP and WOB histograms in the Pine Salt Sandstone formation exemplify this poor drilling data quality, which must be corrected with data filters:
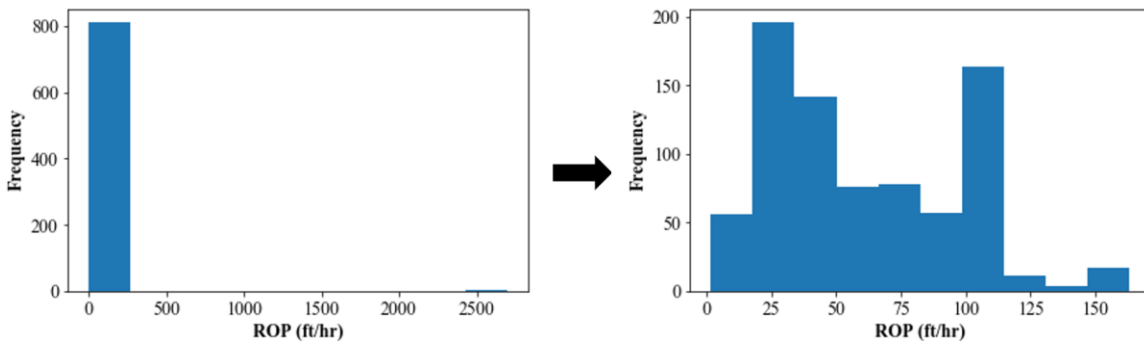
Figure 4.3: Unfiltered (left) and filtered (right) ROP data histograms in the Pine Salt Sandstone formation.
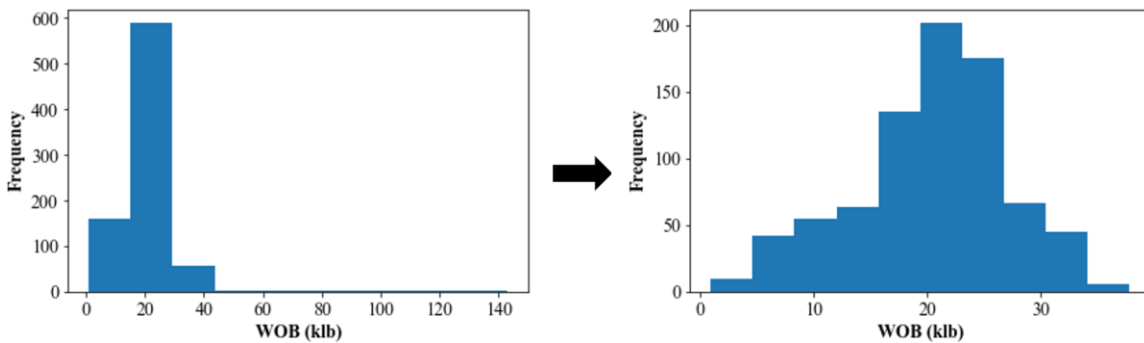
Figure 4.4: Unfiltered (left) and filtered (right) WOB data histograms in the Pine Salt Sandstone formation.

Data were filtered by removing samples with ROP or WOB values two standard deviations away from the mean in each rock formation, leaving 7,079 data points for analysis. By removing only 18 out of 819 (2.2%) data points collected in the Pine Salt Sandstone formation, the histograms on the right-hand side of Figs. 4.3 and 4.4 appear much more realistic.

Referring back to Table 4.1, depth, WOB, RPM and mud flow rate are operational parameters constantly measured at surface while drilling. Analytical ROP modeling equations require additional drilling parameters as inputs. Rock properties for each formation were derived from the operator's proprietary hydro-mechanical specific energy model. Mud density (10ppg) and viscosity (16cP) provided in hydraulics reports are assumed to be constant throughout the interval, and ECD is set equal to static mud weight. As revealed earlier in this section, the 4,873ft-long well segment in question was drilled with an 8-$^3/_4$in Smith 616 PDC bit containing 56 total (18 backup) 16mm (0.63in) cutters and six $^{12}/_{32}$in nozzles (TFA = 0.66in^2). After drilling the interval, the bit was pulled out of the hole exhibiting IADC dull grading fractional cutter wear average of $\frac{\overline{\Delta h}}{8} = 0.1875$. The wear function defined by Eq. 2.26 (Section 2.3.4) linearly reduces drilling efficiency with depth until it reaches $1 - \frac{\overline{\Delta h}}{8}$ at the end of the bit run. Lastly, PDC bit cutter design parameters include backrake and siderake angles:
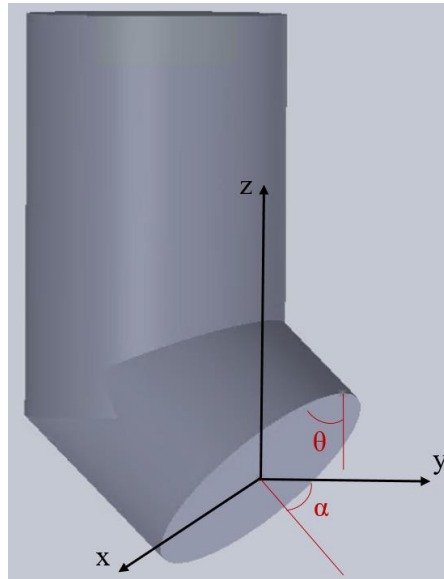
Figure 4.5: Representation of a single PDC cutter with siderake angle α and backrake angle θ. Previously published in Soares *et al.* (2016).

PDC cutters' backrake and siderake angles are proprietary information. A backrake of 10 degrees and a siderake of 30 degrees were established as inputs for the Hareland and Rampersad (1994) PDC bit model based on the work of Rajabov *et al.* (2012) (see Soares *et al.*, 2016). Number of PDC cutters and cutter diameter were obtained from the manufacturer's catalog (*SHARC*, 2015). Table 4.3 summarizes PDC cutter design properties utilized in ROP model training:

Table 4.3: Given and inferred PDC cutter design properties for 8-^{3}/$_4$in Smith 616 PDC bit.

PDC Cutter Design Properties	Value	Units
Number of Cutters, N_c	38	
Cutter Diameter, d_c	0.63	in
Cutter Siderake Angle, α	30	deg
Cutter Backrake Angle, θ	10	deg

Constraints for the drilling parameter selection problem (Section 3.3, Eq. 3.34) are determined based on equipment limitations (when supplied) and actual drilling data

measurements. The manufacturer's recommended WOB operating values for Smith 616 PDC bits range from 3.5klbf to 30klbf (*SHARC*, 2015), but WOB readings in deeper sections of this well reach slightly past 35klbf. These WOB values are reasonable when accounting for friction, so WOB is constrained to a lower bound of 5klbf and an upper bound of 35klbf. In this dataset, surface RPM measurements of up to 80rev/min are reported and RPM ratings of downhole tools are not available. Since the well segment was drilled with a five-stage mud motor providing 100RPM on average, RPM values are bounded between a minimum of 100rev/min and a maximum of 180rev/min to avoid failure of downhole tools. Instead of adding uncertainties with hydraulics models and pore pressure and fracture gradient estimations (not provided), flow rate is maintained within the minimum and maximum values experienced in the training dataset. Drilling mud flow rate also conforms to pump power constraints, defined with average SPP values measured in drilling the well. Top drive power (800HP), pump power (2x1600HP) and drillpipe make-up torque rating (23.8 klbf-ft) are derived from similar drilling rigs operating in the Bakken shale region. Torque limits are imposed by determining bit aggressiveness (dependent on lithology) from torque and WOB training data. Table 4.4 outlines the constraints prescribed for optimization of drilling parameters in this Williston Basin well interval:

Table 4.4: Drilling optimization constraints for Williston Basin dataset.

Drilling Variable	Lower Bound	Upper Bound	Units
WOB	5	35	klbf
RPM	100	180	rev/min
q	Training Data Min.	Training Data Max.	gpm
T	0	23.8	klbf-ft
SPP	Training Data Avg.	Training Data Avg.	psi
P_{TD}	0	800	HP
P_{pump}	0	3200	HP

The constraints listed in Table 4.4 are utilized for drilling parameter optimization throughout this dissertation. Flow rate and SPP bounds vary depending on the training data segmentation technique employed in ROP model fitting.

Chapter 5: Lithology-Dependent Post-Drilling Optimization

Drilling parameter optimization and ROP prediction studies in the literature routinely assume that all data measured when drilling a well have already been recorded and are available for examination, in a post-drilling framework. Although evaluation of real-time continuous model learning and drilling interval optimization is the main objective of this study, post-drilling data analysis presents an opportunity for inspecting and refining modeling and optimization processes. These investigations are also vital to establishing computational feasibility in real-time. In this chapter, seven experiments are performed with all data collected in a vertical segment of a Bakken shale well (Section 4.3) to explore modeling and optimization alternatives posed in previous chapters: hypothesis testing for machine learning models' input selection, assessment of analytical model fitting techniques, comparison between Bourgoyne and Young ROP model formulations, hyperparameter optimization define ML model architectures, cross-validation gauges overall model errors, appraisal of drilling optimization methods, and model performance variation with incremental training data availability. Average computing times are reported for experiments performed with a 7th Generation Intel® Core™ i5 processor @ 2.50GHz and 8GB RAM.

5.1. HYPOTHESIS TESTING

Hypothesis testing establishes a methodology to confirm the importance of operational drilling variables as inputs for machine learning ROP models. Following scrutiny of Table 4.1, intuition from analytical ROP model equations and real-time data availability indicate that depth, WOB, RPM and flow rate constitute inputs of interest. Here, hypothesis testing is applied to validate the statistical relevance of the relationship between ROP and such parameters. Assuming a linear model between ROP and WOB:

$$ROP = \theta_0 + \theta_1 WOB + \varepsilon \qquad (5.1)$$

where θ_0 is the intercept, θ_1 is the slope and ε is an error term. The null hypothesis states that the statistical relationship between ROP and WOB is inexistent, meaning that θ_1 should be equal to (or very close to) zero in the equation above. Hence, the null hypothesis must be rejected in order to ratify the relation between ROP and WOB. Frequently, the null hypothesis is tested with a t-statistic, which measures how many standard deviations θ_1 is away from zero. Derived from the t-statistic, the p-value represents the probability of θ_1 being the amount of calculated standard deviations away from zero if the null hypothesis was true. In summary, a large t-statistic will lead to a low p-value, implying that θ_1 is far enough from zero and that there exists a relationship between ROP and WOB, rejecting the null hypothesis. This hypothesis testing concept, illustrated in Eq. 5.1 for the relationship between ROP and WOB, applies to all other operational drilling features.

James *et al*. (2013) suggest that p-values of 0.01 or 0.05 are common thresholds to reject the null hypothesis. Previous hypothesis testing applications in ROP modeling tend to be more lenient due to data quality limitations. Driver *et al*. (2016) describe such process in a study that starts out by identifying 27 drilling variables and eventually narrows down the final ROP model to the 6 most relevant parameters by eliminating measurements with high p-value (greater than 0.55) or multicollinearity. Atwal and Knight (2016) extend the previous approach by substituting the weighted average of model coefficients (deterministic) by a probability distribution (stochastic).

Fitting linear models between ROP and each of the proposed relevant variables and calculating p-values for all nineteen formations in the Williston Basin dataset presented earlier:

Table 5.1: Hypothesis testing for the relationships between ROP and depth, WOB, RPM and flow rate in nineteen Williston Basin formations.

Number of Formations	Depth	WOB	RPM	Flow Rate
p-value < 0.01	13	14	10	9
p-value < 0.05	14	16	11	9
p-value < 0.20	17	18	14	11

Table 5.1 shows how many formations, out of nineteen total, satisfy the specified p-value thresholds. At least half of all formations demonstrate significant statistical relevance in the relationships between ROP and depth, WOB and RPM. WOB and depth measurements display the strongest connections to ROP. The ROP relation with flow rate falls one short of the formation majority with the stringiest p-value cutoffs, likely due to steady mud flow rates throughout lithological intervals. Nevertheless, a more tolerant p-value threshold identifies drilling fluid flow rate as a relevant variable in ROP prediction, as expected from field observations. Depth, WOB, RPM and flow rate will compose ML model inputs based on Table 5.1 results, surface data availability and comparability with analytical models.

5.2. ANALYTICAL ROP MODEL FITTING STRATEGIES

Experimenters are faced with loss function and optimization algorithm choices when determining analytical ROP model coefficients that best fit field data (see Chapter 3). The objective of model fitting is to find the coefficients which minimize the difference between modeled values and the ROP measured on the field. Several researchers have investigated different approaches to calculate B&Y ROP model coefficients. The original Bourgoyne and Young (1974) publication suggests a multiple regression methodology minimizing the sum of residuals squared (l_2 loss). Studies published in the literature adhere to the l_2 cost function, but recommend various optimization algorithms as the best alternative to fit B&Y coefficients: trust region interior-reflective Newton method (Bahari and Seyed, 2007), genetic algorithm (Bahari et al., 2008), fuzzy system with simulated

annealing (Moradi *et al*., 2010), progressive stochastic optimization (Rahimzadeh *et al*., 2011), genetic algorithm followed by neural network (Bahari *et al*., 2011), Markov Chain Monte Carlo simulation (Formighieri and Filho, 2015) and cuckoo optimization algorithm (Anemangely *et al*., 2017). In this section, coefficients for the four analytical ROP models presented in Section 2.3 are computed with the trust region reflective and basin-hopping implementations in Python's *scipy.optimize* (Oliphant, 2007) library and the particle swarm optimization algorithm in Python's *pyswarm* (Lee and Castillo-Hair, 2013) package. These three optimization procedures explore an assortment of strategies, with one gradient-based approach in the TRF algorithm and two direct search methods in basin-hopping (with COBYLA as the local minimizer) and PSO.

Table 5.2 displays absolute and normalized RMSE percentage errors obtained with the proposed optimization algorithms and the dataset presented in Section 4.3:

Table 5.2: Model performance of four analytical ROP models in nineteen Williston Basin rock formations with varying optimization methods.

Bingham (1964)						
Optimization Method	Trust Region Reflective		Basin Hopping		Particle Swarm Optimization	
Error Metric	Absolute Error	Norm. RMSE	Absolute Error	Norm. RMSE	Absolute Error	Norm. RMSE
Average	29.21	30.45	29.21	30.45	DNC	DNC
Weighted by Points	31.72	31.54	31.72	31.54	DNC	DNC
Weighted by Length	30.69	30.79	30.69	30.79	DNC	DNC
Bourgoyne *et al*. (1986)						
Optimization Method	Trust Region Reflective		Basin Hopping		Particle Swarm Optimization	
Error Metric	Absolute Error	Norm. RMSE	Absolute Error	Norm. RMSE	Absolute Error	Norm. RMSE
Average	28.50	29.68	28.50	29.68	29.03	30.12
Weighted by Points	29.85	29.43	29.85	29.43	30.42	29.80
Weighted by Length	29.26	29.20	29.26	29.20	29.81	29.64
Corrected Hareland and Rampersad (1994)						
Optimization Method	Trust Region Reflective		Basin Hopping		Particle Swarm Optimization	
Error Metric	Absolute Error	Norm. RMSE	Absolute Error	Norm. RMSE	Absolute Error	Norm. RMSE
Average	28.96	30.08	28.96	30.08	32.15	33.38
Weighted by Points	31.59	31.30	31.59	31.30	32.59	32.21
Weighted by Length	30.49	30.46	30.49	30.46	33.15	33.05
Motahhari *et al*. (2010)						
Optimization Method	Trust Region Reflective		Basin Hopping		Particle Swarm Optimization	
Error Metric	Absolute Error	Norm. RMSE	Absolute Error	Norm. RMSE	Absolute Error	Norm. RMSE
Average	29.21	30.40	29.21	30.40	29.73	31.27
Weighted by Points	31.72	31.53	31.72	31.53	32.12	32.55
Weighted by Length	30.71	30.77	30.71	30.77	31.25	31.76

The 1986 Bourgoyne and Young model formulation (Bourgoyne *et al.*, 1986) was utilized for consistency with respect to studies discussed earlier in this section. Particle swarm optimization did not converge (DNC) for the Bingham model, likely due to low dimensionality. Model performance was identical with TRF and basin-hopping algorithms, yielding with same coefficient values. Slightly higher model errors were observed with coefficients optimized by the particle swarm algorithm in most instances. Agreement in optimal model coefficient values between the two best performing methodologies implies that global optimal coefficients were discovered. In basin-hopping, Monte Carlo simulation with random perturbations increases the chances of finding a global optimal solution. However, the global stepping procedure also demands increased computational expense. The average computing time (7th Generation Intel® Core™ i5 processor @ 2.50GHz and 8GB RAM) to perform 10-fold cross-validation for the four models in each formation was 15.6 seconds for TRF, 2292 seconds for basin-hopping, and 601 seconds for PSO. Hence, the trust region reflective algorithm in Python's *scipy.optimize* (Oliphant, 2007) library is employed as the standard optimization method to compute analytical ROP model coefficients throughout this study.

Following optimization algorithm selection, three loss function alternatives are investigated in ROP model training. Introduced in Section 3.2.2, absolute difference (l_1), squared difference (l_2) and Huber norm cost functions were considered when fitting coefficients and model performance was evaluated:

Table 5.3: Model performance of four analytical ROP models in nineteen Williston Basin rock formations with varying loss functions.

	Bingham (1964)					
Loss Function	**Squared Difference**		**Absolute Difference**		**Huber Norm**	
Error Metric	**Absolute Error**	**Norm. RMSE**	**Absolute Error**	**Norm. RMSE**	**Absolute Error**	**Norm. RMSE**
Average	29.21	30.45	27.02	31.34	26.88	31.10
Weighted by Points	31.72	31.54	27.48	32.46	27.54	32.34
Weighted by Length	30.69	30.79	27.51	31.65	27.51	31.48
	Bourgoyne _et al_. (1986)					
Loss Function	**Squared Difference**		**Absolute Difference**		**Huber Norm**	
Error Metric	**Absolute Error**	**Norm. RMSE**	**Absolute Error**	**Norm. RMSE**	**Absolute Error**	**Norm. RMSE**
Average	28.50	29.68	27.66	31.44	26.82	30.22
Weighted by Points	29.85	29.43	27.80	31.08	27.29	29.93
Weighted by Length	29.26	29.20	27.91	30.73	27.36	29.68
	Corrected Hareland and Rampersad (1994)					
Loss Function	**Squared Difference**		**Absolute Difference**		**Huber Norm**	
Error Metric	**Absolute Error**	**Norm. RMSE**	**Absolute Error**	**Norm. RMSE**	**Absolute Error**	**Norm. RMSE**
Average	28.96	30.08	26.90	31.11	26.63	30.72
Weighted by Points	31.59	31.30	27.40	32.26	27.43	32.10
Weighted by Length	30.49	30.46	27.41	31.43	27.32	31.15
	Motahhari _et al_. (2010)					
Loss Function	**Squared Difference**		**Absolute Difference**		**Huber Norm**	
Error Metric	**Absolute Error**	**Norm. RMSE**	**Absolute Error**	**Norm. RMSE**	**Absolute Error**	**Norm. RMSE**
Average	29.21	30.40	27.94	32.83	26.85	31.06
Weighted by Points	31.72	31.53	27.97	33.33	27.54	32.32
Weighted by Length	30.71	30.77	28.16	32.64	27.52	31.47

The pre-defined residual distance threshold distinguishing between squared difference and absolute difference losses for the Huber norm cost function (δ) varied in each formation, defined as 10% of the mean test data ROP. As expected, the absolute difference cost function reduces absolute error but increases normalized RMSE compared to models trained with squared difference loss. Interestingly, Huber loss results in further reduction of absolute error and more modest normalized RMSE increase. These results indicate that the Huber norm cost function is a reasonable alternative for analytical ROP model fitting, especially since the threshold residual distance δ may be manipulated towards a particular goal. However, machine learning models are generally trained with squared difference loss. In order to conduct performance comparisons with errors achieved by equivalent objectives across all models, analytical ROP model coefficients will be fitted with l_2 cost function in this dissertation.

Intuitively, analytical ROP model fitting is conducive to gradient-based optimization methods since loss function derivatives with respect to model coefficients are accessible. Results in Tables 5.2 and 5.3 support training analytical ROP models with l_2 loss function and the trust region reflective algorithm implemented in Python's *scipy.optimize* (Oliphant, 2007) library. These choices are optimal from both performance and computational efficiency perspectives.

5.3. BOURGOYNE AND YOUNG MODEL FORMULATIONS

Model performance for four separate Bourgoyne and Young model formulations is investigated:

- Bourgoyne and Young (1974), first set of Eqs. 2.3-2.11

- Bourgoyne *et al*. (1986), second set of Eqs. 2.3-2.11

- Bourgoyne *et al*. (1986) v2, similar to previous but with HSI as the hydraulics parameter (Eq. 2.16 instead of Eq. 2.11)

- Modified Bourgoyne and Young, Eq. 2.17

Cross-validation errors evaluated with coefficient bounds suggested in Table 2.1 are shown below:

Table 5.4: Model performance in nineteen Williston Basin rock formations for different formulations of the Bourgoyne and Young ROP model.

Bourgoyne and Young (1974)		
Error Metric	Absolute Error	Norm. RMSE
Average	28.82	30.15
Weighted by Points	30.69	30.61
Weighted by Length	29.82	30.04
Best in Formation	1	0
Bourgoyne *et al.* (1986)		
Error Metric	Absolute Error	Norm. RMSE
Average	28.50	29.68
Weighted by Points	29.85	29.43
Weighted by Length	29.26	29.20
Best in Formation	2	1
Bourgoyne *et al.* (1986) v2		
Error Metric	Absolute Error	Norm. RMSE
Average	28.35	29.67
Weighted by Points	29.57	29.46
Weighted by Length	28.97	29.17
Best in Formation	2	2
Modified Bourgoyne and Young		
Error Metric	Absolute Error	Norm. RMSE
Average	28.49	29.90
Weighted by Points	30.47	30.73
Weighted by Length	29.49	29.94
Best in Formation	14	16

Models were fitted by the TRF algorithm with l_2 loss function (Section 5.2). Formation average error metrics vary at most 1.5% between all four B&Y equations. Even though the novel model performs slightly worse than the two Bourgoyne *et al.* (1986) formulations in overall formation average error, it exhibits the lowest error in an overwhelming majority of the nineteen formations. Averaged results are skewed by the two formations with highest overall error, where modified B&Y model errors are 4-5% higher than errors for the other three formulations. Five empirical coefficients are trained for the new model, in comparison to the eight original B&Y model coefficients. Moreover, implementation of the modified Bourgoyne and Young model requires only surface drilling parameters.

Disregarding pore pressure gradient, ECD and bit wear data without loss of ROP prediction accuracy, the proposed modified B&Y model is better suited for real-time applications.

5.4. HYPERPARAMETER OPTIMIZATION

Hyperparameters control machine learning models' architectures and complexity, invoking the bias-variance trade-off discussed in Section 2.5.1. Generally, increasing model complexity leads to lower bias and higher variance. For the random forests algorithm, the number of trees hyperparameter defines the amount of decision tree models fitted with random subsets of training data and averaged out when determining the response. Variance is reduced with additional trees, as mentioned in Section 2.4.1. However, extra trees increase computational expense and do not necessarily result in improved model performance. In addition to fitting trees to different subsets of data (with bootstrap sampling), RF only considers a maximum number of variables at each node split to further decorrelate trees. Tree nodes split groups of data points into two subgroups according to the one variable segmentation that yields the highest error reduction at that particular node (a greedy approach). Since depth, WOB, RPM and flow rate are the drilling parameters utilized in training ML ROP models, a maximum of four features can be considered per split (although the maximum number would cause all variables to be examined at all splits, producing more correlated trees and limiting variance reduction). RF trees are commonly grown deep, and a third hyperparameter regulates tree depth by requiring a minimum number of data points to further split a group. The smaller this quantity is, the deeper trees will grow, reducing bias and increasing variance.

Support vector machines utilize kernel functions to implicitly map input data to a higher-dimensional feature space in which separation of groups of data is less troublesome. Linear, polynomial (3rd degree) and Gaussian (radial basis) function alternatives are

analyzed for the kernel function hyperparameter. As described in Section 2.4.2, SVM's extension to regression defines a region (ε-tube) around model predictions where training data points are not penalized (ε-insensitive loss function). Figure 2.11 demonstrates that only support vectors, data points that lie on or inside the margin, affect the SVM model. The epsilon (ε) hyperparameter sets a threshold distance for support vectors, which are located outside the ε-tube. Thus, higher epsilon values lead to fewer support vectors. In classification problems with SVM, the hyperparameter C establishes a budget for margin violations. As C decreases, the margin widens, leading to a higher number of support vectors. For support vector regression, C controls the tolerance to deviations outside the ε-tube. Therefore, both ε and C influence the amount of support vectors and, consequently, model complexity. With small C and epsilon values, more support vectors are established and model complexity is high, resulting in low bias and high variance. Finally, the gamma (γ) hyperparameter appears as a coefficient in Gaussian and polynomial kernel function formulations and alters the measure of similarity between data points established by these kernels. Support vectors have a small radius of influence with large γ values, leading to a low-complexity model with high bias and low variance. Conversely, an extremely small gamma results in support vectors impacting the whole dataset regardless of distance, reducing bias and increasing variance.

Hyperparameters for neural networks vary depending on the solver selected to train the models. Momentum and/or learning rate are common hyperparameters when fitting neural network weights with stochastic gradient descent (SGD) or SGD adaptive moment estimation (Adam) solvers. However, as shown in Table 5.5, the BFGS algorithm performs better in training NN ROP models with the relatively small depth-based dataset in this study. Regardless of solver choice, the number of hidden layers and number of neurons in each hidden layer are hyperparameters that define the total quantity of computational units

in the model. As expected, model complexity increases as more neurons are utilized. Each neuron carries an activation function that adds non-linearity to its weighted combination of features. It is not uncommon to designate different activation functions to separate hidden layers, but *scikit-learn*'s neural networks implementation does not support this capability. Identity, logistic (sigmoid), hyperbolic tangent (tanh) and rectified linear unit (relu) functions constitute the options investigated for the activation function hyperparameter. Lastly, the regularization hyperparameter alpha (α) seeks to reduce variance by introducing a l_2 penalty to the neural network weights. Larger alpha values lead to increased l_2 penalty and further variance reduction.

Python's *scikit-learn* (Pedregosa *et al*., 2011) implementations of random forests, support vector machines and neural networks compose the machine learning algorithms tested for ROP prediction. Input data for SVM and NN models are standardized to zero mean and variance equal to one to remove effects of differing drilling parameters' magnitudes. There are no definite rules for hyperparameter selection, as optimal model structure varies by application. Researchers typically define a grid and search for the best hyperparameter combinations with cross-validation. The same methodology is applied in this study:

Table 5.5: Hyperparameter grid search for random forests, support vector machines and neural networks ROP models.

Random Forests Grid		Best Hyperparameter
Number of Trees	{10, 25, 50, 100, 1000}	25
Max. Features per Split	{2, 3, 4}	2
Min. Samples to Split	{2, 3, 4}	2
Total Combinations	45	
Computational Time (s)	536	
Support Vector Machines Grid		Best Hyperparameter
Kernel Function	{Linear, 3rd Degree Polynomial, Gaussian}	Gaussian
Epsilon (ε)	{0.01, 0.1, 1, 10}	1
Budget (C)	{1, 10, 100, 1000}	100
Kernel Coefficient (γ)	{0.0001, 0.001, 0.01, 0.1}	0.1
Total Combinations	192	
Computational Time (s)	45	
Neural Networks Grid		Best Hyperparameter
Solver	{SGD, Adam, LBFGS}	LBFGS
Number of Neurons in the Hidden Layer(s)	{2, 3, 4, (2,1), (2,2), (3,1), (3,2), (3,3), (4,1), (4,2), (4,3), (4,4)}	(4,2)
Activation Function	{Identity, Logistic, Tanh, Relu}	Logistic
l_2 Regularization (α)	{0.00001, 0.0001, 0.001, 0.01, 0.1}	0.0001
Total Combinations	720	
Computational Time (s)	1112	

Hyperparameters selected in Table 5.5 represent optimal combinations for the majority of the nineteen Williston Basin formations. While it is possible to pick optimal hyperparameter combinations for each formation, the chosen values provide a good starting point for general depth-based ROP modeling applications. The modest accuracy improvement obtained with formation-specific hyperparameters does not justify the computational expense of attempting a high number of combinations in real-time.

In the Neural Networks Grid section of Table 5.5, numbers of neurons in the hidden layer(s) appear as either a single number or a pair of numbers. Single numbers represent a network with as many neurons in one hidden layer. A pair of numbers describes a neural

network with two hidden layers, each containing the respective number of neurons. Hence, the best hyperparameter combination favors a 2-layer neural network with four neurons in the first hidden layer and two neurons in the second hidden layer. Some authors (e.g. Hastie *et al*., 2009) recommend training neural networks with a large number of neurons and larger regularization parameter (α). This approach was also tested and only yielded marginal (if any) performance improvement in scattered formations, with significant increase in computational demands. The relatively small number of samples in this dataset also supports using the quasi-Newton BFGS (Broyden-Fletcher-Goldfarb-Schanno) optimization algorithm instead of the popular Adam (Kingma and Ba, 2015) stochastic gradient descent solver for large-scale machine learning applications. Similar preference for less complex, lower-variance models was also observed with the selected SVM hyperparameters (large γ, ε and C), indicating highly complex models are not needed for this depth-based dataset. RF models reduce variance resulting from deeply grown trees (up to groups of individual samples) by averaging out predictions from 25 distinct trees which only consider 2 variables at every split. Reducing model complexity also alleviates the risk of overfitting.

5.5. CROSS-VALIDATION ERRORS

Data filtering, optimization algorithm for analytical model fitting, ML models' input features and architectures have been established in previous sections. Now, post-drilling error metrics for each ROP model are calculated by performing cross-validation with the entire dataset in each formation. There are a few possible options to display prediction error results for the seven ROP models in the nineteen formations investigated. Tables with 133 entries for each error metric would be cumbersome to interpret. Histograms are capable of illustrating a model's error distribution across all formations,

but seven separate plots would be required for every metric. The most concise solution to visualize ROP modeling errors is provided by box and whisker plots, which allow for fast comparison of key formation error distribution features for all seven models in one graph. Box plots, composed of a box and two whiskers, divide formation error data for each model into quartiles, four groups of approximately the same size. The top of the box defines the 75th percentile, while the bottom of the box portrays the 25th percentile. A horizontal line inside the box represents the median. Nineteen formations (Table 4.2) are divided into three groups of five formations and one group of four formations. Therefore, after sorting formation ROP prediction errors for a model in increasing order, the box and whisker plots introduced in this section are interpreted as follows:

- Error range between the bottom whisker (minimum error) and the bottom of the box encompasses the five formations exhibiting lowest errors for each model
- Next five formations with lowest errors constitute the range inside the box up to (and including) the median line
- Following five formation errors are located inside the box above the median line
- Range between the top of the box and the top whisker (maximum error) encapsulates the remaining four formations, with highest model prediction errors

Formation-dependent cross-validated errors in a post-drilling framework are presented below:
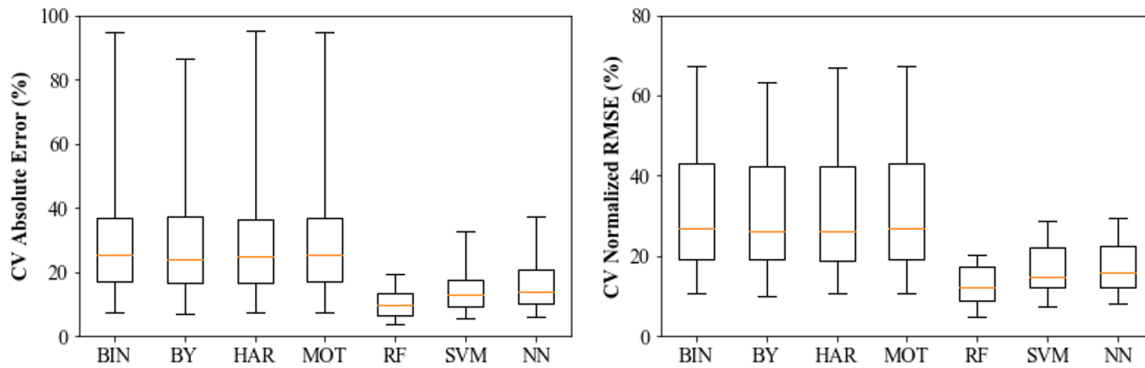
Figure 5.1: Cross-validation model performance in lithology-dependent post-drilling data analysis.

In Fig. 5.1, analytical models are abbreviated as – BIN: Bingham (1964), BY: modified Bourgoyne and Young, HAR: corrected Hareland and Rampersad (1994), MOT: Motahhari *et al*. (2010); and machine learning models have acronyms – RF: random forests, SVM: support vector machines, NN: neural networks. ML models considerably outperform analytical models according to absolute error and normalized RMSE when the entirety of data collected during drilling is available as the training set. A few formations displayed extremely high errors, with absolute errors for analytical models nearing 100%. Nonetheless, models were able to predict ROP reasonably well for most formations, as indicated by three quartiles under 40% absolute error for analytical models and under 20% for ML models. Modified Bourgoyne and Young boasted the lowest cross-validation errors among analytical models, while random forests led ML algorithms in performance. The random forests ROP model performed best in all but one formation. In fact, ML models composed the top three post-drilling highest prediction accuracy models in all nineteen formations. Error metrics for the best overall analytical and machine learning models are shown below:

Table 5.6: Best analytical (modified Bourgoyne and Young) and machine learning (random forests) cross-validation ROP model performance in post-drilling framework. Results are presented in percentages.

ROP Model	Modified Bourgoyne and Young		Random Forests	
Error Metric	Absolute Error	Norm. RMSE	Absolute Error	Norm. RMSE
Average	28.49	29.90	10.29	12.58
Weighted by Points	30.47	30.73	9.99	12.58
Weighted by Length	29.49	29.94	11.01	13.40

The first numerical row in Table 5.6 reveals average error metrics for all nineteen formations. Average formation errors are then weighted by both formation thickness (vertical length) and number of data points. These metrics account for shorter formations contributing less to total drilling time. Table 5.7 considers the computational expense of the cross-validation procedure:

Table 5.7: Average formation cross-validation errors and computational time for seven ROP models.

	Cross Validation Errors (%)		
Analytical ROP Model	Absolute Error	Norm. RMSE	Time (s)
Bingham (1964)	29.21	30.46	0.28
Modified B&Y	28.49	29.90	4.61
Hareland and Rampersad (1994)	28.88	29.96	6.92
Motahhari *et al.* (2010)	29.21	30.40	3.46
Machine Learning ROP Model	Absolute Error	Norm. RMSE	Time (s)
Random Forests	10.29	12.58	5.00
Support Vector Machines	14.18	16.39	0.32
Neural Networks	15.43	17.29	0.91
		Total Time (s)	21.51

The table above indicates that it takes, on average, about 22 seconds to cross-validate all seven models with data from one formation. Surprisingly, SVM and NN model training was faster than three out of the four analytical ROP models.

Results in Figure 5.1 and Tables 5.6 and 5.7 show that ML algorithms substantially outperform analytical ROP models when trained with all measured data in a formation.

Average and weighted errors for the best performing ML model (random forests) are about 20% lower compared to errors for the best analytical model (modified Bourgoyne and Young). Flexibility in model form provides a significant advantage for ML algorithms, as both models were trained with the same surface operational variables: depth, WOB, RPM and drilling fluid flow rate. ML model performance could be further improved by considering additional data sources (if available in real-time), such as gamma ray logs, sonic travel times, bit torque and bottomhole pressure. In this case, care must be taken to avoid collinearity between closely related features (e.g. WOB and torque). Another approach to boost ML accuracy is to refine hyperparameter grid search, although this strategy poses a risk of developing a very specialized model architecture that works favorably for one application but not as much in a more general framework.

5.6. DRILLING PARAMETER OPTIMIZATION

Section 3.3 formulates the drilling parameter optimization problem (Eq. 3.34) and Table 4.4 presents constraints specific to the Williston Basin dataset. In this section, optimization methods described in Section 3.1 are evaluated according to ROP improvement, proposed change in drilling parameters and computational time required. As a reminder, SLSQP, COBYLA, basin-hopping (if using SLSQP or COBYLA as local optimizers) and PSO are the only algorithms from Table 3.1 that can handle top drive and pump power constraints. Weight on bit, drillstring rotational speed, and drilling fluid flow rate are optimized for drilling each of the nineteen Williston Basin formations according to lithology-dependent analytical and machine learning ROP models trained in a post-drilling framework.

Optimization results for gradient-based methods are displayed in the table below:

Table 5.8: Gradient-based optimization of drilling parameters in lithology-dependent post-drilling framework.

Optimization Method: L-BFGS-B - Analytical Optimization: 0.0014 sec, ML Optimization: 0.618 sec				
ROP Model	ΔWOB (klb)	ΔRPM (rev/min)	Δq (gpm)	ΔROP (ft/hr)
Bingham (1964)	11.75	44.73	0.00	90.61
Modified B&Y	11.75	44.73	8.70	74.94
Hareland and Rampersad (1994)	10.50	44.73	0.00	50.14
Motahhari *et al.* (2010)	11.75	44.73	0.00	72.30
Random Forests	0.00	0.00	0.00	7.86
Support Vector Machines	-2.78	0.05	1.07	37.12
Neural Networks	-7.48	-1.94	-2.39	23.71
Optimization Method: SLSQP - Analytical Optimization: 0.015 sec, ML Optimization: 0.866 sec				
ROP Model	ΔWOB (klb)	ΔRPM (rev/min)	Δq (gpm)	ΔROP (ft/hr)
Bingham (1964)	11.75	44.73	0.00	90.61
Modified B&Y	11.75	44.73	8.70	74.94
Hareland and Rampersad (1994)	10.50	44.73	0.00	50.14
Motahhari *et al.* (2010)	11.75	44.73	0.00	72.30
Random Forests	0.00	0.00	0.00	7.86
Support Vector Machines	-2.94	-0.50	0.96	36.88
Neural Networks	-6.47	-3.33	-2.87	23.06

Values in the table above represent the nineteen formations' average adjustment in operational drilling parameters suggested by each optimization method and the resulting ROP improvement predicted by each ROP model. For the four analytical models considered, both gradient-based optimization techniques drove drilling parameters to their upper bounds and achieved high ROP improvements in a computationally-efficient manner. Note that modified Bourgoyne and Young is the only analytical model capable of optimizing drilling mud flow rate. Gradient-based methods did not perform well with random forests models. In fact, drilling parameters were left unchanged and the 7.86ft/hr positive difference in ROP is simply due to model error. ROP gains obtained with the three machine learning models are significantly more modest than their analytical optimization counterparts. However, cross-validation error results from the previous section indicate that ML models are much more accurate than analytical models in this lithology-dependent post-drilling context.

Direct search optimization results are split into two tables for displaying purposes. In the first table, Nelder-Mead, COBYLA and basin-hopping (with COBYLA as local optimizer) performances are analyzed:

Table 5.9: Direct search optimization of drilling parameters in lithology-dependent post-drilling framework. Part 1 with Nelder-Mead, COBYLA and basin-hopping (with COBYLA) algorithms.

ROP Model	ΔWOB (klb)	ΔRPM (rev/min)	Δq (gpm)	ΔROP (ft/hr)
Optimization Method: Nelder-Mead - Analytical Optimization: 0.049 sec, ML Optimization: 14.96 sec				
Bingham (1964)	1.40E+54	1.56E+55	0.00	2.96E+81
Modified B&Y	4.66E+53	2.75E+54	6.55E+54	1.88E+180
Hareland and Rampersad (1994)	131.00	6.06E+32	0.00	2.35E+30
Motahhari *et al*. (2010)	1.75E+54	1.56E+55	0.00	9.08E+80
Random Forests	-0.17	-2.52	10.60	21.00
Support Vector Machines	-2.61	1.21	5.24	39.16
Neural Networks	-45.87	-9.50	-62.38	28.71
Optimization Method: COBYLA - Analytical Optimization: 0.027 sec, ML Optimization: 4.05 sec				
Bingham (1964)	11.75	44.73	0.00	90.61
Modified B&Y	11.75	44.73	8.70	74.94
Hareland and Rampersad (1994)	10.50	44.73	0.00	50.14
Motahhari *et al*. (2010)	11.75	44.73	0.00	72.30
Random Forests	-0.25	-0.24	0.53	15.98
Support Vector Machines	-3.86	0.27	3.02	37.58
Neural Networks	-5.62	-2.44	-0.48	22.48
Optimization Method: Basin Hopping - Analytical Optimization: 0.438 sec, ML Optimization: 420 sec				
Bingham (1964)	11.75	44.73	0.00	90.61
Modified B&Y	11.75	44.73	8.70	74.94
Hareland and Rampersad (1994)	10.50	44.73	0.00	50.14
Motahhari *et al*. (2010)	11.75	44.73	0.00	72.30
Random Forests	-0.72	-0.32	0.51	24.64
Support Vector Machines	-4.56	0.21	4.38	38.92
Neural Networks	-14.80	-12.13	-36.38	31.22

Nelder-Mead optimization is unbounded, causing analytical ROP models to extrapolate drilling behavior to extremely high, unfeasible operational parameter values. Similar results are observed for models trained by the neural networks algorithm. Contrary to gradient-based optimization, direct search methods are capable of locating improved

drilling parameters with random forests models. ROP improvements are more substantial

when optimizing machine learning models with direct search methods.

Particle swarm and brute force optimizations are shown next:

Table 5.10: Direct search optimization of drilling parameters in lithology-dependent post-drilling framework. Part 2 with particle swarm optimization and brute force algorithms.

Optimization Method: PSO - Analytical Optimization: 1.21 sec, ML Optimization: 2067 sec				
ROP Model	ΔWOB (klb)	ΔRPM (rev/min)	Δq (gpm)	ΔROP (ft/hr)
Bingham (1964)	11.75	44.73	0.00	90.61
Modified B&Y	11.75	44.73	8.70	74.94
Hareland and Rampersad (1994)	10.50	44.73	0.00	50.14
Motahhari *et al*. (2010)	11.75	44.73	0.00	72.30
Random Forests	-4.72	-13.90	-13.63	27.61
Support Vector Machines	-6.49	-0.76	-2.49	42.53
Neural Networks	-9.45	-4.67	-1.83	31.73
Optimization Method: Brute Force (1:1:1) - Analytical Optimization: 2.54 sec, ML Optimization: 16084 sec				
ROP Model	ΔWOB (klb)	ΔRPM (rev/min)	Δq (gpm)	ΔROP (ft/hr)
Bingham (1964)	11.75	44.73	0.00	90.61
Modified B&Y	11.75	44.73	8.70	74.94
Hareland and Rampersad (1994)	10.50	44.73	0.00	50.14
Motahhari *et al*. (2010)	11.75	44.73	0.00	72.30
Random Forests	-3.93	-7.17	-4.96	28.62
Support Vector Machines	-6.51	-0.69	-2.33	40.83
Neural Networks	-13.83	-7.85	-6.96	31.98
Optimization Method: Brute Force (1:5:5) - Analytical Optimization: 0.114 sec, ML Optimization: 707 sec				
ROP Model	ΔWOB (klb)	ΔRPM (rev/min)	Δq (gpm)	ΔROP (ft/hr)
Bingham (1964)	11.75	44.73	0.00	90.61
Modified B&Y	11.75	44.73	7.19	73.51
Hareland and Rampersad (1994)	10.50	44.73	0.00	50.14
Motahhari *et al*. (2010)	11.75	44.73	0.00	72.30
Random Forests	-3.93	-24.75	-13.33	23.00
Support Vector Machines	-4.72	-0.27	-3.86	21.48
Neural Networks	-9.72	-8.43	-10.96	31.77

PSO yields larger ROP gains with machine learning models than Nelder-Mead, COBYLA,

and basin-hopping (with COBYLA) direct search optimizations. Two sets of results are

presented for brute force optimization. In the first experiment, drilling parameters were

varied by unit increments in brute force search (Brute Force 1:1:1, middle portion of the

table). Even though this approach generally results in the highest ROP gains for ML ROP

models, computational requirements are extremely demanding for attempting a large number of possible parameter combinations. The average optimization time for the three ML models in a formation exceeded four hours (16084 seconds), making brute force search in this fine grid computationally prohibitive in real-time. Hence, in the second attempt, increments of 1klbf for WOB, 5rev/min for RPM, and 5gpm for flow rate were utilized (Brute 1:5:5, bottom portion of Table 5.10). This coarser brute force grid results in alleviated computational requirements, at the expense of ROP gains. Referring to Table 4.4, WOB and RPM are constrained between 5-35klb and 100-180rev/min, respectively. After the initial 5klb trials, both brute force search grids span 30 WOB steps. With unit variations, the original grid (1klbf:1rev/min:1gpm) performs 80 RPM increments, while the second grid (1klbf:5rev/min:5gpm) accounts for sixteen 5rev/min increases. The number of flow rate steps depends on training data flow rate range. In the Lodgepole Limestone optimization case study conducted at the end of this section, nineteen 1gpm increments separate minimum and maximum flow rate values observed while drilling the formation. Therefore, for post-drilling optimization of drilling parameters in the Lodgepole Limestone formation, the finer brute force search grid requires 50,220 (31x81x20) ROP model predictions compared to 2,108 (31x17x4) function evaluations with the coarser grid.

Analytical ROP models, due to their positively bounded coefficient nature, will always push WOB, RPM and flow rate to their upper bounds, within constraints. This notion is evidenced in Tables 5.8-5.10, displaying identical change in drilling parameters and ROP improvements for all bounded optimization algorithms tested. The only exception is the corrected Hareland and Rampersad (1994) model, which suggests optimal WOB values slightly below the upper limit due to possible ROP reduction at high WOB and low rock strength values in its convoluted formulation (Section 2.3.3). Since analytical model coefficients must average drilling behavior (Fig 2.3), field knowledge about ROP

relationships with drilling variables dictate that coefficient bounds (Table 2.1) should guarantee a positive relation. The top drive power constraint, a trade-off between WOB and RPM, prioritizes increases in whichever variable is modeled with higher exponent value to maximize ROP. Pump power caps flow rate according to average SPP (pressure optimizations are not considered in this dissertation). In the Bakken shale well dataset analyzed, rig equipment power was not a limiting factor. Other constraints (bit WOB operating range upper bound, downhole tools' maximum RPM rating, fracture gradient) restricted further drilling parameter augmentations.

Machine learning ROP models can identify regions in the operational parameter space that are proponent to drilling dysfunctions (e.g. excessive vibrations, inadequate hole cleaning, bit balling). Consequently, unlike analytical models, optimization with ML models may suggest optimal operational parameters that are not maximized to their upper bounds. Drilling parameter adjustments in Tables 5.8-5.10 differ depending on optimization method, with no clear trend. ROP gains are the highest with the finer grid brute force search for RF and NN models, but computational demands are restrictive with regards to real-time optimization. With SVM, particle swarm optimization achieved slightly higher ROP improvements than brute force, indicating that the model predicts large ROP changes with small parameter increments (less than unit) and that the 1klbf:1rev/min:1gpm brute force grid was not fine enough to locate global optimal parameters. Further refinement of the brute force search grid introduces additional computational expense and eventually leads to diminishing ROP gains.

Difference in optimization philosophy between analytical and ML ROP models is evidenced by comparing optimizations with the highest predicted ROP improvements for the most accurate models in each category:

Table 5.11: Lithology-dependent post-drilling optimization summary for modified
Bourgoyne and Young ROP models with SLSQP optimization algorithm.

Rock Formations	Modified Bourgoyne and Young - SLSQP				
	Norm. RMSE	ΔWOB (klb)	ΔRPM (rev/min)	Δq (gpm)	ΔROP (ft/hr)
Greenhorn Limestone	26.87	18.21	22.66	1.98	145.38
Newcastle Sandstone	16.61	21.70	27.83	13.20	233.32
Dakota Sandstone	22.64	21.46	47.92	2.50	197.12
Swift Shale	31.25	26.83	47.93	2.59	292.41
Rierdon Limestone	26.12	15.10	46.70	2.14	144.23
Piper Limestone	25.31	12.43	47.00	2.42	54.99
Spearfish Sandstone	20.39	14.67	44.70	22.01	101.41
Pine Salt Sandstone	63.36	14.78	42.70	17.70	46.33
Broom Creek Sandstone	46.80	12.12	48.53	9.21	37.01
Tyler Sandstone	45.01	10.27	47.76	2.93	19.34
Kibbey Lime Limestone	19.90	4.98	45.01	1.22	7.56
Kibbey Lime Shale	13.90	9.79	47.86	1.22	13.06
Charles Sandstone	47.70	10.44	47.56	18.74	24.09
Charles Limestone	31.56	3.44	47.49	2.32	20.94
Ratcliffe Sandstone	39.64	11.78	47.32	1.97	19.03
Base Last Salt Limestone	48.05	11.84	47.60	24.21	15.63
Base Last Salt Sandstone	14.66	0.35	47.74	2.42	14.33
Mission Canyon Limestone	18.37	2.92	47.78	25.63	20.07
Lodgepole Limestone	9.89	0.16	47.76	10.98	17.63
Average	29.90	11.75	44.73	8.70	74.94

Drilling parameters are maximized to their upper bounds in every formation when optimized according to the modified B&Y model. Optimization results in Table 5.11 suggest that shallower formations offer the biggest potential for ROP improvement, as WOB values remained low in actual drilling of the upper portion of this well segment. Comparing SLSQP optimization with modified B&Y models to brute force (1klbf:1rev/min:1gpm) optimization with random forests models:

Table 5.12: Lithology-dependent post-drilling optimization summary for random forests
ROP models with brute force search optimization algorithm.

Rock Formations	Random Forests - Brute Force 1:1:1				
	Norm. RMSE	ΔWOB (klb)	ΔRPM (rev/min)	Δq (gpm)	ΔROP (ft/hr)
Greenhorn Limestone	18.86	-0.79	-0.34	0.87	73.29
Newcastle Sandstone	11.31	-2.30	-49.17	9.93	16.26
Dakota Sandstone	12.04	-6.54	-24.08	1.57	53.57
Swift Shale	13.30	-1.17	-0.07	-0.30	47.27
Rierdon Limestone	16.98	0.10	-1.30	0.36	73.53
Piper Limestone	13.60	-6.57	-2.00	-1.84	24.61
Spearfish Sandstone	9.49	-1.33	1.70	-106.35	37.00
Pine Salt Sandstone	20.12	-7.22	-0.30	4.93	31.70
Broom Creek Sandstone	18.62	-1.88	-3.47	6.45	35.16
Tyler Sandstone	12.86	-5.73	2.76	-2.63	17.11
Kibbey Lime Limestone	4.84	-2.02	-1.99	0.97	8.79
Kibbey Lime Shale	6.48	-3.21	0.86	-0.15	6.23
Charles Sandstone	19.05	-7.56	-0.44	17.98	44.84
Charles Limestone	17.70	-3.56	1.49	1.72	25.11
Ratcliffe Sandstone	11.92	-10.22	-32.68	0.25	19.36
Base Last Salt Limestone	8.39	3.84	-0.40	-46.40	2.44
Base Last Salt Sandstone	7.67	-3.65	-0.26	0.61	6.32
Mission Canyon Limestone	10.06	-11.08	-0.22	15.31	12.34
Lodgepole Limestone	5.73	-3.84	-26.24	2.41	8.92
Average	12.58	-3.93	-7.17	-4.96	28.62

Similar to Table 5.11, ROP gains display a general negative trend with deeper formations. In the table above, all but two formations (Rierdon Limestone, ΔWOB = +0.10klb and Base Last Salt Limestone, ΔWOB = +3.84klb) require a negative change in WOB to optimize ROP and the average suggested WOB modification is ΔWOB = -3.93klb. Drilling dysfunctions can demand such adjustments, but it is unlikely that dysfunctions dominated drilling behavior in seventeen out of nineteen formations. Instead, the negative WOB influence on ROP modeled by the random forests algorithm is likely a consequence of bad data quality. Optimization in most formations favor a reduction in RPM, while flow rate adjustments vary wildly. Predicted ROP gains are not as significant as in optimization with modified B&Y models (ΔROP_{avg} = 28.62ft/hr in Table 5.12 vs. ΔROP_{avg} = 74.94ft/hr in Table 5.11). However, random forests models are substantially more accurate than modified B&Y models, with average absolute error lower by 18.2% and average

normalized RMSE lower by 17.32% in Table 5.6, predicting more realistic results. The prediction error gap widens if error metrics are weighted by the number of training samples collected in each rock formation.

Next, optimizations with individual ML ROP models are examined separately to identify the source of extensive computational requirements. Starting with the SVM model:

Table 5.13: ROP difference and computational time for all optimization methods with support vector machines ROP models.

Support Vector Machines		
Optimization Method	ROP Difference (ft/hr)	Computational Time (sec)
L-BFGS-B	37.12	0.04
SLSQP	36.88	0.04
Nelder-Mead	39.16	0.09
COBYLA	37.58	0.19
Basin Hopping (COBYLA)	38.92	9.60
Particle Swarm Optimization	42.53	0.66
Brute Force 1:5:5	21.48	1.47
Brute Force 1:1:1	40.83	32.38

Particle swarm optimization, followed by brute force (1klbf:1rev/min:1gpm) and Nelder-Mead, leads to the highest ROP improvements. Performance variation between optimization methods is not as accentuated as with other ML models, except for coarser brute force (1klbf:5rev/min:5gpm) search due to model sensitivity to small changes in drilling parameters. Interestingly, computational times for all SVM optimizations were not as high as originally anticipated, representing a small fraction of the computational expense reported in Tables 5.8-5.10 for optimization of all three ML models.

Table 5.14 displays results for optimizations with NN models:

Table 5.14: ROP difference and computational time for all optimization methods with neural networks ROP models.

Neural Networks		
Optimization Method	ROP Difference (ft/hr)	Computational Time (sec)
L-BFGS-B	23.71	0.04
SLSQP	23.06	0.04
Nelder-Mead	28.71	0.05
COBYLA	22.48	0.18
Basin Hopping (COBYLA)	31.22	9.14
Particle Swarm Optimization	31.73	1.38
Brute Force 1:5:5	31.77	1.42
Brute Force 1:1:1	31.98	31.64

ROP gains are highest for brute force (1klbf:1rev/min:1gpm), brute force (1klbf:5rev/min:5gpm), particle swarm optimization and basin-hopping (with COBYLA), with all four methods obtaining similar improvements. Again, computational requirements were not as high as expected.

Results in Tables 5.13 and 5.14 suggest that optimizations with RF models are responsible for almost all computational demand previously attributed to the three ML ROP models in Tables 5.8-5.10. Investigating random forests optimizations individually:

Table 5.15: ROP difference and computational time for all optimization methods with random forests ROP models.

Random Forests		
Optimization Method	ROP Difference (ft/hr)	Computational Time (sec)
L-BFGS-B	7.86	0.54
SLSQP	7.86	0.76
Nelder-Mead	21.00	0.76
COBYLA	15.98	3.94
Basin Hopping (COBYLA)	24.64	401
Particle Swarm Optimization	27.61	2065
Brute Force 1:5:5	23.00	704
Brute Force 1:1:1	28.62	16020

The table above confirms that drilling parameter optimization with RF models requires substantially more computational power than with other ROP models. Fig. 2.10 illustrates divisions in the operational parameter space created by a simplistic decision tree model. With trees grown a lot deeper, random forests models develop extremely segmented parameter spaces. This severe partitioning generates two contrasting effects: random forests ROP models are the most accurate because the algorithm separates training data into groups where operating parameters exhibit similar drilling behavior, but such models are also the hardest to optimize drilling parameters for. While optimizations with other ROP models frequently navigate the parameter space seamlessly and converge fast, RF optimizations struggle to locate optimal drilling variables in a discontinuous parameter space.

Unsurprisingly, gradient-based optimization techniques cannot effectively operate in RF parameter spaces. Brute force search with 1klbf:1rev/min:1gpm increments yields the best ROP improvements in Table 5.15 but takes over four hours (16020 seconds) per formation optimization. The Nelder-Mead method converges very fast and produces acceptable ROP gains, possibly representing a good alternative for real-time RF optimization. Nevertheless, Nelder-Mead does not support any constraints and could be dangerous for closed-loop drilling control if models suggest drilling parameters outside the feasible region (as NN did in Table 5.9). For the dataset analyzed here, parameters optimized by Nelder-Mead with the random forests model remained within acceptable bounds. The author believes this is caused by random forests ROP models not extrapolating drilling behavior and relying only on information contained in the training data, but additional investigation is required to confirm this hypothesis. Particle swarm optimization leads to nearly as much ROP improvement as brute force search with finer grid for the RF

132

model. However, PSO computational requirements with RF ROP models are still very taxing for real-time implementation.

PSO metrics displayed in Tables 5.10 and 5.13-5.15 were obtained by initializing a swarm of 50 particles and limiting optimizations to a maximum of 300 iterations, as suggested by Anemangely *et al*. (2017). With analytical, SVM and NN ROP models, PSO converges fast and yields excellent ROP improvements. While PSO also achieves vast ROP gains with the RF model, the algorithm requires over 30 minutes (2065 seconds) for each formation optimization and still does not converge to the prescribed tolerance within the maximum 300 iterations. Conducting PSO optimizations for RF models with lower limit of maximum iterations:

Table 5.16: ROP difference and computational time for PSO with random forests ROP models by varying the maximum number of iterations.

Random Forests		
Particle Swarm Optimization	**ROP Difference (ft/hr)**	**Computational Time (sec)**
300 iterations	27.61	2065
100 iterations	26.87	692
50 iterations	28.63	388
25 iterations	28.00	193
10 iterations	26.60	77

The stochastic nature of PSO results in an unpredictable relationship between ROP improvement and maximum number of iterations. If the optimization is repeated multiple times with different initial particle positions and velocities, average results will likely indicate that more iterations lead to higher ROP gains. However, as evidenced in Table 5.16, it is possible for PSO to locate a more optimal solution with fewer iterations due to varying random starting conditions prescribed by the algorithm. PSO with 10 maximum iterations attains better ROP improvements for RF models than all methods in Table 5.15 apart from PSO (300 iterations) and brute force (1klbf:1rev/min:1gpm) search, while

133

maintaining computational feasibility in real-time applications. This approach takes advantage of the large swarm size (50 particles), pursuing a limited number of improvements (10 iterations) to the 50 initial particle solutions instead of seeking convergence. Intuitively, it will perform well in the heavily segmented parameter spaces of random forests models when at least one of the particles is initialized near a region with high ROP values.

Post-drilling optimizations in the Lodgepole Limestone formation are analyzed to reveal insights about the parameter space of ROP models. Table 5.17 summarizes information about the data collected in this particular formation:

Table 5.17: Properties and data statistics for Lodgepole Limestone formation.

Lodgepole Limestone				
Properties	Thickness (ft)	Data Points	Rock Strength (psi)	Bit Aggressiveness
Value	257	705	19544	1.05
Measured Data	Minimum	Maximum	Standard Deviation	Average
ROP (ft/hr)	13.61	69.71	4.18	42.09
Depth (ft)	8871	9128	74.61	9002
WOB (klb)	30.28	40.88	1.15	34.84
RPM (rev/min)	131.7	133.2	0.41	132.2
Flow Rate (gpm)	354.5	373.0	7.06	362.1
Torque (klb-ft)	6.72	11.38	0.69	8.89
SPP (psi)	3729	3986	54.57	3854

Deepest out of all formations in this Williston Basin dataset, Lodgepole Limestone spans a depth interval nearly identical to the average of all formations (256ft), possesses a large number of measured data points, and exhibits low ROP model errors (Tables 5.11 and 5.12). Even in this final formation for the bit run investigated, the maximum required top drive power (289HP, with 11.38klb-ft torque and 133.2rev/min RPM) does not approach the rig's top drive capability (800HP). Mud pumps (3200HP) are also not challenged by a maximum 867HP demand (with 373.0gpm flow rate and 3986psi SPP).

Starting with the only analytical ROP model accounting for flow rate in its formulation, the 3D optimization space for the Lodgepole Limestone modified Bourgoyne and Young model is illustrated below:
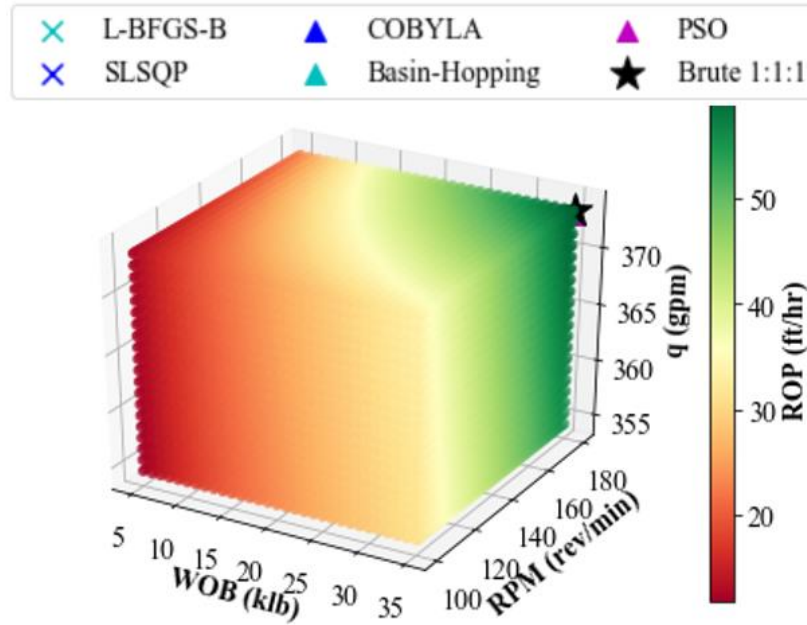
Figure 5.2: Optimization parameter space for modified Bourgoyne and Young Lodgepole Limestone ROP model with solution markers for six optimization methods.

The optimization space is derived from brute force search with unit increments and color-coded in red-yellow-green stoplight style according to ROP values. With positively bounded model coefficients as exponents for WOB, RPM and flow rate, analytical models display predictable parameter spaces with gradually increasing ROP towards higher operational variables' values. All optimization methods arrive at the same solution in the top right corner of Fig 5.2, maximizing WOB, RPM and flow rate in this simple parameter space. Nelder-Mead solutions are not shown due to their unbounded nature. Analyzing the WOB-RPM response surface for the brute force parameter combinations closest to the average flow rate (362.5gpm) in the Lodgepole Limestone formation:
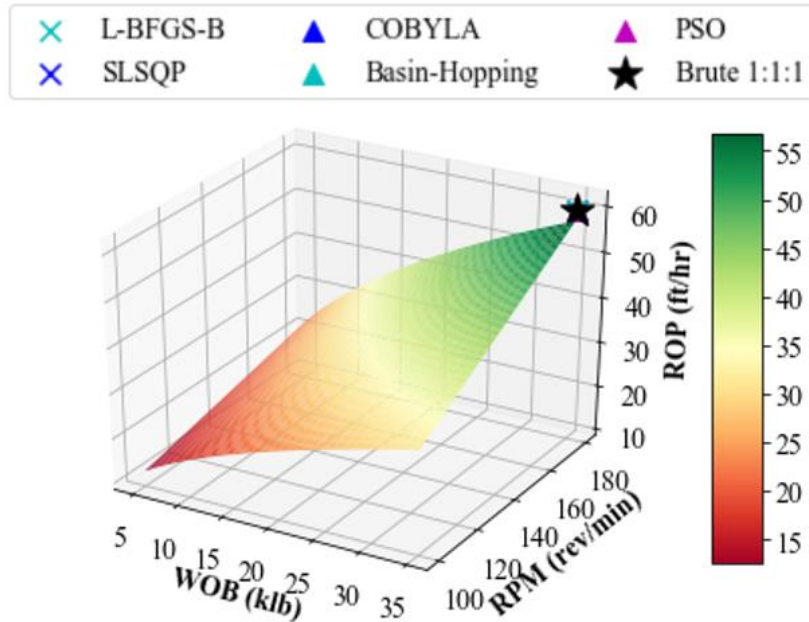
Figure 5.3: WOB-RPM optimization surface (at average flow rate) for modified
Bourgoyne and Young Lodgepole Limestone ROP model with solution
markers for six optimization methods.

As expected, higher WOB and RPM values lead to increasing ROP. The WOB-RPM
surface exhibits the same shape regardless of flow rate, with higher ROP as flow rate
increases.

Next, the optimization parameter space for the Lodgepole Limestone random
forests ROP model is investigated:
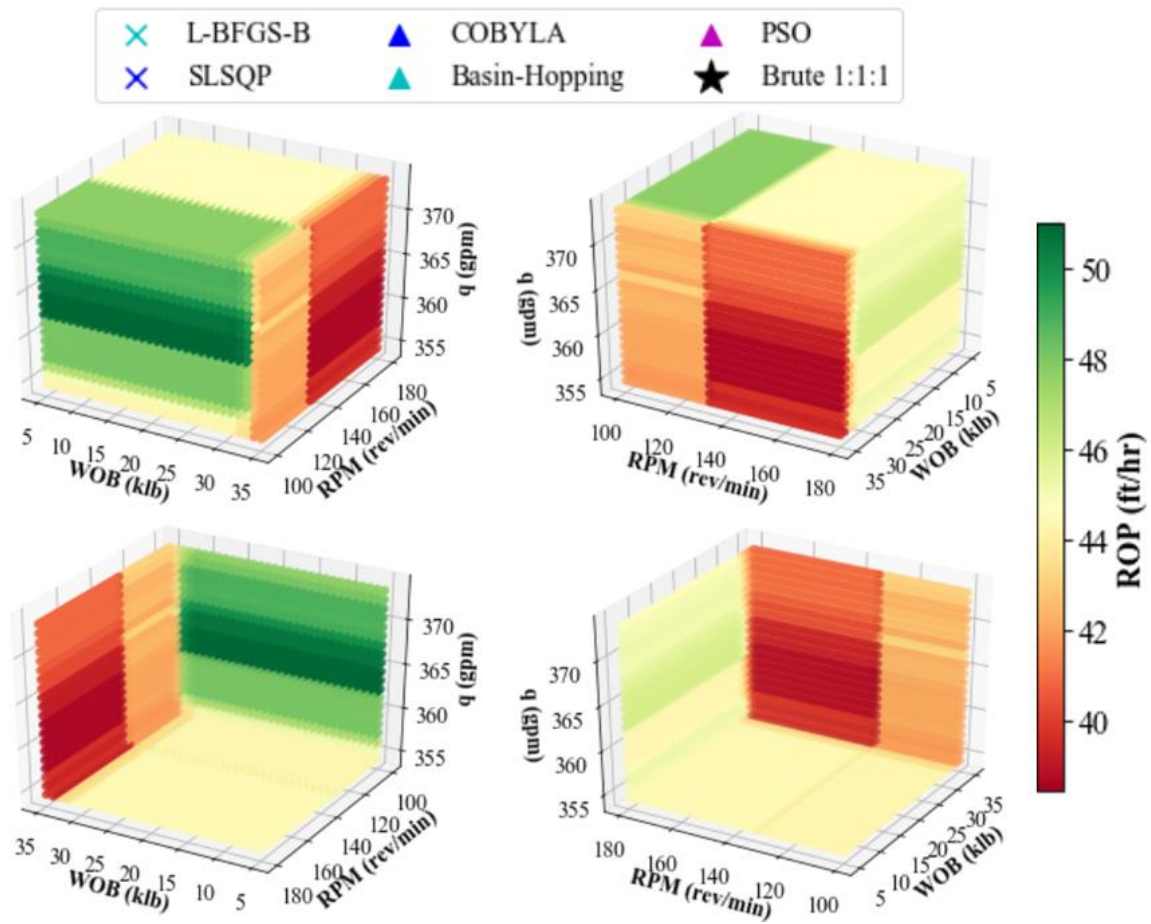
Figure 5.4: Different views of optimization parameter space for random forests Lodgepole Limestone ROP model with solution markers for six optimization methods.

First demonstrated in Figure 2.10, models generated by the random forests algorithm create segmented parameter spaces. The four plots above indicate that according to this Lodgepole Limestone random forests model, WOB does not exert substantial influence on ROP. There is a high ROP region (dark green) at 100rev/min RPM and 360-365gpm flow rate. Unlike Fig. 5.2, ROP transitions are not always gradual in the figure above and discontinuities are experienced (e.g. 35klb WOB, 360gpm flow rate and 140rev/min RPM). Rotated views provide more information about the optimization space, but the closer faces

of the cube are cropped in the two bottom plots of Fig 5.4, possibly due to the large number of data points plotted. Solutions computed by the different optimization methods are not visible since they are not located on the outer faces of the brute force grid. In order to locate them, the parameter space is sliced halfway through the WOB grid:
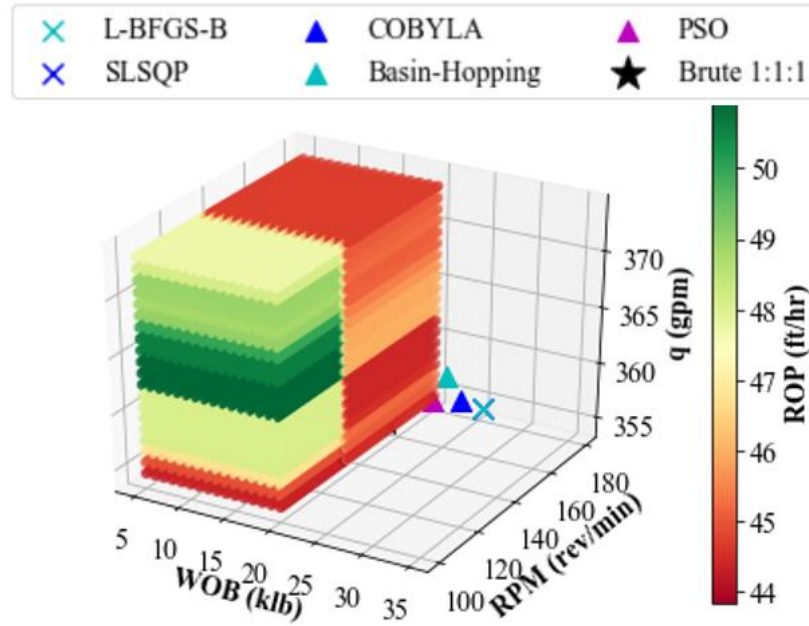
Figure 5.5: Cut through optimization parameter space for random forests Lodgepole Limestone ROP model with solution markers for six optimization methods.

Note that heatmap colors are different than in Fig 5.4 because of the color bar scale. L-BFGS-B and SLSQP solutions overlap. Similar response patterns to the outer 35klb face occur at 20klb WOB. However, with this lower WOB value, the dark green high ROP strip extends to RPM values near 140rev/min. Hence, the RF ROP model suggests that higher WOB values require lower RPM for faster drilling in the Lodgepole Limestone formation. Full investigation of drilling responses demands several cuts through the parameter space (similar to Fig 5.5). In an attempt to enhance visualization, the parameter space is triangulated into a surface:
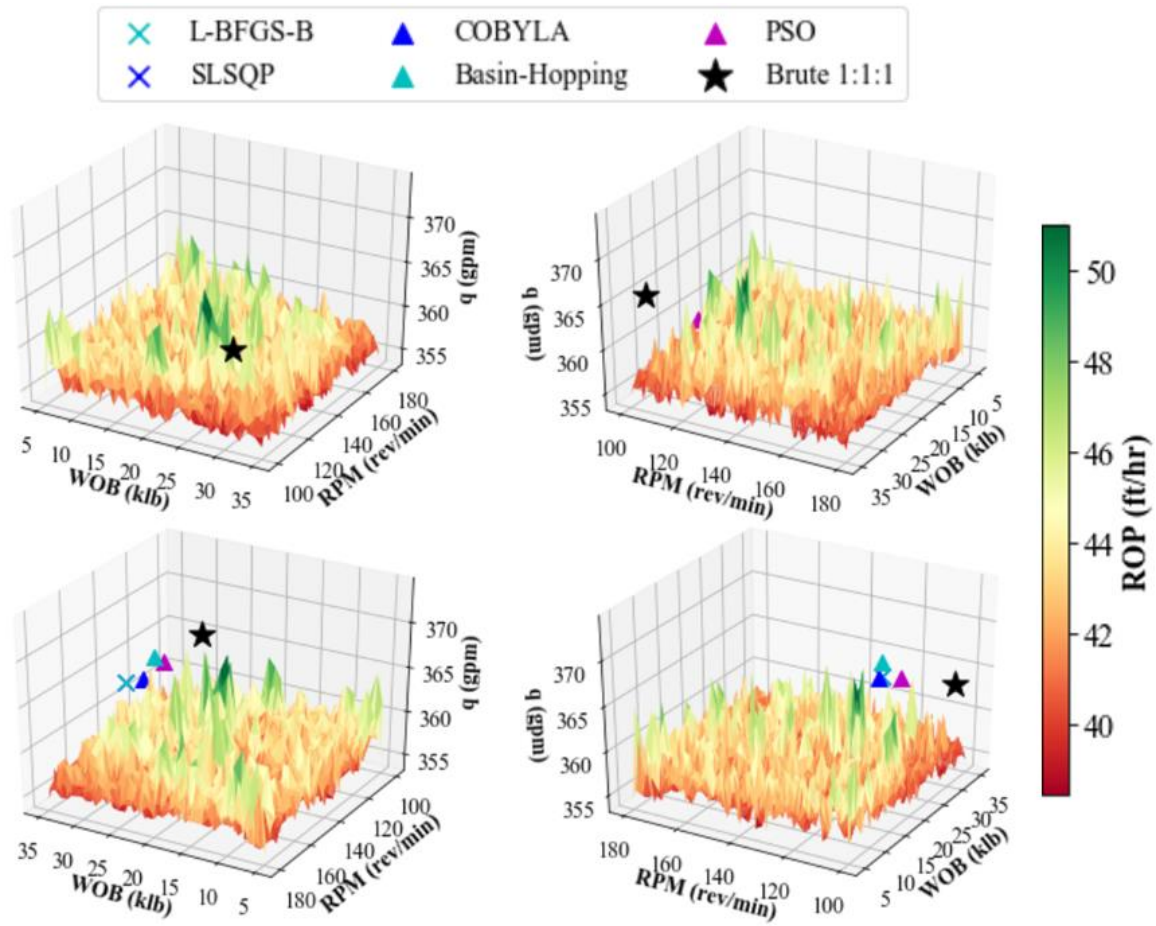
Figure 5.6: Different views of triangulated optimization parameter space for random forests Lodgepole Limestone ROP model with solution markers for six optimization methods.

While optimization solutions can be clearly seen with rotated views of this triangulated surface, triangulation is subjective and does not necessarily represent the same space as in Figure 5.4.

Transparency is introduced to Fig. 5.4 as an alternative approach to analyze the parameter space:
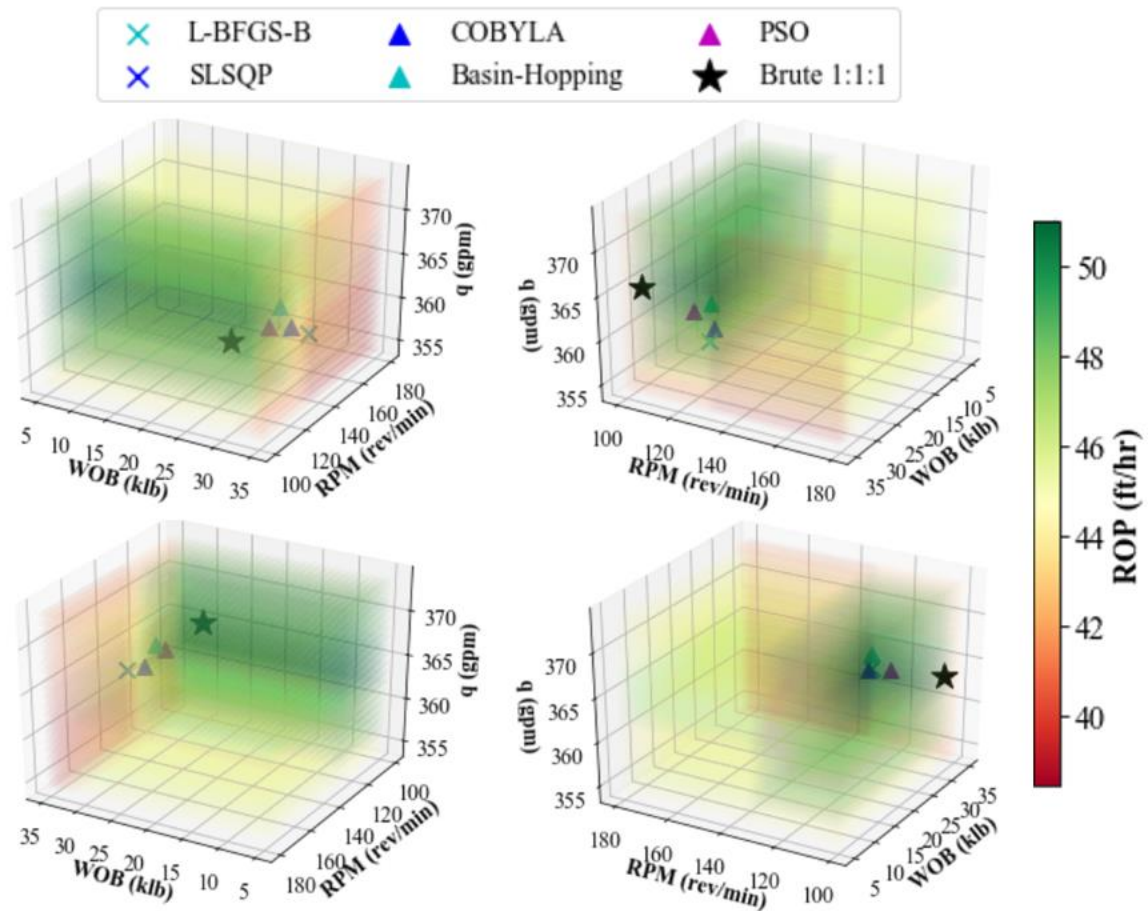
Figure 5.7: Different views of semitransparent optimization parameter space for random forests Lodgepole Limestone ROP model with solution markers for six optimization methods.

From the four plots in the figure above, it is clear that PSO comes closest to the brute force optimal solution with this Lodgepole Limestone random forests ROP model. PSO optimal parameters reach the bottom part of the high ROP dark green region (bottom left plot). Basin-hopping achieves the second nearest solution to brute force and gradient-based methods (L-BFGS-B and SLSQP) overlap far away, in the low ROP dark red region.

Scrutinizing the WOB-RPM surface at average flow rate (362.5gpm):
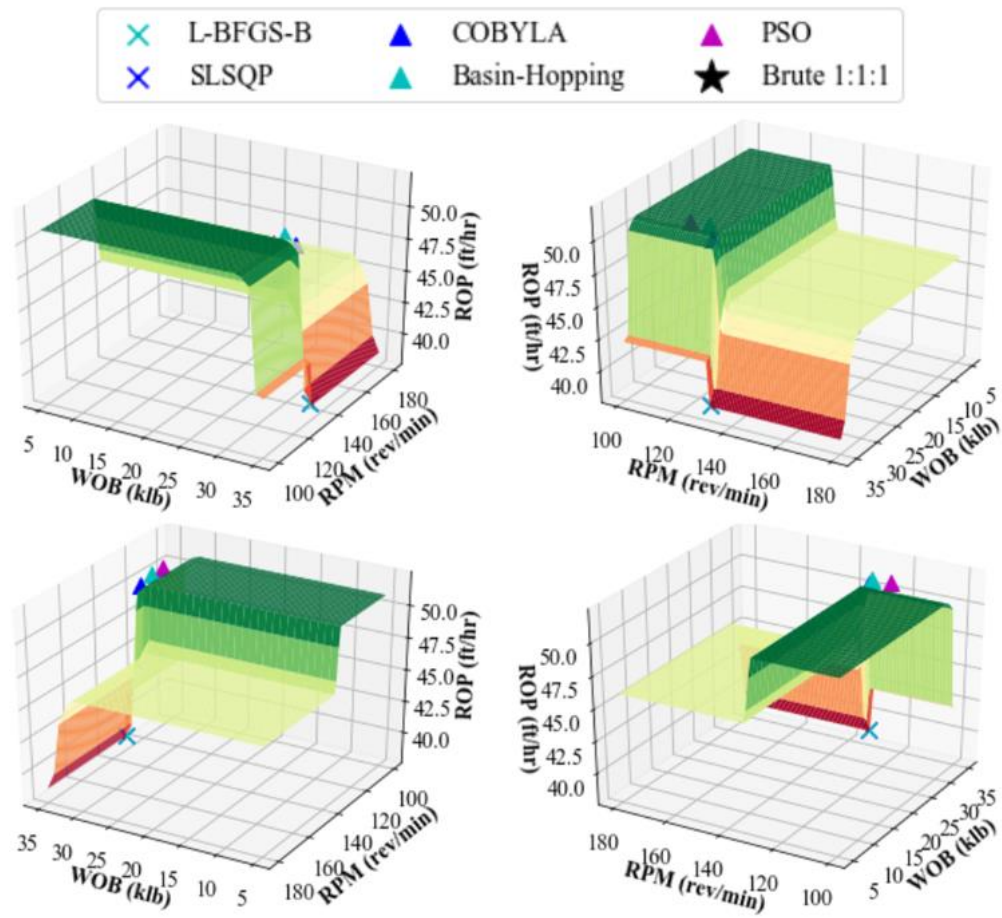
Figure 5.8: Different views of WOB-RPM optimization surface (at average flow rate) for random forests Lodgepole Limestone ROP model with solution markers for six optimization methods.

Rotated views of this WOB-RPM response surface exemplify discontinuities created by the random forests algorithm. With ML models, two-parameter ROP response surfaces exhibit different shapes depending on the value of the third parameter:
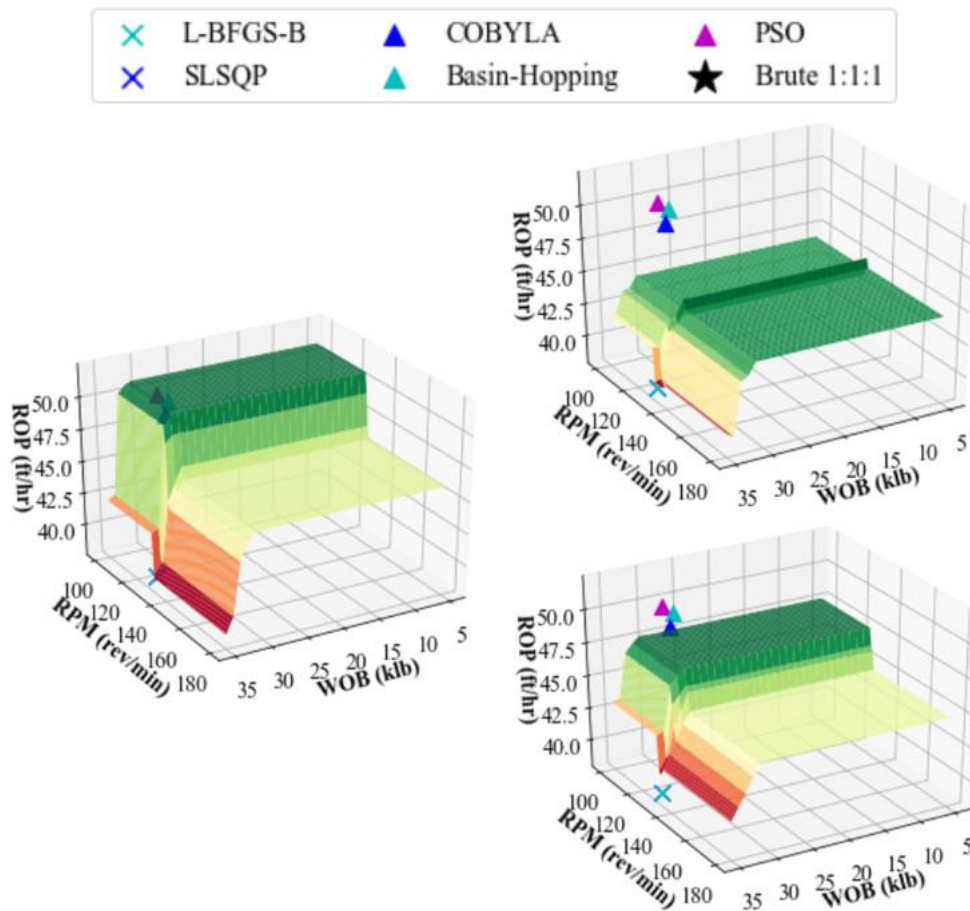
Figure 5.9: WOB-RPM optimization surfaces at varying flow rates for random forests Lodgepole Limestone ROP model with solution markers for six optimization methods.

In Fig. 5.9, the left-hand WOB-RPM surface is constructed at average flow rate (362.5gpm), the top right surface is at minimum flow rate (354.5gpm) and the bottom right surface is at maximum flow rate (373.5gpm). ROP values at average flow rate are actually higher than at maximum flow rate. All three surfaces display distinct shapes.

Analyzing the parameter space for the Lodgepole Limestone SVM ROP model:
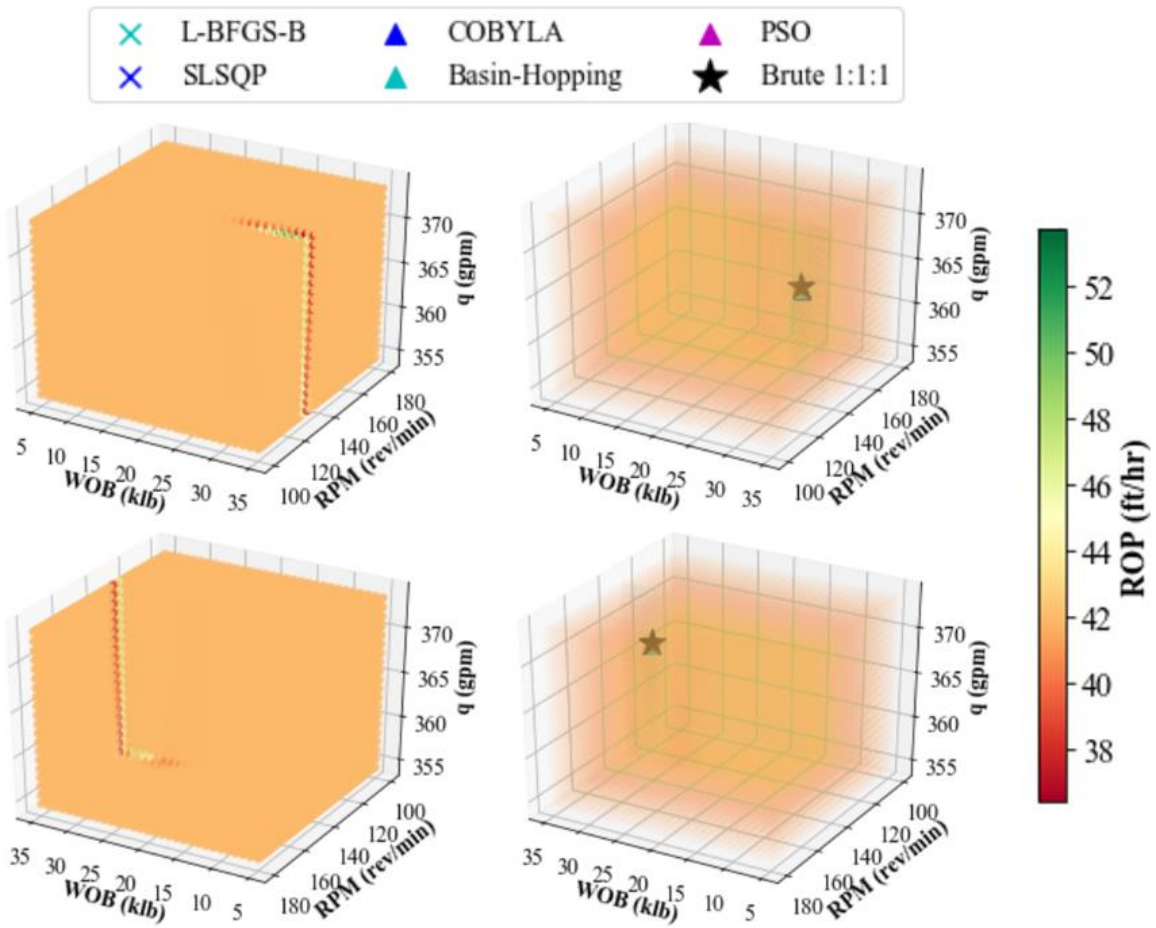
Figure 5.10: Different views of solid and semitransparent optimization parameter spaces for support vector machines Lodgepole Limestone ROP model with solution markers for six optimization methods.

This SVM optimization parameter space is highly uniform, except for a sliver where rapid changes occur. The high ROP region is contained in a very narrow band. Almost all optimization solutions overlap. Reproducing the WOB-RPM response surface at average flow rate:
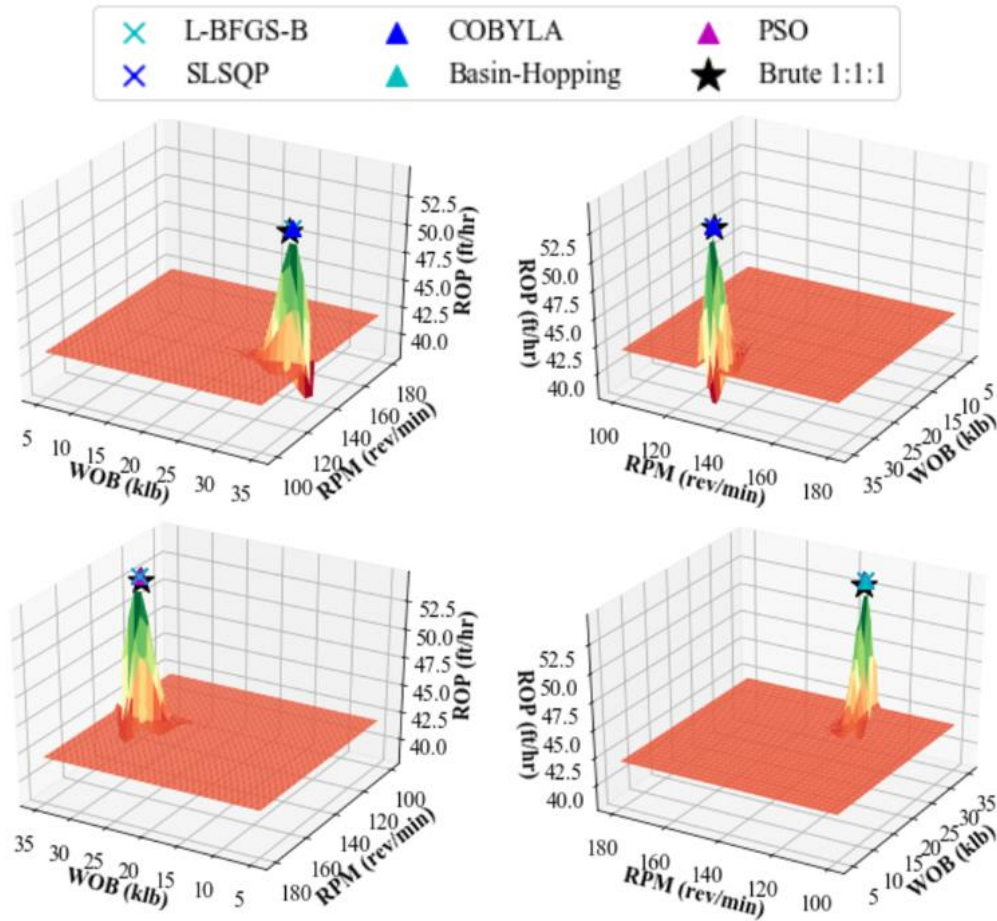
Figure 5.11: Different views of WOB-RPM optimization surface (at average flow rate) for support vector machines Lodgepole Limestone ROP model with solution markers for six optimization methods.

In Fig. 5.11, the majority of the WOB-RPM surface results in the same low ROP value. This SVM model, likely not representative of drilling field conditions, predicts the same ROP for all WOB if RPM is not within the 120-140rev/min range. ROP increases significantly in a small region of WOB and RPM values, which all optimization methods are successful in locating.

Finally, the Lodgepole Limestone NN ROP model parameter space is illustrated below:
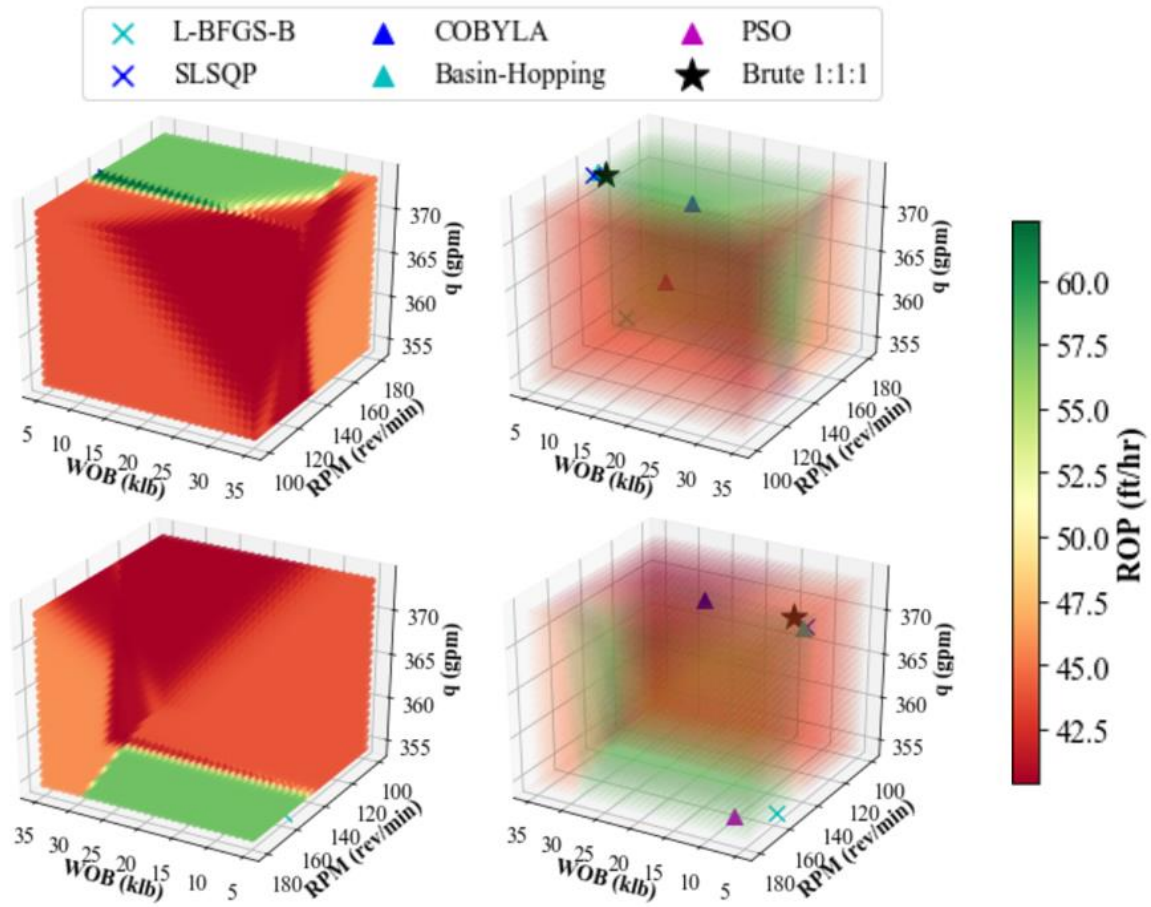
Figure 5.12: Different views of solid and semitransparent optimization parameter spaces for neural networks Lodgepole Limestone ROP model with solution markers for six optimization methods.

This NN parameter space is more segmented than the SVM model (Fig 5.10), but not as discontinuous as the one produced by the RF algorithm (Fig. 5.4). Optimal solutions vary substantially, but most methods (except COBYLA) suggest very low WOB values. PSO's solution is located far from brute force optimal parameters, but still yields high ROP values in a green zone of the parameter space. Scrutinizing the WOB-RPM response surface at average flow rate:
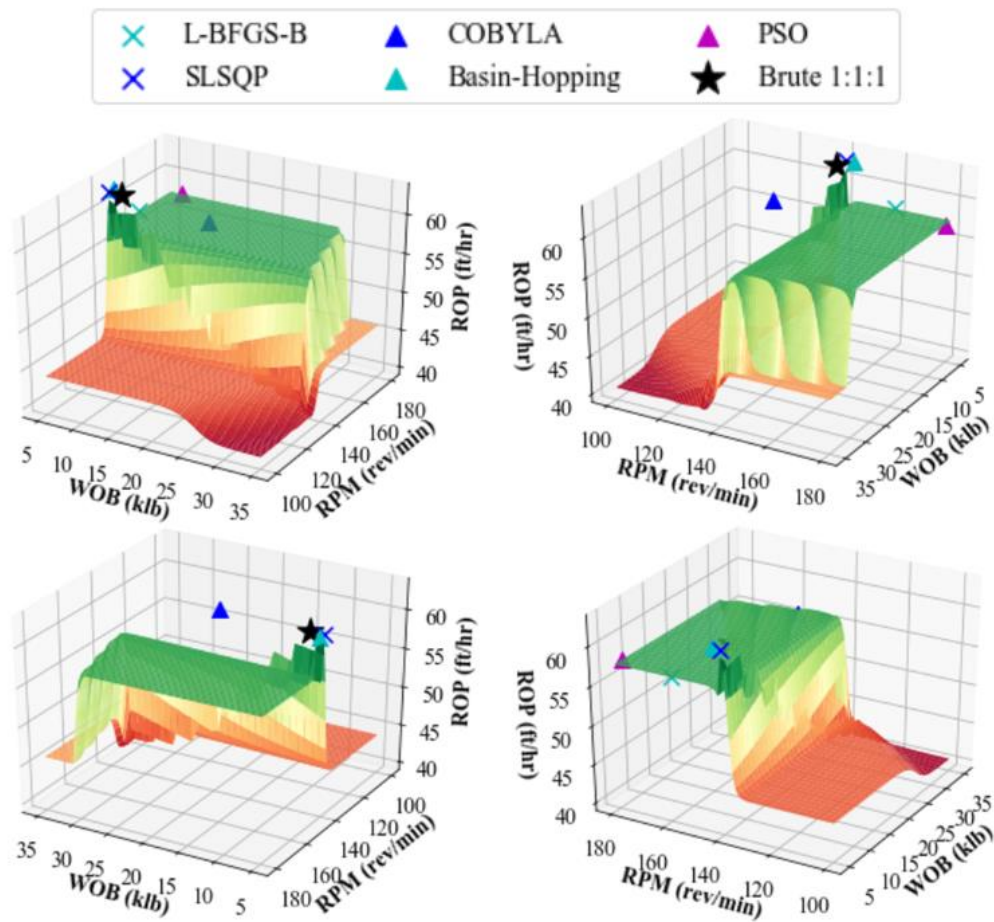
Figure 5.13: Different views of WOB-RPM optimization surface (at average flow rate) for neural networks Lodgepole Limestone ROP model with solution markers for six optimization methods.

Fig. 5.13 displays a highly complex WOB-RPM surface. Unexpectedly, the gradient-based SLSQP algorithm was able to navigate this intricate surface well and approach the brute force solution. Gradient-based optimization performed much better in comparison to the random forests WOB-RPM surface (Fig. 5.8), probably due to more gradual transitions in ROP values. PSO did not achieve great results in this particular case, but the algorithm works better with NN models than other optimization methods (excluding brute force) on average (Table 5.14).

Results presented in this section support utilization of the SLSQP algorithm for optimizing drilling parameters with analytical ROP models. All optimization methods, except the unbounded Nelder-Mead, suggest maximizing operational parameters to their upper bounds based on analytical models' ROP predictions. SLSQP handles any type of constraints and efficiently establishes optimal drilling parameters that lead to the highest ROP improvements. PSO is adopted as the standard optimization algorithm for ML ROP models, with a maximum of 300 iterations for both SVM and NN and a maximum of 10 iterations for RF. Achieving almost the same ROP gains as brute force search, PSO diminishes computational requirements and supports equality and inequality constraints. Basin-hopping (with COBYLA) is a respectable alternative for power-constrained optimization with ML models, accomplishing satisfactory ROP gains. Computational expense is acceptable with SVM and NN models but may be prohibitive to real-time applications with random forests. For this Williston Basin dataset, rig equipment power constraints did not impose any limitations. Drilling parameters utilized in the field or proposed as constraints (Table 4.4) did not come close to full top drive or pump power capacity. However, in situations where constraints other than parameter bounds are critical, SLSQP, COBYLA, basin-hopping, PSO, or other optimization methodologies which support all constraint categories must be employed.

From Table 5.7, cross-validating the seven suggested ROP models requires about 22 seconds of computational time. With optimization strategies established in this section, drilling parameter optimization takes at most 77 seconds (for RF models). Thus, a maximum of one minute and forty seconds are needed to select the best performing ROP model according to CV and optimize drilling parameters with respect to such model. If an analytical ROP model is the best performer by CV error, optimal drilling parameters are determined almost instantaneously with the SLSQP algorithm. In this case, the modeling

147

and optimization process occurs in 22 seconds (the time for cross-validation of the seven ROP models). These results indicate that it is possible to optimize drilling operational parameters with continuous ROP model learning in real-time with an inexpensive modern laptop computer (7th Generation Intel® Core™ i5 processor @ 2.50GHz and 8GB RAM). In the next section, the merits of continuous model learning are examined from a performance perspective.

5.7. MODEL PERFORMANCE WITH INCREMENTAL TRAINING DATA AVAILABILITY

Drilling data are constantly recorded and transmitted to the driller's cabin in modern drilling rigs. Assuming adequate data quality, it is plausible to expect that the drilling system can be better understood as more data become available. Therefore, a fundamental question for real-time ROP modeling is whether models can learn more about the drilling process with additional data. In other words, it is desirable to evaluate the ability of ROP models to reduce test error with incremental training data availability. Machine learning models are predicated on statistics, and thus expected to become more accurate as data from different portions of the drilling response curve (e.g. efficient drilling, high vibrations, inadequate hole cleaning) are collected. Conversely, analytical ROP models must average drilling behavior into empirical model coefficients (see Figure 2.3).

The incremental training data availability experiment is performed in nine iterations. In the first iteration, 10% of randomized data in a formation is utilized to train each ROP model, which is then tested against the remaining data points. The percentage of randomized data included in the training set increases by 10% at each iteration, until it reaches a ratio of 90% training data and 10% test data. Four learning metrics of interest are defined to evaluate model performance. An example of this experimental setup is displayed for two ROP models in the Lodgepole Limestone formation:

Table 5.18: Visualization of incremental data availability learning metrics for one run in the Lodgepole Limestone formation.

Lodgepole Limestone		Random Forests		Modified Bourgoyne and Young	
Iteration	Train/Test Percentage	Absolute Error	Norm. RMSE	Absolute Error	Norm. RMSE
1	10%/90%	6.33	8.82	7.10	10.23
2	20%/80%	5.80	8.30	7.01	10.30
3	30%/70%	5.18	7.38	7.07	10.08
4	40%/60%	5.13	7.04	7.02	10.08
5	50%/50%	4.82	6.83	7.09	10.19
6	60%/40%	4.31	6.52	6.52	9.84
7	70%/30%	3.54	5.10	6.30	9.36
8	80%/20%	3.43	4.50	6.11	8.45
9	90%/10%	3.44	4.79	6.56	9.45
Average Error		4.66	6.59	6.75	9.77
Learning Metrics of Interest					
Average Difference		0.36	0.50	0.07	0.10
First-Last Iteration Difference		2.89	4.03	0.54	0.78
New Minima (max. 8)		7	7	4	4
Best Improvement		0.77	1.42	0.57	0.89

Average difference is simply the average error difference between each consecutive iteration (red). The second metric represents the error difference between the first and last iterations (blue). Next, the new minima indicator (yellow) shows how many times the model was able to achieve a new overall test error minimum out of all previous iterations (maximum of eight, one for each iteration following the first). Note that while the absolute error for the modified Bourgoyne and Young model decreases in the fourth iteration with respect to the third iteration, it is not a new minimum since second iteration error is lower. Finally, best improvement (green) portrays the biggest error drop at any pair of consecutive iterations. Learning metrics of interest illustrated in Table 5.18 depend on the random segmentation of data. Hence, the experiment is repeated one hundred times with different seeding for randomized data partitions and results are averaged out to ensure statistical relevance.

Model learning performance with incremental training data availability is presented in Figure 5.14 with absolute error learning metrics:

149
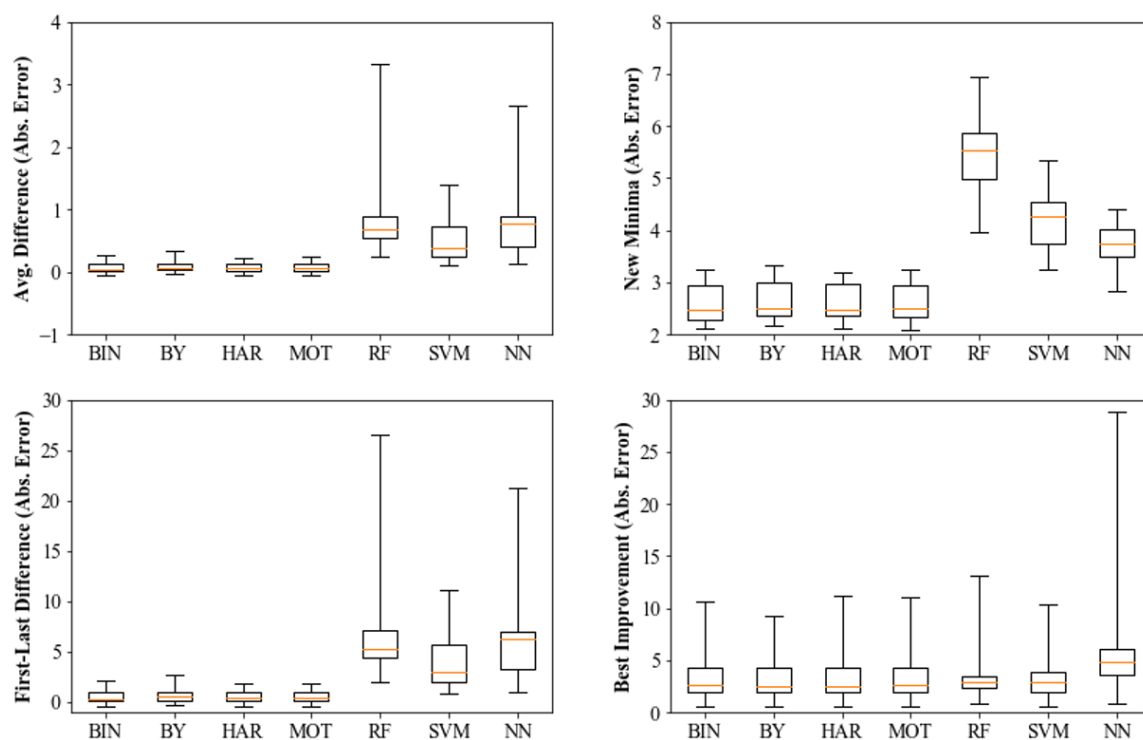
Figure 5.14: Absolute error learning metrics of interest for increasing training set length – Top left: average difference between iterations; Bottom left: difference between first (10% training data) and last (90% training data) iterations; Top right: new minima; Bottom right: best improvement in consecutive iterations.

Boxplots in Fig. 5.14 are interpreted in opposite manner to CV error boxplots (Fig. 5.1), as the learning metrics displayed above represent an improvement in performance (lower error). With more data gathered in a specific rock formation, machine learning ROP models are able to lower test absolute error significantly and predict ROP with much more accuracy. ML models achieve new minima in more than half of the eight possible iterations for the majority of formations in the dataset. The same is not true for analytical models, with new minima mostly ranging between two and three out of eight potential opportunities and negative average difference between iterations for some formations. Similar results were obtained for normalized RMSE learning metrics:

150
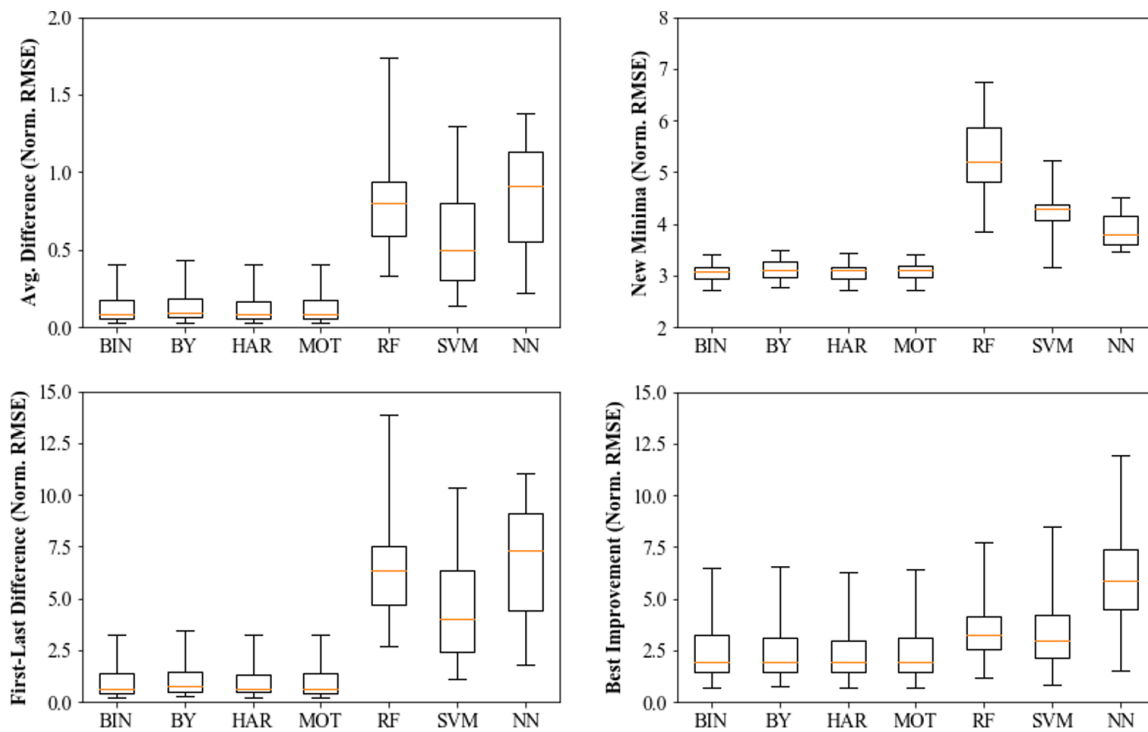
Figure 5.15: Normalized RMSE learning metrics of interest for increasing training set length – Top left: average difference between iterations; Bottom left: difference between first (10% training data) and last (90% training data) iterations; Top right: new minima; Bottom right: best improvement in consecutive iterations.

By all metrics analyzed, machine learning models reduce test error much more effectively than analytical models with increasing training set size. Additional learning information is obtained by examining which iteration experienced the biggest error improvement and the total percentage of new minima:

Table 5.19: Best improvement iteration and new minimum percentage according to absolute error and normalized RMSE.

ROP Model	Best Improvement Iteration		New Minimum Percentage	
	Absolute Error	Norm. RMSE	Absolute Error	Norm. RMSE
Bingham (1964)	5.17	5.43	32.77%	38.26%
Modified Bourgoyne & Young	5.15	5.41	33.61%	38.95%
Hareland and Rampersad (1994)	5.20	5.44	32.89%	38.45%
Motahhari *et al*. (2010)	5.19	5.43	32.89%	38.53%
Random Forests	3.26	3.54	67.95%	66.04%
Support Vector Machines	3.79	3.77	52.49%	52.95%
Neural Networks	3.48	3.37	46.28%	48.76%

New minimum percentage is given by the overall ratio of iterations attaining a new minimum error value out of eight possibilities in each formation. ML models achieve the biggest error drop in the third or fourth iterations (out of nine) on average, demonstrating that their capability of repeatedly reaching new minima is not hampered by faster improvement with additional training data.

The incremental training data availability experiment in this section demonstrated that, by all learning metrics introduced, machine learning models are able to reduce test error more effectively than analytical models as more data are acquired. This outcome is important for real-time drilling optimization, proving that machine learning models become more reliable for ROP prediction as more data are collected in a given formation. Based on these results, analytical ROP models are expected to be more relevant as drilling begins in a new formation and ML models should become more accurate once enough meaningful data becomes available.

Chapter 6: Lithology-Dependent Real-Time Drilling Interval Optimization with Continuous Model Learning

Previous drilling optimization studies published in the literature generally fit ROP models to offset well data and, subsequently, optimize drilling operational parameters for another well based on the predicted ROP. This type of post-drilling analysis, conducted in Chapter 5, does not take advantage of data constantly collected in real-time as the well is drilled. Results in Sections 5.5 and 5.6 established that cross-validation of the seven ROP models analyzed and optimization of drilling parameters with the best performing model last between 22 and 100 seconds, indicating this process is not computationally prohibitive in real-time. Furthermore, Section 5.7 proved that ROP models, particularly ML algorithms, can significantly reduce test error when trained with a higher volume of data. In real-time, ROP models can evolve and adapt as more data become available by being retrained in intervals. This concept of continuous model learning is introduced in this chapter. Model performance is scrutinized with respect to retraining interval length and cross-validation is evaluated as a methodology to select the best ROP model to optimize operational parameters for the next drilling interval.

6.1. MODEL RETRAINING IN REAL-TIME

The customary lithology-dependent post-drilling optimization of operational parameters was investigated in the preceding chapter. Post-drilling analysis is typically performed to obtain insights from a previously drilled well and improve drilling performance for a future well in the same region. Respecting the classical lithology dependency of ROP models, all the data collected during drilling of one rock formation are employed in training a model capable of predicting ROP in the formation in question:
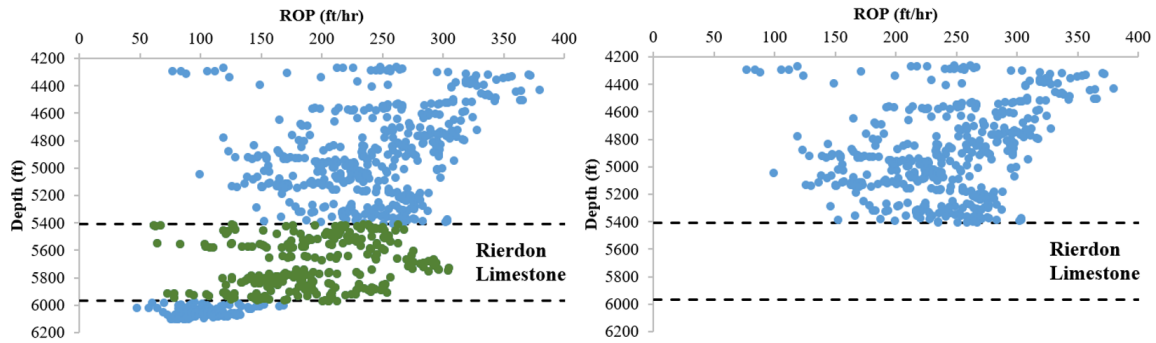
Figure 6.1: Post-drilling formation-dependent model training and subsequent parameter optimization for drilling the Rierdon Limestone formation in a new well.

Black dashed lines in Fig. 6.1 illustrate formation boundaries for the Rierdon Limestone formation. Data measured when drilling a well through this formation (left plot, green data) are utilized to fit a ROP model. This model is then employed in determining optimal drilling parameters for drilling the Rierdon Limestone formation in an upcoming nearby well (right-hand plot). Ambrus *et al*. (2017) advise caution against relying on optimal drilling parameters derived in such context, stating that post-well parameters should be used as a starting reference but must adjust to insights obtained from real-time data.

Real-time continuous model learning is accomplished by dividing formation data in intervals:
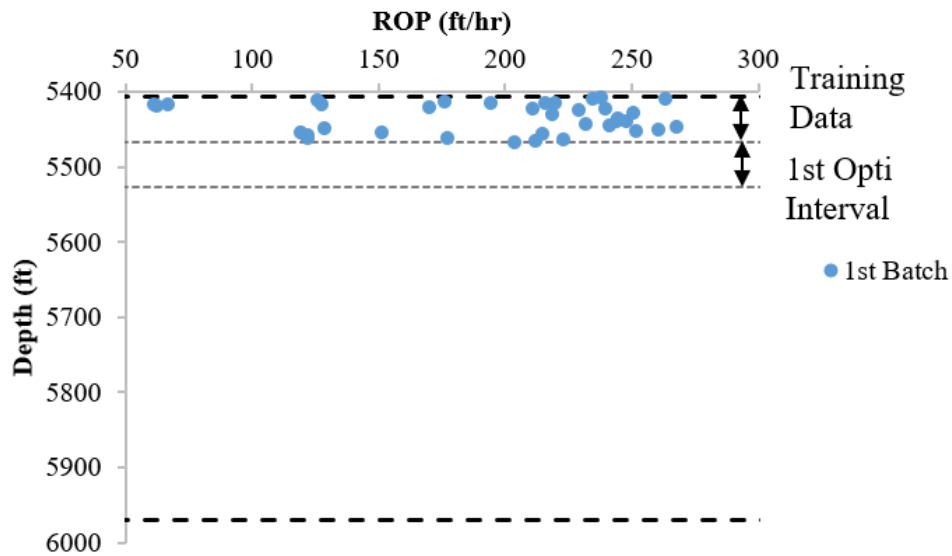
Figure 6.2: First optimization interval in drilling a new formation (Rierdon Limestone).

Conforming to the traditional ROP modeling lithology dependency assumption, model training begins after the first batch of data is collected in a newly-drilled formation. ROP models are fitted to this data and the best performing model is employed in optimizing drilling parameters for the first optimization interval, delineated by the thinner black dashed lines in the figure above. Once the second interval (first optimization interval) is drilled, data measured in both intervals are used to retrain ROP models. Optimal drilling parameters for the following interval (second optimization interval) are determined by the most accurate ROP model fitted with the first two batches of data. This procedure is repeated with continuous model retraining at the end of each drilled interval until the lower boundary of the formation is reached:
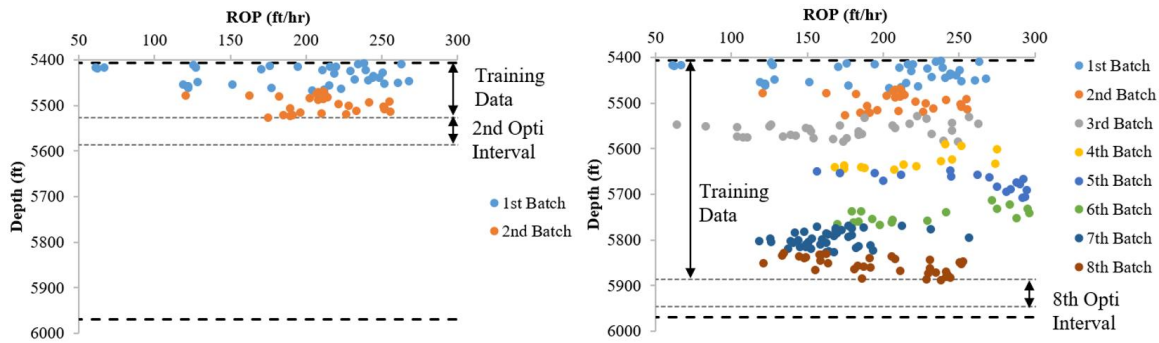
Figure 6.3: 60ft drilling optimization intervals in the 566ft-long Rierdon Limestone formation.

In Fig 6.3, the 566ft-long Rierdon Limestone formation is divided into nine 60ft intervals and one 26ft interval. After every 60ft, ROP models are retrained with the batches of data available up to that point and utilized in optimizing drilling parameters for the next interval.

In theory, given enough computational power, ROP models could be retrained after every foot to select the best operational variables to drill the next foot of rock. However, in practice, it would be unrealistic to adjust drilling parameters this often. A more reasonable and natural approach is characterized by optimizing parameters at the beginning of drilling each drillpipe stand (~90ft). During pipe connections, mud circulation and drillstring rotation are interrupted. Once drilling resumes, operational parameters can be brought up to the desired levels. Although this tactic makes sense operationally, thinner formations may present a challenge. Table 4.2 shows that three formations in the Williston Basin dataset span a vertical section under 90ft in length. These formations would be completely ignored from an optimization standpoint with model retraining every 90ft. An additional issue arises if drilling slowly, as a 90ft optimization interval may encompass hours of sub-optimal drilling.

The length of a range 2 drillpipe joint (~30ft) establishes a good starting point for optimization interval demarcation, which can then be shortened or lengthened according

156

to necessity. Optimization interval length dictates how often ROP models are retrained. Drilling optimization and model retraining intervals can be stipulated by length (Figure 6.3), by number of data points acquired, or by time elapsed (for time-based data). For this Williston Basin depth-based dataset, model prediction accuracy is analyzed with respect to retraining intervals defined by varying depth length and number data points in Section 6.3.

6.2. CONTINUOUS LEARNING REAL-TIME DRILLING INTERVAL OPTIMIZATION WORKFLOW

The concept of optimizing drilling in intervals is not new. Drilling engineers typically provide field personnel with a drilling roadmap containing operational parameter setpoints to be enforced by the (auto)driller at different depth intervals. These setpoints are derived from previous experience in the region and drilling models. Bentsen and Wilson (1976, 1977) discuss point, interval and multi-interval techniques in optimizing WOB and RPM, emphasizing that the entire drilling process must be considered by optimization strategies. Nygaard *et al*. (2002) perform optimization of drilling parameters in lithology intervals, some of them 500ft long. Many other studies conducting drilling optimization in intervals can be cited. Nevertheless, their approaches rely on a model trained with historical offset well data, incapable of adapting to data acquired in real-time. Drilling heat maps have recently been introduced as real-time adaptive modeling techniques to optimize drilling. ExxonMobil's DAS drilling response surface (Fig 1.3), first presented by Payette *et al.* (2015), and the drilling efficiency parameter described by Ambrus *et al*. (2017) both optimize WOB and RPM with ROP heat maps that can adjust to real-time data. However, these models are only retrained when drilling dysfunctions or changes in drilling conditions occur, at which point entirely new model calibrations are required.

Continuous model learning, proposed in Section 6.1, constantly retrains several ROP models in intervals of specified length and optimizes drilling parameters for the next interval according to the most accurate model. In real-time, the data required to evaluate model performance in an optimized interval is only available after said interval has already been drilled. Therefore, the strategy suggested here chooses the most accurate ROP model for optimization at each interval based on the CV error with batches of data already collected, simulating a real-time model selection scenario. Complying with formation-dependent ROP models, the continuous learning real-time drilling interval optimization workflow presented in this chapter can be summarized as follows:

1) Collect first batch of data while drilling in the beginning interval of a new formation
2) Set first batch of data as the training data for ROP modeling
3) Perform 10-fold cross-validation on training data for seven ROP models
    a. Analytical: Bingham (1964), modified Bourgoyne and Young, corrected Hareland and Rampersad (1994) and Motahhari *et al.* (2010). Model formulations can be found in Section 2.3. Analytical model fitting is accomplished by the trust region reflective algorithm in Python's *scipy.optimize* (Oliphant, 2007) library
    b. Machine learning: random forests (Breiman, 2001), support vector regression machines (Drucker *et al.*, 1996) and neural networks (McCulloch and Pitts, 1943) implementations in Python's *scikit-learn* (Pedregosa *et al.*, 2011) package. ML models are trained with depth, WOB, RPM and flow rate as inputs (Section 5.1). Optimal hyperparameters provided in Table 5.5
4) Select the most accurate ROP model according to CV error and train it with all training data (following instructions in Steps 3.a or 3.b)

158

5) Optimize drilling parameters conforming to constraints established in Table 4.4 for the next optimization interval with the ROP model obtained in Step 4. Optimization method is dependent on the type of ROP model from Step 4

   a. Analytical ROP models: SLSQP algorithm in Python's *scipy.optimize* (Oliphant, 2007) library

   b. RF ROP model: PSO algorithm in Python's *pyswarm* (Lee and Castillo-Hair, 2013) package with a swarm of 50 particles and 10 maximum iterations

   c. SVM or NN ROP model: PSO algorithm in Python's *pyswarm* (Lee and Castillo-Hair, 2013) package with a swarm of 50 particles and 300 maximum iterations

6) Aggregate data collected during drilling the optimized interval to training dataset

7) Repeat steps 3-6 until drilling reaches the end of the formation

The optimization workflow described above is repeated for all formations in the Williston Basin dataset (Table 4.2) with a specified optimization and model retraining interval length.

Data collected during drilling an optimized interval are defined as the test data. Even though such data is not actually available for decision making in real-time, test data provide many insights on model performance. For performance evaluation purposes, all seven ROP models are trained with all training data (in Step 4 above). These models' errors on test data are recorded and three key performance metrics are established:

- Test errors for the most accurate ROP model according to CV on training data at each optimization interval are stored in a "best by cross validation" metric

- Test errors for the most accurate ROP model according to test data at each optimization interval are stored in a "best by test error" metric

- Percentage of optimization intervals in which the "best by cross validation" model is the same as the "best by test error" model is stored in a "best CV/test error agreement" metric

Averages of the first two metrics are compared to determine the test data performance gap between the collection of models selected by CV on training data in each interval and the (unattainable in real-time) collection of models that would have been selected in each interval if test data were available ahead of the interval's drilling. The third metric assesses how often CV was successful in choosing the model with best performance on test data based solely on training data.

According to Sections 5.5 and 5.6, the time required to execute the optimization workflow above for each optimization interval (Steps 3-6) varies between a minimum of 22 seconds (if an analytical ROP model is chosen in Step 4) and a maximum of one minute and 40 seconds (if the RF ROP model is chosen in Step 4). The table below analyzes drilling time in individual intervals for real-time considerations:

Table 6.1: Time spent drilling intervals of different lengths at varying speeds.

Time Spent Drilling Interval of Length L at Speed ROP (min)						
ROP \ L	10ft	20ft	30ft	60ft	90ft	120ft
300ft/hr	2	4	6	12	18	24
250ft/hr	2.4	4.8	7.2	14.4	21.6	28.8
200ft/hr	3	6	9	18	27	36
150ft/hr	4	8	12	24	36	48
100ft/hr	6	12	18	36	54	72
80ft/hr	7.5	15	22.5	45	67.5	90
60ft/hr	10	20	30	60	90	120
40ft/hr	15	30	45	90	135	180
20ft/hr	30	60	90	180	270	360

Suppose the bit is drilling ahead at 200ft/hr and parameter optimization is performed every 10ft. Even in this unlikely scenario of adjusting drilling parameters every three minutes, optimal operational parameters determined by the real-time drilling interval optimization workflow can always be applied in the last one minute and twenty seconds of interval drilling. The average on-bottom ROP for the Williston Basin dataset was 73.1ft/hr. Rounding this value up to 80ft/hr and using the reference 30ft optimization interval definition, about 21 out of 22.5 interval minutes will be drilled optimally in the slowest computational case.

6.3. RETRAINING INTERVAL ANALYSIS

6.3.1. Optimization Interval Length

Model performance variation with respect to optimization interval length is scrutinized in a continuous learning setting. Models are trained with the data available up to a certain point in a formation and tested on the following interval to be optimized. Boxplots in this section are interpreted in the same manner as CV error boxplots in Section 5.5, with formation errors determined by the average of errors in all intervals within a

161

formation. Starting with a retraining segment defined by the typical range 2 drillpipe joint length of 30ft:
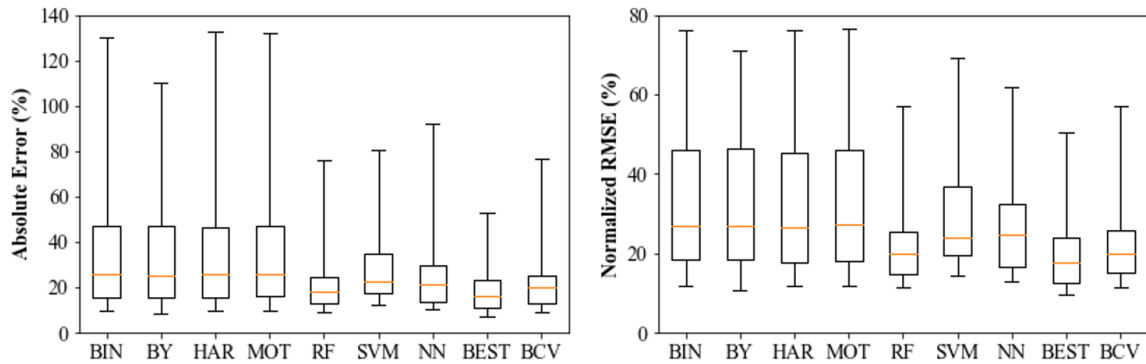
Figure 6.4: ROP model performance with 30ft retraining intervals in nineteen rock formations.

In Figure 6.4, "BEST" (or "best by test error") represents formation errors obtained by combining models with the highest ROP prediction accuracy (lowest test error) in each interval and "BCV" (or "best by cross validation") represents the formation errors of the best model combination according to cross-validation error on the training data, indicative of a realistic model selection scenario in real-time. The "BEST" benchmark is displayed for comparison purposes, as the data required to validate this model selection is not available until after the interval is drilled. Note that model performance difference between analytical and machine learning ROP models is not as accentuated as in Fig. 5.1, where models were trained with all formation data. Shortening model retraining interval to 20ft:
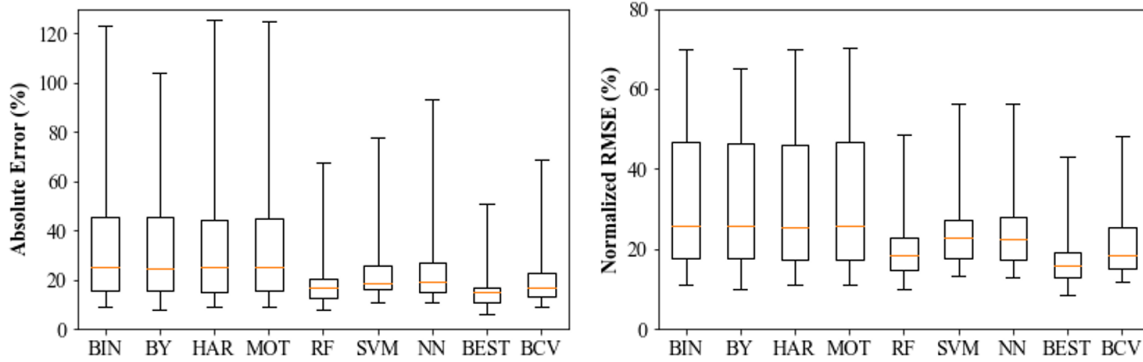
Figure 6.5: ROP model performance with 20ft retraining intervals in nineteen rock formations.

Comparing Figures 6.4 and 6.5, formation errors for all models are lower with shorter retraining intervals. By retraining models in even shorter intervals of 10ft:
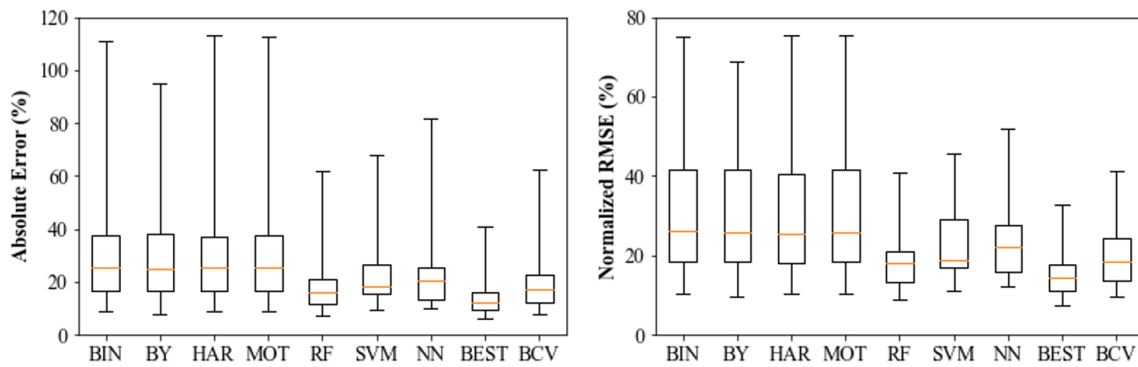
Figure 6.6: ROP model performance with 10ft retraining intervals in nineteen rock formations.

Lower median (orange line) and 75th percentile (top of the boxes) errors are again observed, suggesting a trend of decreasing error as models are retrained more often. This trend is evidenced when contrasting error metrics for optimal model combinations selected by cross-validation training error and by test error:

Table 6.2: Test error for best models picked by cross-validation on the training data and best models picked by test error at every retraining interval. Intervals defined by depth lengths of 30ft, 20ft and 10ft.

Best Optimization Model - 30ft Retraining Intervals				
ROP Model	Best by Cross Validation		Best by Test Error	
Error Metric	Absolute Error	Norm. RMSE	Absolute Error	Norm. RMSE
Average	24.20	24.06	19.44	20.30
Weighted by Points	25.78	23.83	20.18	20.19
Weighted by Length	24.38	23.01	19.18	19.57
Best Optimization Model - 20ft Retraining Intervals				
ROP Model	Best by Cross Validation		Best by Test Error	
Error Metric	Absolute Error	Norm. RMSE	Absolute Error	Norm. RMSE
Average	21.70	21.43	17.43	18.38
Weighted by Points	23.58	21.27	18.66	18.53
Weighted by Length	22.40	20.78	17.82	17.97
Best Optimization Model - 10ft Retraining Intervals				
ROP Model	Best by Cross Validation		Best by Test Error	
Error Metric	Absolute Error	Norm. RMSE	Absolute Error	Norm. RMSE
Average	20.68	20.32	15.40	16.21
Weighted by Points	22.07	20.55	16.26	16.68
Weighted by Length	20.77	19.73	15.45	15.98

Performance differences of 3-6% are experienced when predicting ROP with models selected by cross-validation on the training data as opposed to the unattainable best test error models. Analyzing how often each model was chosen by these two criteria:

Table 6.3: Model selection percentages by cross-validation error and test error according to retraining interval length.

Best Optimization Model - 30ft Retraining Intervals				
ROP Model	**CV Abs. Error**	**CV Norm. RMSE**	**Abs. Error**	**Norm. RMSE**
Bingham (1964)	0.00%	0.00%	2.03%	1.35%
Modified B&Y	0.00%	0.00%	7.43%	3.38%
Hareland and Rampersad (1994)	1.35%	1.35%	6.08%	9.46%
Motahhari *et al*. (2010)	0.00%	0.00%	0.00%	2.03%
Random Forests	85.81%	87.84%	44.59%	47.97%
Support Vector Machines	10.81%	10.14%	17.57%	15.54%
Neural Networks	2.03%	0.68%	22.30%	20.27%
Best CV / Test Error Agreement			**43.02%**	**45.27%**
Best Optimization Model - 20ft Retraining Intervals				
ROP Model	**CV Abs. Error**	**CV Norm. RMSE**	**Abs. Error**	**Norm. RMSE**
Bingham (1964)	0.00%	0.00%	3.10%	2.21%
Modified B&Y	0.00%	0.00%	4.87%	2.65%
Hareland and Rampersad (1994)	1.77%	1.33%	6.64%	7.96%
Motahhari *et al*. (2010)	0.00%	0.00%	1.33%	1.77%
Random Forests	85.40%	87.17%	52.65%	52.21%
Support Vector Machines	11.50%	11.06%	15.93%	15.49%
Neural Networks	1.33%	0.44%	15.49%	17.70%
Best CV / Test Error Agreement			**50.44%**	**52.21%**
Best Optimization Model - 10ft Retraining Intervals				
ROP Model	**CV Abs. Error**	**CV Norm. RMSE**	**Abs. Error**	**Norm. RMSE**
Bingham (1964)	0.00%	0.00%	3.11%	2.44%
Modified B&Y	0.00%	0.00%	6.00%	6.44%
Hareland and Rampersad (1994)	1.33%	1.11%	4.89%	7.56%
Motahhari *et al*. (2010)	0.00%	0.00%	1.56%	1.11%
Random Forests	85.11%	86.44%	44.00%	43.56%
Support Vector Machines	11.56%	11.78%	18.44%	18.67%
Neural Networks	2.00%	0.67%	22.00%	20.22%
Best CV / Test Error Agreement			**42.67%**	**42.00%**

The "Best CV / Test Error Agreement" metric reveals the frequency of optimization intervals where the model selected by cross-validation on the training data matched the model with highest prediction accuracy. Table 6.3 indicates that irrespective of retraining interval length, the random forests algorithm dominated performance according to cross-validation on the training data and, to a lesser extent, exhibited higher accuracy on test data.

Changing retraining interval definition to data points instead of depth length, investigation begins by retraining models after every 30 measured data points. Then,

retraining intervals are shortened to every 20 points collected and, subsequently, 10 data points. Figures and tables similar to Figs. 6.4-6.6 and Tables 6.2 and 6.3 are reproduced below:
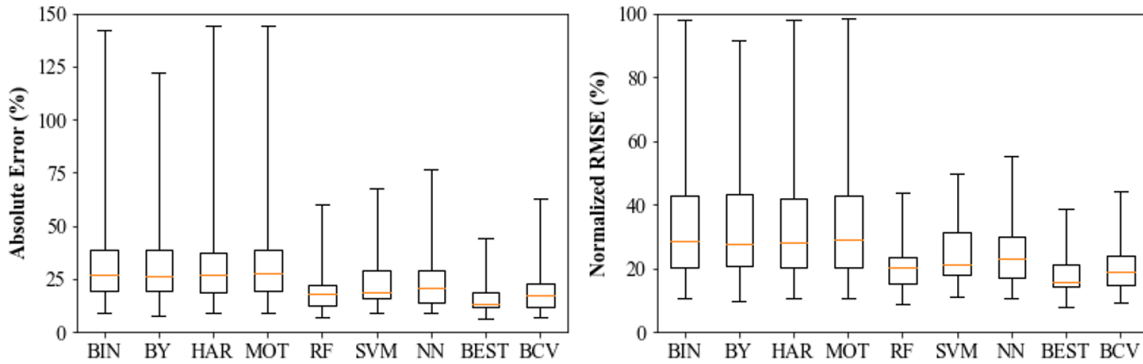
Figure 6.7: ROP model performance with retraining intervals defined by 30 data points in nineteen rock formations.
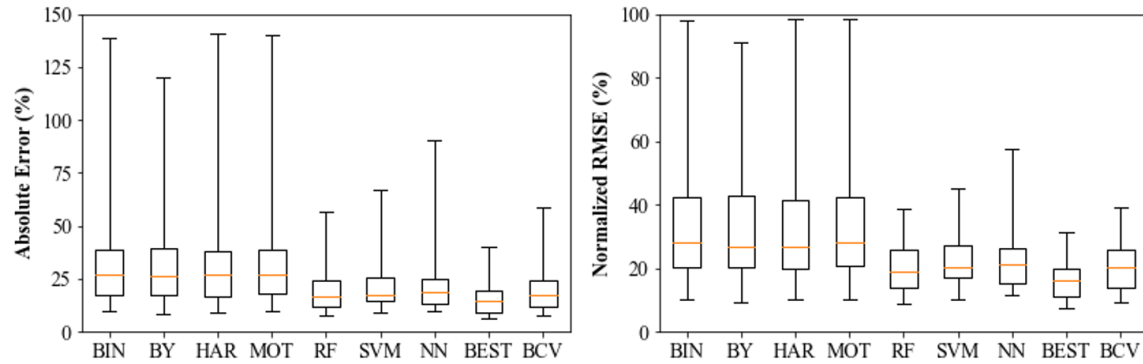
Figure 6.8: ROP model performance with retraining intervals defined by 20 data points in nineteen rock formations.
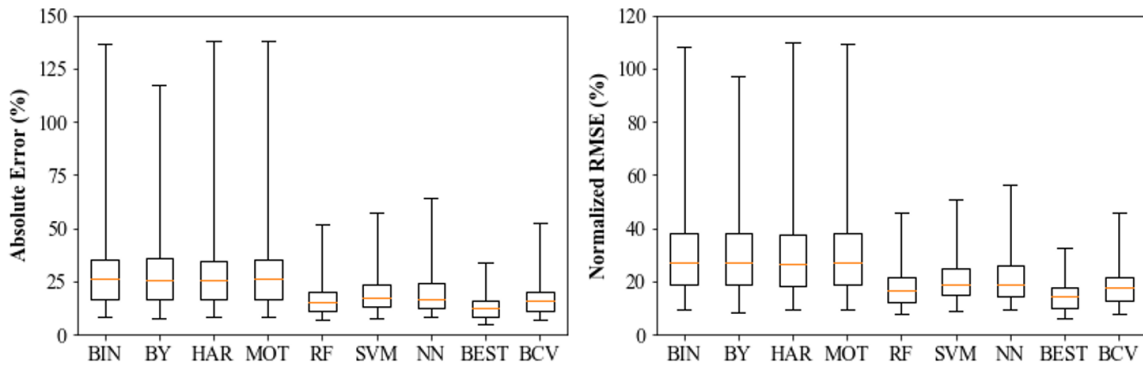
Figure 6.9: ROP model performance with retraining intervals defined by 10 data points in nineteen rock formations.

Table 6.4: Test error for best models picked by cross-validation on the training data and best models picked by test error at every retraining interval. Intervals defined by number of data points collected: 30pts, 20pts and 10pts.

Best Optimization Model - 30pts Retraining Intervals				
ROP Model	**Best by Cross Validation**		**Best by Test Error**	
Error Metric	**Absolute Error**	**Norm. RMSE**	**Absolute Error**	**Norm. RMSE**
Average	19.74	20.42	16.27	17.98
Weighted by Points	21.20	20.65	16.99	18.15
Weighted by Length	21.52	21.39	17.64	19.05
Best Optimization Model - 20pts Retraining Intervals				
ROP Model	**Best by Cross Validation**		**Best by Test Error**	
Error Metric	**Absolute Error**	**Norm. RMSE**	**Absolute Error**	**Norm. RMSE**
Average	20.11	20.61	15.80	16.95
Weighted by Points	20.72	19.91	16.16	16.60
Weighted by Length	21.58	21.31	17.12	17.79
Best Optimization Model - 10pts Retraining Intervals				
ROP Model	**Best by Cross Validation**		**Best by Test Error**	
Error Metric	**Absolute Error**	**Norm. RMSE**	**Absolute Error**	**Norm. RMSE**
Average	17.78	18.68	13.65	14.90
Weighted by Points	18.71	19.11	13.92	15.03
Weighted by Length	19.21	19.86	14.68	15.93

167

Table 6.5: Model selection percentages by cross-validation error and test error according to number of data points in retraining interval.

Best Optimization Model - 30pts Retraining Intervals				
ROP Model	CV Abs. Error	CV Norm. RMSE	Abs. Error	Norm. RMSE
Bingham (1964)	0.00%	0.00%	1.78%	0.44%
Modified B&Y	0.00%	0.00%	4.00%	5.78%
Hareland and Rampersad (1994)	0.00%	0.00%	7.56%	6.67%
Motahhari et al. (2010)	0.00%	0.00%	1.78%	0.89%
Random Forests	91.56%	92.44%	47.11%	48.89%
Support Vector Machines	7.11%	7.11%	15.56%	14.67%
Neural Networks	1.33%	0.44%	22.22%	22.67%
Best CV / Test Error Agreement			**44.89%**	**46.22%**
Best Optimization Model - 20pts Retraining Intervals				
ROP Model	CV Abs. Error	CV Norm. RMSE	Abs. Error	Norm. RMSE
Bingham (1964)	0.00%	0.00%	1.74%	0.29%
Modified B&Y	0.00%	0.00%	4.65%	5.81%
Hareland and Rampersad (1994)	0.00%	0.00%	6.10%	6.98%
Motahhari et al. (2010)	0.00%	0.00%	1.74%	0.58%
Random Forests	90.12%	91.28%	45.93%	45.93%
Support Vector Machines	7.27%	7.56%	19.48%	19.19%
Neural Networks	2.62%	1.16%	20.35%	21.22%
Best CV / Test Error Agreement			**44.19%**	**43.61%**
Best Optimization Model - 10pts Retraining Intervals				
ROP Model	CV Abs. Error	CV Norm. RMSE	Abs. Error	Norm. RMSE
Bingham (1964)	0.00%	0.00%	1.00%	0.72%
Modified B&Y	0.00%	0.00%	5.16%	5.60%
Hareland and Rampersad (1994)	0.29%	0.29%	5.45%	6.03%
Motahhari et al. (2010)	0.00%	0.00%	1.00%	1.00%
Random Forests	89.24%	90.53%	43.76%	44.76%
Support Vector Machines	8.03%	7.89%	22.81%	22.24%
Neural Networks	2.44%	1.29%	20.80%	19.66%
Best CV / Test Error Agreement			**42.75%**	**42.47%**

Once again, model performance improves by retraining models more frequently and the random forests algorithm paces cross-validated error performance.

Results in this section show that, regardless of whether retraining intervals are defined by length or number of data points, ROP prediction accuracy improves for all models as retraining intervals are shortened. This outcome justifies the concept of continuous model learning, since better predictive performance is observed with models that adapt more frequently to real-time data. For the remainder of this dissertation, a

standard model retraining (and optimization) length of 30ft is established in a compromise between model accuracy and field applicability.

Best performing model selection remains very similar throughout the experiments, with no discernible patterns due to interval lengths or number of points. According to cross-validation on the training data, random forests models are the most accurate in 85-90% of intervals, while analytical models are rarely present in that category. Therefore, agreement between best performing models selected by cross-validation on the training data and by test data is correlated to the number of intervals where RF models are the most accurate on test data. The 42-50% agreement proportion is considerably better than picking one out of the seven models at random (14.3%) and could be improved by reducing the number of models considered. Still, the discrepancy between the frequency at which random forests models perform best according to CV and on test data is puzzling. A possible explanation is that NN models, which are not selected by cross-validation on training data often, performs marginally better than RF on test data in a significant number of intervals. Another reasonable justification for the CV/test error model selection differences is poor data quality. Test error is highly dependent on the few data points in an optimization interval, and an argument can be made that the cross-validation error on training data is a better indicator of a model's generalization capability. Nevertheless, the collection of models chosen by cross-validation displayed only 3-6% lower accuracy than the unattainable best by test error benchmark, justifying application of this methodology for model selection in real-time.

6.3.2. 1st Optimization Interval

ROP modeling lithology dependency is a major limiter to the continuous learning drilling optimization workflow established in Section 6.2. Since models are fitted with data

specific to a formation, training data are scarce in the first few optimization intervals of a newly drilled formation. Learning metrics introduced in Section 5.7 demonstrated that ML ROP models are much more effective than analytical models in becoming more accurate with incremental data availability. Based on these two observations and intuition that ML models require a substantial amount of data to produce accurate predictions, analytical ROP models are expected to perform better than ML models in the beginning optimization intervals of a formation. Once enough meaningful formation data are collected, ML models should outpace analytical models. Model performance in the first optimization interval of each formation was analyzed to test this hypothesis:

Table 6.6: Best ROP models by absolute error in first optimization intervals of each formation.

Absolute Error	Best Model in 1st Optimization Interval					
	Depth Length			Data Points		
ROP Model	30ft	20ft	10ft	30pts	20pts	10pts
Bingham (1964)	0	2	0	1	0	0
Modified B&Y	0	1	0	0	0	0
Hareland and Rampersad (1994)	2	4	2	0	2	1
Motahhari *et al.* (2010)	0	0	0	0	0	1
Analytical ROP Models Sum	2	7	2	1	2	2
Random Forests	8	8	8	7	6	6
Support Vector Machines	2	2	2	5	2	4
Neural Networks	7	2	7	6	9	7
ML ROP Models Sum	17	12	17	18	17	17

Table 6.7: Best ROP models by normalized RMSE in first optimization intervals of each formation.

Normalized RMSE	Best Model in 1st Optimization Interval					
	Depth Length			Data Points		
ROP Model	30ft	20ft	10ft	30pts	20pts	10pts
Bingham (1964)	0	1	0	0	0	0
Modified B&Y	0	1	0	1	1	0
Hareland and Rampersad (1994)	2	3	4	0	1	1
Motahhari *et al*. (2010)	0	0	0	0	0	1
Analytical ROP Models Sum	2	5	4	1	2	2
Random Forests	9	7	6	10	6	6
Support Vector Machines	3	3	4	2	2	6
Neural Networks	5	4	5	6	9	5
ML ROP Models Sum	17	14	15	18	17	17

Tables 6.6 and 6.7 display the amount of first formation intervals (out of 19 formations) in which each ROP model was selected as the best performing model. Contrary to intuition, ML ROP models vastly outperformed analytical models in formations' first optimization intervals according to both absolute error and normalized RMSE. Even when only ten data points were used in model training, analytical ROP models produced the lowest error in only two out of nineteen first formation intervals. Referring to Tables 6.3 and 6.5, analytical models were selected as the best performing model according to test error in about 15% of optimization intervals for all interval specifications. Nonetheless, those selections happened sparingly throughout the formations, instead of concentrating in the first few optimization intervals as originally conceived.

6.3.3. 0th Optimization Interval

When the bit is drilling ahead and a formation boundary is reached, the lithology-dependent real-time drilling interval optimization workflow proposed in Section 6.2 requires training of a new ROP model. In such lithology transition zones, drilling is sub-optimal, as the first batch of data is collected in the beginning drilling interval of a new

formation and no optimization occurs. This non-optimized starting formation interval is defined here as the "0th optimization interval". Without optimization of operational parameters, 0th optimization intervals of all formations are the drilling segments most likely to develop to drilling inefficiencies. In practice, this lack of optimization would result in maintaining the same drilling parameters utilized in the previous formation or adhering to parameters prescribed in the drilling roadmap.

In this section, ROP modeling lithology dependency is questioned by evaluating the 0th optimization interval performance of ROP models trained with data collected in the preceding formation. This metric is compared to average errors for models trained with actual formation data in the subsequent formation intervals, analyzing if the violation of the historical lithology dependence of ROP models results in loss of accuracy. The standard 30ft-long retraining interval definition (Section 6.3.1) is used, thus models fitted with data from a previous formation must predict ROP for the initial 30ft (0th optimization interval) of each formation. Greenhorn Limestone, the first formation in Table 4.2, is not analyzed since there are no data from preceding formations available.

Beginning with analytical ROP models' performance:

Table 6.8: Analytical ROP modeling average absolute error in formation intervals and 0th optimization interval modeled with data from previous formation.

Absolute Error (%)	Bingham		Mod. B&Y		Hareland		Motahhari	
Rock Formations	Form. Avg.	0th Opti.	Form. Avg.	0th Opti.	Form. Avg.	0th Opti.	Form. Avg.	0th Opti.
Newcastle Sandstone	17.96	16.82	17.26	16.94	15.61	16.81	16.64	16.81
Dakota Sandstone	20.37	26.13	18.43	25.59	19.33	18.87	20.35	18.87
Swift Shale	27.63	9.17	27.70	12.49	27.02	9.17	27.63	9.17
Rierdon Limestone	26.41	65.36	25.14	64.73	26.02	64.73	26.49	65.36
Piper Limestone	25.61	73.34	25.63	57.37	25.42	73.34	25.74	73.34
Spearfish Sandstone	15.18	20.04	15.65	19.62	15.26	19.59	15.49	19.59
Pine Salt Sandstone	132.30	19.75	111.68	19.77	135.12	19.75	134.45	19.75
Broom Creek Sandstone	55.20	40.50	55.18	40.07	54.95	40.50	55.63	40.50
Tyler Sandstone	60.25	44.06	56.80	46.75	59.66	44.06	60.27	44.06
Kibbey Lime Limestone	13.10	75.98	12.18	65.91	12.03	73.42	12.15	73.42
Kibbey Lime Shale	11.64	18.62	11.45	18.08	11.54	18.05	11.60	18.05
Charles Sandstone	57.72	18.96	69.75	19.93	57.36	18.97	57.79	18.97
Charles Limestone	27.73	33.62	27.55	33.83	27.62	33.59	27.80	33.59
Ratcliffe Sandstone	38.98	25.07	39.00	25.06	38.10	25.07	38.89	25.07
Base Last Salt Limestone	56.86	63.34	59.90	63.51	55.91	63.51	56.86	63.51
Base Last Salt Sandstone	13.06	54.99	13.01	55.65	12.96	55.29	13.06	55.29
Mission Canyon Limestone	13.54	12.33	13.76	13.36	13.46	12.33	13.54	12.33
Lodgepole Limestone	8.71	14.98	7.54	14.93	8.67	14.98	8.71	14.98
Average	**34.57**	**35.17**	**33.76**	**34.09**	**34.22**	**34.56**	**34.62**	**34.59**

Table 6.9: Analytical ROP modeling average normalized RMSE in formation intervals and 0th optimization interval modeled with data from previous formation.

Normalized RMSE (%)	Bingham		Mod. B&Y		Hareland		Motahhari	
Rock Formations	Form. Avg.	0th Opti.	Form. Avg.	0th Opti.	Form. Avg.	0th Opti.	Form. Avg.	0th Opti.
Newcastle Sandstone	19.61	17.42	19.01	17.52	16.94	17.39	18.11	17.39
Dakota Sandstone	22.04	28.54	20.53	28.06	20.95	21.94	22.02	21.94
Swift Shale	30.89	11.50	30.99	14.59	30.22	11.49	30.89	11.49
Rierdon Limestone	27.21	62.12	26.65	61.52	26.75	61.52	27.26	62.12
Piper Limestone	26.99	66.46	27.08	52.86	26.78	66.46	27.08	66.46
Spearfish Sandstone	17.12	27.97	17.62	27.27	17.16	27.24	17.41	27.24
Pine Salt Sandstone	77.42	23.31	72.02	23.33	77.56	23.31	77.76	23.31
Broom Creek Sandstone	48.92	40.51	49.75	41.07	48.42	40.51	49.07	40.51
Tyler Sandstone	54.43	46.37	51.49	48.92	53.85	46.37	54.44	46.37
Kibbey Lime Limestone	13.44	74.80	12.37	65.17	12.23	72.04	12.35	72.04
Kibbey Lime Shale	13.21	21.76	13.01	21.00	13.10	20.98	13.18	20.98
Charles Sandstone	60.57	28.36	60.99	29.28	60.15	28.35	60.59	28.35
Charles Limestone	30.79	34.60	30.63	35.02	30.67	34.62	30.86	34.62
Ratcliffe Sandstone	42.74	38.06	42.74	38.06	41.82	38.06	42.65	38.06
Base Last Salt Limestone	62.28	63.00	60.90	63.19	61.34	63.19	62.28	63.19
Base Last Salt Sandstone	15.25	54.66	15.36	55.30	15.14	54.96	15.25	54.96
Mission Canyon Limestone	16.82	21.13	17.34	21.95	16.71	21.13	16.82	21.13
Lodgepole Limestone	10.82	15.64	9.83	15.60	10.77	15.64	10.82	15.64
Average	**32.81**	**37.57**	**32.13**	**36.65**	**32.25**	**36.96**	**32.71**	**36.99**

Analytical ROP models exhibit lower absolute error and normalized RMSE in the 0th optimization interval (with data from previous formation) than in formation intervals (with data from the actual formation) for only a small number of formations. There are no identifiable patterns with formation depth or thickness. For the majority of formations, and according to overall average error, the lithology dependence assumption is justified for analytical ROP models.

Repeating the same experiment with machine learning ROP models:

Table 6.10: ML ROP modeling average absolute error in formation intervals and 0th optimization interval modeled with data from previous formation.

Absolute Error (%)	Random Forests		Support Vector		Neural Networks	
Rock Formations	Form. Avg.	0th Opti.	Form. Avg.	0th Opti.	Form. Avg.	0th Opti.
Newcastle Sandstone	14.72	10.83	17.98	19.53	19.39	7.93
Dakota Sandstone	13.81	7.76	14.11	7.88	15.95	8.74
Swift Shale	13.30	12.35	12.86	8.92	14.34	10.64
Rierdon Limestone	20.73	15.48	25.41	16.59	25.75	22.03
Piper Limestone	31.30	69.35	29.94	50.83	28.92	65.54
Spearfish Sandstone	11.87	19.31	13.17	12.50	12.50	18.76
Pine Salt Sandstone	81.71	13.14	82.13	13.00	108.79	19.75
Broom Creek Sandstone	26.94	31.95	33.03	33.63	38.02	39.38
Tyler Sandstone	22.56	7.92	32.03	16.38	29.00	17.93
Kibbey Lime Limestone	12.68	16.77	31.77	44.47	22.74	25.26
Kibbey Lime Shale	12.05	15.46	22.24	32.65	12.26	12.81
Charles Sandstone	58.14	13.21	55.18	14.57	72.24	14.96
Charles Limestone	32.17	30.53	37.93	95.65	28.59	44.60
Ratcliffe Sandstone	19.69	21.42	19.02	34.16	17.08	22.82
Base Last Salt Limestone	31.14	25.67	41.01	48.61	29.55	57.75
Base Last Salt Sandstone	8.04	11.80	13.94	12.44	10.91	15.61
Mission Canyon Limestone	12.56	15.57	14.75	13.00	14.02	12.59
Lodgepole Limestone	8.22	6.36	11.45	5.60	6.53	7.49
Average	23.98	19.16	28.22	26.69	28.14	23.59

Table 6.11: ML ROP modeling average normalized RMSE in formation intervals and 0th optimization interval modeled with data from previous formation.

Normalized RMSE (%)	Random Forests		Support Vector		Neural Networks	
Rock Formations	Form. Avg.	0th Opti.	Form. Avg.	0th Opti.	Form. Avg.	0th Opti.
Newcastle Sandstone	16.40	12.67	20.22	20.43	21.69	11.49
Dakota Sandstone	15.91	9.34	16.25	9.04	17.99	9.50
Swift Shale	15.24	14.02	15.30	10.29	16.08	12.87
Rierdon Limestone	22.82	17.41	28.38	18.27	27.95	26.23
Piper Limestone	32.59	64.71	31.95	50.50	30.37	59.82
Spearfish Sandstone	13.84	22.59	15.31	17.13	14.84	21.61
Pine Salt Sandstone	46.94	16.09	49.17	14.15	64.97	23.95
Broom Creek Sandstone	28.36	31.20	36.80	27.56	37.36	46.29
Tyler Sandstone	22.84	9.54	32.93	19.16	30.04	20.40
Kibbey Lime Limestone	12.96	21.41	33.33	49.01	23.47	31.06
Kibbey Lime Shale	13.59	17.59	25.16	41.64	13.87	15.02
Charles Sandstone	56.86	19.88	60.58	19.20	76.61	21.26
Charles Limestone	33.68	27.79	38.60	80.16	31.60	50.29
Ratcliffe Sandstone	20.65	24.67	20.82	38.40	19.03	26.47
Base Last Salt Limestone	35.91	27.62	45.56	54.88	34.32	63.19
Base Last Salt Sandstone	10.26	13.13	17.01	13.85	13.22	16.93
Mission Canyon Limestone	14.87	23.53	17.37	22.10	16.67	21.36
Lodgepole Limestone	10.29	8.14	13.52	6.38	8.61	9.06
Average	23.56	21.19	28.79	28.45	27.70	27.04

Tables 6.10 and 6.11 display the reverse outcome observed in Tables 6.8 and 6.9. With machine learning ROP models, errors are lower in 0th optimization intervals compared to the remainder of formation intervals. Although ROP in some individual formations is still more accurately predicted with lithology-dependent models, average errors favor models trained with data from the preceding formation. This is particularly true with the random forests algorithm. The likely explanation for this behavior is that models trained in the same formation lack substantial data in the first few retraining intervals. Models tested on 0th optimization intervals benefit from all data measured in the previous formation, possibly containing information about combinations of drilling parameters that lead to drilling dysfunctions not yet experienced in the first batches of data in a new formation. As previously shown (Section 5.7), machine learning models perform significantly better with

larger volumes of data. Results in Tables 6.10 and 6.11 support this notion. The same is not observed with analytical ROP models (Tables 6.8 and 6.9) since they must average drilling behavior into model coefficients, not taking advantage of the full array of information obtained in the preceding formation.

At least from a ML modeling perspective, the traditional lithology dependency requirement for ROP models is contested in this section. Chapter 7 introduces different methodologies to segment the drilling training dataset ignoring formation boundaries.

6.4. DRILLING PARAMETER OPTIMIZATION

The lithology-dependent real-time drilling interval optimization workflow presented in Section 6.2 establishes a performance baseline for comparison of novel data segmentation techniques in Chapter 7. Hence, all portions of the optimization workflow are investigated here. Results are reported with the standard 30ft retraining interval definition, generating a total of 148 formation-specific intervals. Tables, instead of boxplots, are mainly utilized from this point forward to facilitate one-on-one metric comparisons for all seven ROP models and collections of most accurate models selected by cross-validation on the training data and by test error. As a reminder, computational times for experiments in this section and in Chapter 7 were recorded with an inexpensive modern laptop computer (7th Generation Intel® Core™ i5 processor @ 2.50GHz and 8GB RAM).

Analysis begins by evaluating modeling errors and cross-validation computational time:

Table 6.12: Model error metrics and computational time for formation-dependent training
dataset with 30ft retraining intervals.

Formation Dependent - 30ft Retraining Intervals				
ROP Model	Absolute Error	Norm. RMSE	CV Time (s)	Opti. Time (s)
Bingham (1964)	37.46	33.34	0.45	0.001
Modified B&Y	35.23	32.67	4.53	0.003
Hareland and Rampersad (1994)	37.35	32.91	6.49	0.003
Motahhari *et al*. (2010)	37.69	33.36	5.72	3.02
Random Forests	23.81	22.61	4.97	76.79
Support Vector Machines	27.98	26.96	0.20	1.64
Neural Networks	27.96	26.87	1.07	3.02
Best by Cross Validation	24.20	24.06	23.44	67.83
Best by Test Error	19.44	20.30		
Best CV / Test Error Agreement	43.02%	45.27%		

As expected, model performance is significantly worse for all models when compared to models previously trained with all formation data (Section 5.5). Comparing the table above to Table 5.7, ML ROP models experience larger error increase (~10-14%) than analytical models (~3-8%). CV computational time is comparable to previous results. In the "best by cross-validation" row, optimization time represents the average computational time needed to optimize the best performing model selected by cross-validation at each interval. This constitutes the collection of models utilized to optimize drilling parameters in a practical field application of the real-time interval optimization workflow. Combining CV and optimization time, the total of about 90 seconds on average to define optimal drilling parameters in each interval is not computationally prohibitive in real-time (see Table 6.1). Examining statistics for model selection by CV, optimization time is largely driven by the random forests model:

Table 6.13: Model selection and cross-validation/test error agreement for formation-dependent training dataset with 30ft retraining intervals.

Formation Dependent - 30ft Retraining Intervals				
ROP Model	CV Abs. Error	CV Norm. RMSE	Abs. Error	Norm. RMSE
Bingham (1964)	0.00%	0.00%	2.03%	1.35%
Modified B&Y	0.00%	0.00%	7.43%	3.38%
Hareland and Rampersad (1994)	1.35%	1.35%	6.08%	9.46%
Motahhari *et al*. (2010)	0.00%	0.00%	0.00%	2.03%
Random Forests	85.81%	87.84%	44.59%	47.97%
Support Vector Machines	10.81%	10.14%	17.57%	15.54%
Neural Networks	2.03%	0.68%	22.30%	20.27%
Best CV / Test Error Agreement			43.02%	45.27%

Conforming to previous results, the table above indicates that analytical ROP models are rarely the best performers according to CV on training data, while contributing to the collection of most accurate models on test data in around 15% of the 148 optimization intervals. Neural networks exhibit the biggest CV/test error selection discrepancy in Table 6.13, an enigma previously mentioned in Section 6.3.1.

Suggested drilling parameter adjustments and ROP gains derived from interval optimizations of each ROP model are presented next:

Table 6.14: Model normalized RMSE and drilling parameter optimization results for formation-dependent training dataset with 30ft retraining intervals.

Formation Dependent - 30ft Retraining Intervals					
ROP Model	Norm. RMSE	ΔWOB (klb)	ΔRPM (rev/min)	Δq (gpm)	ΔROP (ft/hr)
Bingham (1964)	33.34	12.82	45.62	0.00	118.95
Modified B&Y	32.67	12.82	45.62	8.28	93.21
Hareland and Rampersad (1994)	32.91	11.94	45.62	0.00	73.07
Motahhari *et al*. (2010)	33.36	12.82	45.62	0.00	97.74
Random Forests	22.61	-6.56	-5.48	-6.32	24.36
Support Vector Machines	26.96	-3.64	-0.01	-7.04	35.11
Neural Networks	26.87	-7.19	0.74	-9.48	31.85
Best by Cross Validation	24.06	-6.06	-3.49	-6.32	25.32
Best by Test Error	20.30	-3.21	5.32	-7.95	34.65

Section 5.5 has established that analytical ROP model optimizations drive operational parameters to their maximum bound, while optimizations according to ML models attempt to locate regions in the parameter space where drilling speed is high. Similar to previous

results (Tables 5.8-5.10 and 5.12), ML model optimizations to this Williston Basin dataset generally suggest a reduction in drilling operational parameter values. This notion is further explored by inspecting ROP and WOB difference distributions over all optimized intervals for the most accurate analytical (modified B&Y) and ML (random forests) ROP models:
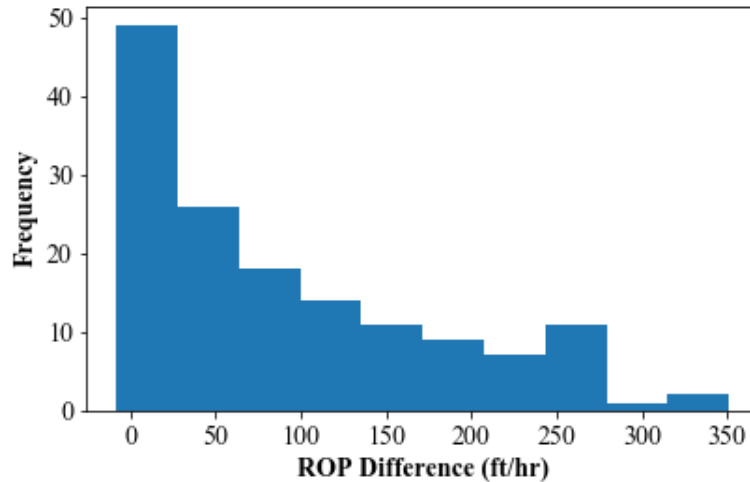
Figure 6.10: ROP difference distribution in 148 interval optimizations for modified Bourgoyne and Young ROP models with formation-dependent training dataset and 30ft retraining intervals.

Figure 6.10 illustrates that optimizations according to modified B&Y models are very optimistic about achievable ROP improvements, with a large portion of intervals displaying possible ROP gains of over 100ft/hr. In comparison, random forests optimized predictions are more moderate:
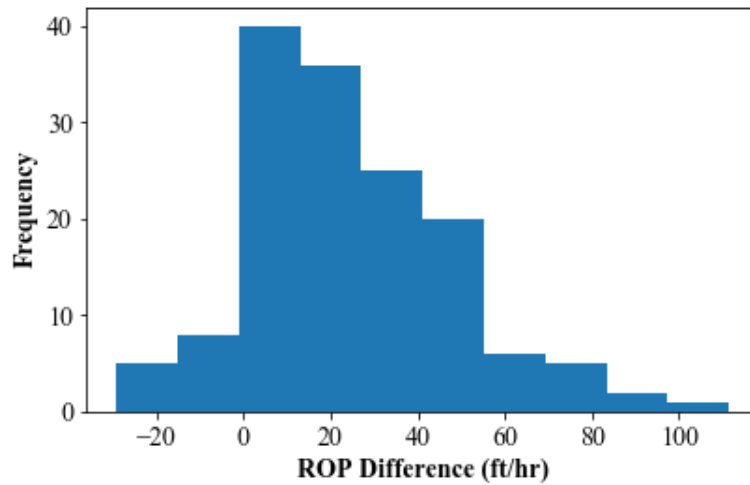
Figure 6.11: ROP difference distribution in 148 interval optimizations for random forests ROP models with formation-dependent training dataset and 30ft retraining intervals.

The ROP distribution in the figure above is much more concentrated around the mean than in Fig. 6.10. Negative ROP differences are represented, indicating that some drilled intervals overperformed random forests' optimized predictions.

WOB difference distributions are depicted next:
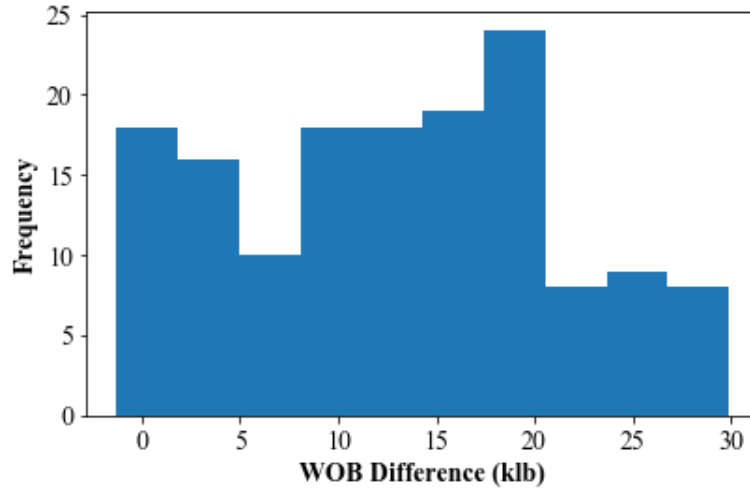
Figure 6.12: WOB difference distribution in 148 interval optimizations for modified
Bourgoyne and Young ROP models with formation-dependent training
dataset and 30ft retraining intervals.

Due to the positively bounded nature of analytical ROP model coefficients, drilling

variables are forced to always have a positive relationship with ROP in the modified B&Y

model. Several intervals are optimized to WOB increases greater than 20klbf. Constraints

established in Table 4.4 limit WOB to an upper bound of 35klbf. Therefore, intervals with

large optimized WOB differences were originally drilled with low bit weight. Drilling

behavior in such intervals is extrapolated by the modified B&Y model to WOB values

much higher than seen in the training data, resulting in the extremely high, but possibly

unrealistic ROP improvements shown in Fig. 6.10. Optimized WOB differences with

random forests models portray a significantly distinct modeling philosophy:
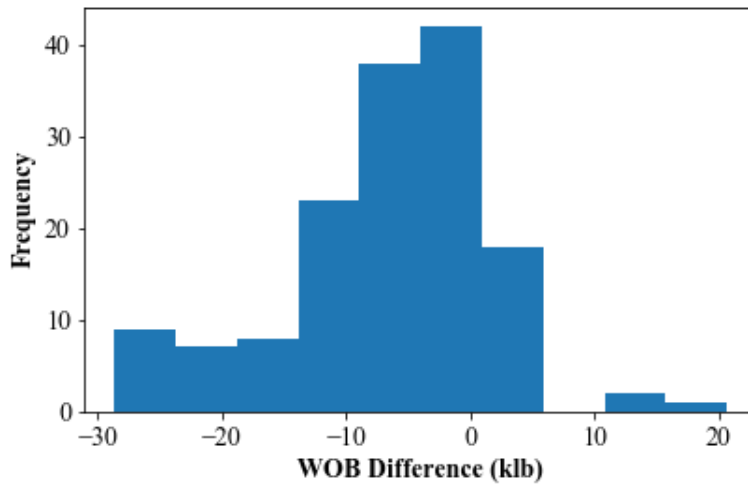
Figure 6.13: WOB difference distribution in 148 interval optimizations for random forests ROP models with formation-dependent training dataset and 30ft retraining intervals.

Fig. 6.13 demonstrates that random forests models suggest reductions in WOB for most optimized intervals. These reductions approach 30klbf in certain intervals, nearing the imposed 5klbf WOB lower bound. Since WOB is optimized to high ROP regions determined by RF models, it is reasonable to speculate that the recommended negative WOB adjustments avoid parameter combinations that lead to drilling dysfunctions. However, it is highly unlikely that over 125 out of 148 total formation intervals were drilled experiencing dysfunctional behavior. Field personnel are trained to avoid such issues, and the blame for these dubious WOB-ROP relationships modeled by the RF algorithm probably lies with poor drilling data quality.

Chapter 7: Data Segmentation Techniques for Real-Time Optimization of Drilling Parameters

The traditional methodology of training lithology-dependent ROP models has a strong foundation, as rock properties vastly affect drilling behavior. Nevertheless, data collected in drilling previous rock formations possibly explore different regions of the operational parameter space and may contribute to enhanced modeling in a new formation, as evidenced in Section 6.3.3. In lithology transition zones, determining optimal drilling parameters in real-time with a lithology-dependent modeling approach may prove particularly tricky, since not much relevant data are available.

This chapter introduces different procedures to partition the training dataset, questioning the classical lithology dependence of ROP models. Training data are partitioned according to a dynamic range of fixed depth length or the full range of data collected in the well, violating lithology dependency. Segmentation approaches then incorporate spatial proximity and parameter similarity weighting techniques to further divide training data according to sample importance. These proposed data segmentation methodologies are evaluated with respect to ROP modeling error and ROP improvement from optimization of drilling parameters. Complying with the continuous learning real-time drilling optimization workflow established in Section 6.2, ROP models are retrained in 30ft intervals. This 30ft optimization interval standard, with reasonable frequency of drilling parameter adjustments and assurance that thinner formations are not left unoptimized, facilitates field applicability. Experiments with dynamic range, full range and data weighting techniques will be compared to the baseline formation-dependent continuous learning with 30ft retraining intervals presented in Section 6.4. The impact of aggregating historical data to the training dataset is also analyzed. Model performance,

ROP gains and CV's ability to select the most accurate ROP model are the assessment metrics of interest.

7.1. DYNAMIC RANGE OF TRAINING DATA

Dynamic range ignores formation boundaries and imposes a fixed training dataset length. Illustrating this segmentation technique with the Rierdon Limestone formation:
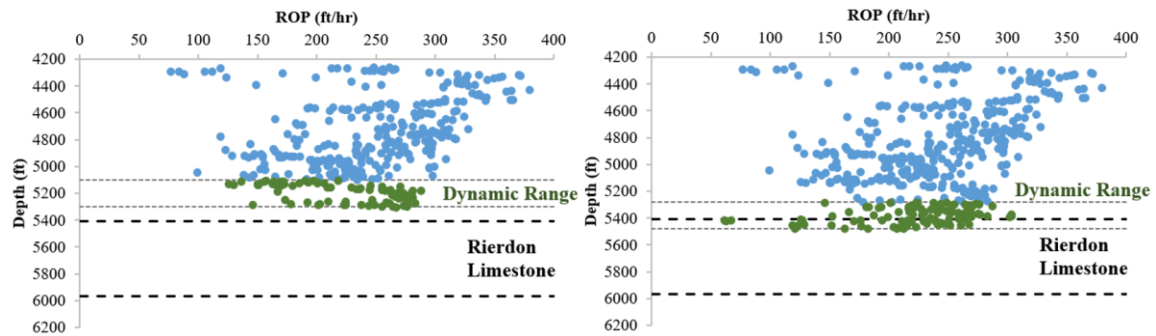
Figure 7.1: 200ft dynamic range training dataset moving through Rierdon Limestone formation boundary.

In the left plot of Fig. 7.1, the 200ft-long dynamic training data range is entirely located within the formation preceding the Rierdon Limestone formation. However, after drilling optimization in six 30ft intervals (right-hand plot), the dynamic range spans two separate formations. Zooming in on the interval to be optimized in the second plot:
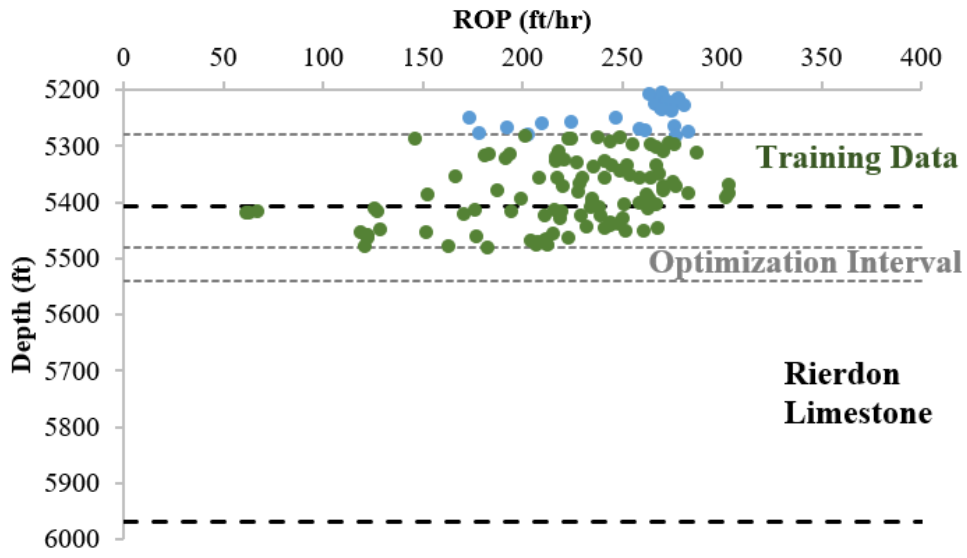
Figure 7.2: Rierdon Limestone optimization interval for 200ft dynamic range training dataset segmentation.

Optimization with dynamic training data range follows the continuous learning workflow, established in Section 6.2. Dynamic range neglects operational parameter optimization in only one interval (in the beginning of a bit run), compared to sub-optimal first drilling intervals in each formation with a lithology-dependent approach. Moreover, this segmentation technique ensures that a substantial amount of training data is available at all optimization intervals. With 30ft retraining intervals, the training dataset is divided into 162 intervals for the Williston Basin dataset, 14 more than the 148 formation-dependent intervals (Section 6.4).

Optimal dynamic range length for highest ROP modeling predictive accuracy must be determined before analysis begins. Starting out with a dynamic range as long as the average formation thickness in the Williston Basin dataset (~250ft) and varying its length in 50ft steps:

Table 7.1: ROP model performance with increasing dynamic range depth length and 30ft retraining intervals.

Dynamic Range Length	250ft		300ft		350ft	
ROP Model	Abs. Error	Norm. RMSE	Abs. Error	Norm. RMSE	Abs. Error	Norm. RMSE
Bingham (1964)	37.20	34.03	38.17	34.65	39.50	35.64
Modified B&Y	34.81	33.08	35.63	33.51	36.67	34.25
Hareland and Rampersad (1994)	36.83	33.28	37.78	33.91	38.88	34.86
Motahhari et al. (2010)	37.32	33.90	38.27	34.54	39.42	35.53
Random Forests	22.95	21.82	23.01	21.81	22.82	21.88
Support Vector Machines	27.62	26.15	27.16	25.79	27.13	25.82
Neural Networks	26.90	26.12	26.37	25.83	26.44	25.10
Best by Cross Validation	23.06	21.87	23.03	21.82	22.89	21.89
Best by Test Error	18.94	19.17	18.93	19.27	18.56	19.02
Best CV / Test Error Agreement	44.44%	45.68%	40.74%	47.53%	46.91%	49.38%

With increasing dynamic range length, analytical ROP model performance worsens. This is expected, as analytical models must represent the averaged drilling behavior in a longer data span. Conflicting results are observed for ML models, as no clear performance trend is observed with longer dynamic training data ranges. Shortening dynamic range length in increments of 50ft:

Table 7.2: ROP model performance with decreasing dynamic range depth length and 30ft retraining intervals.

Dynamic Range Length	200ft		150ft		100ft	
ROP Model	Abs. Error	Norm. RMSE	Abs. Error	Norm. RMSE	Abs. Error	Norm. RMSE
Bingham (1964)	36.13	33.48	34.90	32.64	33.19	31.45
Modified B&Y	33.97	32.76	32.89	31.94	31.59	31.02
Hareland and Rampersad (1994)	35.74	32.70	34.48	31.80	32.95	30.85
Motahhari et al. (2010)	36.29	33.38	35.08	32.54	33.38	31.38
Random Forests	22.94	21.56	23.11	21.87	23.09	21.79
Support Vector Machines	27.87	26.36	27.74	26.13	28.35	26.32
Neural Networks	25.96	24.76	26.30	25.15	28.25	25.93
Best by Cross Validation	22.93	21.65	23.51	22.12	23.44	22.07
Best by Test Error	18.24	18.45	18.04	18.52	18.03	18.70
Best CV / Test Error Agreement	39.51%	41.98%	40.12%	43.21%	34.57%	39.51%

Analytical ROP models perform better with shorter dynamic training data ranges, due to their averaging nature described earlier. Agreement between best model selected by CV and by test error mostly hovers between 40% and 50%. RF performs best with a 350ft dynamic range according to absolute error and with a 200ft dynamic range according to

normalized RMSE. SVM performs best with a 350ft dynamic range according to absolute error and with a 300ft dynamic range according to normalized RMSE. Finally, NN performs best with a 200ft dynamic range according both error metrics. The 200ft dynamic training data range represents a sweet spot for compromise between analytical and machine learning model performance and is utilized as the standard dynamic range length for the remainder of this study.

Evaluating model error and CV time for the 200ft dynamic training data range:

Table 7.3: Model error metrics and computational time for 200ft dynamic range training dataset with 30ft retraining intervals.

200ft Dynamic Range - 30ft Retraining Intervals				
ROP Model	Absolute Error	Norm. RMSE	CV Time (s)	Opti Time (s)
Bingham (1964)	36.13	33.48	0.25	0.001
Modified B&Y	33.97	32.76	4.30	0.002
Hareland and Rampersad (1994)	35.74	32.70	7.28	0.003
Motahhari *et al*. (2010)	36.29	33.38	3.54	1.80
Random Forests	22.94	21.56	4.89	78.53
Support Vector Machines	27.87	26.36	0.14	0.83
Neural Networks	25.96	24.76	0.80	1.80
Best by Cross Validation	22.93	21.65	21.20	74.30
Best by Test Error	18.24	18.45		
Best CV / Test Error Agreement	39.51%	41.98%		

These results are compared to the formation-dependent baseline (Table 6.12). Model performance improves for both analytical and ML ROP models with dynamic range training data segmentation, bringing the classical ROP modeling lithology dependence assumption into question. Computational expenses are similar to the baseline. Best model selection is investigated next:

Table 7.4: Model selection and cross-validation/test error agreement for 200ft dynamic range training dataset with 30ft retraining intervals.

200ft Dynamic Range - 30ft Retraining Intervals				
ROP Model	CV Abs. Error	CV Norm. RMSE	Abs. Error	Norm. RMSE
Bingham (1964)	0.00%	0.00%	1.85%	2.47%
Modified B&Y	0.00%	0.00%	8.64%	7.41%
Hareland and Rampersad (1994)	0.00%	0.00%	4.94%	4.94%
Motahhari *et al.* (2010)	0.00%	0.00%	0.62%	1.85%
Random Forests	93.21%	94.44%	40.74%	43.21%
Support Vector Machines	6.17%	5.56%	16.05%	16.67%
Neural Networks	0.62%	0.00%	27.16%	23.46%
Best CV / Test Error Agreement			39.51%	41.98%

Comparing Table 7.4 to the formation-dependent baseline (Table 6.13), random forests models claim the lowest CV error in an even higher percentage of intervals with 200ft dynamic range. On the other hand, RF models are not the best performers according to test error as often, resulting in 3.51% (absolute error) and 3.29% (RMSE) fewer drilling intervals where the same model is the most accurate in terms of both cross-validation and test error.

Finally, Table 7.5 displays interval optimization results for the 200ft dynamic range segmentation technique:

Table 7.5: Model normalized RMSE and drilling parameter optimization results for 200ft dynamic range training dataset with 30ft retraining intervals.

200ft Dynamic Range - 30ft Retraining Intervals					
ROP Model	Norm. RMSE	ΔWOB (klb)	ΔRPM (rev/min)	Δq (gpm)	ΔROP (ft/hr)
Bingham (1964)	33.48	12.75	45.30	0.00	114.59
Modified B&Y	32.76	12.75	45.30	9.64	86.55
Hareland and Rampersad (1994)	32.70	11.06	45.30	0.00	59.45
Motahhari *et al.* (2010)	33.38	12.75	45.30	0.00	88.59
Random Forests	21.56	-6.92	-6.60	-7.51	26.45
Support Vector Machines	26.36	-6.00	0.59	-0.23	41.31
Neural Networks	24.76	-8.51	0.85	-9.92	28.95
Best by Cross Validation	21.65	-6.84	-5.66	-7.46	26.62
Best by Test Error	18.45	-4.22	4.81	-3.46	39.05

Besides improved performance, ML ROP models achieve ROP gains higher than the formation-dependent baseline (Table 6.14) with 200ft dynamic training data range.

Optimization with SVM models produced the biggest increase in average ROP improvement, from 35.11ft/hr with formation-dependent training data to 41.31ft/hr with 200ft dynamic training data range. This outcome is further investigated by analyzing ROP difference histograms for intervals optimized by the SVM model with both segmentation techniques:
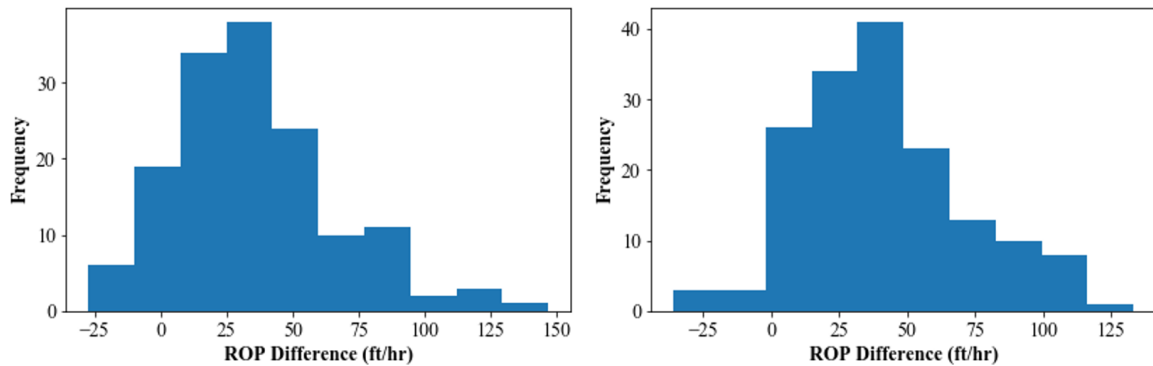
Figure 7.3: ROP difference distribution in interval optimizations for SVM ROP models with 30ft retraining intervals. Left plot: formation-dependent training dataset (148 intervals); Right plot: 200ft dynamic range training dataset (162 intervals).

ROP difference distributions in the figure above have similar shape, but the dynamic range distribution (right-hand plot) is shifted towards higher ROP improvements. Interestingly, SVM models recommend more negative average flow rate differences for the formation-dependent approach (-7.04gpm in Table 6.14 and -0.23gpm in Table 7.5):
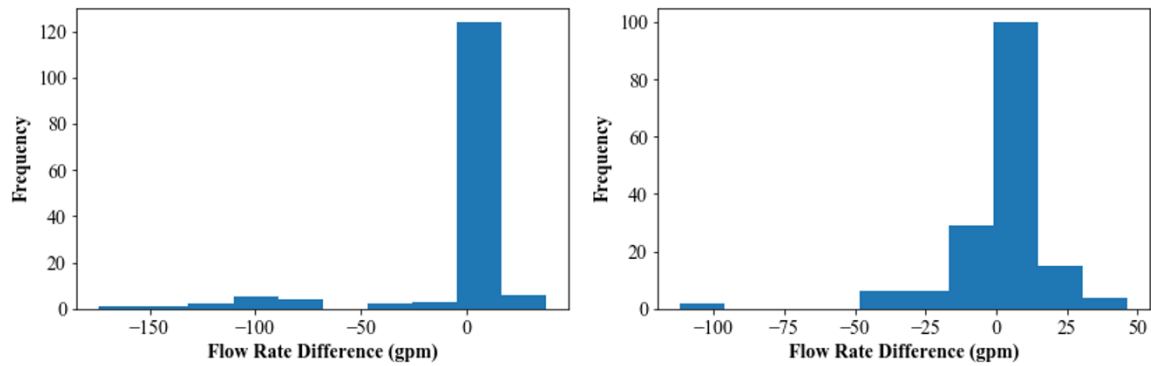
Figure 7.4: Flow rate difference distribution in interval optimizations for SVM ROP models with 30ft retraining intervals. Left plot: formation-dependent training dataset (148 intervals); Right plot: 200ft dynamic range training dataset (162 intervals).

SVM optimizations with 200ft dynamic range (right-hand plot) result in positive flow rate differences for more optimization intervals and less significantly negative recommended flow rate adjustments.

7.2. FULL RANGE OF TRAINING DATA

Instead of establishing a fixed-length moving range of training data, the full range training dataset encompasses all data measured in drilling the well up to each optimization interval. The intuition behind this approach is to take full advantage of all available data, as ML models were shown to reduce test error very effectively with incremental training data in Section 5.7. Analyzing the same Rierdon Limestone optimization interval as in Fig. 7.2:
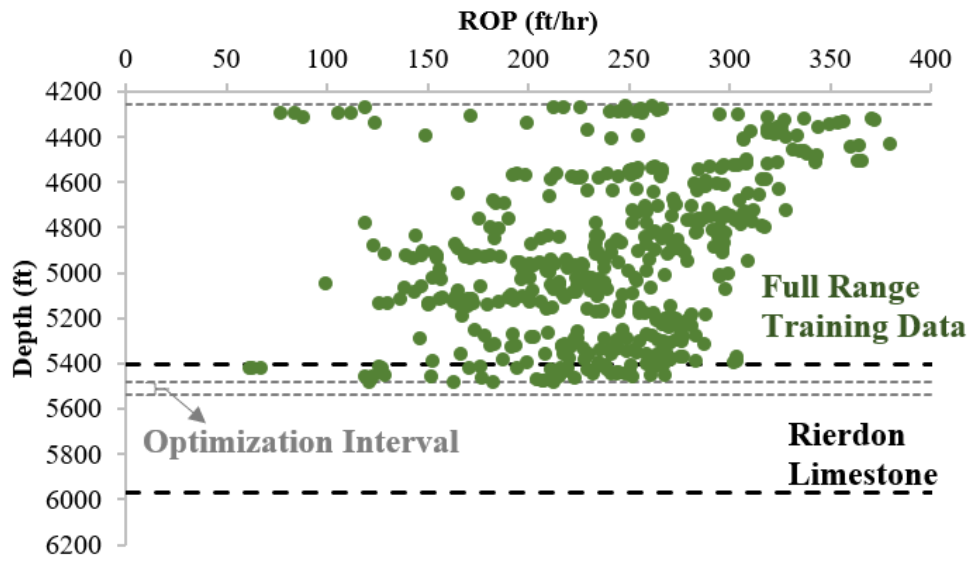
Figure 7.5: Rierdon Limestone optimization interval for full range training dataset segmentation.

Models are still retrained every 30ft, leading to the same 162 intervals optimized by the 200ft dynamic training data range methodology. ROP modeling error and computational metrics analogous to Table 7.3 are presented:

Table 7.6: Model error metrics and computational time for full range training dataset with 30ft retraining intervals.

Full Range - 30ft Retraining Intervals				
ROP Model	Absolute Error	Norm. RMSE	CV Time (s)	Opti Time (s)
Bingham (1964)	94.82	81.69	0.50	0.00
Modified B&Y	61.96	54.40	5.75	0.00
Hareland and Rampersad (1994)	93.99	80.56	6.06	0.00
Motahhari *et al*. (2010)	94.86	81.66	3.58	3.83
Random Forests	23.70	22.08	5.28	79.11
Support Vector Machines	27.49	25.91	9.99	1.33
Neural Networks	39.73	31.42	2.50	3.83
Best by Cross Validation	23.77	22.09	33.66	75.98
Best by Test Error	19.69	19.57		
Best CV / Test Error Agreement	44.44%	47.53%		

Analytical ROP models perform much worse compared to 200ft dynamic range (Table 7.3) or the formation-dependent baseline (Table 6.12), as expected from behavior previously

191

observed when increasing dynamic range length (Table 7.1). Interestingly, modified B&Y models display significantly lower error than other analytical models when trained with full training data ranges. It is possible that analytical model equation constants, such as bit diameter, aggravate averaging behavior established by model coefficients. Random forests and SVM models predict ROP more accurately than their formation-dependent counterparts, but NN errors are significantly higher with full training data range. Dynamic range segmentation of training data is better suited for RF and NN models, while full range is effective for SVM. CV time increases considerably for SVM and slightly for NN, leading to ten additional seconds required for cross-validating the seven ROP models. CV and test error model selection agreement increases with respect to the baseline (and significantly improves compared to dynamic range), as analytical models are rarely ever selected as best performers according to test data:

Table 7.7: Model selection and cross-validation/test error agreement for full range training dataset with 30ft retraining intervals.

Full Range - 30ft Retraining Intervals				
ROP Model	CV Abs. Error	CV Norm. RMSE	Abs. Error	Norm. RMSE
Bingham (1964)	0.00%	0.00%	1.23%	1.23%
Modified B&Y	0.00%	0.00%	0.62%	0.62%
Hareland and Rampersad (1994)	0.00%	0.00%	1.85%	2.47%
Motahhari *et al*. (2010)	0.00%	0.00%	0.62%	0.62%
Random Forests	96.91%	95.68%	43.83%	46.30%
Support Vector Machines	3.09%	4.32%	32.72%	29.63%
Neural Networks	0.00%	0.00%	19.14%	19.14%
Best CV / Test Error Agreement			44.44%	47.53%

Random forests models persist as dominant leaders in cross-validation error performance and SVM almost doubles in test data selection. Surprisingly, NN models remain the most accurate in 19% of intervals based on test error (about the same as in lithology-dependent), even though average interval errors are much higher than in the two previous training data segmentation techniques.

Interval optimizations with full range of training data are summarized below:

Table 7.8: Model normalized RMSE and drilling parameter optimization results for full range training dataset with 30ft retraining intervals.

Full Range - 30ft Retraining Intervals					
ROP Model	Norm. RMSE	ΔWOB (klb)	ΔRPM (rev/min)	Δq (gpm)	ΔROP (ft/hr)
Bingham (1964)	81.69	12.75	45.30	0.00	173.53
Modified B&Y	54.40	12.75	45.30	27.68	125.09
Hareland and Rampersad (1994)	80.56	11.10	45.30	0.00	126.75
Motahhari *et al*. (2010)	81.66	12.75	45.30	0.00	159.32
Random Forests	22.08	-9.42	1.29	14.64	44.39
Support Vector Machines	25.91	-4.30	16.30	-23.44	103.70
Neural Networks	31.42	-8.18	6.06	-12.54	53.80
Best by Cross Validation	22.09	-9.33	2.80	14.61	44.41
Best by Test Error	19.57	-7.30	8.18	-5.01	66.16

Table 7.8 displays substantial optimized ROP improvements for all ROP models, particularly for analytical ones. However, ROP gains predicted by analytical models are unlikely to materialize, as their error metrics are also very high. For machine learning models, large ROP improvements present a huge opportunity. With the same 162 intervals as 200ft dynamic range segmentation, RF optimizations with full training data range improved ROP gains from 26.45ft/hr to 44.39ft/hr on average. This is a distinguished accomplishment, obtained according to the most accurate ROP model. RF errors were very similar for both methodologies, 21.56% normalized RMSE for dynamic range and 22.08% normalized RMSE for full range.

Investigating random forests ROP difference histograms for both dynamic range and full range segmentation approaches:
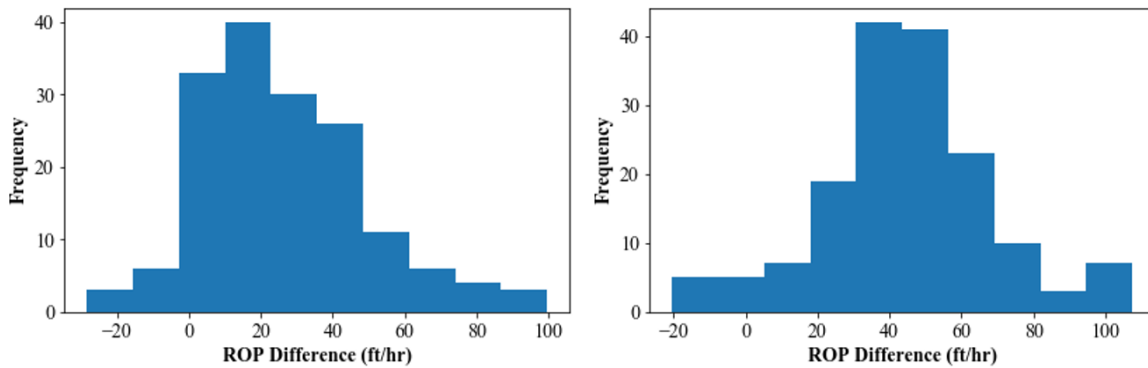
Figure 7.6: ROP difference distribution in 162 interval optimizations for RF ROP models with 30ft retraining intervals. Left plot: 200ft dynamic range training dataset; Right plot: full range training dataset.

Full range optimizations (right-hand plot) produce ROP improvements in the range of 40ft/hr-60ft/hr for several intervals, and around 100ft/hr for a considerable number of intervals. Drilling parameter recommendations are shown next:
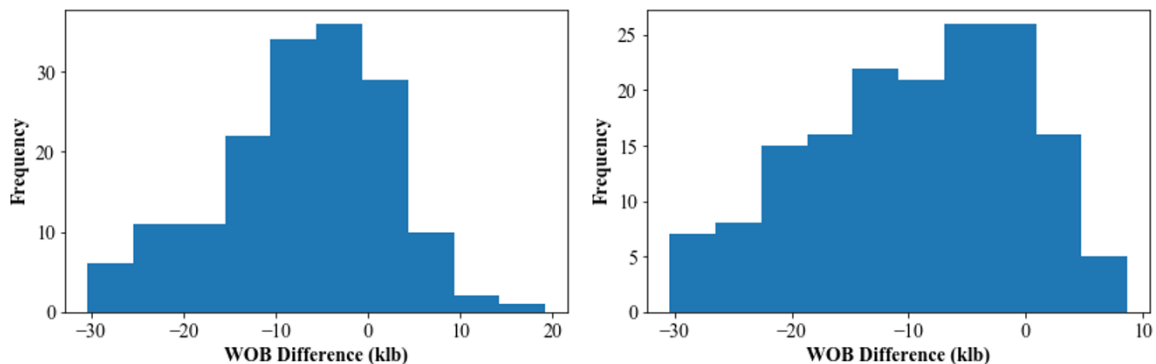
Figure 7.7: WOB difference distribution in 162 interval optimizations for RF ROP models with 30ft retraining intervals. Left plot: 200ft dynamic range training dataset; Right plot: full range training dataset.

RF models trained with full range of training data suggest more drastic reductions in WOB. Notice the large increase in the number of intervals with WOB differences between -10klbf to -30klbf. On average, full range RF models recommend -9.42klbf WOB adjustment,

compared to -6.92klbf with 200ft dynamic range. Conversely, RPM difference histograms indicate that full range optimizations result in significantly more positive RPM changes:
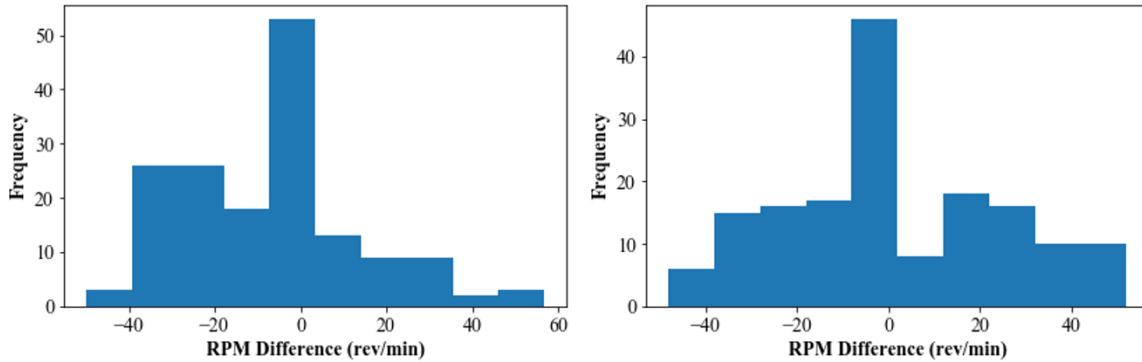
Figure 7.8: RPM difference distribution in 162 interval optimizations for RF ROP models with 30ft retraining intervals. Left plot: 200ft dynamic range training dataset; Right plot: full range training dataset.

Optimizations with dynamic range RF models advise -6.60rev/min average RPM adjustments, compared to +1.29rev/min for full range. Lastly, flow rate difference histograms are presented:
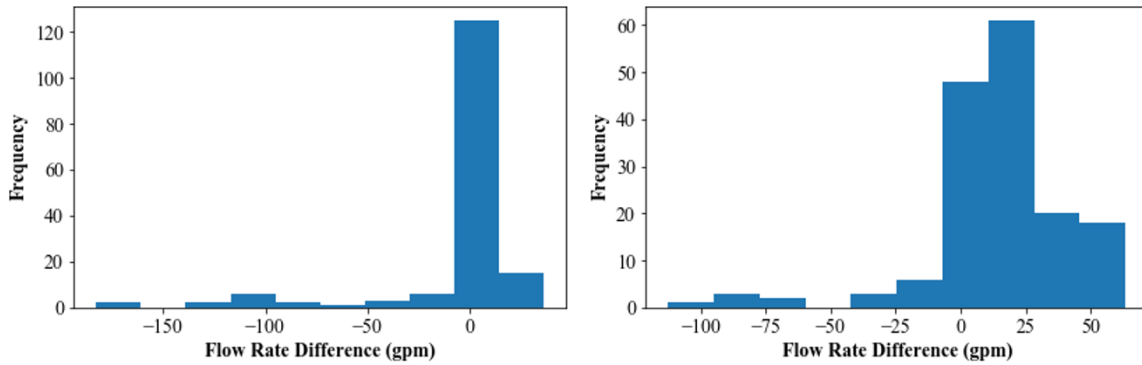
Figure 7.9: Flow rate difference distribution in 162 interval optimizations for RF ROP models with 30ft retraining intervals. Left plot: 200ft dynamic range training dataset; Right plot: full range training dataset.

195

Similar to RPM differences, dynamic range intervals average -7.51GPM flow rate adjustment while full range optimizations propose +14.64GPM. It is important to note that, as established in Table 4.4, mud flow rate is constrained between the minimum and maximum values encountered in the training data to avoid inadequate hole cleaning and lost circulation. With training datasets spanning significantly more than 200ft (as in dynamic range), full range optimizations enjoy wider flow rate adjustment windows, possibly culminating in the larger ROP improvements experienced in Fig. 7.6. In summary, optimizations with RF models fitted to full training data ranges favor increasing flow rate and RPM in most intervals and drastically decreasing WOB, as opposed to recommendations to reduce all three drilling parameters with 200ft dynamic range RF models.

7.3. SPATIAL PROXIMITY WEIGHTING

Data weighting attaches a measure of significance to individual training data samples in an attempt to develop more reliable models. This weighting concept is incorporated to the traditional lithology-dependent approach and data segmentation techniques described in Sections 7.1 and 7.2, further extending training data partitioning capabilities. Spatial proximity weighting exploits the notion that data points measured closest to the interval to be optimized are likely the most representative of drilling behavior expected within the interval. This methodology is illustrated with 200ft dynamic training data range for the same Rierdon Limestone interval analyzed in Fig. 7.2:
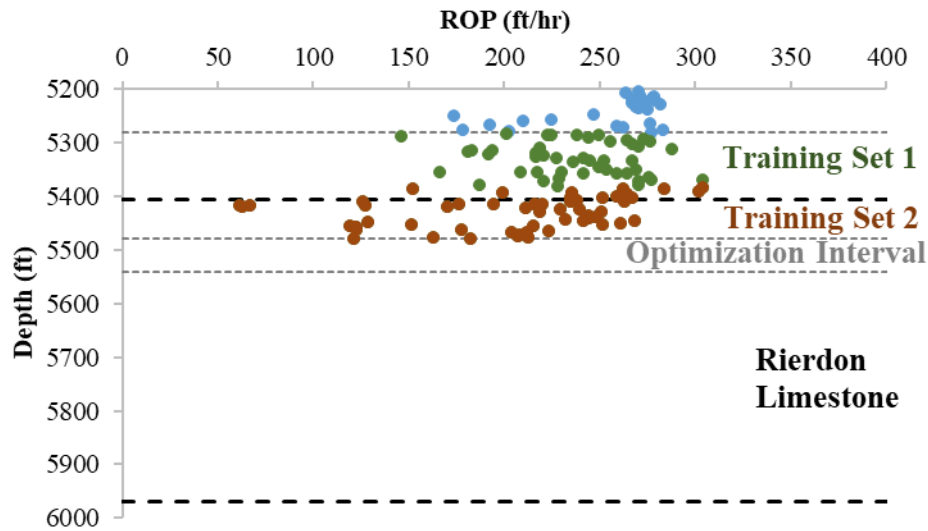
Figure 7.10: Rierdon Limestone optimization interval for 200ft dynamic range training dataset segmentation incorporating spatial proximity weighting.

In Fig. 7.10, the 200ft-long dynamic training data range is split into two 100ft segments. Samples in the second partition ("Training Set 2") are attributed higher weights than the first 100ft of data ("Training Set 1"), based on proximity to the optimization interval. Larger weights cause ROP modeling fitting procedures to place more emphasis on samples located in the second half of the training dataset, adjusting model coefficients accordingly.

Described in Section 3.2.1, l_2 loss (least squares regression) was established as the standard technique for analytical ROP model fitting in this dissertation (Section 5.2). Spatial proximity weighting illustrated in Fig 7.10 is accomplished by splitting training data residuals into two groups in the l_2 loss model fitting objective function formulation:

$$\min \left(w_1 \sum_{i=1}^{N_1} r_i{}^2 + w_2 \sum_{i=1}^{N_2} r_i{}^2 \right)$$

$$= \min \left(w_1 \sum_{i=1}^{N_1} \left(ROP_{Field,i} - ROP_{Model,i} \right)^2 \right.$$

$$\left. + w_2 \sum_{j=1}^{N_2} \left(ROP_{Field,j} - ROP_{Model,j} \right)^2 \right) \tag{7.1}$$

where w_1 is the weight assigned to the first training set segment with N_1 data points and w_2 is the weight assigned to the second training set segment with N_2 data points. With w_2 greater than w_1, as suggested for the dynamic range in Fig. 7.10, the objective function in Eq. 7.1 conditions the ROP model to be more representative of drilling data spatially proximal to the optimization interval. This training data partitioning concept can be extended to attribute different weights to multiple segments of the training dataset:

$$\min \left(\sum_{j=1}^{P} \sum_{i=1}^{N_j} w_i r_i{}^2 \right) = \min \left(\sum_{j=1}^{P} \sum_{i=1}^{N_j} w_i \left(ROP_{Field,i} - ROP_{Model,i} \right)^2 \right) \tag{7.2}$$

where P is the number of training data partitions and w_i is the weight assigned to the ith sample in the jth partition. In Eq. 7.2, the training dataset can be segmented into any number of P partitions. Progressive spatial proximity weighting assigns incremental significance to samples as they inch closer to the optimization interval. Conceptually, this technique is particularly useful in conjunction with full range training dataset segmentation.

In Section 5.2, the trust region reflective algorithm in Python's *scipy.optimize* (Oliphant, 2007) library was designated as the algorithm of choice for analytical ROP model fitting. This trust region implementation in *scipy.optimize* was designed for least-squares problems, with a limited selection of pre-defined loss functions. Since the objective

function in Eq. 7.2 incorporates linear weights in its formulation, TRF cannot be used for fitting sample-weighted analytical ROP models. The L-BFGS-B technique provided in the same Python package is a suitable substitute supporting stipulation of any objective function, with similar gradient-based approach. L-BFGS-B computes model coefficients identical to the ones obtained with TRF in the experiment described in Table 5.2, with comparable computing performance. Hence, L-BFGS-B is elected as the standard algorithm for analytical ROP model fitting with data weighting techniques. RF and SVM implementations in Python's *scikit-learn* (Pedregosa *et al*., 2011) have embedded sample weighting support. In random forests, highly weighted training data points bear heavier influence on node splitting decisions. For SVM, *scikit-learn* rescales the budget parameter *C*, which controls toleration to margin violations, to prioritize classifying higher-weighted samples on the correct side of the margin. Regrettably, *scikit-learn*'s neural networks algorithm does not support training data weighting. In order to overcome this deficiency, samples are repeated a number of times equivalent to their weights. Eqs. 7.1 and 7.2 reveal that attributing a weight value of 2 to a data point has the same effect as adding the sample twice to the training dataset. Therefore, for neural networks model training with data weighting strategies, weights are rounded to the nearest integer and their corresponding samples are repeated an equivalent number of times. This approach has the disadvantage of requiring approximate weights and additional computational time if the number of samples in the training dataset increases considerably.

7.3.1. Formation-Dependent Training Data

Section 6.4 covers real-time drilling interval optimization with unweighted lithology-dependent ROP models, providing a baseline for weighting techniques. Cross-validation and optimization computational expenses are very similar regardless of whether

training data weights are prescribed, and CV/test error weighted model selection agreement remains within 40-50%. Thus, the analysis here focuses on model error (normalized RMSE) and optimization outcomes. Assigning weights twice as large for the second half of the training dataset ($w_1 = 1$ and $w_2 = 2$ in Eq. 7.1, with N_1 representing the first half of training data points):

Table 7.9: Model normalized RMSE and drilling parameter optimization results for formation-dependent training dataset with 30ft retraining intervals and second half of training samples weighted double.

Formation Dependent with Spatial Weights - Second Half of Training Dataset Double Weighted					
ROP Model	Norm. RMSE	ΔWOB (klb)	ΔRPM (rev/min)	Δq (gpm)	ΔROP (ft/hr)
Bingham (1964)	31.86	12.82	45.62	0.00	117.33
Modified B&Y	31.38	12.82	45.62	8.28	93.52
Hareland and Rampersad (1994)	31.48	11.97	45.62	0.00	77.24
Motahhari *et al.* (2010)	31.84	12.82	45.62	0.00	100.32
Random Forests	22.38	-6.15	-5.61	-9.95	24.16
Support Vector Machines	27.86	-4.10	-0.17	-3.13	41.68
Neural Networks	27.49	-8.22	-0.10	-13.77	31.98
Best by Cross Validation	22.90	-5.91	-4.11	-9.82	25.34
Best by Test Error	19.10	-2.94	4.87	-8.58	35.97

These results are compared to the unweighted formation-dependent baseline (Table 6.14). Model performance improves by an average of 1.5% normalized RMSE for all analytical models, and 0.23% normalized RMSE for RF. SVM and NN models perform slightly worse. ROP differences are equivalent, except for higher gains in optimizations with SVM. However, since SVM models exhibit higher errors, there is no guarantee that these ROP improvements are actually significant.

Comparison between Tables 7.9 and 6.14 establishes potential for ROP modeling predictive accuracy improvement with spatial proximity sample weighting. Additional spatial weighting scenarios are tested for dynamic and full training data ranges.

7.3.2. Dynamic Range of Training Data

Section 7.1 institutes the baseline for dynamic range weighting techniques. Optimization results for two-way partitioning with double weighting ($w_1 = 1$ and $w_2 = 2$ in Eq. 7.1) are presented in the table below:

Table 7.10: Model normalized RMSE and drilling parameter optimization results for 200ft dynamic range training dataset with 30ft retraining intervals and second half of training samples weighted double.

ROP Model	Norm. RMSE	ΔWOB (klb)	ΔRPM (rev/min)	Δq (gpm)	ΔROP (ft/hr)
200ft Dynamic Range with Spatial Weights - Second Half of Training Dataset Double Weighted					
Bingham (1964)	32.18	12.75	45.30	0.00	113.74
Modified B&Y	31.71	12.75	45.30	9.64	87.76
Hareland and Rampersad (1994)	31.51	11.06	45.30	0.00	65.20
Motahhari *et al*. (2010)	32.09	12.75	45.30	0.00	90.97
Random Forests	21.62	-7.29	-6.57	-8.64	25.92
Support Vector Machines	27.52	-5.99	0.49	-1.92	46.89
Neural Networks	26.26	-6.26	-1.34	-8.83	31.43
Best by Cross Validation	21.85	-7.13	-6.06	-8.51	26.65
Best by Test Error	18.98	-3.57	4.60	-4.50	38.33

Normalized RMSE is lower for analytical models, but slightly higher for ML models with respect to the unweighted dynamic range baseline (Table 7.5). ROP gains remain virtually unchanged.

In the following simulation, the second half of training data is weighted five times as much as the first 100ft ($w_1 = 1$ and $w_2 = 5$ in Eq. 7.1):

Table 7.11: Model normalized RMSE and drilling parameter optimization results for 200ft dynamic range training dataset with 30ft retraining intervals and second half of training samples weighted five times more than first half.

200ft Dynamic Range with Spatial Weights - Second Half of Training Dataset Weighted 5 Times More					
ROP Model	Norm. RMSE	ΔWOB (klb)	ΔRPM (rev/min)	Δq (gpm)	ΔROP (ft/hr)
Bingham (1964)	31.38	12.75	45.30	0.00	113.49
Modified B&Y	31.05	12.75	45.30	9.64	86.29
Hareland and Rampersad (1994)	30.75	11.06	45.30	0.00	63.84
Motahhari *et al*. (2010)	31.28	12.75	45.30	0.00	90.16
Random Forests	21.56	-7.52	-8.90	-6.49	25.60
Support Vector Machines	29.95	-5.83	0.44	-1.38	61.49
Neural Networks	27.65	-6.82	-1.20	-7.31	28.67
Best by Cross Validation	21.76	-7.39	-8.08	-6.44	26.18
Best by Test Error	19.12	-3.98	2.57	-1.29	35.18

Analytical model performance improves with larger weights for samples closer to the optimized interval. Random forests errors are slightly lower than in Table 7.10, reverting back to the normalized RMSE achieved in the baseline (Table 7.5). ROP improvements are very similar, except for huge gains in SVM optimizations. Nevertheless, SVM errors increase with respect to Table 7.10.

Next, second-partition samples receive 10 times more emphasis in model training ($w_1 = 1$ and $w_2 = 10$ in Eq. 7.1):

Table 7.12: Model normalized RMSE and drilling parameter optimization results for 200ft dynamic range training dataset with 30ft retraining intervals and second half of training samples weighted ten times more than first half.

200ft Dynamic Range with Spatial Weights - Second Half of Training Dataset Weighted 10 Times More					
ROP Model	Norm. RMSE	ΔWOB (klb)	ΔRPM (rev/min)	Δq (gpm)	ΔROP (ft/hr)
Bingham (1964)	31.18	12.75	45.30	0.00	113.58
Modified B&Y	30.88	12.75	45.30	9.64	86.45
Hareland and Rampersad (1994)	30.56	11.10	45.30	0.00	65.08
Motahhari *et al*. (2010)	31.10	12.75	45.30	0.00	90.70
Random Forests	21.60	-7.20	-6.15	-7.13	24.74
Support Vector Machines	32.10	-4.12	0.52	-2.35	73.31
Neural Networks	25.53	-6.25	-0.39	-11.46	29.09
Best by Cross Validation	21.83	-7.23	-5.44	-7.09	26.51
Best by Test Error	18.91	-3.13	2.57	-2.90	35.01

Table 7.12 ratifies the trend of decreasing analytical model errors with higher spatial proximity weights, while ML model performance remains unpredictable.

Progressive spatial proximity weighting is investigated by splitting the dynamic training data range into four segments and incrementally attributing higher weights to partitions closer to the optimized interval ($w_1 = 1$, $w_2 = 2$, $w_3 = 3$, $w_4 = 4$ in Eq. 7.2):

Table 7.13: Model normalized RMSE and drilling parameter optimization results for 200ft dynamic range training dataset with 30ft retraining intervals and training samples divided into four partitions of equal size weighted progressively.

200ft Dynamic Range with Spatial Weights - Training Data Divided into 4 Partitions Weighted Progressively					
ROP Model	Norm. RMSE	ΔWOB (klb)	ΔRPM (rev/min)	Δq (gpm)	ΔROP (ft/hr)
Bingham (1964)	31.89	12.75	45.30	0.00	113.45
Modified B&Y	31.50	12.75	45.30	9.64	87.02
Hareland and Rampersad (1994)	31.25	11.11	45.30	0.00	64.97
Motahhari *et al*. (2010)	31.79	12.75	45.30	0.00	90.76
Random Forests	21.66	-6.40	-8.28	-5.54	25.34
Support Vector Machines	29.27	-6.07	0.45	-1.45	58.43
Neural Networks	25.83	-7.82	-1.06	-13.26	30.35
Best by Cross Validation	21.85	-6.16	-7.64	-5.46	26.42
Best by Test Error	18.85	-3.65	3.64	-2.39	37.03

Analytical models display lower errors than the initial two-way partition (Table 7.10), but higher errors than 5-fold weighting (Table 7.11). This four-way progressive weighting technique is conducive to neural networks, which display low normalized RMSE and large ROP improvements.

Finally, further progressive spatial proximity weighting analysis is conducted with 10 data partitions ($w_1 = 1$, $w_2 = 2$, $w_3 = 3$, $w_4 = 4$, $w_5 = 5$, $w_6 = 6$, $w_7 = 7$, $w_8 = 8$, $w_9 = 9$, $w_{10} = 10$ in Eq. 7.2):

Table 7.14: Model normalized RMSE and drilling parameter optimization results for 200ft dynamic range training dataset with 30ft retraining intervals and training samples divided into ten partitions of equal size weighted progressively.

200ft Dynamic Range with Spatial Weights - Training Data Divided into 10 Partitions Weighted Progressively					
ROP Model	**Norm. RMSE**	**ΔWOB (klb)**	**ΔRPM (rev/min)**	**Δq (gpm)**	**ΔROP (ft/hr)**
Bingham (1964)	31.63	12.75	45.30	0.00	113.36
Modified B&Y	31.32	12.75	45.30	9.64	86.59
Hareland and Rampersad (1994)	31.02	11.08	45.30	0.00	65.25
Motahhari *et al*. (2010)	31.54	12.75	45.30	0.00	91.52
Random Forests	21.84	-7.24	-8.82	-7.19	25.87
Support Vector Machines	32.52	-5.33	0.39	-3.03	75.00
Neural Networks	26.29	-6.94	0.03	-10.79	26.82
Best by Cross Validation	22.16	-7.05	-6.95	-7.37	27.54
Best by Test Error	19.01	-4.41	3.39	-1.76	37.64

Table 7.14 shows a modest analytical performance improvement with respect to four-way partition (Table 7.13), but higher errors compared to two-partition five-fold weighting (Table 7.11). All ML models performed worse than the previous weighting scenario with four partitions.

Figures 7.11 and 7.12 summarize modeling and optimization results for 200ft dynamic training data range with spatial proximity weighting:
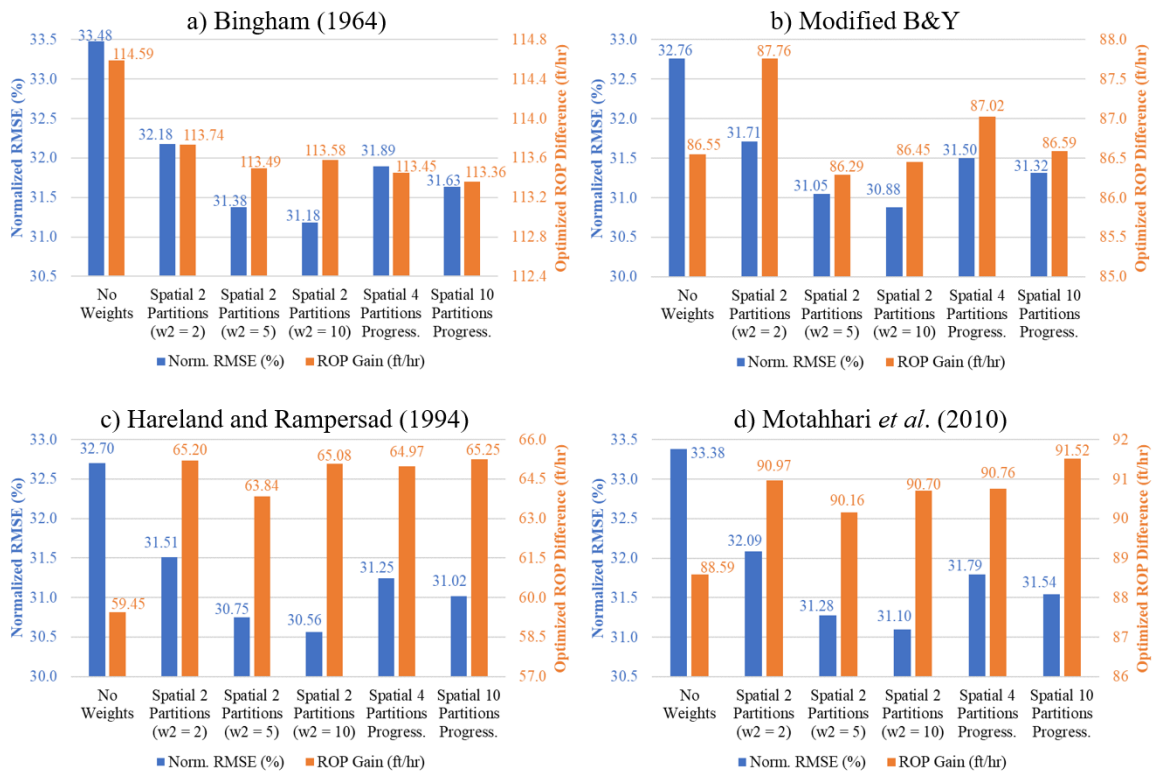
Figure 7.11: Normalized RMSE and ROP improvement for analytical ROP models in all 200ft dynamic range spatial proximity weighting scenarios.
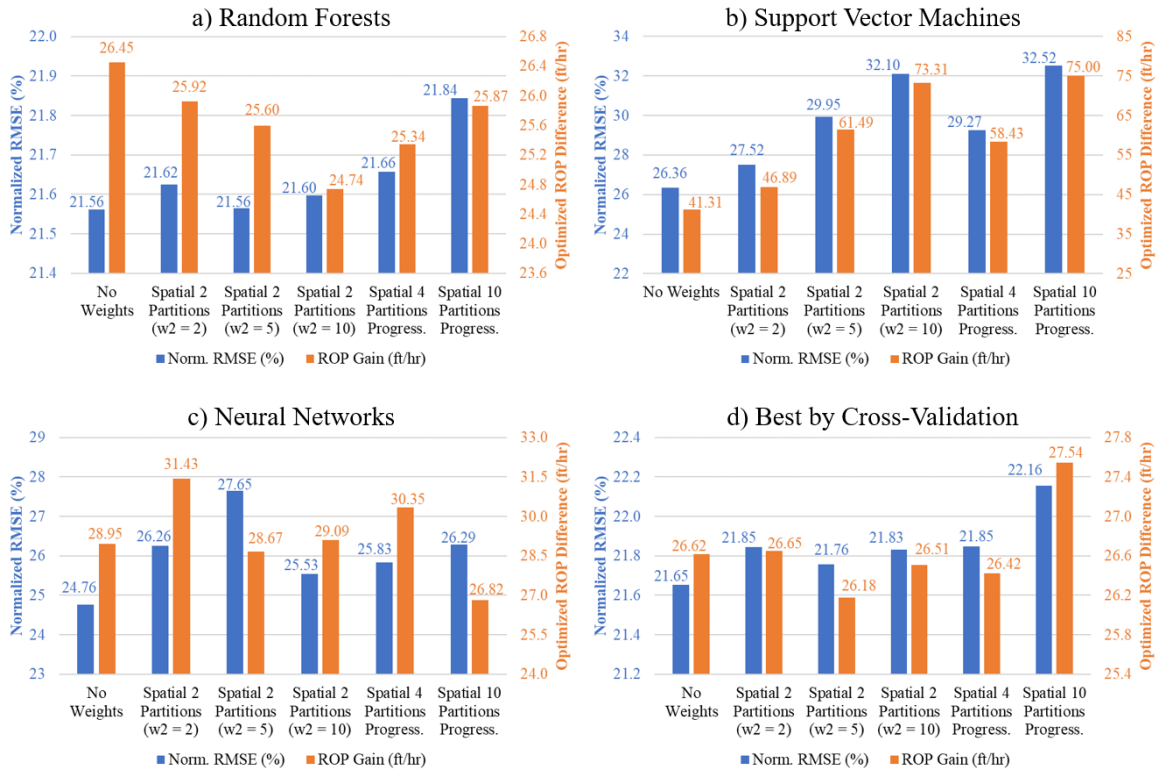
Figure 7.12: Normalized RMSE and ROP improvement for machine learning and cross-validation best performing ROP models in all 200ft dynamic range spatial proximity weighting scenarios.

Dynamic range analytical ROP modeling errors decrease with larger proximity weights or more training data partitions weighted progressively, with two-partition ten-fold weighting as the best alternative. Optimized ROP differences with analytical models do not vary significantly according to weighting. ML models trained with 200ft dynamic range performed better without sample weighting, with only RF two-partition five-fold weighting reaching the unweighted baseline. Therefore, normalized RMSE for the collection of best performing models according to CV error, heavily influenced by RF models, is lowest for the unweighted scenario.

7.3.3. Full Range of Training Data

Optimization results presented in Section 7.2 (Table 7.8) establish the baseline for full range weighting simulations. Table 7.15 displays two-way partition of full range training datasets with double spatial proximity weighting:

Table 7.15: Model normalized RMSE and drilling parameter optimization results for full range training dataset with 30ft retraining intervals and second half of training samples weighted double.

Full Range with Spatial Weights - Second Half of Training Dataset Double Weighted					
ROP Model	Norm. RMSE	ΔWOB (klb)	ΔRPM (rev/min)	Δq (gpm)	ΔROP (ft/hr)
Bingham (1964)	63.67	12.75	45.30	0.00	156.58
Modified B&Y	49.08	12.75	45.30	27.68	119.00
Hareland and Rampersad (1994)	62.81	11.13	45.30	0.00	112.32
Motahhari *et al*. (2010)	63.62	12.75	45.30	0.00	141.91
Random Forests	22.42	-9.38	1.57	15.03	45.09
Support Vector Machines	26.01	-2.46	18.86	-26.28	104.02
Neural Networks	28.90	-10.06	5.10	-18.97	62.65
Best by Cross Validation	22.46	-9.32	2.85	14.99	45.16
Best by Test Error	19.59	-6.34	8.78	-7.72	72.35

Significant improvements of almost 20% normalized RMSE are seen for analytical models. This massive performance gap is explained by analytical models emphasizing drilling behavior nearby optimized intervals out of the large number of samples in the training dataset. RF and SVM models perform slightly worse than the unweighted full range baseline, while NN achieves 3% lower normalized RMSE and 10ft/hr additional gains in ROP.

Increasing second partition weights to five times as much as samples in the first half of the full range training data ($w_1 = 1$ and $w_2 = 5$ in Eq. 7.2):

Table 7.16: Model normalized RMSE and drilling parameter optimization results for full range training dataset with 30ft retraining intervals and second half of training samples weighted five times more than first half.

Full Range with Spatial Weights - Second Half of Training Dataset Weighted 5 Times More					
ROP Model	Norm. RMSE	ΔWOB (klb)	ΔRPM (rev/min)	Δq (gpm)	ΔROP (ft/hr)
Bingham (1964)	48.87	12.75	45.30	0.00	141.26
Modified B&Y	41.33	12.75	45.30	27.68	112.75
Hareland and Rampersad (1994)	48.02	11.13	45.30	0.00	94.45
Motahhari *et al*. (2010)	48.82	12.75	45.30	0.00	124.55
Random Forests	22.27	-9.22	-0.20	12.65	45.38
Support Vector Machines	26.12	-1.81	20.73	-28.06	110.46
Neural Networks	28.20	-8.74	10.18	-11.67	66.53
Best by Cross Validation	22.40	-9.13	0.32	12.66	45.57
Best by Test Error	19.43	-6.30	9.00	-1.00	68.84

Normalized RMSE decreases substantially for analytical models and slightly for RF and NN in comparison with Table 7.15. Further enlarging proximity weights ($w_1 = 1$ and $w_2 = 10$ in Eq. 7.2):

Table 7.17: Model normalized RMSE and drilling parameter optimization results for full range training dataset with 30ft retraining intervals and second half of training samples weighted ten times more than first half.

Full Range with Spatial Weights - Second Half of Training Dataset Weighted 10 Times More					
ROP Model	Norm. RMSE	ΔWOB (klb)	ΔRPM (rev/min)	Δq (gpm)	ΔROP (ft/hr)
Bingham (1964)	43.50	12.75	45.30	0.00	134.79
Modified B&Y	38.06	12.75	45.30	27.68	108.56
Hareland and Rampersad (1994)	42.64	11.15	45.30	0.00	86.05
Motahhari *et al*. (2010)	43.44	12.75	45.30	0.00	117.04
Random Forests	22.22	-9.80	-0.62	11.73	43.46
Support Vector Machines	26.68	-3.97	12.87	-21.52	132.90
Neural Networks	27.91	-8.92	11.93	-12.92	75.49
Best by Cross Validation	22.29	-9.76	-0.08	11.72	43.64
Best by Test Error	19.17	-5.14	10.52	0.71	77.63

Once more, all models' performance improves except for SVM.

Full range progressive spatial proximity weighting with four-way partitioning is scrutinized next:

Table 7.18: Model normalized RMSE and drilling parameter optimization results for full range training dataset with 30ft retraining intervals and training samples divided into four partitions of equal size weighted progressively.

Full Range with Spatial Weights - Training Data Divided into 4 Partitions Weighted Progressively					
ROP Model	Norm. RMSE	ΔWOB (klb)	ΔRPM (rev/min)	Δq (gpm)	ΔROP (ft/hr)
Bingham (1964)	54.73	12.75	45.30	0.00	148.84
Modified B&Y	43.22	12.75	45.30	27.68	114.16
Hareland and Rampersad (1994)	53.86	11.17	45.30	0.00	100.85
Motahhari *et al*. (2010)	54.70	12.75	45.30	0.00	131.71
Random Forests	22.29	-10.05	1.66	15.04	43.70
Support Vector Machines	26.28	-1.70	18.16	-20.44	109.65
Neural Networks	27.76	-10.59	2.97	-21.56	54.68
Best by Cross Validation	22.34	-9.94	2.49	15.04	44.11
Best by Test Error	19.57	-6.44	10.04	-1.11	64.76

Contrasting Tables 7.15 and 7.18, model errors (except SVM) decrease with additional training data partitions. Increasing the number of full training data range divisions:

Table 7.19: Model normalized RMSE and drilling parameter optimization results for full range training dataset with 30ft retraining intervals and training samples divided into ten partitions of equal size weighted progressively.

Full Range with Spatial Weights - Training Data Divided into 10 Partitions Weighted Progressively					
ROP Model	Norm. RMSE	ΔWOB (klb)	ΔRPM (rev/min)	Δq (gpm)	ΔROP (ft/hr)
Bingham (1964)	50.14	12.75	45.30	0.00	144.39
Modified B&Y	40.57	12.75	45.30	27.68	112.91
Hareland and Rampersad (1994)	49.21	11.12	45.30	0.00	94.53
Motahhari *et al*. (2010)	50.13	12.75	45.30	0.00	126.83
Random Forests	22.13	-9.60	-0.01	12.70	42.20
Support Vector Machines	27.32	-5.62	5.24	1.88	140.80
Neural Networks	27.93	-10.77	6.20	-14.47	54.97
Best by Cross Validation	22.21	-9.54	0.65	12.70	43.17
Best by Test Error	19.40	-6.22	5.06	6.60	68.10

Normalized RMSE decreases for RF and the four analytical models with additional training data partitions. Analytical ROP models in Table 7.19 perform significantly better than the full range unweighted baseline (Table 7.8). However, their normalized RMSE errors are still higher than metrics for unweighted formation-dependent (Table 6.14) and dynamic range (Table 7.5) techniques.

Summarizing results for full training data range with spatial proximity weighting:
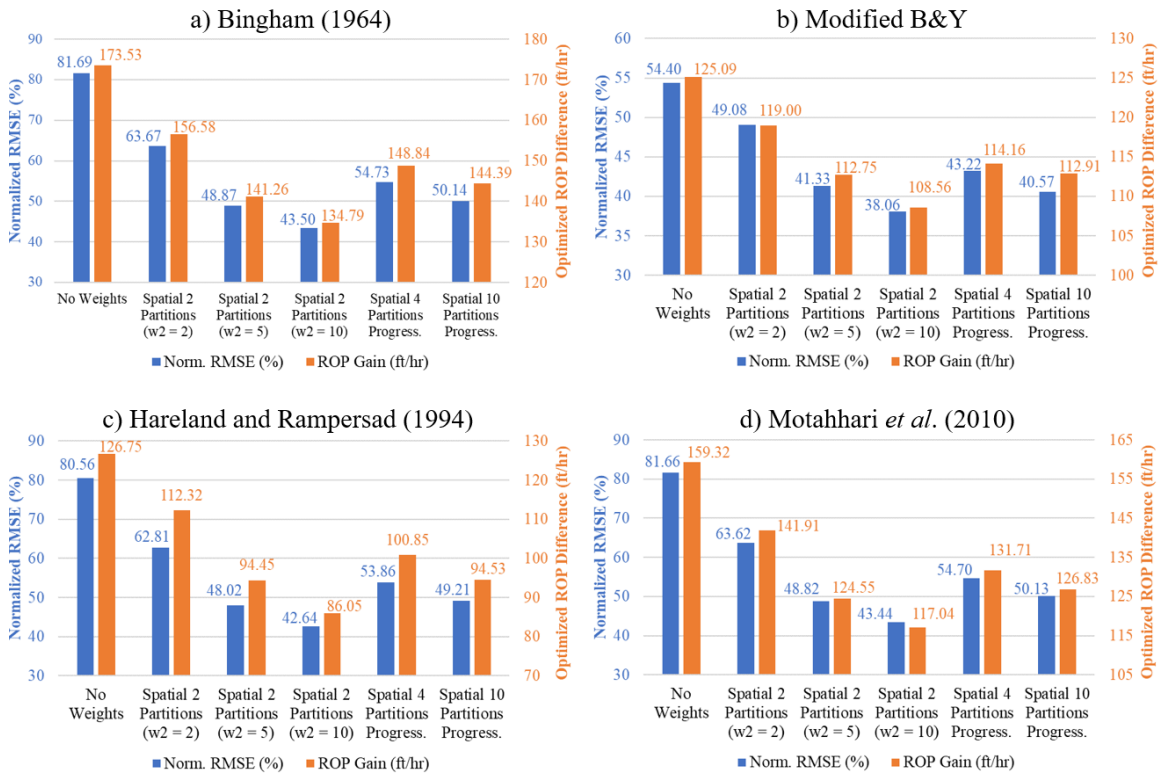
Figure 7.13: Normalized RMSE and ROP improvement for analytical ROP models in all full range spatial proximity weighting scenarios.
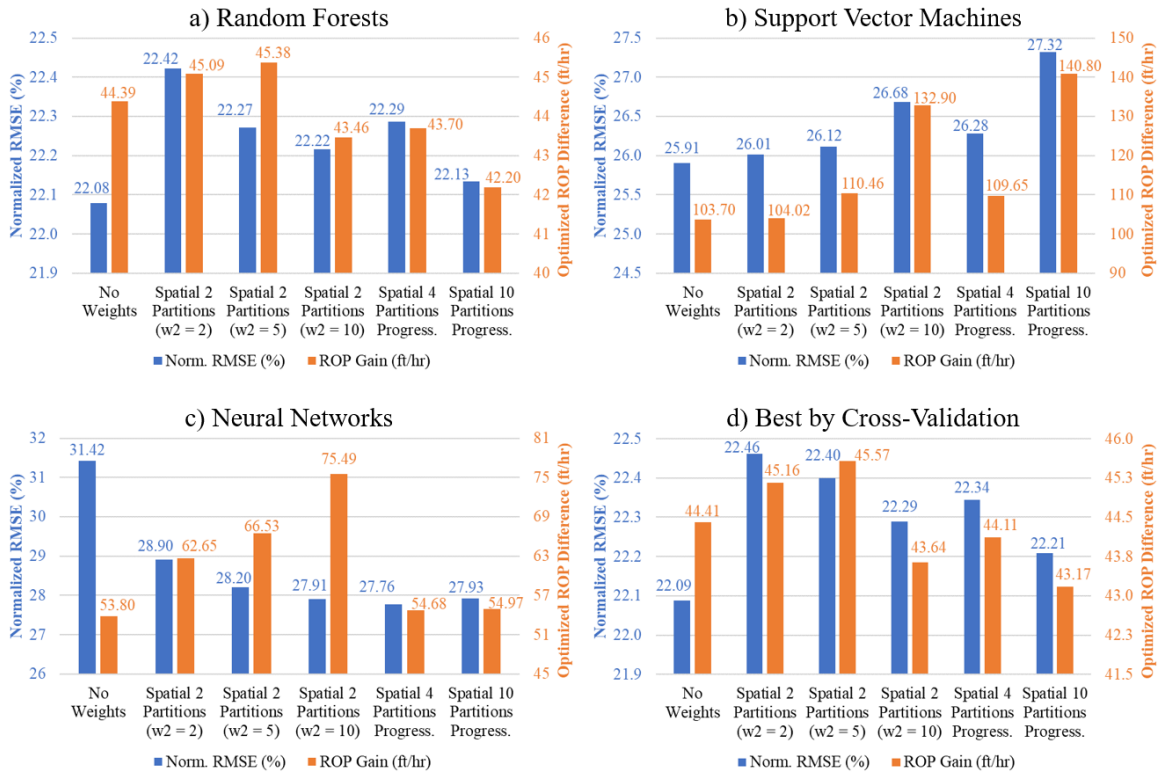
Figure 7.14: Normalized RMSE and ROP improvement for machine learning and cross-validation best performing ROP models in all full range spatial proximity weighting scenarios.

Spatial proximity weighting accomplishes substantial normalized RMSE reduction for full range analytical models. Similar to dynamic range spatial weighting, trends of decreasing error with more partitions or larger proximity weights are observed, with ten-fold weighting in two training data segments achieving the best analytical model performance. ROP improvements predicted by the four analytical models follow the opposite trend, decreasing in magnitude as models become more accurate even though operational parameter recommendations remain the same. Full range RF and SVM models do not improve with spatial weighting techniques, while NN adheres to the same normalized RMSE decreasing trends as analytical models. The collection of best performing models according to CV error is once again governed by RF results.

7.4. PARAMETER SIMILARITY WEIGHTING

Parameter similarity weighting appraises data samples by considering operational parameters' closeness to the mean depth, WOB, RPM and flow rate nearby the optimization interval. Parameter averages in the second half of the preceding optimization interval (last 15ft) are proposed as the references for similarity weighting. This approach presumes that data points with similar operational parameters experience comparable drilling conditions, seeking to generate ROP models predisposed to drilling behavior adjacent to the interval to be optimized. Generalizing the model fitting objective function in Eq. 7.2 to incorporate different weights for each sample in the training dataset:

$$\min\left(\sum_{i=1}^{N} w_i r_i^2\right) = \min\left(\sum_{i=1}^{N} w_i \left(ROP_{Field,i} - ROP_{Model,i}\right)^2\right) \tag{7.3}$$

where N is the number of samples in the training dataset and w_i is the weight assigned to ith sample. Similarity metrics according to WOB are defined as:

$$w_{WOB,i} = \max\left[0, \left(1 - k_{WOB}\frac{|WOB_i - WOB_{avg}|}{WOB_{avg}}\right)\right] \tag{7.4}$$

where k_{WOB} is a weighting constant for the WOB parameter and WOB_{avg} is the mean WOB in the 15ft preceding the optimized interval. In Eq. 7.4, if k_{WOB} equals to one and WOB_i more than doubles WOB_{avg}, the maximum function determines that $w_{WOB,i}$ is zero for the data point in question. Weights analogous to Eq. 7.4 are derived for depth, RPM and flow rate. Equation 7.5 combines all four parameter weights into one sample similarity weighting formulation:

$$w_i = 1 + w_{D,i} + w_{WOB,i} + w_{RPM,i} + w_{q,i} \tag{7.5}$$

Weighting constants, such as k_{WOB} in Eq. 7.4, can be customized to specific needs, placing more emphasis on individual operational drilling parameters. Since similarity weights are nonnegative, the minimum sample weight given by Eq. 7.5 is equal to one.

7.4.1. Formation-Dependent Training Data

Similar to spatial proximity weighting, cross-validation and optimization computational times with parameter similarity weights do not vary significantly from the unweighted lithology-dependent baseline (Section 6.4). Model selection agreement between CV and test error drift around 40-50%, with no clear trends. Hence, normalized RMSE and optimization results compose the comparison metrics of interest. The potential of parameter similarity weighting is investigated with weighting constants (k) for all four drilling parameters equal to one:

Table 7.20: Model normalized RMSE and drilling parameter optimization results for formation-dependent training dataset with 30ft retraining intervals and parameter similarity weighting.

Formation Dependent with Parameter Similarity Weights throughout Training Dataset					
ROP Model	Norm. RMSE	ΔWOB (klb)	ΔRPM (rev/min)	Δq (gpm)	ΔROP (ft/hr)
Bingham (1964)	33.11	12.82	45.62	0.00	119.20
Modified B&Y	32.44	12.82	45.62	8.28	92.48
Hareland and Rampersad (1994)	32.72	11.98	45.62	0.00	79.34
Motahhari *et al*. (2010)	33.12	12.82	45.62	0.00	102.41
Random Forests	22.44	-5.91	-7.01	-7.37	24.13
Support Vector Machines	30.29	-3.21	-0.04	-2.26	51.96
Neural Networks	26.35	-5.21	-1.07	-11.19	30.39
Best by Cross Validation	22.86	-5.55	-5.31	-7.38	24.58
Best by Test Error	19.33	-2.46	5.49	-4.35	38.06

All ROP models, except SVM, exhibit slightly lower errors compared to the unweighted baseline in Table 6.14. ROP improvements remain similar.

7.4.2. Dynamic Range of Training Data

Dynamic range parameter closeness weighting analysis begins with exclusive WOB similarity scrutiny ($k_{WOB} = 1$ in Eq. 7.4 and $w_D = w_{RPM} = w_q = 0$ in Eq. 7.5):

Table 7.21: Model normalized RMSE and drilling parameter optimization results for 200ft dynamic range training dataset with 30ft retraining intervals and WOB similarity weighting ($k_{WOB} = 1$).

200ft Dynamic Range with WOB Similarity Weights throughout Training Dataset ($kWOB$ = 1)					
ROP Model	Norm. RMSE	ΔWOB (klb)	ΔRPM (rev/min)	Δq (gpm)	ΔROP (ft/hr)
Bingham (1964)	33.05	12.75	45.30	0.00	114.76
Modified B&Y	32.46	12.75	45.30	9.64	87.24
Hareland and Rampersad (1994)	32.48	11.08	45.30	0.00	65.32
Motahhari *et al.* (2010)	32.95	12.75	45.30	0.00	92.17
Random Forests	21.57	-7.04	-8.74	-7.59	26.53
Support Vector Machines	27.51	-6.22	0.34	0.65	47.95
Neural Networks	25.01	-6.61	-1.81	-8.16	28.40
Best by Cross Validation	21.67	-6.77	-7.58	-7.63	26.76
Best by Test Error	18.61	-4.53	4.33	-4.68	37.19

Normalized RMSE decreases marginally and ROP gains increase for all models in relation to the unweighted dynamic range baseline (Table 7.5). Increasing the WOB weighting constant to five ($k_{WOB} = 5$ in Eq. 7.4 and $w_D = w_{RPM} = w_q = 0$ in Eq. 7.5):

Table 7.22: Model normalized RMSE and drilling parameter optimization results for 200ft dynamic range training dataset with 30ft retraining intervals and WOB similarity weighting ($k_{WOB} = 5$).

200ft Dynamic Range with WOB Similarity Weights throughout Training Dataset ($kWOB$ = 5)					
ROP Model	Norm. RMSE	ΔWOB (klb)	ΔRPM (rev/min)	Δq (gpm)	ΔROP (ft/hr)
Bingham (1964)	32.51	12.75	45.30	0.00	113.13
Modified B&Y	31.97	12.75	45.30	9.64	86.11
Hareland and Rampersad (1994)	31.92	11.08	45.30	0.00	65.49
Motahhari *et al.* (2010)	32.39	12.75	45.30	0.00	90.69
Random Forests	21.58	-7.10	-7.40	-5.46	25.74
Support Vector Machines	27.02	-5.65	0.57	-0.46	42.30
Neural Networks	26.57	-7.06	-1.74	-13.27	29.79
Best by Cross Validation	21.70	-6.92	-6.78	-5.41	25.49
Best by Test Error	18.91	-4.51	2.66	-5.14	34.27

With $k_{WOB} = 5$, samples measuring WOB values distanced more than 20% from the reference WOB average (last half of preceding optimization interval) are attributed w_{WOB}

$= 0$ and $w_i = 1$. This scenario adds more variability to WOB similarity weights and samples with WOB closer to the reference nearby the optimized interval have increased impact in model training. In comparison to $k_{WOB} = 1$, normalized RMSE decreases for analytical and SVM models.

Including all four drilling parameters into the similarity weighting scheme with $k = 1$ weighting constants:

Table 7.23: Model normalized RMSE and drilling parameter optimization results for 200ft dynamic range training dataset with 30ft retraining intervals and parameter similarity weighting.

200ft Dynamic Range with Parameter Similarity Weights throughout Training Dataset					
ROP Model	Norm. RMSE	ΔWOB (klb)	ΔRPM (rev/min)	Δq (gpm)	ΔROP (ft/hr)
Bingham (1964)	33.28	12.75	45.30	0.00	114.72
Modified B&Y	32.75	12.75	45.30	9.64	87.53
Hareland and Rampersad (1994)	32.68	11.09	45.30	0.00	67.45
Motahhari *et al.* (2010)	33.19	12.75	45.30	0.00	92.25
Random Forests	21.56	-6.35	-6.87	-7.60	26.27
Support Vector Machines	29.80	-5.96	0.36	-0.34	60.66
Neural Networks	25.43	-7.23	-0.27	-12.65	35.44
Best by Cross Validation	21.78	-6.05	-5.93	-7.46	27.17
Best by Test Error	18.73	-4.05	3.41	-3.71	39.19

Model performance for all ROP models except RF worsens with respect to exclusive WOB importance with $k_{WOB} = 1$ (Table 7.21). Analytical model errors are almost identical to the unweighted baseline (Table 7.5), indicating that unit similarity weighting constants for all four parameters did not introduce many model training changes with dynamic range segmentation. SVM and NN perform slightly worse than the baseline and ROP improvements are equivalent.

Next, varying weighting constants are attributed to the four drilling parameters ($k_D = 10$, $k_{WOB} = 5$, $k_{RPM} = 10$, $k_q = 10$ in Eq. 7.4):

Table 7.24: Model normalized RMSE and drilling parameter optimization results for 200ft dynamic range training dataset with 30ft retraining intervals and parameter similarity weighting. Varying weighting constants established for different parameters.

200ft Dynamic Range with Parameter Similarity Weights throughout Training Dataset (k = 10, 5, 10, 10)					
ROP Model	Norm. RMSE	ΔWOB (klb)	ΔRPM (rev/min)	Δq (gpm)	ΔROP (ft/hr)
Bingham (1964)	31.88	12.75	45.30	0.00	113.49
Modified B&Y	31.43	12.75	45.30	9.64	85.78
Hareland and Rampersad (1994)	31.24	11.07	45.30	0.00	67.11
Motahhari *et al*. (2010)	31.81	12.75	45.30	0.00	91.56
Random Forests	21.76	-7.57	-9.26	-5.73	25.49
Support Vector Machines	34.55	-4.73	0.34	-2.95	84.29
Neural Networks	25.72	-7.41	-1.40	-13.77	27.95
Best by Cross Validation	21.94	-7.36	-8.19	-5.70	26.78
Best by Test Error	18.96	-3.46	2.05	-5.49	37.56

Following analysis of the previous k_{WOB} = 5 similarity weighting technique, data points where depth, RPM or flow rate differ more than 10% from the 15ft mean references will be assigned weights equal to zero for such variables. This weighting strategy emphasizes WOB similarities based on field knowledge and hypothesis testing conclusions (Table 5.1) that WOB is the operational parameter with biggest effect on ROP. Model performance improves considerably for analytical ROP models, with the lowest errors among parameter similarity weighting simulations. ML models' normalized RMSE increase in comparison to the previous weighting scheme. All models, apart from SVM, display lower average errors than unweighted formation-dependent models in Table 6.14. These results suggest that defining lithology by geomechanical properties that directly affect drilling behavior (and operational parameters) may be more beneficial to ROP modeling than the standard depositional facies classification, which incorporates heterogeneity.

The figures below encompass all dynamic range spatial proximity and parameter similarity weighting scenarios:

a) Bingham (1964)

b) Modified B&Y

c) Hareland and Rampersad (1994)

d) Motahhari *et al*. (2010)
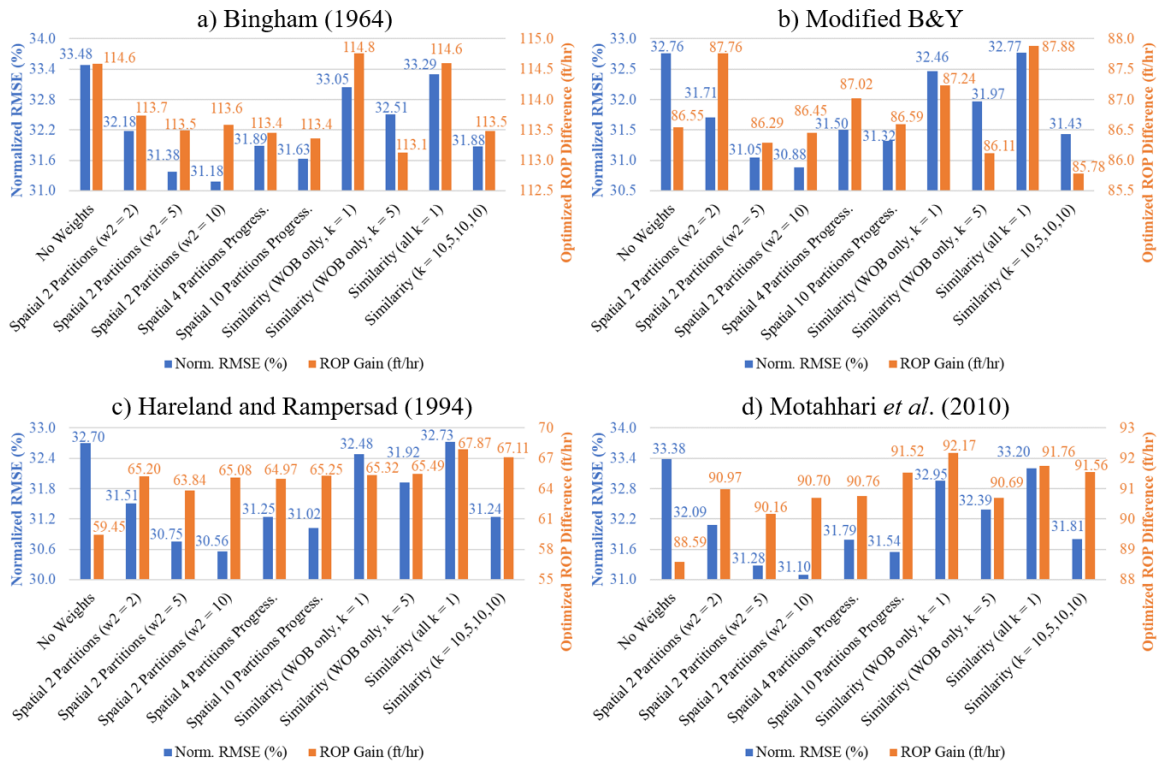
Figure 7.15: Normalized RMSE and ROP improvement for analytical ROP models in all 200ft dynamic range weighting scenarios.
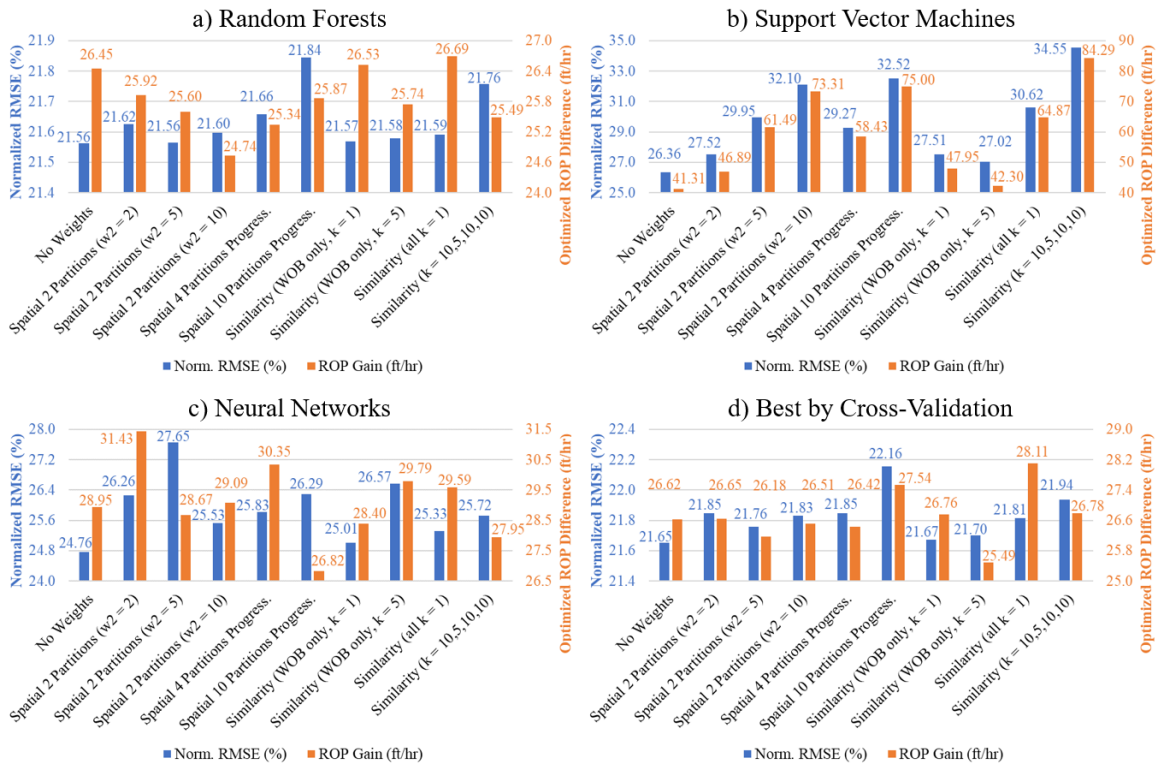
Figure 7.16: Normalized RMSE and ROP improvement for machine learning and cross-validation best performing ROP models in all 200ft dynamic range weighting scenarios.

Based on Fig. 7.15, two-partition spatial proximity weighting with $w_2 = 10$ is the recommendation for dynamic range analytical ROP models. ML models trained with 200ft dynamic training data range are best left unweighted (Fig. 7.16).

7.4.3. Full Range of Training Data

WOB similarity with unit weighting constant ($k_{WOB} = 1$ in Eq. 7.4 and $w_D = 0$, $w_{RPM} = 0$, $w_q = 0$ in Eq. 7.5) leads to the following optimized parameter recommendations for models trained with full training data ranges:

Table 7.25: Model normalized RMSE and drilling parameter optimization results for full range training dataset with 30ft retraining intervals and WOB similarity weighting ($k_{WOB} = 1$).

Full Range with WOB Similarity Weights throughout Training Dataset ($kWOB = 1$)					
ROP Model	Norm. RMSE	ΔWOB (klb)	ΔRPM (rev/min)	Δq (gpm)	ΔROP (ft/hr)
Bingham (1964)	77.10	12.75	45.30	0.00	169.82
Modified B&Y	52.04	12.75	45.30	27.68	119.37
Hareland and Rampersad (1994)	76.05	11.15	45.30	0.00	126.89
Motahhari *et al*. (2010)	77.04	12.75	45.30	0.00	156.44
Random Forests	22.10	-9.11	0.46	13.91	44.88
Support Vector Machines	26.19	-2.73	15.40	-20.65	113.39
Neural Networks	30.48	-8.72	4.60	-19.14	66.34
Best by Cross Validation	22.16	-9.02	1.56	13.89	44.51
Best by Test Error	19.68	-5.53	10.39	-1.12	72.21

Model errors are lower than the full range unweighted baseline (Table 7.8) for all analytical models and neural networks. With larger WOB weighting constant ($k_{WOB} = 5$ in Eq. 7.4 and $w_D = 0$, $w_{RPM} = 0$, $w_q = 0$ in Eq. 7.5):

Table 7.26: Model normalized RMSE and drilling parameter optimization results for full range training dataset with 30ft retraining intervals and WOB similarity weighting ($k_{WOB} = 5$).

Full Range with WOB Similarity Weights throughout Training Dataset ($kWOB = 5$)					
ROP Model	Norm. RMSE	ΔWOB (klb)	ΔRPM (rev/min)	Δq (gpm)	ΔROP (ft/hr)
Bingham (1964)	73.15	12.75	45.30	0.00	165.45
Modified B&Y	50.97	12.75	45.30	27.68	119.74
Hareland and Rampersad (1994)	72.29	11.16	45.30	0.00	122.11
Motahhari *et al*. (2010)	73.14	12.75	45.30	0.00	151.89
Random Forests	22.12	-9.88	0.97	15.71	45.37
Support Vector Machines	26.16	-2.59	16.49	-25.45	105.93
Neural Networks	31.91	-8.90	4.02	-9.37	55.54
Best by Cross Validation	22.18	-9.75	2.21	15.66	45.45
Best by Test Error	19.64	-5.86	6.94	2.14	68.51

Analytical and SVM full range ROP models benefit from more WOB weighting variability (higher k_{WOB}). On the other hand, NN normalized RMSE increases and exceeds baseline error.

Optimization results with unit k constants for all four drilling parameters are presented in the table below:

Table 7.27: Model normalized RMSE and drilling parameter optimization results for full range training dataset with 30ft retraining intervals and parameter similarity weighting.

Full Range with Parameter Similarity Weights throughout Training Dataset (k = 1, 1, 1, 1)					
ROP Model	Norm. RMSE	ΔWOB (klb)	ΔRPM (rev/min)	Δq (gpm)	ΔROP (ft/hr)
Bingham (1964)	77.83	12.75	45.30	0.00	170.27
Modified B&Y	53.50	12.75	45.30	27.68	121.59
Hareland and Rampersad (1994)	76.86	11.16	45.30	0.00	125.95
Motahhari *et al*. (2010)	77.79	12.75	45.30	0.00	156.24
Random Forests	22.01	-9.57	0.85	14.12	43.59
Support Vector Machines	26.98	-4.91	11.55	-0.83	135.17
Neural Networks	29.97	-9.46	11.73	-11.78	62.27
Best by Cross Validation	22.16	-9.55	1.57	14.10	43.92
Best by Test Error	19.60	-6.89	8.99	5.55	79.35

This weighting scheme works particularly well for RF models, which perform better than the unweighted baseline for the first time out of all dynamic and full range weighting scenarios. Analytical ROP models display lower normalized RMSE with exclusive unit WOB weighting constant, in analogous manner to dynamic range weighting observations. Finally, establishing separate weighting constants for each parameter (k_D = 10, k_{WOB} = 5, k_{RPM} = 10, k_q = 10 in Eq. 7.4) in order to emphasize WOB similarities:

Table 7.28: Model normalized RMSE and drilling parameter optimization results for full range training dataset with 30ft retraining intervals and parameter similarity weighting. Varying weighting constants established for different parameters.

Full Range with Parameter Similarity Weights throughout Training Dataset (k = 10, 5, 10, 10)					
ROP Model	Norm. RMSE	ΔWOB (klb)	ΔRPM (rev/min)	Δq (gpm)	ΔROP (ft/hr)
Bingham (1964)	53.08	12.75	45.30	0.00	147.41
Modified B&Y	42.34	12.75	45.30	27.68	113.53
Hareland and Rampersad (1994)	52.28	11.16	45.30	0.00	99.86
Motahhari *et al*. (2010)	53.08	12.75	45.30	0.00	129.80
Random Forests	22.22	-9.95	-1.18	8.04	40.79
Support Vector Machines	27.73	-5.61	6.91	0.66	154.63
Neural Networks	27.80	-9.69	5.12	-12.70	57.53
Best by Cross Validation	22.41	-9.87	-1.01	8.05	42.62
Best by Test Error	19.44	-7.37	3.91	0.99	73.07

Table 7.28 demonstrates that vast performance improvements can be achieved for full range analytical models with parameter similarity weighting. Bingham (1964), corrected Hareland and Rampersad (1994) and Motahhari *et al*. (2010) accomplish nearly 30% lower

normalized RMSE than unweighted full range models in Table 7.8. NN models also boast lower errors than the baseline, but RF and SVM perform slightly worse. All ML models exhibit higher ROP improvements.

Figures 7.17 and 7.18 illustrate spatial proximity and parameter similarity weighting errors and ROP improvements for models trained with full training data range:
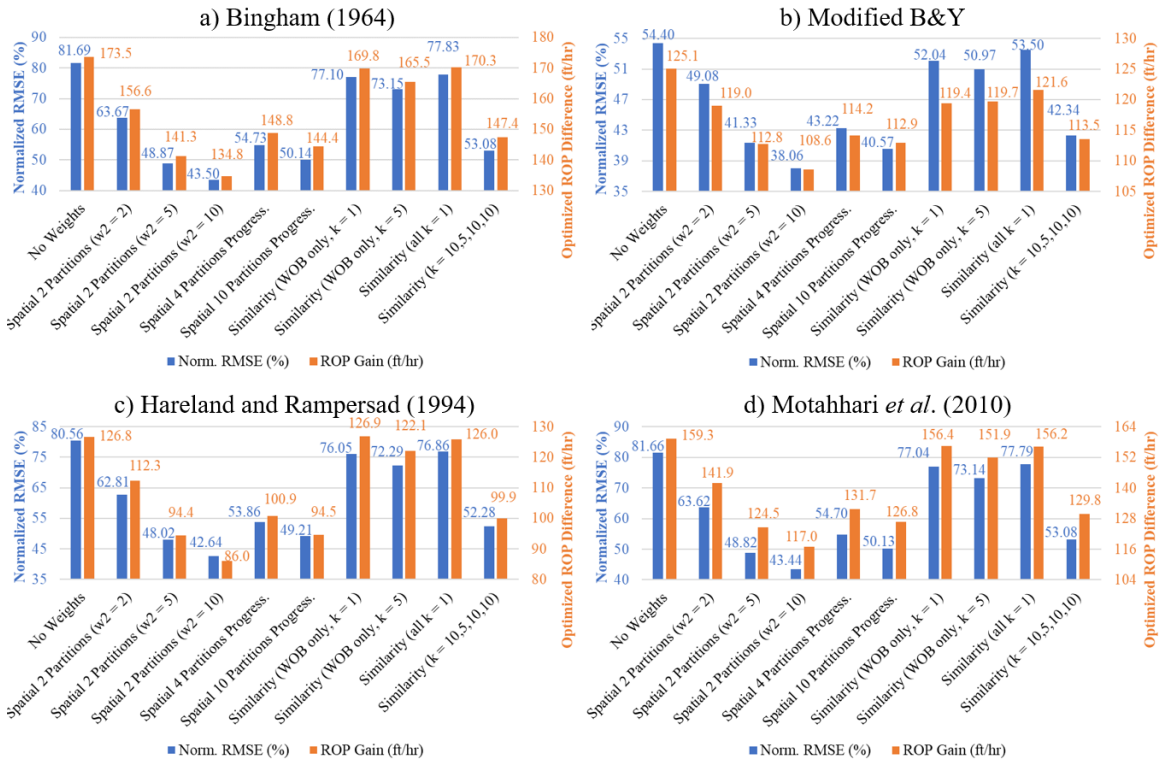
Figure 7.17: Normalized RMSE and ROP improvement for analytical ROP models in all full range weighting scenarios.
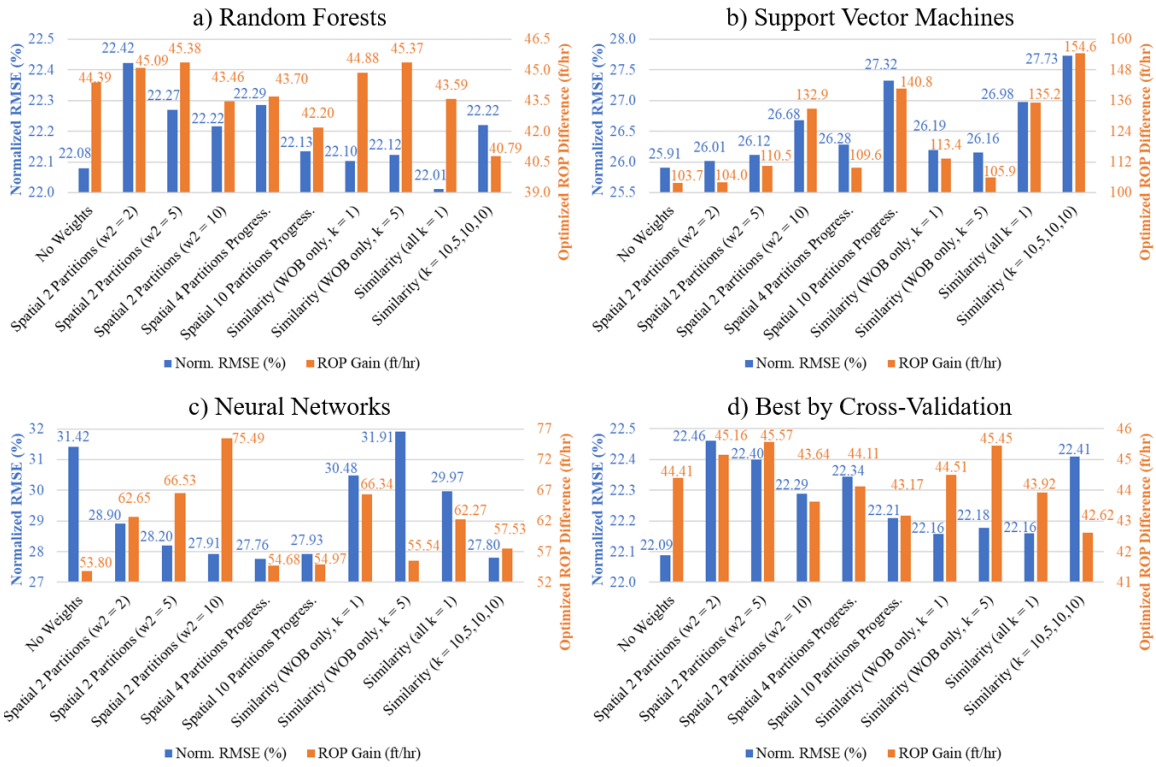
Figure 7.18: Normalized RMSE and ROP improvement for machine learning and cross-validation best performing ROP models in all full range weighting scenarios.

In terms of parameter similarity, full range analytical ROP models perform best in the last simulation, with varying weighting constants ($k_D = 10$, $k_{WOB} = 5$, $k_{RPM} = 10$, $k_q = 10$). Nonetheless, two-partition ten-fold ($w_2 = 10$) spatial weighting produces the lowest normalized RMSE for all analytical models with full range training dataset. The same weighting technique delivers the best performing analytical ROP models overall when applied in conjunction with 200ft dynamic training data ranges. Full range random forests models yield the lowest errors with unit similarity weighting constants for all four drilling parameters (22.01% average normalized RMSE). However, this error metric is still higher than the one with unweighted 200ft dynamic range RF models (21.56% normalized RMSE). SVM models are not conducive to any weighting scenario but benefit the most

from full range of training data, as the unweighted full range scenario results in 25.91% normalized RMSE and 103.7ft/hr ROP improvement compared to 26.36% normalized RMSE and 41.31ft/hr ROP improvement with unweighted dynamic range. Referring to Fig. 2.11, only support vector data points affect SVM models. This circumstance is probably the reason why such models were the only to favor training with full training data ranges.

Lastly, NN showed similar error reduction trends as analytical models with full range weighting techniques, likely due to the simple model architecture (2 hidden layers with 4 and 2 neurons, respectively). Full range NN models with four-partition progressive spatial proximity weighting result in the lowest errors (27.76% normalized RMSE and 54.68ft/hr ROP difference), which are still higher than metrics observed with unweighted dynamic range NN models (24.76% normalized RMSE and 28.95ft/hr ROP difference). Curiously, the two-partition ten-fold spatial proximity weighting scheme generated ROP gains significantly higher than any other full range NN scenario. ROP, WOB, RPM and flow rate difference histograms for optimizations according to NN models trained with such weighting technique are reproduced below in comparison with unweighted full range NN models:
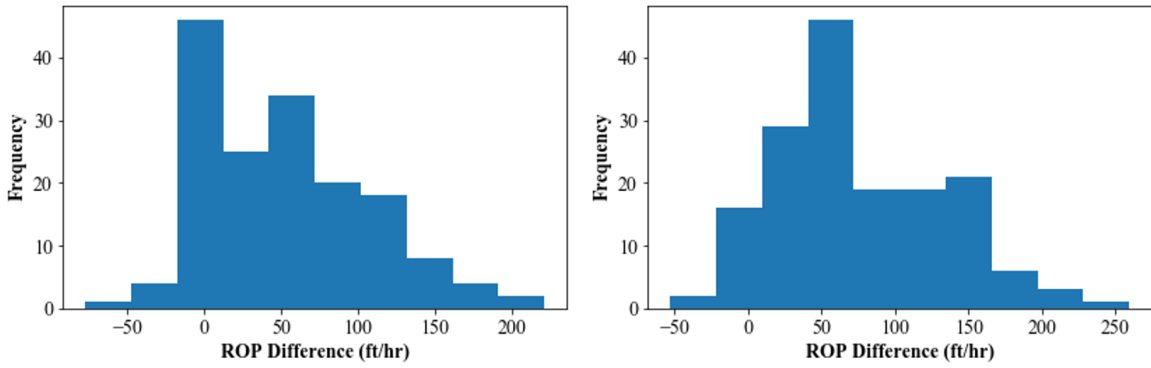
Figure 7.19: ROP difference distribution in 162 interval optimizations for full range NN ROP models with 30ft retraining intervals. Left plot shows results for unweighted models and right plot displays models fitted with two-partition ten-fold spatial proximity weighting.
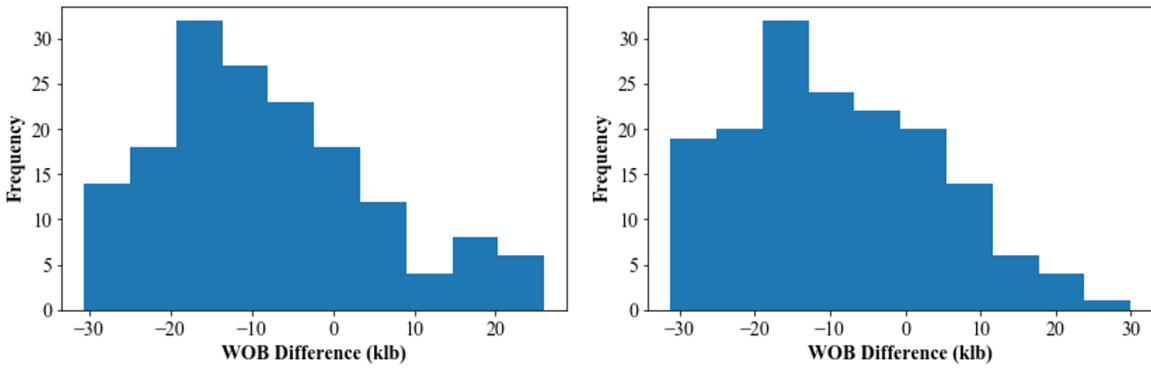
Figure 7.20: WOB difference distribution in 162 interval optimizations for full range NN ROP models with 30ft retraining intervals. Left plot shows results for unweighted models and right plot displays models fitted with two-partition ten-fold spatial proximity weighting.
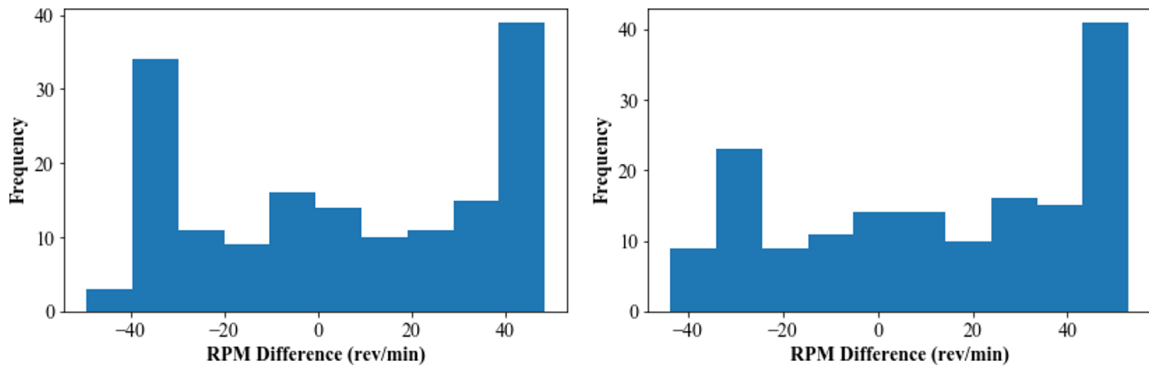
Figure 7.21: RPM difference distribution in 162 interval optimizations for full range NN ROP models with 30ft retraining intervals. Left plot shows results for unweighted models and right plot displays models fitted with two-partition ten-fold spatial proximity weighting.
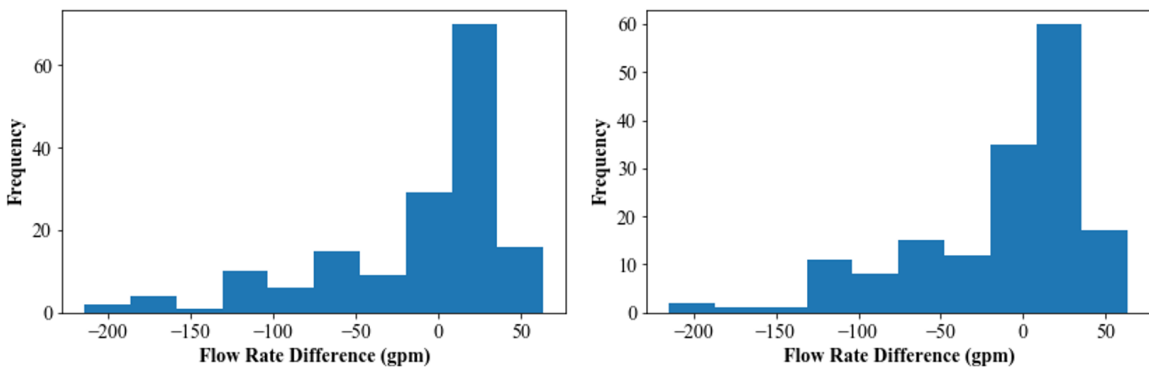
Figure 7.22: Flow rate difference distribution in 162 interval optimizations for full range NN ROP models with 30ft retraining intervals. Left plot shows results for unweighted models and right plot displays models fitted with two-partition ten-fold spatial proximity weighting.

Unweighted and weighted distributions in Figs 7.19-7.22 exhibit very similar shapes. Weighted ROP and RPM difference histograms are shifted towards more positive values, while WOB optimization recommendations tend towards the more negative portion of the curve. Flow rate difference distributions are virtually the same. Table 7.8 displays average full range NN unweighted modeling performance and optimization results (normalized RMSE = 31.42%, ΔWOB = -8.18klb, ΔRPM = 6.06rev/min, Δq = -12.54gpm, ΔROP =

53.80ft/hr), while Table 7.17 presents the same metrics for two-partition ten-fold spatial weighting (normalized RMSE = 27.91%, ΔWOB = -8.92klb, ΔRPM = 11.93rev/min, Δq = -12.92gpm, ΔROP = 75.49ft/hr). The additional 22ft/hr ROP improvements predicted by more accurate weighted models are a consequence of more negative WOB values and higher RPM in most optimized intervals.

Results presented in this section indicate that establishing appropriate weighing constants is paramount in achieving adequate model performance with parameter similarity weighting. With the exception of RF, spatial proximity weighting techniques outperformed parameter similarity weighting for models fitted to full training data ranges. Unweighted SVM produced the only full range models to perform best overall, as 200ft dynamic range data segmentation dominated in terms of model accuracy.

7.5. INCORPORATING HISTORICAL DATA

Historical data from offset wells provide valuable information about drilling experience within a geographical region. Knowledge about drilling behavior in the later portions of a rock formation helps ROP models prepare effective operational parameter recommendations in advance of reaching such segments. Even though offset well data are typically employed in a post-drilling framework (Chapter 5) to produce drilling roadmaps for an upcoming well, rock formations tend to display high degree of heterogeneity and possibly react to drilling very differently compared to nearby wells. Furthermore, exploratory wells are drilled with no access to historical drilling data in the region. Hence, the approach explored in this section takes advantage of both historical and real-time data in training ROP models. Behounek *et al*. (2017a) explored this general idea of constructing drilling models with both historical and real-time data. Unfortunately, no additional datasets near the Bakken shale well analyzed in this study were available. To circumvent

this issue, the suggested strategy sets aside a portion of each formation's measured samples as historical data. In a lithology-dependent setting, the historical data for each formation is available as early as the formation's first optimization interval. For dynamic range and full range segmentation techniques, formation historical data is aggregated to the training dataset once the interval to be optimized starts in said formation, ensuring that only one formation's historical data are available for model fitting at each retraining interval. The effect of increasing historical data availability is investigated by varying the percentage of data separated from the real-time dataset (10%-20%-30%).

7.5.1. Formation-Dependent Training Data

Before analyzing the impact of incorporating historical data to the training dataset, performance results for formation-dependent training data with weighting techniques from Sections 7.3.1 and 7.4.1 are summarized:

Table 7.29: ROP model performance comparison for formation-dependent training
dataset with 30ft retraining intervals and different weighting techniques.

Formation Dependent	No Weights		Spatial Weights 2 Partitions		Param. Similarity Weights	
ROP Model	Abs. Error	Norm. RMSE	Abs. Error	Norm. RMSE	Abs. Error	Norm. RMSE
Bingham (1964)	37.46	33.34	35.19	31.86	37.15	33.11
Modified B&Y	35.23	32.67	33.39	31.38	34.94	32.44
Hareland and Rampersad (1994)	37.35	32.91	35.10	31.48	37.06	32.72
Motahhari *et al*. (2010)	37.69	33.36	35.35	31.84	37.37	33.12
Random Forests	23.81	22.61	23.55	22.38	23.44	22.44
Support Vector Machines	27.98	26.96	28.60	27.86	30.24	30.29
Neural Networks	27.96	26.87	29.12	27.49	29.03	26.35
Best by Cross Validation	24.20	24.06	24.14	22.90	23.82	22.86
Best by Test Error	19.44	20.30	18.67	19.10	18.92	19.33
Best CV / Test Error Agreement	43.02%	45.27%	39.19%	46.62%	43.24%	44.59%

A percentage of random data points in all formations, varying from 10% to 30%, is removed from the original dataset and set aside as historical data. Historical samples are combined with the training dataset in the first optimization interval of each formation:

227

Table 7.30: ROP model performance comparison for formation-dependent training dataset with 30ft retraining intervals incorporating varying amounts of historical data.

Formation Dependent	10% Historical Data		20% Historical Data		30% Historical Data	
ROP Model	Abs. Error	Norm. RMSE	Abs. Error	Norm. RMSE	Abs. Error	Norm. RMSE
Bingham (1964)	34.15	31.87	33.65	31.78	32.94	31.38
Modified B&Y	32.29	31.13	31.93	31.06	31.34	30.70
Hareland and Rampersad (1994)	33.89	31.44	33.34	31.33	32.61	30.91
Motahhari *et al*. (2010)	34.19	31.85	33.64	31.73	32.94	31.33
Random Forests	16.64	17.46	15.93	16.60	14.96	15.60
Support Vector Machines	19.34	21.34	18.52	20.51	17.56	19.57
Neural Networks	19.16	21.14	19.30	20.58	18.75	19.64
Best by Cross Validation	16.65	17.49	15.98	16.61	14.92	15.63
Best by Test Error	14.44	16.22	13.50	15.30	12.78	14.37
Best CV / Test Error Agreement	58.39%	57.72%	63.09%	66.44%	71.81%	69.80%

Aggregation of historical data to the training dataset results in much lower errors for all formation-dependent ROP models, which perform significantly better compared to Table 7.29. Best CV/test error model selection agreements are substantially higher and improve with incremental percentages of historical data. Model errors with 30% historical data approach those obtained with the entire formation data available (Table 5.7). Computational times remain similar to previous investigations. Analyzing model selections according to CV and test error for the 30% historical data scenario:

Table 7.31: Model selection and cross-validation/test error agreement for formation-dependent training dataset with 30ft retraining intervals and 30% historical data.

Formation Dependent - 30% Historical Data				
ROP Model	CV Abs. Error	CV Norm. RMSE	Abs. Error	Norm. RMSE
Bingham (1964)	0.00%	0.00%	0.67%	0.67%
Modified B&Y	0.00%	0.00%	2.01%	1.34%
Hareland and Rampersad (1994)	0.00%	0.00%	0.67%	2.01%
Motahhari *et al*. (2010)	0.00%	0.00%	0.00%	0.67%
Random Forests	96.64%	96.64%	72.48%	71.81%
Support Vector Machines	3.36%	2.68%	12.75%	9.40%
Neural Networks	0.00%	0.67%	11.41%	14.09%
Best CV / Test Error Agreement			71.81%	69.80%

Table 7.31 shows that random forests models are the best performers on test data much more frequently with historical data in the training set, driving up CV/test error model agreement considerably. Analytical ROP models rarely display the lowest error in optimized intervals.

Optimization results for formation-dependent models with 30% historical data are presented in the table below:

Table 7.32: Model normalized RMSE and drilling parameter optimization results for formation-dependent training dataset with 30ft retraining intervals and 30% historical data.

Formation Dependent with 30% Historical Data in Training Dataset					
ROP Model	Norm. RMSE	ΔWOB (klb)	ΔRPM (rev/min)	Δq (gpm)	ΔROP (ft/hr)
Bingham (1964)	31.38	12.87	45.39	0.00	107.21
Modified B&Y	30.70	12.87	45.39	9.69	88.08
Hareland and Rampersad (1994)	30.91	11.87	45.39	0.00	64.54
Motahhari *et al*. (2010)	31.33	12.87	45.39	0.00	89.74
Random Forests	15.60	-6.18	-7.13	-16.10	25.32
Support Vector Machines	19.57	-5.11	-0.13	-3.34	36.04
Neural Networks	19.64	-6.50	-4.46	-9.60	30.66
Best by Cross Validation	15.63	-6.03	-6.61	-16.08	25.75
Best by Test Error	14.37	-5.26	-3.47	-15.42	32.13

Although model performance improves, ROP improvements are very similar to the baseline in Table 6.14.

7.5.2. Dynamic Range of Training Data

Model errors for 200ft dynamic range training datasets with the best performing weighting techniques from Sections 7.3.2 and 7.4.2 are displayed in Table 7.33:

Table 7.33: ROP model performance comparison for 200ft dynamic range training dataset with 30ft retraining intervals and different weighting techniques.

Dynamic Range	No Weights		Spatial Proximity Weights 2 Partitions ($w_2 = 10$)		Param. Similarity Weights ($k = 10, 5, 10, 10$)	
ROP Model	Abs. Error	Norm. RMSE	Abs. Error	Norm. RMSE	Abs. Error	Norm. RMSE
Bingham (1964)	36.13	33.48	32.79	31.18	33.89	31.88
Modified B&Y	33.97	32.76	31.44	30.88	32.16	31.43
Hareland and Rampersad (1994)	35.74	32.70	32.55	30.56	33.65	31.24
Motahhari *et al*. (2010)	36.29	33.38	32.95	31.10	34.07	31.81
Random Forests	22.94	21.56	23.11	21.60	23.26	21.76
Support Vector Machines	27.87	26.36	32.18	32.10	34.56	34.55
Neural Networks	25.96	24.76	27.28	25.53	26.81	25.72
Best by Cross Validation	22.93	21.65	24.13	21.83	23.62	21.94
Best by Test Error	18.24	18.45	18.37	18.91	18.17	18.96
Best CV / Test Error Agreement	39.51%	41.98%	41.98%	48.15%	41.98%	49.38%

Historical data percentages varying from 10% to 30% are incorporated to the dynamic training data range as optimization intervals reach each formation:

Table 7.34: ROP model performance comparison for 200ft dynamic range training dataset with 30ft retraining intervals incorporating varying amounts of historical data.

Dynamic Range	10% Historical Data		20% Historical Data		30% Historical Data	
ROP Model	Abs. Error	Norm. RMSE	Abs. Error	Norm. RMSE	Abs. Error	Norm. RMSE
Bingham (1964)	32.89	31.58	32.61	31.24	32.25	30.92
Modified B&Y	31.31	31.11	31.06	30.79	30.77	30.48
Hareland and Rampersad (1994)	32.51	30.97	32.20	30.66	31.89	30.39
Motahhari *et al*. (2010)	32.91	31.49	32.58	31.14	32.25	30.84
Random Forests	17.07	17.99	16.24	17.11	15.27	16.08
Support Vector Machines	19.50	21.38	19.09	20.85	18.15	20.09
Neural Networks	22.36	21.73	22.82	22.05	22.37	21.48
Best by Cross Validation	17.19	18.12	16.33	17.17	15.21	16.04
Best by Test Error	14.66	16.64	14.24	16.06	13.18	14.99
Best CV / Test Error Agreement	58.02%	60.49%	64.81%	64.81%	73.46%	73.46%

All ROP models fitted to datasets encompassing historical samples perform significantly better than with previous dynamic range evaluations in Table 7.33. This is particularly true for ML ROP models.

Average interval optimization recommendations derived from dynamic range models with 30% historical data are shown next:

Table 7.35: Model normalized RMSE and drilling parameter optimization results for 200ft dynamic range training dataset with 30ft retraining intervals and 30% historical data.

200ft Dynamic Range with 30% Historical Data in Training Dataset					
ROP Model	Norm. RMSE	ΔWOB (klb)	ΔRPM (rev/min)	Δq (gpm)	ΔROP (ft/hr)
Bingham (1964)	30.92	12.75	45.28	0.00	105.34
Modified B&Y	30.48	12.75	45.28	10.97	84.51
Hareland and Rampersad (1994)	30.39	11.69	45.28	0.00	60.29
Motahhari *et al*. (2010)	30.84	12.75	45.28	0.00	84.99
Random Forests	16.08	-7.35	-5.03	-10.39	26.01
Support Vector Machines	20.09	-6.45	1.31	-5.03	38.35
Neural Networks	21.48	-7.22	0.18	-13.48	33.47
Best by Cross Validation	16.04	-7.35	-4.66	-10.37	25.88
Best by Test Error	14.99	-6.65	-1.32	-10.45	35.40

NN models produce the highest ROP gains compared to the baseline (Table 7.5). Interestingly, these models suggest less negative WOB changes than in Table 7.5, opposing the trend of drastically lowering WOB to obtain the highest ROP improvements observed so far.

7.5.3. Full Range of Training Data

ROP modeling performance results with full range training data and the most successful spatial proximity and parameter similarity weighting scenarios from Sections 7.3.3 and 7.4.3 are exhibited below:

Table 7.36: ROP model performance comparison for full range training dataset with 30ft retraining intervals and different weighting techniques.

Full Range	No Weights		Spatial Proximity Weights 2 Partitions (w_2 = 10)		Param. Similarity Weights (k = 10, 5, 10, 10)	
ROP Model	Abs. Error	Norm. RMSE	Abs. Error	Norm. RMSE	Abs. Error	Norm. RMSE
Bingham (1964)	94.82	81.69	50.18	43.50	62.06	53.08
Modified B&Y	61.96	54.40	42.03	38.06	47.82	42.34
Hareland and Rampersad (1994)	93.99	80.56	49.54	42.64	61.52	52.28
Motahhari *et al*. (2010)	94.86	81.66	50.16	43.44	62.19	53.08
Random Forests	23.70	22.08	23.78	22.22	23.72	22.22
Support Vector Machines	27.49	25.91	28.03	26.68	28.60	27.73
Neural Networks	39.73	31.42	32.05	27.91	34.35	27.80
Best by Cross Validation	23.77	22.09	23.86	22.29	23.82	22.41
Best by Test Error	19.69	19.57	18.36	19.17	19.49	19.44
Best CV / Test Error Agreement	44.44%	47.53%	43.21%	47.53%	38.89%	44.44%

Historical data are incorporated to the training dataset as optimized intervals begin in a new formation:

Table 7.37: ROP model performance comparison for full range training dataset with 30ft retraining intervals incorporating varying amounts of historical data.

Full Range	10% Historical Data		20% Historical Data		30% Historical Data	
ROP Model	Abs. Error	Norm. RMSE	Abs. Error	Norm. RMSE	Abs. Error	Norm. RMSE
Bingham (1964)	91.17	79.58	88.87	77.21	85.21	74.03
Modified B&Y	60.39	53.76	59.97	53.21	58.98	52.28
Hareland and Rampersad (1994)	90.34	78.51	88.11	76.20	84.59	73.13
Motahhari *et al.* (2010)	91.12	79.48	88.79	77.07	85.16	73.90
Random Forests	17.30	18.24	16.88	17.46	14.96	16.24
Support Vector Machines	20.85	22.63	20.11	22.09	19.35	21.34
Neural Networks	36.09	28.95	33.16	28.63	32.47	28.07
Best by Cross Validation	17.25	18.21	16.85	17.47	14.91	16.21
Best by Test Error	15.70	17.19	15.00	16.50	13.77	15.40
Best CV / Test Error Agreement	63.58%	67.28%	71.60%	69.14%	72.84%	70.99%

Weighting techniques presented in Table 7.36 are much more effective in reducing full range analytical model errors than aggregating historical data to the training samples. Nevertheless, RF and SVM model errors decrease significantly with historical data, improving cross-validation and test error model selection agreement.

Optimizations with full range models containing 30% historical data yield the following adjustments:

Table 7.38: Model normalized RMSE and drilling parameter optimization results for full range training dataset with 30ft retraining intervals and 30% historical data.

Full Range with 30% Historical Data in Training Dataset					
ROP Model	Norm. RMSE	ΔWOB (klb)	ΔRPM (rev/min)	Δq (gpm)	ΔROP (ft/hr)
Bingham (1964)	74.03	12.75	45.28	0.00	163.43
Modified B&Y	52.28	12.75	45.28	26.78	120.39
Hareland and Rampersad (1994)	73.13	11.47	45.28	0.00	121.73
Motahhari *et al.* (2010)	73.90	12.75	45.28	0.00	151.12
Random Forests	16.24	-10.61	2.16	12.79	44.58
Support Vector Machines	21.34	-4.99	12.93	-38.43	99.46
Neural Networks	28.07	-10.01	3.20	-21.06	61.08
Best by Cross Validation	16.21	-10.61	2.29	12.79	44.73
Best by Test Error	15.40	-9.29	5.55	5.21	58.25

By recommending substantial reductions in WOB, RPM and especially flow rate compared to the full range baseline (Table 7.8), NN models with 30% historical data achieve an additional 7ft/hr ROP improvement on average.

As demonstrated in this section, incorporating historical samples to the training dataset can significantly improve model performance and agreement in best performing models selected by CV and by test error. If offset well data are available, ROP models are more accurate than when trained solely with real-time data. The sample weighting concept can be extended to historical data with Eq. 7.1 (Section 7.3). Offset well data should be assigned lower weights than real-time data, prioritizing drilling knowledge obtained in actual operating conditions. This approach is not coherent in this study, since all samples were measured in the same well. Instead, weighting of historical data is suggested as a recommendation for future work with expectations for favorable results.

Chapter 8: Conclusions

8.1. SUMMARY OF FINDINGS

The real-time drilling parameter optimization problem was introduced in Chapter 1. A review of industry optimization approaches revealed that ExxonMobil's Drilling Advisory System consistently appears in the literature as the state-of-the-art approach for real-time adjustment of drilling operational parameters. Numerous successful implementations of the system are described, realizing huge cost savings for the operator.

Chapter 2 presented the history of ROP modeling and examined the equations utilized in this study. A novel modified version of the Bourgoyne and Young (1974) ROP model was proposed for specific use in real-time implementations, and a correction was applied to the Hareland and Rampersad (1994) PDC model to enforce consistent units and appropriate drilling behavior. Random forests, support vector machines and neural networks were explained in a drilling context, making statistical concepts behind these ML algorithms accessible to the general drilling audience.

Gradient-based and direct search optimization methods were discussed in Chapter 3. Eight optimization techniques (three gradient-based, five direct search) were introduced as candidates to solve the two optimization problems in real-time drilling parameter optimization. ROP model fitting, the first of these two optimization problems, was established with three loss function choices. Constrained operational parameter selection was formulated accounting for rig equipment and drilling tools limitations.

Chapter 4 described drilling data workflows and presented the Williston Basin dataset analyzed in this study. Surface measurements were designated as the appropriate data source for ROP model fitting and drilling optimization due to availability in real-time.

Operational parameter optimization constraints specific to the Williston Basin dataset were established.

In Chapter 5, many modeling and optimization decisions essential for real-time considerations were investigated in a lithology-dependent post-drilling analysis framework. With hypothesis testing, depth, WOB, RPM and drilling fluid flow rate were confirmed to constitute statistically relevant parameters for ROP modeling. Gradient-based optimization techniques were determined as the standard to fit analytical ROP model coefficients, producing adequate results in a computationally efficient manner. The proposed modified version of the Bourgoyne and Young ROP model was compared against previous model formulations, yielding encouraging results. Hyperparameter optimization showed that simpler machine learning models are preferred with the amount of data in a depth-based drilling dataset and established a set of reference hyperparameters that can be utilized in similar settings. Cross-validation on training data demonstrated that machine learning ROP models predict drilling speed significantly more accurately than analytical models with the same surface measurements generally utilized by the latter. For the Williston Basin dataset analyzed, the modified Bourgoyne and Young model proposed in this dissertation resulted in the best performance among analytical ROP models while the random forests algorithm achieved lowest error overall. Novel learning metrics proved that ML models are capable of reducing test error much more effectively with increasing training data availability.

Furthermore, Chapter 5 investigations also determined that ROP model type exerts a major influence on the nature of optimization techniques suitable to determine optimal operational drilling parameters. Optimization with ML ROP models demands direct search methods and considerable computational power to locate global optimal parameters, while analytical models can be optimized extremely fast with gradient-based approaches. The

random forests algorithm produced the best performing ROP models, but RF models were also the hardest to optimize drilling parameters for. Severe segmentation of RF models' parameter spaces restricted any success with gradient-based optimization techniques and required significant computational expense with direct search approaches. Particle swarm optimization limited to a small number of maximum iterations displayed satisfactory results for optimization with random forests models while maintaining the plausibility of real-time implementations. PSO was also determined as the standard optimization algorithm for SVM and NN models based on attained ROP improvements.

Chapter 6 introduced the concept of continuous ROP model learning as more data are measured in real-time. A continuous learning real-time drilling interval optimization workflow, applicable to all drilling scenarios, was proposed. Retraining models more frequently resulted in improved model performance, demonstrating the value of this approach. Cross-validation achieved satisfactory results as a technique to select models with high ROP prediction accuracy in real-time. This model selection procedure is essential when drilling exploratory wells, as no information about previous drilling experience in the region is available. The amount of data required for adequate ML ROP modeling performance proved lower than expected. ML models exhibited lower error than their analytical counterparts in optimization intervals with as few as ten data points available for model training. In terms of drilling parameter optimization, analytical models were shown to enforce previous beliefs about drilling behavior, extrapolating positively-bounded relationships between ROP and drilling parameters to the maximum bounds. Conversely, it was determined that optimization with ML models searches for parameter space regions with high ROP in the training data to find the "sweet spot" for drilling a particular interval. Uncharacteristic ROP-WOB relations in optimization recommendations with ML models

established that poor drilling data quality unquestionably hinders drilling optimization efforts.

The traditional ROP modeling lithology dependency was contested in Chapter 7. Dynamic range with a specified depth length of training data and full training data range were introduced as alternative data segmentation strategies. An optimal dynamic range length of 200ft was determined for the Williston Basin dataset. Model performance and optimization results for dynamic and full range training data partitioning demonstrated that these methods outperform the classical lithology-dependent approach. ROP gains predicted by ML models trained with full training data range were extremely promising, but recommendations to drill at very low WOB values create suspicion around poor data quality. Spatial proximity and parameter similarity weighting techniques were incorporated to formation-dependent, dynamic range and full range methodologies to further segment training data according to sample importance. Experiments conducted in these scenarios revealed significantly improved analytical ROP model performance, particularly with 200ft dynamic training data ranges using two-partition ten-fold spatial weighting. Lastly, historical data availability was shown to have immense impact on ROP modeling accuracy. Significant reduction in model errors were experienced as the prescribed percentage of historical data increased.

8.2. MAJOR CONTRIBUTIONS

Novel techniques proposed by the author encompass:

- Modified version of the classic Bourgoyne and Young (1974) ROP model specifically designed for real-time applications

237

- Corrected Hareland and Rampersad (1994) ROP model formulation for PDC bits to ensure units consistency and appropriate WOB behavior

- Novel learning performance benchmarks prove that machine learning models reduce test error much more effectively than analytical models with increasing training data availability

- Continuous learning real-time drilling optimization workflow with ROP model retraining and drilling parameter optimization in intervals

- Cross-validation as a methodology to select the best performing ROP model for the upcoming drilling interval in real-time

- Dynamic range with specified depth length and full range training data segmentation strategies that challenge the traditional lithology-dependent ROP modeling approach

- Spatial proximity and parameter similarity data weighting techniques attach importance to individual samples during model training

ROP model fitting insights derived in this dissertation include:

- Established that analytical ROP models can be trained efficiently with gradient-based methods such as the trust region reflective and L-BFGS-B algorithms, with no need for complex optimization schemes presented in previous studies

- Defined basic set of hyperparameters for random forests, support vector machines and neural networks models with depth-based drilling data, developing computationally inexpensive models simple enough for real-time applications while maintaining satisfactory performance

238

Contributions to the continuous learning framework, with ROP models constantly adapting to newly captured real-time data, encompass:

- Shortening retraining interval length improves ROP model performance, justifying the continuous learning approach

- Lithology dependence of ROP models is avoidable, with dynamic and full range training data partitioning introduced as alternatives

- Even though neural networks ROP models benefit from incremental training data availability, the training dataset must remain within a certain proximity to the optimized interval. This is evidenced by models trained with 200ft dynamic training data ranges performing significantly better than full range models in this study

- Spatial proximity and parameter similarity weighting improve analytical ROP model performance considerably

- Random forests ROP models were consistently the most accurate, but also the hardest to optimize due to severe segmentation of the parameter space

The real-time drilling optimization workflow introduced in this dissertation is highly customizable and should serve as a frame of reference for further applications. Additional ROP models, drilling parameters considered in machine learning model fitting (downhole data with wired drillpipe), optimization methods, constraints, segmentation and weighting techniques may be included. It is important to note that drilling parameter optimization best practices depend on the dataset. As an example, shale plays benefit from a large number of drilled wells and historical samples, which should be incorporated to real-time datasets in ROP model training. If rig equipment power constraints (or any other constraints besides design variable bounds) play an important role in optimization,

algorithms such as COBYLA, SLSQP, basin-hopping and PSO must be implemented and accounted for in terms of computational expense. Out of the optimization algorithms tested, only SLSQP is capable of providing knowledge about active constraints (via Lagrange multipliers). This information is crucial in redesigning equipment and processes to extend drilling limitations (the founder point). Since SLSQP optimizations with ML ROP models were not satisfactory, analytical models must be employed in such efforts. Reliable closed-loop control of drilling parameters is contingent on accurate ROP modeling and computationally-efficient optimization. Therefore, insights derived in this study have vast implications for drilling automation applications.

8.3. RECOMMENDATIONS FOR FUTURE WORK

This section extends concepts presented in this dissertation and proposes novel techniques to be explored. The bright future of machine learning algorithms for real-time drilling optimization is discussed as concluding remarks. Future work recommendations are divided into individual aspects of the modeling and optimization workflow.

Drilling parameter optimization problem formulation:

- Incorporate multi-objective optimization accounting for bit wear, excessive vibrations and other drilling dysfunctions
- Include hydraulics models for downhole pressure constraints
- Add support for constraints in mud motor applications
- Explore additional optimization algorithms that are computationally-efficient with machine learning models and support bound, equality, and inequality constraints

Data quality:

- Correct for correlated errors at adjacent data points in a time series (tracking)
- Correct for sensor calibration errors with temperature data
- Implement more advanced signal processing techniques such as Kalman filtering
- Evaluate the concept of time series stability filtering, with less but more reliable data points available for model training

Continuous learning real-time drilling interval optimization workflow:

- Develop adaptive retraining interval lengths according to how fast drilling is proceeding
- Adjust drilling parameters in advance for formation changes
- Implement online learning with neural networks models, updating network weights from the previous solution instead of retraining them from scratch as more data points are measured

Sample weighting strategies in ROP model training:

- Explore more parameter similarity weighting alternatives with varying weighting constants
- Incorporate historical data weighted less than real-time data
- Evaluate variograms as a sample weighting methodology by finding well sections with similar parameter variance trends and spatially correlating them
- Investigate the feasibility of assigning data quality measures for sample weighting

- Assess parameter similarity weighting as a technique for formation boundary detection and, alternatively, as a methodology to define lithology based on drilling parameters (proxy for geomechanical properties)

Shallow machine learning techniques were employed in this study. New developments in machine learning have given rise to deep learning methods, producing neural networks models with many hidden layers and much more complex architecture. Deep learning models have stimulated great progress in the fields of image recognition (convolutional neural networks), natural language processing (recurrent neural networks, long short-term memory networks) and genomics (LeCun *et al.*, 2015). These more complicated models require a large amount of data and could be viable for ROP modeling with higher frequency drilling data. As the volume of data collected in the oil and gas industry grows exponentially, deep learning emerges as a promising concept for models in drilling and many other disciplines. In deep reinforcement learning (Mnih *et al.*, 2015), models learn from experience in a set environment with established rewards. Without prior knowledge of gaming rules, reinforcement learning models successfully taught themselves how to play Atari games to human-level skill in a popular contemporary application (Mnih *et al.*, 2013). This idea could be implemented in drilling optimization by allowing the model to experiment with values of WOB, RPM and mud flow rate in a drilling simulator with rewards for drilling faster, eventually detecting the drilling sweet spot and expanding its knowledge for future field drilling applications.

As machine learning models become even more complex, model interpretability suffers. Currently, many researchers are working on methods to improve the explainability of deep learning models in order to avoid treating them as "black boxes". Generative models such as deep belief nets (Hinton *et al.*, 2006) recreate inputs by learning features

probabilistically in their hidden layers. Soft attention methods reveal insights about model behavior in deep learning image interpretation, as shown in retinal fundus images by Poplin *et al.* (2018). Much of the opposition against machine learning models in the oil and gas industry arises from lack of interpretability. Uncertainty does not bode well in a high-risk business where human lives and the environment are at stake. Hopefully sufficient progress in ML model explainability can be achieved in the near future, breaking down barriers for machine learning implementation in closed-loop real-time drilling parameter optimization. Drillers may remain in the loop with advisory input in constraints and formation changes from RTOCs. Undeniably, modern computers possess the capability to process large amounts of data from multiple sensors and assist in producing hydrocarbons swiftly and safely, providing cheap and abundant energy to human society for years to come.

Glossary

Adam: adaptive moment estimation

AI: artificial intelligence

BHA: bottomhole assembly

BHP: bottomhole pressure

BIN: Bingham (1964) ROP model

BY (B&Y): Bourgoyne and Young (1974) ROP model

CCS: confined compressive strength

COBYLA: constrained optimization by linear approximation

CV: cross validation

DAS: drilling advisory system

DNC: did not converge

DOC: depth of cut

DS: drilling strength

DSATS: Drilling Systems Automation Technical Section

ECD: equivalent circulating density

GDL: geologic drilling log

HAR: Hareland and Rampersad (1994) ROP model

HSI: horsepower per square inch

IADC: International Association of Drilling Contractors

KKT: Karush-Kuhn-Tucker (optimality conditions)

L-BFGS-B: limited(-memory) Broyden–Fletcher–Goldfarb–Shanno bound (constrained)

LWD: logging-while-drilling

MD: measured depth

ML: machine learning

MOT: Motahhari *et al.* (2010) ROP model

MPD: managed pressure drilling

MSE: mechanical specific energy

MWD: measurement-while-drilling

OGDQ: Operators Group for Data Quality

NN: neural networks

PDC: polycrystalline diamond compact

PSO: particle swarm optimization

RF: random forests

ROP: rate of penetration

RPM: revolutions per minute

RTOC: real-time operating center

SGD: stochastic gradient descent

SLSQP: sequential least squares quadratic programming

SPE: society of petroleum engineers

STRQ: surface torque

SVM: support vector machines

TFA: total flow area

TOB: torque on bit

TRF: trust region reflective

TSE: torsional severity estimate

UCS: unconfined compressive strength

WITSML: Wellsite Information Transfer Standard Markup Language

WOB: weight on bit

References

Abu-Mostafa, Y. S., Magdon-Ismail, M., and Lin, H. (2012). *Learning from Data: A Short Course*. AMLbook.com.

Al-Betairi, E. A., Moussa, M. M., and Al-Otaibi, S. (1988). Multiple Regression Approach to Optimize Drilling Operations in the Arabian Gulf Area. *SPE Drilling Engineering*, pp. 83-88.

Alum, M. A., and Egbon, F. (2011). Semi-Analytical Models on the Effect of Drilling Fluid Properties on Rate of Penetration (ROP). *Nigeria Annual International Conference and Exhibition*. Abuja, Nigeria, July 30-August 3.

Ambrus, A., Ashok, P., and van Oort, E. (2013). Drilling Rig Sensor Data Validation in the Presence of Real-Time Process Variations. *SPE Annual Technical Conference and Exhibition*. New Orleans, LA, USA, September 30-October 2.

Ambrus, A., Ashok, P., Chintapalli, A., Ramos, D., Behounek, M., Thetford, T. S., and Nelson, B. (2017). A Novel Probabilistic Rig Based Drilling Optimization Index to Improve Drilling Performance. *SPE Offshore Europe Conference & Exhibition*. Aberdeen, United Kingdom, September 5-8.

Amer, M. M., Sattar, A., and El-Sayed, A. H. (2017). An ROP Predictive Model in Nile Delta Area Using Artificial Neural Networks. *SPE Kingdom of Saudi Arabia Annual Technical Symposium and Exhibition*. Dammam, Saudi Arabia, April 24-27.

Anemangely, M., Ramezanzadeh, A., and Tokhmechi, B. (2017). Determination of Constant Coefficients of Bourgoyne and Young Drilling Rate Model Using a Novel Evolutionary Algorithm. *SPE Computer Applications*, v. 8, no. 4, pp. 693-702.

Ansari, H. R., Hosseini, M. J., and Amirpour, M. (2016). Drilling Rate of Penetration Prediction through Committee Support Vector Regression Based on Imperialist Competitive Algorithm. *Carbonates and Evaporites*, v. 32, pp. 205-213.

Appl, F. C., and Rowley, D. S. (1968). Analysis of the Cutting Action of a Single Diamond. *Society of Petroleum Engineers Journal*, pp. 269-280.

Arabjamaloei, R., and Shadizadeh, S. (2011). Modeling and Optimizing Rate of Penetration Using Intelligent Systems in an Iranian Southern Oil Field (Ahwaz Oil Field). *Petroleum Science and Technology*, v. 29, no. 16, pp. 1637-1648.

Arehart, R. A. (1990). Drill-Bit Diagnosis with Neural Networks. *Journal of Mining & Environment*, pp. 24-28.

Armenta, M. (2008). Identifying Inefficient Drilling Conditions Using Drilling-Specific Energy. *SPE Annual Technical Conference and Exhibition*. Denver, CO, USA, September 21-24.

Armenta, M., Hii, K., Hazarika, R., Al-Foudari, S. J., Al-Mohailan, M., and Debroy, A. (2015). Improving Drilling Performance in North Kuwait by Implementing DEO Process. *SPE Kuwait Oil & Gas Show and Conference*. Mishref, Kuwait, October 11-14.

Ashok, P., Ambrus, A., Ramos, D., Lutteringer, J., Behounek, M., Yang, Y. L., Thetford, T., and Weaver, T. (2016). A Step by Step Approach to Improving Data Quality in Drilling Operations: Field Trials in North America. *SPE Intelligent Energy International Conference and Exhibition*. Aberdeen, United Kingdom, September 6-8.

Atwal, H. S., and Knight, S. J. (2016). Enabling Efficient Drilling Operations Through Customized Data Driven Decision-Making. *SPE Eastern Regional Meeting*. Canton, OH, USA, September 13-15.

Auwal, I. H., Ningi, H. Z., Suleiman, A. D. I., Yusuf, I., and Ogundele, O. J. (2012). Optimization of Drilling Parameters in the Development Plan of an Explored Area of Gulf of Guinea. *Journal of Petroleum and Gas Exploration Research*, v. 2, no. 11, pp. 194-201.

Awotunde, A. A., and Mutasiem, M. A. (2014). Efficient Drilling Time Optimization with Differential Evolution. *SPE Nigeria Annual International Conference and Exhibition*. Lagos, Nigeria, August 5-7.

Azar, M., Long, W., White, A., Copeland, C., Hempton, R., and Pak, M. (2015). A New Approach to Fixed Cutter Bits. *Schlumberger Oilfield Review*, v. 27, no. 2, pp. 30-35.

Bahari, A., and Seyed, A. B. (2007). Trust-Region Approach to Find Constants of Bourgoyne and Young Penetration Rate Model in Khangiran Iranian Gas Field. *SPE Latin American and Caribbean Petroleum Engineering Conference*. Buenos Aires, Argentina, April 15-18.

Bahari, M. H., Bahari, A., Moharrami, F. N., and Sistani, M. B. (2008). Determining Bourgoyne and Young Model Coefficients Using Genetic Algorithm to Predict Drilling Rate. *Journal of Applied Sciences*, v. 17, no. 8, pp. 3050-3054.

Bahari, M. H., Bahari, A., and Moradi, H. (2011). Intelligent Drilling Rate Predictor. *International Journal of Innovative Computing, Information and Control*, v. 7, no. 4, pp. 1511-1519.

Bailey, J. R., Biediger E. A., Gupta, V., Ertas, D., Elks, W. C., and Dupriest, F. E. (2008). Drilling Vibrations Modeling and Field Validation. *IADC/SPE Drilling Conference*. Orlando, FL, USA, March 4-6.

Bailey, J. R., Wang, L., Tenny, M. J., Armstrong, N., Zook, J. R., Elks Jr., W. C. (2010). Design Tools and Workflows to Mitigate Drilling Vibrations. *SPE Annual Technical Conference and Exhibition*. Florence, Italy, September 19-22.

Bailey, J. R., and Remmert, S. M. (2010). Managing Drillstring Vibrations Through BHA Design Optimization. *SPE Drilling and Completion*, pp. 458-471.

Bailey, J. R., Pastusek, P. E., Al Junaibi, H., Al Awadhi, M., Al Katheeri, Y., Niznik, M. R., Akyabi, K. S. and Page, C. G. (2016). An Integrated Workflow to Mitigate Drilling Vibrations and Increase Daily Footage. *Abu Dhabi International Petroleum Exhibition and Conference*. Abu Dhabi, UAE, November 7-10.

Bailey, J. R., Payette, G. S., and Wang, L. (2018). Improved Methods to Understand and Mitigate Stick-Slip Torsional Vibrations. *IADC/SPE Drilling Conference and Exhibition.* Fort Worth, TX, USA, March 6-8.

Bataee, M., and Mohseni, S. (2011). Application of Artificial Intelligent Systems in ROP Optimization: A Case Study in Shadegan Oil Field. *SPE Middle East Unconventional Gas Conference and Exhibition*. Muscat, Oman, January 31-February 2.

Baumgartner, T., and van Oort, E. (2015). Maximizing Drilling Sensor Value through Optimized Frequency Selection and Data Processing. *SPE Annual Technical Conference and Exhibition*. Houston, TX, USA, September 28-30.

Baumgartner, T. H. (2017). Maximizing the Value of Information from High-Frequency Downhole Dynamics Data. *PhD Dissertation*. The University of Texas at Austin.

Behounek, M., Hofer, E., Thetford, T., White, M., Yang, L., and Taccolini, M. (2017). Taking a Different Approach to Drilling Data Aggregation to Improve Drilling Performance. *SPE/IADC Drilling Conference and Exhibition*. The Hague, The Netherlands, March 14-16.

Behounek, M., Thetford, T., Yang, L., Hofer, E., White, M., Ashok, P., Ambrus, A., and Ramos, D. (2017). Human Factors Engineering in the Design and Deployment of a Novel Data Aggregation and Distribution System for Drilling Operations. *SPE/IADC Drilling Conference and Exhibition*. The Hague, The Netherlands, March 14-16.

Behounek, M., Nguyen, D., Halloran, S., Isbell, M., Mandava, C., Vinay, N., McMullen, J. and Hoefling, C. (2018). Operators' Group, Rig Contractors, and OEM/Service Company Work to Solve Rig Data Quality Issues. *IADC/SPE Drilling Conference and Exhibition.* Fort Worth, TX, USA, March 6-8.

Bentsen, R. G., and Wilson, D. C. (1976). Optimization Techniques for Weight-On-Bit and Rotary Speed. Part I: Point and Interval Optimization. *Journal of Canadian Petroleum Technology*, v. 7, no. 4, pp. 78-84.

Bentsen, R. G., and Wilson, D. C. (1977). Optimization Techniques for Weight-On-Bit and Rotary Speed Part II. Multi-Interval Optimization. *The Journal of Canadian Petroleum Technology*, v. 8, no. 1, pp. 91-96.

Bilgesu, H. I., Tetrick, L. T., Altmis, U., Mohaghegh, S., and Ameri, S. (1997). A New Approach for the Prediction of Rate of Penetration (ROP) Values. *SPE Eastern Regional Meeting*. Lexington, KY, USA, October 22-24.

Bilgesu, H., Cox, Z. D., Elshehabi, T. A., Smith, C., Idowu, G. O., and Florence, F. R. (2017). A Real-Time Interactive Drill-Off Test Utilizing Artificial Intelligence Algorithm for DSATS Drilling Automation University Competition. *SPE Western Regional Meeting*. Bakersfield, CA, USA, April 23.

Bingham, M. G. (1964). How Rock Properties Are Related to Drilling. *The Oil and Gas Journal*, pp. 94-101.

Bishop, C. M. (2006). *Pattern Recognition and Machine Learning*. Springer.

Boser, B. E., Guyon, I. M., and Vapnik, V. N. (1992). A Training Algorithm for Optimal Margin Classifiers. *Proceedings of the Fifth Annual Workshop on Computational Learning Theory.* Pittsburgh, PA, USA, July 27-29.

Bourgoyne, A. T., Jr., and Young, F. S., Jr. (1973). The Use of Drillability Logs for Formation Evaluation and Abnormal Pressure Detection. *SPWLA Fourteenth Annual Logging Symposium.* Lafayette, LA, USA, May 6-9.

Bourgoyne, A. T., Jr., and Young, F. S., Jr. (1974). A Multiple Regression Approach to Optimal Drilling and Abnormal Pressure Detection. *Society of Petroleum Engineers Journal*, pp. 371-384.

Bourgoyne, A. T., Jr., Millheim, K. K., Chenevert, M. E., and Young, F. S., Jr. (1986). *Applied Drilling Engineering*. Society of Petroleum Engineers.

Boyd, S. P., and Vandenberghe, L. (2004). *Convex Optimization*. Cambridge University Press, 9th Printing 2011.

Branch, M. A., Coleman, T. F., and Li, Y. (1999). A Subspace, Interior, and Conjugate Gradient Method for Large-Scale Bound-Constrained Minimization Problems. *Journal on Scientific Computing*, v. 21, no. 1, pp. 1-23.

Bratli, R. K., Hareland, G., Stene, F., Dunsaed, G. W., and Gjelstad, G. (1997). Drilling Optimization Software Verified in the North Sea. *SPE LACPEC Conference*. Rio de Janeiro, Brazil, August 30-September 2.

Breiman, L. (2001). Random Forests. *Machine Learning*, v. 45, no. 1, pp. 5-32.

Bruton, G., Crockett, R., Taylor, M., DenBoer, D., Lund, J., Fleming, C., Ford, R., Garcia, G., and White, A. (2014). PDC Bit Technology for the 21st Century. *Schlumberger Oilfield Review*, v. 26, no. 2, pp. 48-57.

Byrd, R. H., Schnabel, R. B., and Shultz, G. A. (1988). Approximate Solution of the Trust Region Problem by Minimization over Two-Dimensional Subspaces. *Mathematical Programming*, v. 40, pp. 247-263.

Byrd, R. H., Lu, P., Nocedal, J., and Zhu, C. (1995). A Limited Memory Algorithm for Bound Constrained Optimization. *Journal on Scientific Computing*, v. 16, no. 5, pp. 1190-1208.

Caicedo, H. U., Calhoun, W. M., and Ewy, R. T. (2005). Unique ROP Predictor Using Bit-specific Coefficient of Sliding Friction and Mechanical Efficiency as a Function of Confined Compressive Strength Impacts Drilling Performance. *SPE/IADC Drilling Conference*. Amsterdam, The Netherlands, February 23-25.

Cao, D., Loesel, C., and Paranji, S. (2018). Rapid Development of Real-Time Drilling Analytics System. *IADC/SPE Drilling Conference and Exhibition*. Fort Worth, TX, USA, March 6-8.

Cayeux, E., Dvergsnes, E. W., and Iversen, F. (2009). Real-Time Optimization of the Drilling Process – Challenges in Industrialization. *SPE/IADC Drilling Conference and Exhibition.* Amsterdam, The Netherlands, March 17-19.

Cayeux, E., Daireaux, B., Dvergsnes, E. W., and Florence. F. (2013). Toward Drilling Automation: On the Necessity of Using Sensors that Relate to Physical Models. *SPE/IADC Drilling Conference and Exhibition*. Amsterdam, The Netherlands, March 5-7.

Cayeux, E., Skadsem, H. J., and Kluge, R. (2015). Accuracy and Correction of Hook Load Measurements during Drilling Operations. *SPE/IADC Drilling Conference and Exhibition.* London, United Kingdom, March 17-19.

Centala, P., Challa, V., Durairajan, B., Meehan, R., Paez, L., Partin, U., Segal, S., Wu, S., Garrett, I., Teggart, B., and Tetley, N. (2011). Bit Design – Top to Bottom. *Schlumberger Oilfield Review*, v. 23, no. 2, pp. 4-17.

Chang, D., Payette, G. S., Pais, D., Wang, L., Bailey, J. R., and Mitchell, N. D. (2014). Field Trial Results of a Drilling Advisory System. *International Petroleum Technology Conference*. Doha, Qatar, January 20-22.

Chapman, C. D., Flores, J. L., Perez, R. L., and Yu, H. (2012). Automated Closed-loop Drilling with ROP Optimization Algorithm Significantly Reduces Drilling Time and Improves Downhole Tool Reliability. *IADC/SPE Drilling Conference and Exhibition.* San Diego, CA, USA, March 6-8.

Chen, X., Fan, H., Guo, B., Gao, D., Wei, H., and Ye, Z. (2014). Real-Time Prediction and Optimization of Drilling Performance Based on a New Mechanical Specific Energy Model. *Arabian Journal for Science and Engineering*, v. 39, pp. 8221-8231.

Coley, C. J., and Edwards, S. T. (2013). The Use of Along String Annular Pressure Measurements to Monitor Solids Transport and Hole Cleaning. *SPE/IADC Drilling Conference and Exhibition*. Amsterdam, The Netherlands, March 5-7.

Cortes, C., and Vapnik, V. (1995). Support-Vector Networks. *Machine Learning*, v. 20, no. 3, pp. 273-297.

Craig, A., and Adsit, R. (2014). Drillstring Network 2.0: An Enhanced Drillstring Network Based on 100 Wells of Experience. *SPE Annual Technical Conference and Exhibition*. Amsterdam, The Netherlands, October 27-29.

Crane, D., Zhang, Y., Douglas, C., Song, H., Gan, X., Lin, Z., Mueller, L., Skoff, G., Self, J. and Krough, B. (2017). Innovative PDC Cutter with Elongated Ridge Combines Shear and Crush Action to Improve PDC Bit Performance. *SPE Middle East Oil & Gas Show and Conference*. Manama, Kingdom of Bahrain, March 6-9.

Cui, M., Wang, G. H., Ge, H. Y., Chen, X. Z., and Guo, H. W. (2016). Maximizing Drilling Performance with Real-Time Drilling Vibration Mitigation in the Deep Wells. *SPE Intelligent Energy International Conference and Exhibition*. Aberdeen, United Kingdom, September 6-8.

Cunningham, R. A., and Eenink, J. G. (1959). Laboratory Study of Effect of Overburden, Formation and Mud Column Pressures on Drilling Rate of Permeable Formations. *AIME Petroleum Transactions*, v. 217, pp. 9-17.

Cunningham, R. A. (1978). An Empirical Approach for Relating Drilling Parameters. *Journal of Petroleum Technology*, pp. 987-991.

Darley, H. C. (1965). Designing Fast Drilling Fluids. *Journal of Petroleum Technology*, pp. 465-470.

Dashevskiy, D., Dubinsky, V., and Macpherson, J. D. (1999). Application of Neural Networks for Predictive Control in Drilling Dynamics. *SPE Annual Technical Conference and Exhibition*. Houston, TX, USA, October 3-6.

Deng, Y., Chen, M., Jin, Y., Lu, Y., Zou, D., Du, X., and Jiang, H. (2015). A New Prediction Model of Energy Consumption on Rock Fragmentation and Rate of Penetration Based on Fractal Theory. *49th US Rock Mechanics / Geomechanics Symposium*. San Francisco, CA, USA, June 28-July 1.

Detournay, E., and Defourny, P. (1992). A Phenomenological Model for the Drilling Action of Drag Bits. *International Journal of Rock Mechanics and Mining Sciences*, v. 29, no. 1, pp. 13-23.

Detournay, E., Richard, T., and Shepherd, M. (2008). Drilling Response of Drag Bits: Theory and Experiment. *International Journal of Rock Mechanics and Mining Sciences*, v. 45, pp. 1347-1360.

Dow, B., Harmer, R., and Belaskie, J. (2012). Revolutionizing Drilling Performance through Advanced Real Time Performance Advisory System. *IADC/SPE Drilling Conference and Exhibition.* San Diego, CA, USA, March 6-8.

Driver III, R. P., Atwal, H. S., and Knight, S. J. (2016). Development of a Real-time Decision-Making Dashboard for Drilling Homogeneous Unconventional Shale Plays. *SPE Trinidad and Tobago Section Energy Resources Conference*. Port of Spain, Trinidad and Tobago, June 13-15.

Drucker, H., Burges, C. J., Kaufman, L., Smola, A., and Vapnik, V. (1996). Support Vector Regression Machines. *Proceedings of the Ninth International Conference on Neural Information Processing Systems.* Denver, CO, USA, December 3-5.

Dunlop, J., Isangulov, R., Aldred, W. D., Arismendi Sanchez, H., Sanchez Flores, J. L., Alarcon Herdoiza, J., Belaskie, J., and Luppens, J. C. (2011). Increased Rate of Penetration Through Automation. *SPE/IADC Drilling Conference and Exhibition*. Amsterdam, The Netherlands, March 1-3.

Dupriest, F. E., and Koederitz, W. L. (2005). Maximizing Drill Rates with Real-Time Surveillance of Mechanical Specific Energy. *SPE/IADC Drilling Conference*. Amsterdam, The Netherlands, February 23-25.

Dupriest, F. E., Witt, J. W., and Remmert, S. M. (2005). Maximizing ROP with Real-Time Analysis of Digital Data and MSE. *International Petroleum Technology Conference*. Doha, Qatar, November 21-23.

Dupriest, F. E. (2006). Comprehensive Drill-Rate Management Process to Maximize Rate of Penetration. *SPE Annual Technical Conference and Exhibition*. San Antonio, TX, USA, September 24-27.

Dupriest, F. E., and Sowers, S. F. (2009). Maintaining Steerability While Extending Gauge Length to Manage Whirl. *SPE/IADC Drilling Conference and Exhibition.* Amsterdam, The Netherlands, March 17-19.

Dykstra, M. W., Chen, D. C.-K., Warren, T. M., and Zannoni, S. A. (1994). Experimental Evaluations of Drill Bit and Drill String Dynamics. *69th Annual Technical Conference and Exhibition of the Society of Petroleum Engineers*. New Orleans, LA, USA, September 25-28.

Dykstra, M. W., Neubert, M., Hanson, J. M., and Meiners, M. J. (2001). Improving Drilling Performance by Applying Advanced Dynamics Models. *SPE/IADC Drilling Conference*. Amsterdam, The Netherlands, February 27-March 1.

Eckel, J. R., and Nolley, J. P. (1949). An Analysis of Hydraulic Factors Affecting the Rate of Penetration of Drag-type Rotary Bits. *API Drilling and Production Practice*, pp. 9-37.

Eckel, J. R. (1954). Effect of Mud Properties on Drilling Rate. *API Drilling and Production Practice*, pp. 119-125.

Eckel, J. R. (1958). Effect of Pressure on Rock Drillability. *AIME Petroleum Transactions*, v. 213, pp. 1-6.

Eckel, J. R. (1967). Microbit Studies of the Effect of Fluid Properties and Hydraulics on Drilling Rate. *Journal of Petroleum Technology*, pp. 541-546.

Eckel, J. R. (1968). Microbit Studies of the Effect of Fluid Properties and Hydraulics on Drilling Rate, II. *43rd Annual Fall Meeting of the Society of Petroleum Engineers of AIME*. Houston, TX, USA, September 29-October 2.

Elkatatny, S. M., Tariq, Z., Mahmoud, M. A., and Al-AbdulJabbar, A. (2017). Optimization of Rate of Penetration Using Artificial Intelligent Techniques. *51st US Rock Mechanics / Geomechanics Symposium*. San Francisco, CA, USA, June 25-28.

Emmerich, W., Akimov, O., Brahim, I. B., and Greten, A. (2015). Reliable High-speed Mud Pulse Telemetry. *SPE/IADC Drilling Conference and Exhibition*. London, United Kingdom, March 17-19.

Eren, T. (2010). Real-Time-Optimization of Drilling Parameters during Drilling Operations. *PhD Dissertation*. Middle East Technical University.

Eren, T., and Ozbayoglu, M. E. (2010). Real Time Optimization of Drilling Parameters During Drilling Operations. *SPE Oil and Gas India Conference and Exhibition.* Mumbai, India, January 20-22.

Ertas, D. (2012). Torsional-Axial Drill String Mechanics Model for Surveillance, Root Cause Analysis, and Mitigation of Vibrational Dysfunctions. *Proceedings of the Second International Colloquium on Nonlinear Dynamics and Control of Deep Drilling Systems*, pp. 53-59. Eindhoven, The Netherlands, May 15-16.

Ertas, D., Bailey, J. R., Wang, L., and Pastusek, P. E. (2013). Drillstring Mechanics Model for Surveillance, Root Cause Analysis, and Mitigation of Torsional and Axial Vibrations. *SPE/IADC Drilling Conference and Exhibition*. Amsterdam, The Netherlands, March 5-7.

Ertas, D., Bailey, J. R., Wang, L., and Pastusek, P. E. (2014). Drillstring Mechanics Model for Surveillance, Root Cause Analysis, and Mitigation of Torsional Vibrations. *SPE Drilling and Completion*, pp. 405-417.

Esmaeili, A., Elahifar, B., Fruhwirth, R. K., and Thonhauser, G. (2012). ROP Modeling Using Neural Network and Drill String Vibration Data. *SPE Kuwait International Petroleum Conference and Exhibition*. Kuwait City, Kuwait, December 10-12.

Evangelatos, G. I., and Payne, M. L. (2016). Advanced BHA-ROP Modeling Including Neural Network Analysis of Drilling Performance Data. *IADC/SPE Drilling Conference and Exhibition.* Fort Worth, TX, USA, March 1-3.

Farrelly, M., and Rabia, H. (1987). Bit Performance and Selection: A Novel Approach. *SPE/IADC Drilling Conference*. New Orleans, LA, USA, March 15-18.

Feenstra, R. (1988). Status of Polycrystalline-Diamond-Compact Bits: Part 1 - Development *Journal of Petroleum Technology*, pp. 675-684.

Fletcher, R. (1987). *Practical Methods of Optimization*. John Wiley & Sons, Second Edition.

Florence, F., and Iversen, F. (2010). Real-Time Models for Drilling Process Automation: Equations and Applications. *IADC/SPE Drilling Conference and Exhibition.* New Orleans, LA, USA, February 2-4.

Florence, F., Chapman, C., Macpherson, J., and Cavanaugh, M. (2015). Implementation of Drilling Systems Automation – Halifax Workshop Summary: Industry Standards, Business Models and Next Steps. *SPE Annual Technical Conference and Exhibition*. Houston, TX, USA, September 28-30.

Formighieri, S., and Filho, P. (2015). Estimation of Bourgoyne and Young Model Coefficients Using Markov Chain Monte Carlo Simulation. *Proceedings of the IEEE 2015 Winter Simulation Conference*, pp. 1172-1183.

Forst, W., and Hoffmann, D. (2010). *Optimization – Theory and Practice*. Springer Science and Business Media.

Galle, E. M., and Woods, H. B. (1963). Best Constant Weight and Rotary Speed for Rotary Rock Bits. *API Drilling and Production Practice*, pp. 48-73.

Gandelman, R. A. (2012). Prediction of ROP and Real Time Optimization of Operational Parameters while Drilling Offshore Oil-Wells. *M.S. Thesis*. Universidade Federal do Rio de Janeiro.

Garnier, A. J., and van Lingen, N. H. (1959). Phenomena Affecting Drilling Rates at Depth. *AIME Petroleum Transactions*, v. 216, pp. 232-239.

Gerbaud, L., Menand, S., and Sellami, H. (2006). PDC Bits: All Comes from the Cutter Rock Interaction. *IADC/SPE Drilling Conference.* Miami, FL, USA, February 21-23.

Gidh, Y., Purwanto, A., and Ibrahim, H. (2012). Artificial Neural Network Drilling Parameter Optimization System Improves ROP by Predicting/Managing Bit Wear. *SPE Intelligent Energy International*. Utrecht, The Netherlands, March 27-29.

Gjelstad, G., Hareland, G., Nikolaisen, K. N., and Bratli, R. K. (1998). The Method of Reducing Drilling Costs More Than 50 Percent. *SPE/ISRM Eurock*. Trondheim, Norway, July 8-10.

Glowka, D. A., and Stone, C. M. (1985). Thermal Response of Polycrystalline Diamond Compact Cutters Under Simulated Downhole Conditions. *Society of Petroleum Engineers Journal*, pp. 143-156.

Glowka, D. A. (1989). Use of Single-Cutter Data in the Analysis of PDC Bit Designs: Part 1 – Development of a PDC Cutting Force Model. *Journal of Petroleum Technology*, pp. 797-799,844-849.

Gongora, C., Awan, O., Mota, J., and van Oort, E. (2013). Drilling Unconventional Shale Wells Remotely. *SPE/IADC Drilling Conference and Exhibition*. Amsterdam, The Netherlands, March 5-7.

Gouda, G. M., Maestrami, M., Abu Saif, M. A., Shalaby, S.E., Farhat, M.S., and Dahab, A. S. (2011). A Real Mathematical Model to Compute the PDC Cutter Wear Value to Terminate PDC Bit Run. *SPE Middle East Oil and Gas Show and Conference*. Manama, Bahrain, September 25-28.

Gray, K. E., Armstrong, F., and Gatlin, C. (1962). Two-Dimensional Study of Rock Breakage in Drag-Bit Drilling at Atmospheric Pressure. *Journal of Petroleum Technology*, pp. 93-98.

Guerrero, C. A., and Kull, B. J. (2007). Deployment of an SeROP Predictor Tool for Real-Time Bit Optimization. *SPE/IADC Drilling Conference*. Amsterdam, The Netherlands, February 20-22.

Guria, C., Goli, K. K., and Pathak, A. K. (2014). Multi-Objective Optimization of Oil Well Drilling Using Elitist Non-Dominated Sorting Genetic Algorithm. *Petroleum Science*, v. 11, no. 1, pp. 97-110.

Hareland, G., and Hoberock, L. L. (1993). Use of Drilling Parameters to Predict In-Situ Stress Bounds. *SPE/IADC Drilling Conference*. Amsterdam, The Netherlands, February 23-25.

Hareland, G., and Rampersad, P. R. (1994). Drag-Bit Model Including Wear. *III Latin American/Caribbean Petroleum Engineering Conference*. Buenos Aires, Argentina, April 27-29.

Hareland, G., Wu, A., Rashidi, B., and James, J. A. (2010). A New Drilling Rate Model for Tricone Bits and Its Application to Predict Rock Compressive Strength. *44th US Rock Mechanics Symposium and 5th U.S.-Canada Rock Mechanics Symposium*. Salt Lake City, UT, USA, June 27-30.

Hart, P. *Energy Capital Conference: Silica or Silicon?* Oil and Gas Investor, 9 May 2018. Web.

Hastie, T., Tibshirani, R., and Friedman, J. (2009). *The Elements of Statistical Learning: Data Mining, Inference, and Prediction*. Springer, Second Edition.

Hegde, C., Wallace, S., and Gray, K. (2015). Using Trees, Bagging, and Random Forests to Predict Rate of Penetration During Drilling. *SPE Middle East Intelligent Oil and Gas Conference and Exhibition*. Abu Dhabi, UAE, September 15-16.

Hegde, C. (2016). Application of Statistical Learning Models to Predict and Optimize Rate of Penetration of Drilling. *M.S. Thesis*. The University of Texas at Austin.

Hegde, C., and Gray, K. E. (2017). Use of Machine Learning and Data Analytics to Increase Drilling Efficiency for Nearby Wells. *Journal of Natural Gas Science and Engineering*, v. 40, pp. 327-335.

Hegde, C., Daigle, H., Millwater, H., and Gray, K. (2017). Analysis of Rate of Penetration (ROP) Prediction in Drilling Using Physics-Based and Data-Driven Models. *Journal of Petroleum Science and Engineering*, v. 159, pp. 295-306.

Hegde, C., and Gray, K. E. (2018). Evaluation of Coupled Machine Learning Models for Drilling Optimization. *Journal of Natural Gas Science and Engineering*, v. 56, pp. 397-407.

Hemphill, T., Murphy, B., and Mix, K. (2001). Optimization of Rates of Penetration in Deepwater Drilling: Identifying the Limits. *SPE Annual Technical Conference and Exhibition.* New Orleans, LA, USA, September 30-October 3.

Hinton, G. E., Osindero, S., and Teh, Y. (2006). A Fast Learning Algorithm for Deep Belief Nets. *Neural Computation*, v. 18, no. 7, pp. 1527-1554.

Ho, T. K. (1995). Random Decision Forests. *IEEE Proceedings of the Third International Conference on Document Analysis and Recognition.* Montreal, Canada, August 14-16.

Holdaway, K. R. (2012). Predictive Analytics: Development and Deployment of Upstream Data Driven Models. *SPE Latin American and Caribbean Petroleum Engineering Conference*. Mexico City, Mexico, April 16-18.

Hornik, K., Stinchcombe, M., and White, H. (1989). Multilayer Feedforward Networks are Universal Approximators. *Neural Networks*, v. 2, pp. 359-366.

Hougaz, A. B., Gozzi, D. S., Fujshima, I., Vello, K. L., Alves, S., Thomson, I., Krasuk, R., and Buzzerio, F. (2012). Upgrading the Real-Time Drilling Optimization Culture in Brazil's Challenging Deepwater Operations: The Utilization of a Remote and Rigsite Multidisciplinary Collaborative Concept. *IADC/SPE Drilling Conference and Exhibition.* San Diego, CA, USA, March 6-8.

Huber, P. J. (1964). Robust Estimation of a Location Parameter. *The Annals of Mathematical Statistics*, v. 35, no. 1, pp. 73-101.

Iqbal, F. (2008). Drilling Optimization Technique – Using Real Time Parameters. *SPE Russian Oil & Gas Technical Conference and Exhibition*. Moscow, Russia, October 28-30.

Isaacs, W. R., and Bobo, J. E. (1984). Design and Impact of a Real-Time Drilling Data Center. *59th Annual Technical Conference and Exhibition*. Houston, TX, USA, September 16-19.

Israel, R., Mason, C., Whiteley, N., Gibson, K., Dobson, D., and Andresen, P. A. (2015). Well Advisor – Integrating Real-time Data with Predictive Tools, Processes and Expertise to Enable More Informed Operational Decisions. *SPE/IADC Drilling Conference and Exhibition*. London, United Kingdom, March 17-19.

Israel, R., Farthing, J., Walker, H., Covarrubias, R. G., Bryant, J., and Vahle, C. (2017). Development to Delivery – A Collaborative Approach to Implementing Drilling Automation. *SPE/IADC Drilling Conference and Exhibition*. The Hague, The Netherlands, March 14-16.

258

Jahanbakhshi, R., Keshavarzi, R., and Jafarnezhad, A. (2012). Real-time Prediction of Rate of Penetration during Drilling Operation in Oil and Gas Wells. *46th US Rock Mechanics / Geomechanics Symposium*. Chicago, IL, USA, June 24-27.

Jain, J. R., Ricks, G., Baxter, B., Vempati, C., Peters, V., Bilen, J., Spencer, R., and Stibbe, H. (2016). A Step Change in Drill Bit Technology with Self-Adjusting PDC Bits. *IADC/SPE Drilling Conference and Exhibition.* Fort Worth, TX, USA, March 1-3.

James, G., Witten, D., Hastie, T., and Tibshirani, R. (2013). *An Introduction to Statistical Learning with Applications in R*. Springer, 6th Printing 2015.

Jorden, J. R., and Shirley, O. J. (1966). Application of Drilling Performance Data to Overpressure Detection. *Journal of Petroleum Technology*, pp. 1387-1394.

Judzis, A., Bland, R. G., Curry, D. A., Black, A. D., Robertson, H. A., Meiners, M. J., and Grant, T. C. (2007). Optimization of Deep Drilling Performance: Benchmark Testing Drives ROP Improvements for Bits and Drilling Fluids. *SPE/IADC Drilling Conference*. Amsterdam, The Netherlands, February 20-22.

Karush, W. (1939). Minima of Functions of Several Variables with Inequalities as Side Conditions. *M.S. Thesis*. The University of Chicago.

Kennedy, J., and Eberhart, R. (1995). Particle Swarm Optimization. *IEEE International Conference on Neural Networks.* Perth, Australia, November 27-December 1.

Kerkar, P. B., Hareland, G., Fonseca, E. R., and Hackbarth, C. J. (2014). Estimation of Rock Compressive Strength Using Downhole Weight-on-Bit and Drilling Models. *International Petroleum Technology Conference*. Doha, Qatar, January 20-22.

Kingma, D. P., and Ba, J. L. (2015). Adam: A Method for Stochastic Optimization. *3rd International Conference for Learning Representations.* San Diego, CA, USA, May 7-9.

Koederitz, W. L., and Johnson, W. E. (2011). Real-Time Optimization of Drilling Parameters by Autonomous Empirical Methods. *SPE/IADC Drilling Conference and Exhibition*. Amsterdam, The Netherlands, March 1-3.

Kolda, T. G., Lewis, R. M., and Torczon, V. (2003). Optimization by Direct Search: New Perspectives on Some Classical and Modern Methods. *SIAM Review*, v. 45, no. 3, pp. 385-482.

Kolnes, O., Kluge, R., Halsey, G. W., Bjorkevoll, K. S., and Rommetveit, R. (2007). From Sensors to Models to Visualization – Handling the Complex Data Flow. *SPE Digital Energy Conference and Exhibition*. Houston, TX, USA, April 11-12.

Kowakwi, I., Chen, H., Hareland, G., and Rashidi, B. (2012). The Two-Term Rollercone Rate of Penetration (ROP) Model with Integrated Hydraulics Function. *46th US Rock Mechanics / Geomechanics Symposium*. Chicago, IL, USA, June 24-27.

Kraft, D. (1988). A Software Package for Sequential Quadratic Programming. *Technical Report DFVLR-FB 88-28 German Aerospace Center – Institute for Flight Mechanics.* Koln, Germany, July 28.

Kristjansson, S. D., Neudfeldt, A, Lai, S. W., Wang, J., and Tremaine, D. (2016). Use of Historic Data to Improve Drilling Efficiency: A Pattern Recognition Method and Trial Results. *IADC/SPE Drilling Conference and Exhibition.* Fort Worth, TX, USA, March 1-3.

Kuhn, H. W., and Tucker, A. W. (1951). Nonlinear Programming. *Proceedings of the Second Berkeley Symposium on Mathematical Statistics and Probability*, pp. 481-492.

Kutas, D. T., Nascimento, A., Elmgerbi, A. M., Roohi, A., Prohaska, M., Thonhauser, G., and Mathias, M. H. (2015). A Study of the Applicability of Bourgoyne & Young ROP Model and Fitting Reliability through Regression. *International Petroleum Technology Conference*. Doha, Qatar, December 6-9.

Kyllingstad, A., and Thoresen, K. E. (2018). Improving Surface WOB Accuracy. *IADC/SPE Drilling Conference and Exhibition.* Fort Worth, TX, USA, March 6-8.

Lakhanpal, V., and Samuel, R. (2017). Real-Time Bit Wear Prediction Using Adaptive Data Analytics. *SPE Annual Technical Conference and Exhibition*. San Antonio, TX, USA, October 9-11.

Laurens, M., and Kales, M. (2014). Moving Beyond Real-Time Operations Centres. *International Petroleum Technology Conference*. Doha, Qatar, January 20-22.

LeCun, Y., Bengio, Y., and Hinton, G. (2015). Deep Learning. *Nature*, v. 521, pp. 436-444.

Lee, A., and Castillo-Hair, S. (2013). Particle Swarm Optimization (PSO) with Constraint Support. *pyswarm Python package*.

Liu, Y., Chen, M., Sheng, S., and Zeng, J. (2016). Optimisation Leads to Improved Hybrid Bit Design and Enhanced Drilling Efficiencies in Challenging Vertical Application in Tarim Basin, China. *International Petroleum Technology Conference*. Bangkok, Thailand, November 14-16.

Liu, Y., Kibbey, J., Bai, Y., and Wu, X. (2018). Real-Time Bit Wear Monitoring and Prediction Using Surface Mechanics Data Analytics: A Step Toward Digitization through Agile Development. *IADC/SPE Drilling Conference and Exhibition.* Fort Worth, TX, USA, March 6-8.

Liu, Z., Marland, C., Li, D., and Samuel, R. (2014). An Analytical Model Coupled with Data Analytics to Estimate PDC Bit Wear. *SPE Latin American and Caribbean Petroleum Engineering Conference*. Maracaibo, Venezuela, May 21-23.

Lohne, H. P., Gravdal, J. E., Dvergsnes, E. W., Nygaard, G., and Vefring, E. H. (2008). Automatic Calibration of Real-Time Computer Models in Intelligent Drilling Control Systems – Results from a North Sea Field Trial. *International Petroleum Technology Conference*. Kuala Lumpur, Malaysia, December 3-5.

Macpherson, J. D., de Wardt, J. P., Florence, F., Chapman, C. D., Zamora, M., Laing, M. L., and Iversen, F. P. (2013). Drilling-Systems Automation: Current State, Initiatives, and Potential Impact. *SPE Drilling and Completion*, pp. 296-308.

Mammadov, E., Osayande, N., Breuer, J., and Al-Hashmy, W. (2015). Predicting and Optimizing ROP in Competent Shale by Utilizing MPD Technology. *SPE Annual Technical Conference and Exhibition*. Houston, TX, USA, September 28-30.

Mantha, B., and Samuel, R. (2016). ROP Optimization Using Artificial Intelligence Techniques with Statistical Regression Coupling. *SPE Annual Technical Conference and Exhibition*. Dubai, UAE, September 26-28.

Maurer, W. C. (1962). The "Perfect-Cleaning" Theory of Rotary Drilling. *Journal of Petroleum Technology*, pp. 1270-1274.

McCulloch, W. S., and Pitts, W. (1943). A Logical Calculus of the Ideas Immanent in Nervous Activity. *Bulletin of Mathematical Biophysics*, v. 5, pp. 115-133.

Menand, S., and Mills, K. (2017). Use of Mechanical Specific Energy Calculation in Real-Time to Better Detect Vibrations and Bit Wear While Drilling. *AADE National Technical Conference and Exhibition*. Houston, TX, USA, April 11-12.

Millheim, K. K., and Huggins, R. L. (1983). An Engineering Simulator for Drilling: Part I. *58th Annual Technical Conference and Exhibition*. San Francisco, CA, USA, October 5-8.

Millheim, K. K., and Huggins, R. L. (1983). An Engineering Simulator for Drilling: Part II. *58th Annual Technical Conference and Exhibition*. San Francisco, CA, USA, October 5-8.

Millheim, K. K. (1986). The Role of the Simulator in Drilling Operations *SPE Drilling Engineering*, pp. 347-357.

Mnih, V., Kavukcuoglu, K., Silver, D., Graves, A., Antonoglou, I., Wierstra, D., and Riedmiller, M. (2013). Playing Atari with Deep Reinforcement Learning. *NIPS Deep Learning Workshop.* Lake Tahoe, CA, USA, December 9.

Mnih, V., Kavukcuoglu, K., Silver, D., Rusu, A. A., Veness, J., Bellemare, M. G., Graves, A., Riedmiller, M., Fidjeland, A. K., Ostrovski, G., Petersen, S., Beattie, C., Sadik, A., Antonoglou, I., King, H., Kumaran, D., Wierstra, D., Legg, S., and Hassabis, D. (2015). Human-Level Control through Deep Reinforcement Learning. *Nature*, v. 518, pp. 529-533.

Mohan, K., Adil, F., and Samuel, R. (2009). Tracking Drilling Efficiency Using Hydro-Mechanical Specific Energy. *SPE/IADC Drilling Conference and Exhibition.* Amsterdam, The Netherlands, March 17-19.

Monden, T., and Chia, C. R. (2007). Operation Support Centers – Real Time Drilling Optimization and Risk Mitigation. *SPE Saudi Arabia Technical Symposium*. Dhahran, Saudi Arabia, May 7-8.

Moradi, H., Bahari, M. H., Sistani, M. B., and Bahari, A. (2010). Drilling Rate Prediction Using an Innovative Soft Computing Approach. *Scientific Research and Essays*, v. 13, no. 5, pp. 1583-1588.

Moran, D., Ibrahim, H., Purwanto, A., and Osmond, J. (2010). Sophisticated ROP Prediction Technologies Based on Neural Network Delivers Accurate Drill Time Results. *IADC/SPE Asia Pacific Drilling Technology Conference and Exhibition*. Ho Chi Minh City, Vietnam, November 1-3.

Moraveji, M. K., and Naderi, M. (2016). Drilling rate of penetration prediction and optimization using response surface methodology and bat algorithm. *Journal of Natural Gas Science and Engineering*, v. 31, pp. 829-841.

Motahhari, H. R., Hareland, G., and James, J. A. (2010). Improved Drilling Efficiency Technique Using Integrated PDM and PDC Bit Parameters. *Journal of Canadian Petroleum Technology*, v. 49, no. 10, pp. 45-52.

Murphy, K. P. (2012). *Machine Learning: A Probabilistic Perspective*. The MIT Press, 4th Printing 2013.

Murray, A. S., and Cunningham, R. A. (1955). Effect of Mud Column Pressure on Drilling Rates. *AIME Petroleum Transactions*, v. 204, pp. 196-204.

Nascimento, A., Kutas, D. T., Elmgerbi, A., Thonhauser, G., and Mathias, M. H. (2015). Mathematical Modeling Applied to Drilling Engineering: An Application of Bourgoyne and Young ROP Model to a Presalt Case Study. *Mathematical Problems in Engineering*, v. 2015, pp. 1-9.

Nelder, J. A., and Mead, R. (1965). A Simplex Method for Function Minimization. *The Computer Journal*, v. 7, no. 4, pp. 308-313.

Neufeldt, A. C., Lai, S. W., and Kristjansson, S. D. (2018). An Algorithm to Automatically Zero Weight on Bit and Differential Pressure and Resulting Improvements in Data Quality. *IADC/SPE Drilling Conference and Exhibition*. Fort Worth, TX, USA, March 6-8.

Nocedal, J., and Wright, S. J. (2006). *Numerical Optimization*. Springer New York, 2nd Edition.

Norris, J. A., Dykstra, M. W., Beuershausen, C. C., Christensen, H., Fincher, R. W., and Ohanian, M. P. (1998). Development and Successful Application of Unique Steerable PDC Bits. *IADC/SPE Drilling Conference*. Dallas, TX, USA, March 3-6.

Nygaard, R., Hareland, G., Budiningsih, Y., Terjesen, H. E., and Stene, F. (2002). Eight Years Experience with a Drilling Optimization Simulator in the North Sea. *IADC/SPE Asia Pacific Drilling Technology Conference*. Jakarta, Indonesia, September 9-11.

Oliphant, T. E. (2007). Python for Scientific Computing. *Computing in Science & Engineering*, v. 9, no. 3, pp. 10-20.

Onyia, E. C. (1987). Geology Drilling Log – A Computer Database System for Drilling Simulation. *SPE Drilling Engineering*, pp. 27-36.

Onyia, E. C. (1988). Relationships Between Formation Strength, Drilling Strength, and Electric Log Properties. *63rd Annual Technical Conference and Exhibition*. Houston, TX, USA, October 2-5.

Pastusek, P., Owens, M., Barrette, D., Wilkins, V., Bolzan, A., Ryan, J., Akyabi, K., Reichle, M., and Pais, D. (2016). Drill Rig Control Systems: Debugging, Tuning, and Long Term Needs. *SPE Annual Technical Conference and Exhibition*. Dubai, UAE, September 26-28.

Pastusek, P., Sanderson, D., Minkevicius, A., Blakeman, Z., and Bailey, J. (2018). Drilling Interbedded and Hard Formations with PDC Bits Considering Structural Integrity Limits. *IADC/SPE Drilling Conference and Exhibition*. Fort Worth, TX, USA, March 6-8.

Payette, G. S., Pais, D., Spivey, B., Wang, L., Bailey, J. R., and Pastusek, P. (2015). Mitigating Drilling Dysfunction Using a Drilling Advisory System: Results from Recent Field Applications. *International Petroleum Technology Conference*. Doha, Qatar, December 6-9.

Payette, G. S., Spivey, B. J., Wang, L., Bailey, J. R., Sanderson, D., Kong, R., Pawson, M., and Eddy, A. (2017). A Real-Time Well-Site Based Surveillance and Optimization Platform for Drilling: Technology, Basic Workflows and Field Results. *SPE/IADC Drilling Conference and Exhibition*. The Hague, The Netherlands, March 14-16.

Pedregosa, F., Varoquaux, G., Gramfort, A., Michel, V., Thirion, B., Grisel, O., Blondel, M., Prettenhofer, P., Weiss, R., Dubourg, V., Vanderplas, J., Passos, A., Cournapeau, D., Brucher, M., Perrot, M., and Duchesnay, E. (2011). Scikit-learn: Machine Learning in Python. *Journal of Machine Learning Research*, v. 12, pp. 2825-2830.

Perneder, L., Detournay, E., and Downton, G. (2012). Bit/Rock Interface Laws in Directional Drilling. *International Journal of Rock Mechanics & Mining Sciences*, v. 51, pp. 81-90.

Pessier, R. C., and Fear, M. J. (1992). Quantifying Common Drilling Problems with Mechanical Specific Energy and a Bit-Specific Coefficient of Sliding Friction. *67th Annual Technical Conference and Exhibition of the Society of Petroleum Engineers*. Washington, D.C., USA, October 4-7.

Pessier, R., and Damschen, M. (2011). Hybrid Bits Offer Distinct Advantages in Selected Roller-Cone and PDC-Bit Applications. *SPE Drilling and Completion*, pp. 96-103.

Peterson, J. L. (1976). Diamond Drilling Model Verified in Field and Laboratory Tests. *Journal of Petroleum Technology*, pp. 213-222.

Pink, T., Harrell, L., Perez, D., Carrico, J., and Mackinnon, P. (2011). Integrated Drilling Optimization and Downhole Drilling Dynamics Enables PDC Bits to Drill in the Colorado Region of the San Juan Unconventional Gas Basin. *SPE/IADC Drilling Conference and Exhibition*. Amsterdam, The Netherlands, March 1-3.

Pink, T., Bruce, A., Kverneland, H., and Applewhite, B. (2012). Building an Automated Drilling System Where Surface Machines are Controlled by Downhole and Surface Data to Optimize the Well Construction Process. *IADC/SPE Drilling Conference and Exhibition.* San Diego, CA, USA, March 6-8.

Pink, T., Koederitz, W., Barrie, A., Bert, D., and Overgaard, D. (2013). Closed Loop Automation of Downhole Weight on Bit Improves Sliding Performance and Reduces Conservatism in Unconventional Horizontal Well Development. *SPE Annual Technical Conference and Exhibition*. New Orleans, LA, USA, September 30-October 2.

Poplin, R., Varadarajan, A. V., Blumer, K., Liu, Y., McConnell, M. V., Corrado, G. S., Peng, L. and Webster, D. R. (2018). Prediction of Cardiovascular Risk Factors from Retinal Fundus Photographs via Deep Learning. *Nature Biomedical Engineering*, v. 2, pp. 158-164.

Powell, M. J. D. (1994). A Direct Search Optimization Method that Models the Objective and Constraint Functions by Linear Interpolation. *Advances in Optimization and Numerical Analysis*, pp. 51-67.

Powell, M. J. D. (1998). Direct Search Algorithms for Optimization Calculations. *Acta Numerica*, v. 7, pp. 287-336.

Powell, M. J. D. (2007). A View of Algorithms for Optimization without Derivatives. *Mathematics Today*, v. 43, no. 5, pp. 1-12.

Rabia, H. (1985). Specific Energy as a Criterion for Bit Selection. *SPE Journal of Petroleum Technology*, pp. 1225-1229.

Rahimzadeh, H., Mostofi, M., Hashemi, A., and Salahshoor, K. (2010). Comparison of the Penetration Rate Models Using Field Data for One of the Gas Fields in Persian Gulf Area. *CPS/SPE International Oil & Gas Conference and Exhibition in China*. Beijing, China, June 8-10.

Rahimzadeh, H., Mostofi, M., and Hashemi, A. (2011). A New Method for Determining Bourgoyne and Young Penetration Rate Model Constants. *Petroleum Science and Technology*, v. 29, no. 9, pp. 886-897.

Rajabov, V., Miska, S., Mortimer, L., Yu, M., and Ozbayoglu, E. (2012). The Effects of Back Rake and Side Rake Angles on Mechanical Specific Energy of Single PDC Cutters with Selected Rocks at Varying Depth of Cuts and Confining Pressures. *IADC/SPE Drilling Conference and Exhibition*. San Diego, CA, USA, March 6-8.

Rampersad, P. R., Hareland, G., and Boonyapaluk, P. (1994). Drilling Optimization Using Drilling Data and Available Technology. *III Latin American/Caribbean Petroleum Engineering Conference*. Buenos Aires, Argentina, April 27-29.

Rashidi, B., Hareland, G., and Nygaard, R. (2008). Real-Time Drill Bit Wear Prediction by Combining Rock Energy and Drilling Strength Concepts. *Abu Dhabi International Petroleum Exhibition and Conference*. Abu Dhabi, UAE, November 3-6.

Rashidi, B., Hareland, G., and Wu, A. (2010). New Approach in Real-Time Bit Wear Prediction. *Abu Dhabi International Petroleum Exhibition and Conference*. Abu Dhabi, UAE, November 1-4.

Rashidi, B., Hareland, G., Fazaelizadeh, M., and Svigir, M. (2010). Comparative Study Using Rock Energy and Drilling Strength Models. *44th US Rock Mechanics Symposium and 5th U.S.-Canada Rock Mechanics Symposium*. Salt Lake City, UT, USA, June 27-30.

Rehm, B., Schubert, J., Haghshenas, A., Paknejad, A. S., and Hughes, J. (2008). *Managed Pressure Drilling (Gulf Drilling Series)*. Gulf Publishing Company.

Remmert, S. M., Witt, J. W., and Dupriest, F. E. (2007). Implementation of ROP Management Process in Qatar North Field. *SPE/IADC Drilling Conference*. Amsterdam, The Netherlands, February 20-22.

Robnett, E. W., Heisig, G., McGinley, P. J., and Macpherson, J. D. (2002). Real-Time Downhole Drilling Process Data Complement Surface Data in Drilling Optimization. *IADC/SPE Asia Pacific Drilling Technology Conference*. Jakarta, Indonesia, September 9-11.

Rommetveit, R., Bjorkevoll, K. S., Halsey, G. W., Larsen, H. F., Merlo, A., Nossaman, L. N., Sweep, M. N., Silseth, K. N., and Odegaard, S. I. (2004). Drilltronics: An Integrated System for Real-Time Optimization of the Drilling Process. *IADC/SPE Drilling Conference.* Dallas, TX, USA, March 2-4.

Rowley, D. S., Howe, R. J., and Deily, P. H. (1961). Laboratory Drilling Performance of the Full-Scale Rock Bit. *Journal of Petroleum Technology*, pp. 71-81.

Rumelhart, D. E., Hinton, G. E., and Williams, R. J. (1986). Learning Representations by Back-Propagating Errors. *Nature*, v. 323, pp. 533-536.

Sanderson, D., Payette, G. S., Spivey, B. J., Bailey, J. R., Calvo, M., Kong, R., and Eddy, A. (2017). Field Application of a Real-Time Well-Site Drilling Advisory System in the Permian Basin. *Unconventional Resources Technology Conference*. Austin, TX, USA, July 24-26.

Sankaran, S., Lugo, J., Awasthi, A., and Mijares, G. (2009). The Promise and Challenges of Digital Oilfield Solutions – Lessons Learned from Global Implementations and Future Directions. *SPE Digital Energy Conference and Exhibition*. Houston, TX, USA, April 7-8.

Scott, D. E. (1996). Development of Roller-Cone Bits with Active PDC Shear-Cutting Elements Improves Gage-Holding Ability. *SPE Drilling and Completion*, pp. 44-50.

Self, R., Atashnezhad, A., and Hareland, G. (2016). Reducing Drilling Cost by Finding Optimal Operational Parameters Using Particle Swarm Algorithm. *SPE Deepwater Drilling & Completions Conference*. Galveston, TX, USA, September 14-15.

SHARC 8 3/4 in MSi616 PDC. Smith Bits - A Schlumberger Company, 30 Mar. 2015. Web.

Shi, X., Liu, G., Gong, X., Zhang, J., Wang, J., and Zhang, H. (2016). An Efficient Approach for Real-Time Prediction of Rate of Penetration in Offshore Drilling. *Mathematical Problems in Engineering*, pp. 1-13.

Shishavan, R. A., Hubbell, C., Perez, H. D., Hedengren, J. D., Pixton, D. S., and Pink, A. P. (2016). Multivariate Control for Managed-Pressure-Drilling Systems by Use of High-Speed Telemetry. *SPE Journal*, pp. 459-470.

Sikes, S. T. (1936). Drilling Speeds. *API Drilling and Production Practice*, pp. 54-59.

Simon, R. (1963). Energy Balance in Rock Drilling. *Society of Petroleum Engineers Journal*, pp. 298-306.

Sinor, A., and Warren, T. M. (1989). Drag Bit Wear Model. *SPE Drilling Engineering*, pp. 128-136.

Sinor, L. A., Powers, J. R., and Warren, T. M. (1998). The Effect of PDC Cutter Density, Back Rake, Size, and Speed on Performance. *IADC/SPE Drilling Conference.* Dallas, TX, USA, March 3-6.

Soares, C. (2015). Development and Applications of a New System to Analyze Field Data and Compare Rate of Penetration (ROP) Models. *M.S. Thesis*. The University of Texas at Austin.

Soares, C., Daigle, H., and Gray, K. (2016). Evaluation of PDC Bit ROP Models and the Effect of Rock Strength on Model Coefficients. *Journal of Natural Gas Science and Engineering*, v. 34, pp. 1225-1236.

Soares, C., and Gray, K. (2018). Real-Time Predictive Capabilities of Analytical and Machine Learning Rate of Penetration (ROP) Models. Under Review.

Soares, C., Daigle, H., Pyrcz, M., Millwater, H., and Gray, K. (2018). Data Segmentation Techniques for Real-Time Drilling Interval Optimization with Continuous Learning of Analytical and Machine Learning Rate of Penetration Models. Under Production.

Spivey, B. J., Payette, G. S., Wang, L., Bailey, J. R., Sanderson, D., Lai, S. W., Charkhand, B., and Eddy, A. (2017). Challenges and Lessons from Implementing a Real-Time Drilling Advisory System. *SPE Annual Technical Conference and Exhibition*. San Antonio, TX, USA, October 9-11.

Sugiura, J., Samuel, R., Oppelt, J., Ostermeyer, G. P., Hedengren, J., and Pastusek, P. (2015). Drilling Modeling and Simulation: Current State and Future Goals. *SPE/IADC Drilling Conference and Exhibition*. London, United Kingdom, March 17-19.

Teale, R. (1965). The Concept of Specific Energy in Rock Drilling. *International Journal of Rock Mechanics and Mining Sciences*, v. 2, pp. 57-73.

Tibbitts, G. A., Sandstrom, J. L., Black, A. D., and Green, S. J. (1981). Effects of Bit Hydraulics on Full-Scale Laboratory Drilled Shale. *Journal of Petroleum Technology*, pp. 1180-1188.

Trichel, D. K., Isbell, M., Brown, B., Flash, M., McRay, M., Nieto, J., and Fonseca, I. (2016). Using Wired Drill Pipe, High-Speed Downhole Data, and Closed Loop Drilling Automation Technology to Drive Performance Improvement Across Multiple Wells in the Bakken. *IADC/SPE Drilling Conference and Exhibition.* Fort Worth, TX, USA, March 1-3.

Umez-Eronini, E. I. (1983). Rotary Drill Bit/Rock Model with Cutter Offset. *Journal of Energy Resources Technology*, v. 105, pp. 356-361.

van Lingen, N. H. (1962). Bottom Scavenging – A Major Factor Governing Penetration Rates at Depth. *Journal of Petroleum Technology*, pp. 187-196.

van Oort, E., Rosso, R., and Cabello-Montero, J. (2005). Evolution of Real-Time Operations Monitoring: From Concept to Global Implementation. *SPE Annual Technical Conference and Exhibition*. Dallas, TX, USA, October 9-12.

Veazey, M. V. *Does a Digitization Domino Effect Await Oil and Gas?* RIGZONE, 19 Apr. 2018. Web.

Wales, D. J., and Doye, J. P. (1997). Global Optimization by Basin-Hopping and the Lowest Energy Structures of Lennard-Jones Clusters Containing up to 110 Atoms. *Journal of Physical Chemistry*, v. 101, no. 28, pp. 5111-5116.

Walker, B. H., Black, A. D., Klauber, W. P., Little, T., and Khodaverdian, M. (1986). Roller-Bit Penetration Rate Response as a Function of Rock Properties and Well Depth. *61st Annual Technical Conference and Exhibition of the Society of Petroleum Engineers.* New Orleans, LA, USA, October 5-8.

Wallace, S. P. (2015). ROP in Horizontal Shale Wells: Field Measurements, Model Comparisons, and Statistical Learning Predictions. *M.S. Thesis*. The University of Texas at Austin.

Wallace, S., Hegde, C., and Gray, K. (2015). A System for Real-Time Drilling Performance Optimization and Automation Based on Statistical Learning Methods. *SPE Middle East Intelligent Oil & Gas Conference & Exhibition*. Abu Dhabi, UAE, September 15-16.

Warren, T. M. (1981). Drilling Model for Soft-Formation Bits. *Journal of Petroleum Technology*, pp. 963-970.

Warren, T. M., and Smith, M. B. (1985). Bottomhole Stress Factors Affecting Drilling Rate at Depth. *Journal of Petroleum Technology*, pp. 1523-1533.

Warren, T. M., and Sinor, A. (1986). Drag Bit Performance Modeling. *61st Annual Technical Conference and Exhibition of the Society of Petroleum Engineers.* New Orleans, LA, USA, October 5-8.

Warren, T. M. (1987). Penetration-Rate Performance of Roller-Cone Bits. *SPE Drilling Engineering*, pp. 9-18.

Warren, T. M., and Sinor, L. A. (1994). PDC Bits: What's Needed to Meet Tomorrow's Challenge. *University of Tulsa Centennial Petroleum Engineering Symposium*, pp. 207-214. Tulsa, OK, USA, August 29-31.

Webb, J., Roze, E., Jarret, C., Le Roux, S., and Mejia, C. (2016). Drilling Engineering and Formation Evaluation: An Integrated Approach to Improve Real Time Drilling Optimization. *SPE Western Regional Meeting*. Anchorage, AK, USA, May 23-26.

Winters, W. J., Warren, T. M., and Onyia, E. C. (1987). Roller Bit Model with Rock Ductility and Cone Offset. *62nd Annual Technical Conference and Exhibition of the Society of Petroleum Engineers*. Dallas, TX, USA, September 27-30.

Wiktorski, E., Kuznetcov, A., and Sui, D. (2017). ROP Optimization and Modeling in Directional Drilling Process. *SPE Bergen One Day Seminar*. Bergen, Norway, April 5.

Xu, H., Fear, M., Whelehan, O., Ford, J., and Jensen, J. (1995). How to Organise Mud Logging Data for Modeling Rate of Penetration. *SPE Asia Pacific Oil & Gas Conference*. Kuala Lumpur, Malaysia, March 20-22.

Yan, L., Keshan, X., Seng, Y. S., Suresh, K., Ningbo, W., Jianping, W., Hongliang, Z., Peng, L., and Lu, Z. (2014). Innovative Bit Design Coupled with New Cutter Technology Improves PDC Bit Performance in Challenging Changbei Gas Field Application. *Offshore Technology Conference Asia*. Kuala Lumpur, Malaysia, March 25-58.

Yi, P., Kumar, A., and Samuel, R. (2014). Real-Time Rate of Penetration Optimization Using the Shuffled Frog Leaping Algorithm (SFLA). *SPE Intelligent Energy Conference and Exhibition*. Utrecht, The Netherlands, April 1-3.

Young, F. S., Jr. (1966). Dynamic Filtration During Microbit Drilling. *PhD Dissertation*. The University of Texas at Austin.

Young, F. S., Jr., and Gray, K. E. (1967). Dynamic Filtration During Microbit Drilling. *Journal of Petroleum Technology*, pp. 1209-1224.

Young, F. S., Jr. (1969). Computerized Drilling Control. *Journal of Petroleum Technology*, pp. 483-496.

Zborowski, M. *How ConocoPhillips Solved its Big Data Problem*. Journal of Petroleum Technology, 7 May 2018. Web.

Zhang, W., Ayers, W. J., Brown, J., and Bromhal, G. (2015). Optimizing Drilling Parameters: A Preliminary Model – Drilling Carthage Mable with Oil Based Mud and PDC Bit. *49th US Rock Mechanics / Geomechanics Symposium*. San Francisco, CA, USA, June 28-July 1.

Zhou, Y., Zhang, W., Gamwo, I. K., Lin, J. S., Eastman, H., Gill, M., and Whipple, G. (2012). Mechanical Specific Energy Versus Depth of Cut. *46th US Rock Mechanics / Geomechanics Symposium*. Chicago, IL, USA, June 24-27.